

Molecular Design Principles for Electrochemical Materials

by

Sean Emerson Doris

A dissertation submitted in partial satisfaction of the
requirements for the degree of
Doctor of Philosophy

in

Chemistry

in the

Graduate Division
of the
University of California, Berkeley

Committee in charge:

Dr. Brett Helms, Co-Chair
Professor Omar Yaghi, Co-Chair
Professor Angelica M. Stacy
Professor Kristin A. Ceder-Persson

Fall 2016

Molecular Design Principles for Electrochemical Materials

Copyright 2016
by
Sean Emerson Doris

Abstract

Molecular Design Principles for Electrochemical Materials

by

Sean Emerson Doris

Doctor of Philosophy in Chemistry

University of California, Berkeley

Dr. Brett Helms, Co-Chair

Professor Omar Yaghi, Co-Chair

Electrochemical materials play an increasingly important role in our energy landscape, and understanding their behavior at a molecular level is critical for the design of next-generation electrochemical materials that will meet our energy needs. In this dissertation, I will share my work towards the molecular design of three different classes of electrochemical materials: nanocrystals, membranes, and redox mediators.

In the first part of this dissertation, I describe my work with controlling nanocrystal (NC) surface chemistry. NCs are being actively studied due to their unique optical, thermal, electrochemical, and mechanical properties that make them uniquely suited as energy conversion and storage materials. For applications that involve electron transport to or from the NC, the insulating ligands that are commonly used to stabilize the NCs during their synthesis must be removed. I will describe my work studying and developing a new class of ligand stripping reactions that accomplishes this while preserving colloidal stability for the widest group of NC materials to date. The "naked" NC inks produced by my approach are expected to find use in a wide variety of energy conversion and storage applications.

In the second part of this dissertation, I describe my work developing and studying size-sieving membranes for next-generation batteries. Many next-generation battery chemistries, including Li-O₂, Li-S, and non-aqueous redox-flow batteries store charge with soluble active-species in non-aqueous electrolytes. Each of these chemistries requires the development of new membranes that are capable of blocking active-species crossover while allowing transport of the working-ion. I have established membranes based on polymers of intrinsic microporosity (PIMs) as a class of size-sieving membranes that accomplish this goal. In this dissertation, I outline my work applying these membranes to two different battery chemistries (Li-S and all-organic non-aqueous redox-flow batteries) and explore the impact of membrane reactivity and swelling on its active-species blocking-ability.

In the third and final part of this dissertation, I describe my work with soluble redox-mediators that aid in the electrodeposition of insulating active-materials for next-generation batteries. Many next-generation battery chemistries, including Li-O₂ and

Li-S, rely on the electrodeposition of insulating active materials to store charge. This electrodeposition process is usually self-limiting, and leads to limits on battery capacity for a given surface area of current collector. In this dissertation, I describe how I circumvent this limit by designing redox-mediators that allow electron transfer and electrodeposition to be spatially decoupled, leading to the electrodeposition of thick deposits (rather than thin coatings) of the insulating active material.

To my parents, for their constant love, support, and encouragement

Contents

List of Figures	vii
1 Introduction	1
1.1 The importance of electrochemical materials	2
1.2 Controlling the surface chemistry of nanocrystals	2
1.3 Blocking crossover of soluble active-species in batteries	3
1.3.1 Size-sieving as a mechanism for blocking active-species crossover while allowing high ionic conductivity	4
1.3.2 Polymers of intrinsic microporosity (PIMs) as a material platform for size-sieving membranes	4
1.3.3 Using computational chemistry to find the critical size-regime for active-species blocking	5
1.3.4 Membranes as active components	5
1.4 Controlling the electrodeposition of insulating active-species in batteries . .	6
1.4.1 Criteria for redox-mediators that facilitate electrodeposition	6
1.4.2 Identifying candidate redox-mediators with computational chemistry	8
2 Mechanistic Insight into the Formation of Cationic Naked Nanocrystals Generated Under Equilibrium Control	9
2.1 Introduction and prior art	10
2.2 Equilibrium control over ligand-stripping improves colloidal stability	11
2.3 Evidence for equilibrium control over surface stabilization	13
2.4 Origin of the non-coordinating counter-ion and fate of anionic ligands	15
2.5 Applications of cationic naked nanocrystals	19
2.6 Conclusions	20
2.7 Supporting information	22
2.7.1 Nanocrystal syntheses	22
2.7.2 Ligand stripping procedure	24
2.7.3 In-Situ NMR	24
2.7.4 ESI-MS	24
2.7.5 Preparation of naked nanocrystal thin films and polymer composites	25
2.7.6 Additional figures	26

2.8	Acknowledgements	40
3	A Polysulfide-Blocking Microporous Polymer Membrane Tailored for Hybrid Li–Sulfur Flow Batteries	41
3.1	Introduction and prior art	42
3.2	Molecular dynamics simulations of solvated polysulfides	43
3.3	Transport of supporting electrolyte and active material in PIM-1 membranes	45
3.4	Improved capacity retention for batteries with PIM-1 membranes	46
3.5	Conclusions and future work	47
3.6	Supporting information	49
3.6.1	Materials and methods	49
3.6.2	Computational methods	50
3.6.3	Additional figures	51
3.6.4	Acknowledgements	55
4	Understanding and Controlling the Chemical Evolution and Polysulfide-Blocking Ability of Lithium–Sulfur Battery Membranes Cast from Polymers of Intrinsic Microporosity	56
4.1	Introduction and prior art	57
4.2	Concentration-Dependent crossover behavior	58
4.3	Verification of reaction pathway with a model compound	60
4.4	<i>In-Situ</i> FT-IR of PIM-1 membranes	61
4.5	Nitrogen adsorption of PIM-1 membranes	62
4.6	Cross-Linking of PIM-1 to prevent chemically-induced changes in pore architecture	64
4.7	Lithium–Sulfur batteries incorporating native and cross-linked PIM-1 membranes	65
4.8	Conclusions	66
4.9	Supporting information	67
4.9.1	Materials and methods	67
4.9.2	Crossover measurement and analysis	67
4.9.3	Characterization of chemically transformed model compound	69
4.9.4	Characterization of chemically transformed PIM-1	73
4.9.5	Ionic conductivity of PIM-1 membranes	78
4.9.6	Li–S battery assembly and testing	78
4.9.7	Acknowledgements	80
5	Redox-Switchable Microporous Polymer Membranes that Extend the Cycle-Life of Lithium-Sulfur Batteries	81
5.1	Introduction and prior art	82
5.2	Computational screening of monomers for redox-switchable behavior	83
5.3	Adaptive transport of lithium polysulfides through PIM-7 membranes	85

5.4	Improved cycle-life in lithium sulfur batteries using PIM-7 membranes . . .	89
5.5	Conclusions and future work	90
5.6	Supporting information	91
5.6.1	Materials and methods	91
5.6.2	Materials genome screening for PIM reactivity	100
5.6.3	Scanning electron microscopy of PIM-1 and PIM-7 selective layers on Celgard®	102
5.6.4	Polysulfide crossover measurements and analysis	103
5.6.5	Electrochemical impedance spectroscopy during membrane evolution	104
5.6.6	Acknowledgements	104
6	Macromolecular Design Strategies for Preventing Active-Material Crossover in Non-Aqueous All-Organic Redox-Flow Batteries	106
6.1	Introduction and prior art	107
6.2	Computational prediction of the solvated structures of organic redox-active molecules and oligomers	108
6.3	Controlling the active-material crossover rate by manipulating molecular size	109
6.4	Further improvement in crossover rate by controlling membrane pore size and degree of swelling	111
6.5	Oligomerization as a generalizable strategy	112
6.6	Conclusions and future work	112
6.7	Supporting information	113
6.7.1	Materials and methods	113
6.7.2	Computational methods	118
6.7.3	Electrochemical properties of ROM and RAOs	125
6.7.4	Crossover measurements and analysis	126
6.7.5	Characterization of cross-linked PIM-1 membranes	131
6.7.6	Membrane ionic conductivity	131
6.7.7	Acknowledgements	132
7	Supramolecular Perylene Bisimide-Polysulfide Gel Networks as Nanos- tructured Redox Mediators in Dissolved Polysulfide Lithium-Sulfur Bat- teries	133
7.1	Introduction and prior art	134
7.2	Design criteria of supramolecular redox mediator and electrochemical val- idation of the high-throughput computational platform	135
7.3	Characterization of PBI self-assembly and PBI-PS gel morphology	137
7.4	Supromolecular redox mediators in Li-S cells	138
7.5	Conclusions and future work	141
7.6	Supporting information	142
7.6.1	Synthetic procedures and characterization	142
7.6.2	Computational details	145

7.6.3	CV and Li–S cell testing	150
7.6.4	UV-Vis spectroscopy	155
7.6.5	Scanning electron microscopy	156
7.6.6	Electrochemical impedance spectroscopy	157
7.6.7	NMR spectra	159
7.6.8	Acknowledgements	162
8	3-Dimensional Growth of Li₂S in Lithium–Sulfur Batteries Promoted by a Redox Mediator	163
8.1	Introduction and prior art	164
8.2	Computational screening of candidate molecules and synthesis of a potential-matched redox mediator	165
8.3	Performance of Li–S batteries with the addition of a redox mediator matched to the Li ₂ S deposition potential	167
8.4	Electron microscopy and electrochemical experiments to understand the effect of the redox mediator on Li ₂ S morphology	168
8.5	Conclusions and future work	171
8.6	Supporting information	173
8.6.1	Computational details	173
8.6.2	Synthetic procedures and characterization	175
8.6.3	Electrochemistry	177
8.6.4	Li–S cell testing	178
8.6.5	Scanning electron microscopy at various states of charge	182
8.6.6	Potentiostatic electrodeposition experiments	188
8.6.7	NMR spectra	191
8.6.8	Acknowledgements	193
9	Conclusion and Outlook	194
9.1	Controlling nanocrystal surface chemistry	195
9.2	Size-selective membranes for energy storage applications	195
9.2.1	The effect of electrolyte on PIM pore structure	196
9.2.2	The role of cross-linking in controlling membrane swelling	196
9.2.3	The mechanism for ion conduction in PIM membranes	196
9.3	Controlling the electrodeposition of insulating active-species in batteries	197
	Bibliography	198
A	Materials and Methods	218
A.1	Materials	219
A.1.1	Reagents and chemicals	219
A.1.2	Electrodes for Swagelok cells	220
A.1.3	Other materials	220

A.1.4	Preparation of electrolytes and polysulfides	220
A.2	Instrumentation	221
A.2.1	Spectroscopy	221
A.2.2	Imaging	221
A.2.3	Electrochemistry	221
A.2.4	Mass spectrometry	221
A.2.5	Other instrumentation and general details	222
B	Theory	223
B.1	Crossover analysis	224
B.1.1	Calculation of D_{eff} from measured $C(t)$	224
B.1.2	Calculation of D_{eff} for multi-layer membranes	224
B.2	Membrane ionic conductivity	226

List of Figures

1.1	A new class of ligand-stripping reactions	3
1.2	Partition coefficient of spherical and rod-like solutes in cylindrical pores	4
1.3	Schematic of redox-mediator aided electrodeposition of an insulating active-species in a Li-S battery.	6
2.1	Mechanistic grounds distinguishing ligand-stripping chemistries	12
2.2	NMR titration of PbSe-OA with $\text{BF}_3:\text{Et}_2\text{O}$	14
2.3	^{19}F NMR evidence for BF_4^- as a non-coordinating counter-ion in naked PbSe NC dispersions	15
2.4	Disproportionation of $\text{DMF}:\text{BF}_3$	16
2.5	High resolution negative-ion mode ESI-MS of $\text{Pb}(\text{OA})_2 + \text{BF}_3:\text{Et}_2\text{O}$	17
2.6	Reaction pathways available to OA^- in the presence of $\text{BF}_3:\text{Et}_2\text{O}$ to yield BF_4^-	18
2.7	Comparison of different ligand stripping reagents for PbSe-OA and their effect on film quality	19
2.8	PbSe polymer composites deposited directly from solution	20
2.9	FT-IR of ligand-coated and ligand-stripped NCs	26
2.10	Energy dispersive X-ray (EDX) spectra of ligand-coated and ligand-stripped NCs	27
2.11	^1H and ^{19}F NMR spectra of cationic naked PbSe NCs in DMF	28
2.12	Zeta potential distributions for cationic naked NC dispersions	28
2.13	TEM of ligand-coated and ligand-stripped NC	29
2.14	XRD of ligand-coated and ligand-stripped NCs	30
2.15	^1H -DOSY of PbSe-OA in toluene- d_8	31
2.16	^1H -DOSY of oleic acid in toluene- d_8	32
2.17	^1H -DOSY of alkene resonances of PbSe-OA during $\text{BF}_3:\text{Et}_2\text{O}$ titration	33
2.18	^{19}F NMR spectrum of $\text{BF}_3:\text{Et}_2\text{O}$ and $\text{Pb}(\text{OA})_2 + 2 \text{BF}_3:\text{Et}_2\text{O}$ in benzene- d_6	34
2.19	^{19}F NMR spectrum of $\text{BF}_3:\text{Et}_2\text{O}$ in $\text{DMF}-d_7$	35
2.20	Isotope distribution patterns for ESI-MS of $\text{Pb}(\text{OA})_2 + \text{BF}_3:\text{Et}_2\text{O}$	36
2.21	Grazing incidence small angle X-ray scattering patterns for thin films of PbSe stripped via different methods	37

2.22	SEM of ligand-stripped PbSe thin-film deposited from solution (enlarged view)	38
2.23	SEM of a ligand-stripped PbSe-block copolymer mesostructured composite (enlarged view)	39
3.1	Ion-selective transport across membranes fabricated from PIM-1	43
3.2	Molecular dynamics simulations of solvated polysulfides	44
3.3	Ionic conductivity and active-species crossover of a PIM-1 membrane compared to Celgard®	45
3.4	Performance of a Li-S battery with PIM-1 membrane	47
3.5	Cross-sectional SEM of free-standing PIM-1 membrane	51
3.6	SWV calibration curve for measuring PS concentration	51
3.7	CV calibration curve for measuring PS concentration	52
3.8	EIS of Li-S cells with PIM-1 and Celgard membranes	52
3.9	Volumetric energy densities of all batteries tested	53
3.10	Coulombic efficiencies of all batteries tested	53
3.11	Discharge and charge profiles for Li-S batteries with and without PIM-1 membranes	54
3.12	Coulombic efficiency of a Li-S battery with PIM-1 membrane	55
4.1	Proposed chemical reactivity between PIM-1 and lithium polysulfides	57
4.2	Concentration-Dependent crossover of Li_2S_n through PIM-1	59
4.3	Reactivity of a model compound for PIM-1	60
4.4	FT-IR of PIM-1 in the presence of Li_2S_8	61
4.5	Pore-size distribution of PIM-1 with and without exposure to Li_2S_8	62
4.6	Control over structural evolution of chemically-transformed PIM-1 membranes via cross-linking	63
4.7	Galvanostatic discharge curves for Li-S cells equipped with native and cross-linked PIM-1 membranes	65
4.8	Calibration plot relating current to polysulfide concentration	68
4.9	Assignment of $^1\text{H-NMR}$ of reacted model compound	70
4.10	Variable temperature $^1\text{H-NMR}$ of model compound 1 + 20 equiv. Li_2S_8	71
4.11	$^1\text{H-COSY}$ of model compound 1 + 20 equiv. Li_2S_8	71
4.12	ESI-MS showing the most intense peak assigned to $[\text{M}+\text{SH}]^-$	72
4.13	Lower intensity region from Figure 4.12 highlighting peaks attributed to both nitrile groups of the model compound reacting with polysulfide.	73
4.14	FT-IR of PIM-1 treated with Li_2S_8 and then soaked in electrolyte	74
4.15	FT-IR of PIM-1 in the presence of different concentrations of Li_2S_8	74
4.16	Measured and simulated PIM-1 nitrogen adsorption isotherms	75
4.17	FT-IR of cross-linked PIM-1 membranes before and after thermal treatment	76
4.18	FT-IR of cross-linked PIM-1 soaked in Li_2S_8	77

4.19	Electrochemical impedance spectra of native and cross-linked PIM-1 membranes	78
4.20	Cycling performance and coulombic efficiency of Li–S cells equipped with native and cross-linked PIM-1 membranes	79
5.1	Directed evolution of a microporous polymer membrane’s ion-transport selectivity	82
5.2	Predictive design of redox-switchable monomer segments for adaptive microporous polymer membranes tailored for lithium–sulfur batteries.	84
5.3	Direct evidence that PIM-7 is reduced to a di-lithiated state in the desired potential window for a lithium–sulfur battery and that this reduction occurs on contact with sulfur-based reductants	85
5.4	Superior polysulfide-blocking ability by supported PIM-7 membranes and their adaptive transport behaviors in response to lithium polysulfides	86
5.5	Putting the adaptive polysulfide-blocking ability of supported PIM-7 membranes to work in Li–S electrochemical cells.	88
5.6	^1H NMR of PIM-7 precursor A	92
5.7	^{13}C NMR of PIM-7 precursor A	93
5.8	^1H - ^{13}C HSQC NMR of PIM-7 precursor A	94
5.9	^1H NMR of PIM-7 precursor B	96
5.10	^{13}C NMR of PIM-7 precursor B	97
5.11	^1H - ^{13}C HSQC NMR of PIM-7 precursor B	98
5.12	^1H NMR of PIM-7.	99
5.13	Scatter plot depicting the DFT-calculated first and second reduction potentials for all organic molecules in our candidate pool for redox-active PIM monomer segments.	101
5.14	Cross-sectional SEM of PIM-1 supported on Celgard.	102
5.15	Cross-sectional SEM of PIM-7 supported on Celgard	102
5.16	Calibration plot of CV peak current as a function of sulfur concentration	103
5.17	Representative electrochemical impedance spectrum for electrolyte-soaked PIM-7 on Celgard [®]	104
6.1	Macromolecular design strategies for preventing active-material crossover in all-organic redox-flow batteries	107
6.2	Computed solvation structures of 1a , 2a , and 3a for different states-of-charge.	109
6.3	Crossover behavior of 1a–3a through Celgard [®] , native PIM-1, and cross-linked PIM-1 membranes.	110
6.4	RAO concentration (C_{eq}) in the permeate compartment as a function of time (t) for a) 3b and b) 3c paired with non-selective mesoporous and cross-linked PIM-1 membranes.	111

6.5	Viologen monomer (1a) at 2+ state of charge and optimal configurations of its HOMO and LUMO orbitals.	120
6.6	Viologen dimer (2a) at 4+ state of charge and optimal configurations of its HOMO and LUMO orbitals.	120
6.7	Viologen trimer (3a) at 6+ state of charge and optimal configurations of its HOMO and LUMO orbitals.	121
6.8	Free energy profile for 1a ¹⁺ with PF ₆ ⁻	123
6.9	Free energy profiles for 1a ¹⁺ and 1a ²⁺ with ACN.	124
6.10	Cyclic voltammograms of ROMs and RAOs 1a–3c	125
6.11	Calibration plots for measuring concentration of ROM and RAOs	127
6.12	Measured concentration of ROM or RAO in the permeate compartment as a function of time and linear fits for 1a–3c	129
6.13	FT-IR spectra of cross-linked PIM-1 membranes before and after cross-linking reaction	131
6.14	EIS spectra of Celgard [®] and cross-linked PIM-1	131
7.1	Structure of PBI aggregates in solution and computational screening of candidate molecules	136
7.2	Evidence for the assembly of PBI 1 and the formation of a gel in the presence of lithium polysulfides	137
7.3	Battery performance in the presence of PBI 1	139
7.4	Battery performance in the presence of PBI 1 and carbon cloth	140
7.5	Molecular structures with electron affinity (E_{ea}) and ionization potential (E_i) calculated with the high-throughput computational model	146
7.6	Continuation of Figure 7.5.	147
7.7	Computed structures of PBI crosslinking reaction	150
7.8	Cyclic voltammograms of PBI 1 at various scan rates.	151
7.9	UV-visible-NIR spectroscopic evidence for the reversibility of PBI 1 reduction	156
7.10	Fibrous nanostructured networks of a PBI 1 + Li ₂ S ₈ xerogel imaged with SEM.	157
7.11	Cell impedance of Li–S cells with and without PBI 1	158
7.12	¹ H NMR spectrum of 2	159
7.13	¹ H NMR spectrum of 3	160
7.14	¹ H NMR spectrum of 4	161
7.15	¹ H NMR spectrum of 1	162
8.1	Schematic of Li ₂ S electrodeposition onto C cloth in the absence and presence of a redox mediator	164
8.2	Chemical structure and electrochemical properties of the BPI redox mediator	166
8.3	Progressive electrodeposition of Li ₂ S on C cloth	169
8.4	Current transients during the potentiostatic deposition of Li ₂ S on C cloth .	170
8.5	Structures for which the E_{ea} was calculated.	174

8.6	Cyclic voltammograms of BPI, Li_2S_8 , and $\text{Li}_2\text{S}_8 + \text{BPI}$	178
8.7	BPI at 1–5 <i>wt%</i> in electrolyte.	179
8.8	Li–S cells without C cloth, with and without BPI.	180
8.9	Charge and discharge capacities for Li–S cells with and without BPI at various rates	181
8.10	Discharge capacity and Coulombic efficiency of Li–S cells with and without BPI over 100 cycles at C/8 rate	181
8.11	Discharge capacity and Coulombic efficiency of Li–S cells with and without BPI over 100 cycles at C/2 rate	182
8.12	Progressive electrodeposition of Li_2S on C cloth (lower magnification) . . .	183
8.13	Points at which Li–S cells loaded with BPI were stopped to image the Li_2S electrodeposition on C cloth.	184
8.14	Points at which Li–S cells that do not contain BPI were stopped to image the Li_2S electrodeposition on C cloth.	184
8.15	Li_2S on C cloth after discharge of a cell containing BPI, but introduced as part of the electrolyte.	185
8.16	SEM images of C cloth containing BPI after exposure to polysulfides and washed by the standard procedure.	187
8.17	SEM images of C cloth with no BPI after exposure to polysulfides and washed by the standard procedure.	188
8.18	SEM images of C cloth from a Li–S cell with BPI, but with no polysulfide, washed with the same procedure used to image Li_2S at different states of charge.	188
8.19	Overlaid experimental data and model fits for potentiostatic electrodeposition experiments.	190
8.20	^1H NMR spectrum of 2	191
8.21	^1H NMR spectrum of 3	192
8.22	^1H NMR spectrum of BPI.	193
B.1	Concentration profile across a composite layered membrane.	225
B.2	Equivalent circuit used to model electrochemical impedance spectra of membranes soaked in electrolyte.	227

Acknowledgments

First, I would like to acknowledge the scientific guidance of Dr. Brett Helms, who I have had the pleasure of working with on two separate occasions: first as an undergraduate intern and later as a Ph.D. student. I would also like to thank Prof. Omar Yaghi for serving as my academic advisor and enabling me to pursue research at Lawrence Berkeley National Laboratory. I am also grateful to my dissertation and qualifying exam committees, including Dr. Brett Helms, Prof. Omar Yaghi, Prof. Angie Stacey, Prof. Fiona Doyle, Prof. Kristin Ceder-Persson, Prof. Marcin Majda, and Prof. Tanja Cuk, for their investment in me.

The majority of my Ph.D. tenure was funded by the Department of Defense through the National Defense Science and Engineering Graduate Fellowship, and I am thankful for the academic freedom that this fellowship gave me. I am also appreciative of the Joint Center for Energy Storage Research for kick-starting several very productive interdisciplinary and inter-institutional collaborations that are featured in this dissertation.

The vast majority of the experimental work presented in this dissertation was performed at the Molecular Foundry, and I would like to thank all the staff scientists, technical staff, postdoctoral scholars, and students that have helped me along the way. In particular, this includes all the Helms group members I've had the pleasure of working with, including Dr. Evelyn Rosen, Dr. Andrew Wills, Dr. Georgeta Masson, Teresa Williams, Dr. Laura Gerber, Dr. Pete Frischmann, Dr. Ash Ward, Dr. Lorenzo Maserati, Dr. Changyi Li, Stephen Meckler, Dr. Longjun Li, Dr. Lin Ma, Dr. Peter Christensen, and Dr. Miles Braten. I would also like to thank all my co-authors, which include many of the people named above, as well as Dr. Jared Lynch, Dr. Jeff Urban, Dr. Tod Pascal, Dr. David Prendergast, Erica Tsai, Frank Fan, Dr. Xiaohui Qu, Dr. Anubhav Jain, Prof. Yet-Ming Chiang, Angelique Scheuermann, Dr. Artem Baskin, Prof. Nagarjuna Gavalapalli, Dr. Etienne Chénard, Prof. Jeff Moore, Dr. Christo Sevov, and Mark Hughes Jr.

Finally, I couldn't have done any of this work without the love and support of my family and friends – in particular my wife, Sarah Woldemariam, who has been a supportive partner even as she pursues her own Ph.D. I'm also thankful for my friends, many of which are named above, but also David Herlihy, Heather Jensen, David Hanifi, and others.

Chapter 1

Introduction

1.1 The importance of electrochemical materials

With the explosive growth in worldwide energy demand expected to continue^[1] into the foreseeable future, electrochemical materials play a central role in ongoing efforts to make our society's energy usage more sustainable. Electrochemical materials play an important role in all parts of our energy economy, from serving as light-harvesting elements in photovoltaic cells,^[2-4] to storing renewable energy for the grid and transportation,^[5, 6] to improving energy efficiency.^[7] By understanding, at a molecular level, how to design and improve electrochemical materials for these applications, the scientific community can meet society's growing demand for energy in a sustainable way. In this dissertation, I will outline my efforts to contribute towards our understanding of electrochemical materials as they relate to three classes of materials: nanocrystals, membranes, and redox mediators. A description of each of these research areas follows.

1.2 Controlling the surface chemistry of nanocrystals

Nanocrystals (NCs) are an exciting class of materials that, due to their small size, have interesting properties that are promising for their use in a wide range of applications. Many of these applications depend on the unique optical properties of NCs, including using NCs as light absorbing elements in photovoltaic cells,^[3] as upconverting light absorbers for energy and biological imaging applications,^[8] as phosphors for displays,^[9] and as tunable components in electrochromic devices.^[10] Other applications rely on the mechanical or thermal properties of NCs, including their use as energy storage^[11] or thermoelectric materials.^[12] In all cases, the surface chemistry of NCs has a profound effect on their properties and processability.

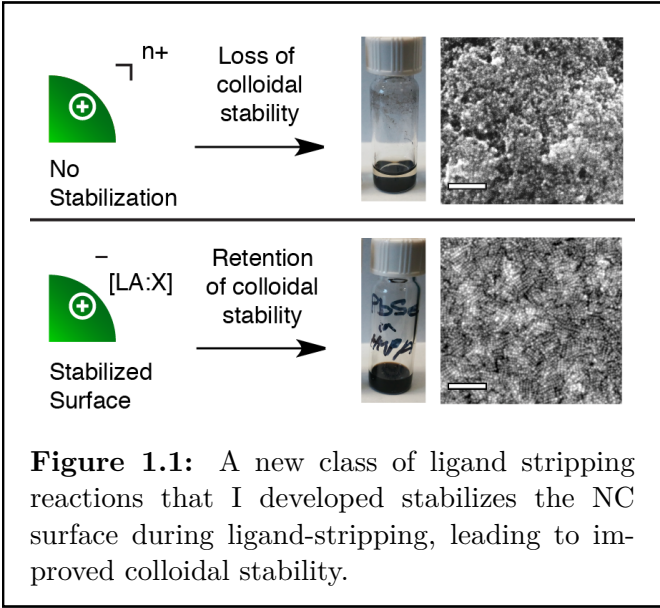
The surface chemistry of NCs is strongly influenced by their synthesis. For NCs that are synthesized colloidally, surface-bound ligands control the rate of crystal growth and ensure dispersibility. While these ligands are useful for synthetic purposes, they are usually electronically insulating and must be removed from the NC surface before charge carriers can freely move to or from the NC. Exchanging long organic surface-bound ligands with short-chain ligands can lower the barrier to inter-NC electron transport, but these shorter ligands are no longer capable of preventing NC aggregation.^[13-15] As a result, these ligand exchanges are usually performed on thin-films of NCs. Due to the large volume change that results from this ligand exchange strategy, cracks develop in the NC films, and additional rounds of NC deposition, stripping, and annealing are required to obtain continuous, conductive films of NCs. On the other hand, if the surface-bound ligands can be removed while keeping the NCs in a stable dispersion, inks of "naked" NCs can be prepared. These naked NC inks can then be directly deposited in a single step to yield ligand-free NC thin films. An additional advantage of this approach is that more complicated mesostructures, including polymer-NC composites, can be

formed in a single step.

Naked NC inks are stabilized by electrostatic repulsion between NCs. Commonly, semiconductor NCs consist of a stoichiometric core with an excess of metal ions on the NC surface.^[16–18] These excess metal ions are then bound by organic ligands, commonly through a carboxylate group.^[19–23] Our group previously developed ligand-stripping reagents that alkylate the surface-bound ligand, rendering it non-coordinating and leaving behind a cationic naked NC (with charge balanced by a non-coordinating anion like BF_4^-).^[24, 25]

While this approach was successful for

a wide variety of NCs, we found that for certain classes of NCs, including lead chalcogenides, the stripping reaction leads to the desorption of surface-bound excess metal cations, which led to the aggregation of NCs. In chapter 2, I show how I solved this problem by developing a new class of ligand-stripping reactions that stabilizes the NC surface and prevents this loss of colloidal stability (Figure 1.1).^[26] Because this approach is so versatile and gentle, it has already found use in the field.^[27] Moving forward, the materials that are newly accessible with this approach are expected to find use as electrochemical materials, including as electrocatalysts, photoelectrocatalysts, and electrodes for batteries and capacitors.



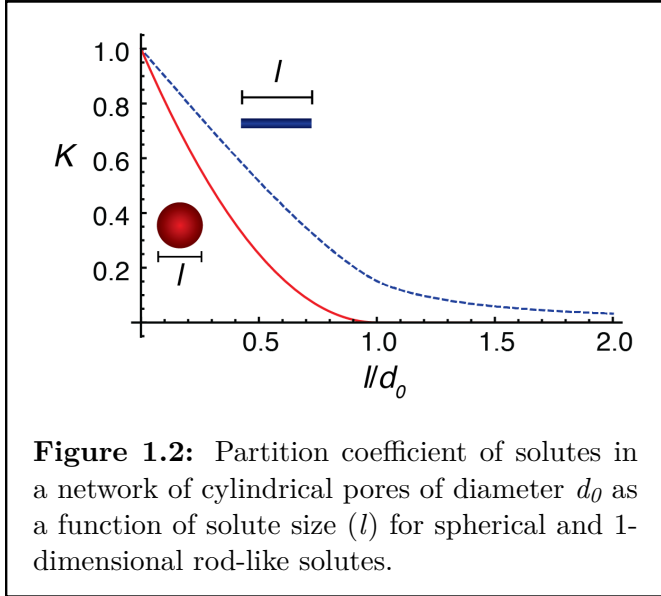
1.3 Blocking crossover of soluble active-species in batteries

Many next-generation batteries, including Li-O_2 ,^[28–30] Li-S ,^[31–36] and non-aqueous redox-flow batteries^[5, 37–40] use dissolved active-species in non-aqueous electrolytes to store charge. These batteries pose a unique challenge, as the active-species can diffuse across the cell and react with the active-species on the other side of the cell, leading to Coulombic inefficiencies, active-material loss, and cell death. This can be avoided by separating the two halves of the cell with a membrane that blocks active-species crossover while allowing conduction of the working ion. Several strategies for ion-selective transport in non-aqueous electrolytes have been suggested, including the use of ion-conducting ceramics,^[41] ion-exchange membranes,^[42, 43] and solid polymer electrolytes.^[44] However, each of these strategies is limited by high cost, poor scalability, or low ionic conductivity. In an effort to circumvent these limitations, I hypothesized that size-sieving membranes with pores

larger than the working ion but smaller than the active-species could block active-species crossover at minimal cost to ionic conductivity.

1.3.1 Size-sieving as a mechanism for blocking active-species crossover while allowing high ionic conductivity

Size-exclusion and diffusion of species within porous networks have been studied extensively for their applications in size-exclusion chromatography, catalysis, and nanofiltration.^[45, 46] For a rigid pore network, species that are comparable in size to the pores are excluded to some extent from the pore volume. The extent of exclusion can be quantified by the equilibrium partition coefficient, K , which is the ratio of the concentration of the species in the pore to the bulk solution concentration of that species. For simple pore systems and well-defined solute size and shape, K can be predicted from statistical mechanics.^[45] The calculated partition coefficients for spherical and one-dimensional rod-like solutes in cylindrical pores are shown in Figure 1.2. Spherical solutes with diameters larger than the pore diameter are completely excluded from the pore volume, while one-dimensional rods that are longer than the pore diameter are only partially excluded. Size-sieving of an active-species can be achieved by selecting a membrane/active-species system where the active-species is larger than the membrane pore, while the working ion is small enough to pass through unimpeded. First, I will address my choice of membrane platform, followed by a discussion of the design of active-materials that will be blocked by size-selective membranes.



The calculated partition coefficients for spherical and one-dimensional rod-like solutes in cylindrical pores are shown in Figure 1.2. Spherical solutes with diameters larger than the pore diameter are completely excluded from the pore volume, while one-dimensional rods that are longer than the pore diameter are only partially excluded. Size-sieving of an active-species can be achieved by selecting a membrane/active-species system where the active-species is larger than the membrane pore, while the working ion is small enough to pass through unimpeded. First, I will address my choice of membrane platform, followed by a discussion of the design of active-materials that will be blocked by size-selective membranes.

1.3.2 Polymers of intrinsic microporosity (PIMs) as a material platform for size-sieving membranes

A number of materials have pores with appropriate dimensions for blocking active-material crossover while allowing ion conduction, including zeolites,^[47] metal organic frameworks,^[48–50] carbon nano-tubes,^[51–53] and microporous organic polymers.^[54, 55] I chose to focus on a class of microporous organic polymers known as polymers of intrinsic microporosity (PIMs) as a selective membrane material due to their processability,

membrane forming characteristics, and scalability. Soluble PIMs feature rigid linear backbones with intermittent kinks. These two features hinder the packing of polymer chains in the solid-state, which creates permanent microporosity in the polymer structure.^[54, 56–59] Since the PIMs are soluble, they can be solution-processed into free-standing or supported membranes via drop-casting, spray-coating, blade-coating, or any other suitable processing approach. Once a suitable membrane is prepared, the membrane’s pores can be filled with a liquid electrolyte to form an ionically conductive membrane.

1.3.3 Using computational chemistry to find the critical size-regime for active-species blocking

Computational chemistry can be used to predict if a given redox-active species is large enough to be excluded by a size-sieving membrane. In chapter 3, we used molecular dynamics simulations of lithium polysulfides and solvated lithium salts to identify the critical size-regime for blocking lithium polysulfides from crossing through the membrane while allowing lithium transport. We found that pores ~ 0.8 – 1.0 nm in diameter should be able to block the crossover of lithium polysulfides in ethereal electrolytes. Indeed, when I tested this hypothesis with membranes prepared from PIM-1 (with ~ 0.9 nm pores in the dry state), I observed a 500-fold improvement in polysulfide blocking ability compared to mesoporous separators. I was able to leverage this improved blocking ability to dramatically improve the cycle-life and efficiency of Li–S cells.

Despite the small size-difference between solvated lithium ions and lithium polysulfides, PIM membranes were able to discriminate between the active-species and working ion and improve the performance of Li–S batteries. I hypothesized that further improvements in membrane blocking-ability could be obtained for larger active-species. To test this hypothesis, we designed a series of redox-active organic oligomers (RAOs) and studied their solvated structure with *ab initio* quantum mechanical calculations and molecular dynamics simulations. As described in chapter 6, by increasing the molecular size to be larger than the membrane’s pore size, I was able to decrease crossover nearly four orders of magnitude compared to a non-selective separator with only a 5-fold decrease in ionic conductivity.

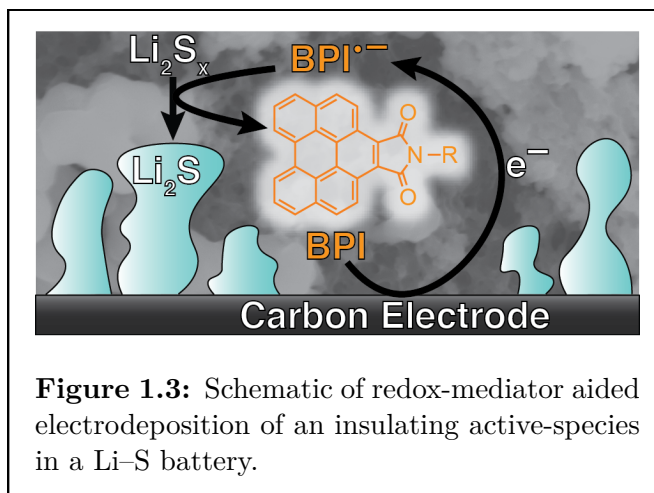
1.3.4 Membranes as active components

PIM membranes are not static components, and understanding how they change during battery operation is critical for tuning their performance. For example, I noted in chapter 4 that PIM membranes react with soluble lithium polysulfides to form a lithiated thioamide group on the polymer backbone. This led to a change in polymer swelling and a decrease in blocking-ability. By understanding the membrane’s reactivity and its role on blocking-ability, I was able to design cross-linked membranes that do not suffer from this undesirable chemically-induced change in membrane selectivity. These cross-linked membranes, in turn, improved the cycle life of Li–S batteries.

Of course, it is also possible to design membranes that react with the active-species in a desirable manner. In chapter 5, I discuss my work in designing PIM membranes that are reduced by lithium polysulfides during the operation of Li-S batteries. In this case, the reactivity of the membrane introduces charges within the polymer structure and leads to an increase, rather than decrease, in membrane selectivity. Li-S batteries prepared with these adaptive PIM membranes had the best performance of any Li-S batteries incorporating PIM membranes to date.

1.4 Controlling the electrodeposition of insulating active-species in batteries

Many next-generation battery chemistries, including Li-S^[31–36] and Li-O₂,^[28–30] store charge though the electrodeposition of insulating solids during discharge and/or charge. This process poses a clear difficulty, namely that the deposition of a thin layer of insulating solid on the battery electrode will prevent further charge transfer at the electrode-electrolyte interface. I hypothesized that the amount of active-material electrodeposited on a given surface of electrode could be increased by introducing a

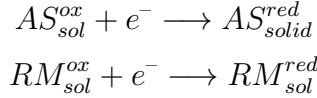


redox-mediator that competes with the active-species for electron transfer and goes on to remotely react with the active-species away from the electrode surface. Thus, instead of growing thin, self-limiting layers of the active-material on the electrode surface, thick deposits of the active material can be formed. This improves the energy storage density for batteries based on chemistries that rely on electrodeposition of insulating active-materials, as less inactive conductive carbon additive is required if more active material can be deposited on a given surface of the electrode.

1.4.1 Criteria for redox-mediators that facilitate electrodeposition

Redox mediators for electrodeposition must meet several requirements. The redox mediator must be soluble in the electrolyte of interest at a reasonably high concentration, should not react with any of the battery components, and must be redox-active within a narrow range of potentials. The narrow range of acceptable potentials is the result of

two additional requirements: 1) The reaction of reduced (for cathodic electrodeposition) or oxidized (for anodic electrodeposition) redox mediator with the soluble active species should be thermodynamically favored and 2) the reduction (or oxidation, as appropriate) should be kinetically faster than the reduction (or oxidation) of the soluble active species. Consider the cathodic electrodeposition of an active-species (AS) in the presence of a redox mediator (RM):



The reaction of the reduced redox mediator (RM^{red}) with oxidized active-species (AS^{ox}) is described by the equilibrium constant K :

$$\begin{aligned} RM_{sol}^{red} + AS_{sol}^{ox} &\rightleftharpoons RM_{sol}^{ox} + AS_{solid}^{red} \\ K &= \frac{[RM^{ox}]}{[RM^{red}][AS^{ox}]} \end{aligned}$$

where $[RM^{ox}]$, $[RM^{red}]$, and $[AS^{ox}]$ are the concentrations of oxidized redox-mediator, reduced redox-mediator, and oxidized active-species, respectively.

K can be expressed in terms of the formal potential of each redox-pair:

$$K = \exp\left(\frac{nF}{RT} [E_{AS}^{0'} - E_{RM}^{0'}]\right)$$

The choice of the minimum value of K is somewhat arbitrary, but for a modest value of $K = 5$, the redox-mediator's formal potential must be ~ 40 mV negative of the active-species' formal potential.

On the other hand, the requirement for faster electron-transfer kinetics favors molecules with more positive formal potentials, as shown below. Neglecting the rate of the back-reaction, the rate constants for electron transfer (at $E = E_{AS}^{0'}$) are given by:

$$k_{forward, RM} = k_{RM}^0 \exp\left(-\alpha_{RM} f (E_{AS}^{0'} - E_{RM}^{0'})\right)$$

$$k_{forward, AS} = k_{AS}^0$$

where $k_{forward, RM}$ and $k_{forward, AS}$ are the forward rate constants for redox-mediator and active-species reduction, respectively, k_{RM}^0 and k_{AS}^0 are the intrinsic rate constants for the redox-mediator and active-species respectively, α is the transfer coefficient, $f = F/RT$ (F is Faraday's constant, R is the gas constant, and T is temperature in K), and $E_{AS}^{0'}$ and $E_{RM}^{0'}$ are the formal potentials for the active-species and redox mediator, respectively. The ratio in rate constants is given by:

$$\frac{k_{forward, RM}}{k_{forward, AS}} = \frac{k_{RM}^0}{k_{AS}^0} \exp\left(-\alpha_{RM} f (E_{AS}^{0'} - E_{RM}^{0'})\right)$$

For redox-mediators with intrinsic rate constants ~ 10 -fold higher than that of the active-species ($k_{RM}^0/k_{AS}^0 = 10$), the rate constant for electron transfer to the redox-mediator is at least twice the rate constant for electrodeposition as long as the redox-mediator’s formal potential no more than ~ 80 mV below the active-species’ formal potential. Thus, for the assumptions given here, the redox mediator’s formal potential should be between 40 and 80 mV below the active-species’ formal potential.

1.4.2 Identifying candidate redox-mediators with computational chemistry

Given the stringent requirements for redox-mediators outlined above, I sought to computationally screen the formal potentials of a large library of candidate molecules. We accomplished this with the aid of the Electrolyte Genome, a high-throughput approach to automating computational chemistry.^[60, 61] By removing human intervention at most steps of the computational process, the Electrolyte Genome is able to screen extensive libraries of candidate molecules in a reasonable time-frame. As a result, we were able to screen a library of over 100 molecules for redox-potentials that matched both electrodeposition reactions that take place in a Li-S battery ($\text{Li}_2\text{S}_4 \rightarrow \text{S}_8$ and $\text{Li}_2\text{S}_4 \rightarrow \text{Li}_2\text{S}$). These results are outlined in chapters 7 and 8, respectively. By incorporating redox mediators that were specifically tuned to aid in the electrodeposition of insulating S_8 or Li_2S , we were able to dramatically improve the discharge capacities of Li-S batteries. This approach is general to other chemistries, and is expected to yield ongoing improvements in the quest for improved battery performance for transportation and the grid.

Chapter 2

Mechanistic Insight into the Formation of Cationic Naked Nanocrystals Generated Under Equilibrium Control

Reproduced with permission from *J. Am. Chem. Soc.* **2014**, *136*(44), 15702–15710. Copyright 2014 American Chemical Society.

2.1 Introduction and prior art

Mesoscale chemistry increasingly relies on assembly of pre-formed nanoscale building units into ordered hybrid architectures.^[62–66] The surface chemistry of the building units strongly influences their assembly trajectory from spatially random to periodically ordered mesostructures, which in turn allows one to engineer new properties from the coupled interactions amongst components in the material.^[67–76] Colloidal nanocrystals (NCs) are versatile building units in this regard. As synthesized, they typically feature a dense packing of hydrophobic organic ligands, chemisorbed to the NC’s inorganic surface. Others and we have shown previously that in order to assemble NCs into ordered mesostructured materials, particularly at high volume fractions, their surfaces must first be transformed chemically to enable favorable interactions with block copolymer (BCP) architecture-directing agents.^[77–85] Understanding the mechanistic origins and outcomes that allow NC surfaces to be primed for BCP-directed assembly is therefore critical to advancing the emerging field of mesoscale science.

Despite the growing number of useful ligand exchange and ligand stripping chemistries now available,^[13–16, 19, 24, 86–99] we are only beginning to understand the mechanistic underpinnings of those transformations.^[16–23, 88] It is still difficult to explain and predict trends in reactivity for different NC compositions for a given transformation. For example, some NC compositions have not been amenable to native ligand removal while also maintaining colloidal dispersability — e.g., the lead chalcogenides.^[24, 25] Disparities in surface reactivity and stability are related to structure and bonding available to the material, and demand that we develop an arsenal of reagents that can be tailored as needed for the desired transformation of a NC of interest.

In the past, we and others have used irreversible chemical reactions, including alkylation with Meerwein’s salt or oxidation by the nitrosyl cation, to drive the removal of ligands from NC surfaces.^[24, 25, 90] These reactions yield charge-stabilized colloids in polar dispersants due to open metal coordination sites left at the NC surface following ligand stripping (Fig. 2.1a). Chemical approaches based on such irreversible reactions leave behind a transiently unstable surface (i.e., absent any stabilizing adsorbates), which can lead to desorption of excess metal cations from the surface and loss of dispersability (due to loss of surface charge) on a timescale similar to re-passivation with coordinating solvent.

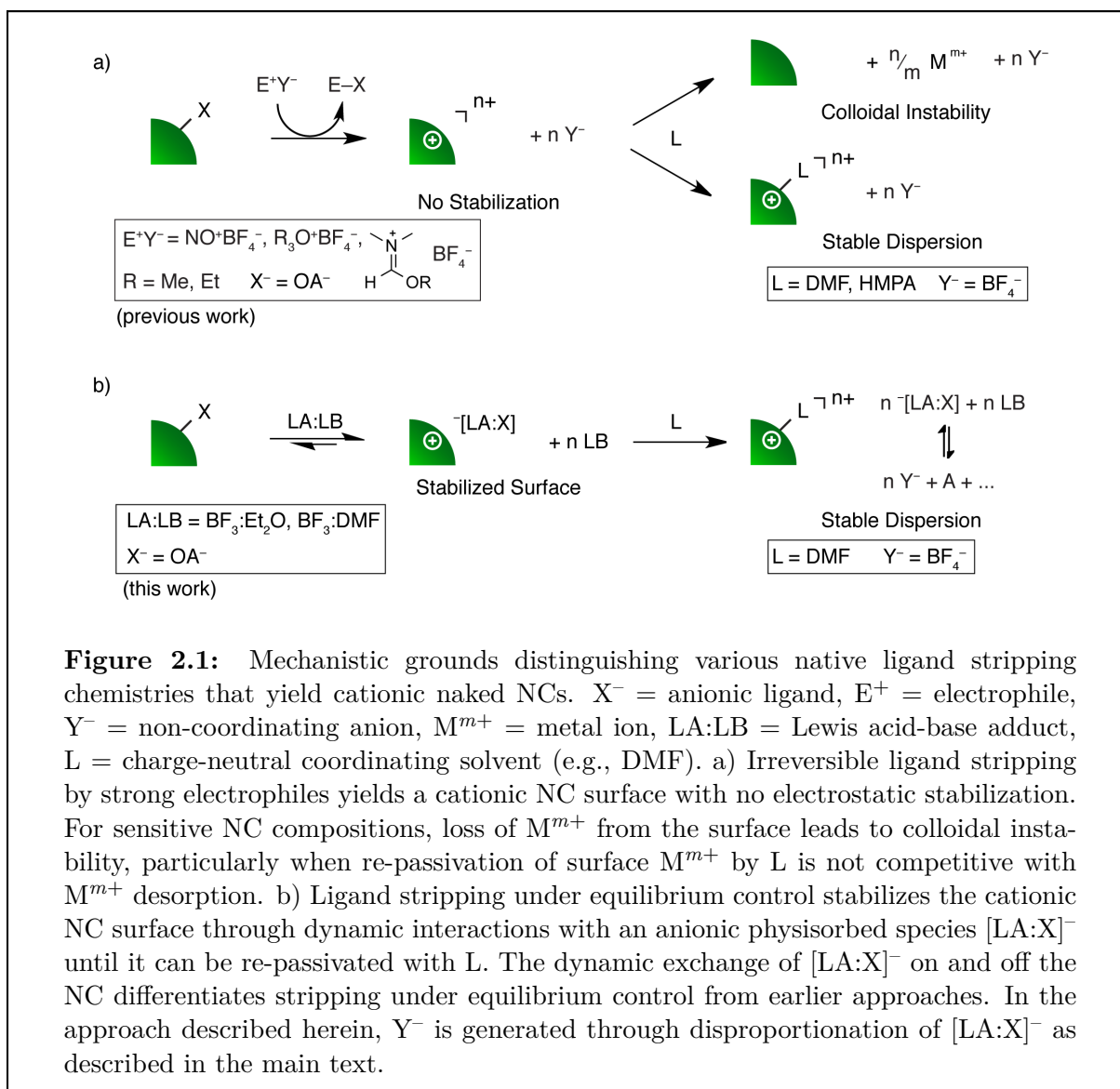
I hypothesized that this undesirable outcome could be avoided if it were possible to stabilize the NC surface through the entire ligand-stripping pathway. Here, I introduce the concept of native ligand stripping under equilibrium control, where reversible Lewis acid-base chemistry is used to generate adduct-stabilized surfaces during ligand stripping. The dynamic exchange of these adducts on and off the NC surface allows for ligand displacement while imparting surface stabilization, in contrast to previous approaches that leave the surface without stabilization. Our concept of equilibrium control over ligand stripping is demonstrated using Lewis base adducts of BF_3 , which yield for the first time naked NC inks of PbSe, along with a wide range of other semiconductor and metallic NCs. Our analysis of excess surface Pb(II) before and after stripping under equilibrium control

indicated near complete retention of excess Pb(II), in contrast with irreversible ligand stripping approaches. To rationalize differences in ligand-stripping outcomes with different reagents, I investigated in detail the mechanism of oleate ligand removal from PbSe NCs using complementary *in situ* techniques, including both 1D and 2D nuclear magnetic resonance (NMR) spectroscopy for both ^1H - and ^{19}F -containing reaction intermediates, as well as electrospray ionization mass spectrometry (ESI-MS) in order to validate our structure assignments. Unique to the chemistry developed herein, I show that BF_3 reacts with the carboxylate terminus of PbSe-bound oleate ligands (OA^-) to form a physisorbed $[\text{OA}:\text{BF}_3]^-$ adduct that is in dynamic exchange (equilibrium) on-and-off the NC surface throughout the stripping reaction. I reason that this dynamic layer of $[\text{OA}:\text{BF}_3]^-$ at PbSe is responsible for the observed surface stabilization, and refer to this effect as equilibrium control over surface stabilization. I further show that anionic $[\text{OA}:\text{BF}_3]^-$ undergoes disproportionation reactions in the presence of excess BF_3 , ultimately leading to the loss of oleate as neutral $\text{OA}_x(\text{B}_y\text{F}_z)$ species and the formation of BF_4^- as the sole charge-compensating species at the cationic NC surface in the final naked nanocrystal dispersion. The quality of these nano-inks allows PbSe NC to be assembled into either single-component ordered NC films or periodic mesostructured composites using block copolymer-directed assembly, highlighting the versatility of these functional nanoscale building units in mesoscale chemistry.

2.2 Equilibrium control over ligand-stripping improves colloidal stability

As a test case to highlight the versatility of native ligand stripping under equilibrium control over previously reported procedures, I investigated in detail the removal of oleate ligands from the surface of PbSe NCs (PbSe-OA) using Lewis base adducts of BF_3 . As Se^{2-} in the NC lattice is easily oxidized, PbSe NCs require mild chemical reagents to strip them of their native ligands. While reagents such as trialkyloxonium salts (e.g., Meerwein’s salt) and 1-alkoxy-*N,N*-dimethylmethaninium salts have so far proven capable of stripping ligands from the NC surface, by either method, the resulting naked PbSe NCs are not dispersable in organic solvents.^[24, 25] Both alkylating agents are high-energy reactants and their use is commensurate with rapid and irreversible removal of chemisorbed organic ligands from NC surfaces. For NCs such as PbSe, loss of native ligands from the coordination sphere of surface Pb(II) can lead to desorption of Pb(II) from the NC surface. Here, I show that by changing the ligand-stripping chemistry to one that allows for equilibrium control over surface stabilization, I am able to completely avoid loss of surface Pb(II) and thereby preserve colloidal stability in the cationic naked PbSe NC inks.

Stable dispersions of cationic naked PbSe NCs with BF_4^- counter-ions were obtained by direct transfer of PbSe-OA into *N,N*-dimethylformamide (DMF) containing $\text{BF}_3:\text{Et}_2\text{O}$. The resulting PbSe dispersions — purified first by hexanes washes and then precipitation from DMF with toluene — were stable to centrifugation and filtration for days. The



efficient removal of ligands by Lewis base adducts of BF_3 ($\text{BF}_3\text{:LB}$) was confirmed by FT-IR and EDX, which show a dramatic decrease in intensity of the C-H vibrational stretching frequencies and carbon content, respectively (Figs. 2.9 and 2.10). Ligand removal was further verified by carrying out the stripping procedure in DMF- d_7 and acquiring the ^1H NMR spectrum (Fig. 2.11), which showed no residual oleate. In order to establish the compositional diversity afforded by ligand stripping under equilibrium control, I showed that charge-stabilized dispersions of naked ZnO, Mn_3O_4 , TiO_2 , and Ni can be prepared in a similar manner to that described for PbSe (Figs. 2.12 and 2.13). Despite the dramatic change in NC surface chemistry, I did not observe dramatic changes in size or crystal structure, as evidenced by TEM and XRD (Figs. 2.13 and 2.14). Thus, this approach efficiently removes organic ligands from NC surfaces while preserving the integrity of the inorganic NC core.

2.3 Evidence for equilibrium control over surface stabilization

In order to understand the microscopic chemical processes leading to stable dispersions of naked PbSe NCs, I followed the ligand stripping chemistry of PbSe-OA *in situ* in toluene- d_8 using diffusion-ordered spectroscopy (DOSY). DOSY is a 2D NMR technique that provides information about the chemical shifts and diffusion coefficients of NMR active species, and has been used to identify and track the dynamics of ligand exchange (but not stripping) on a variety of NC surfaces.^[17, 18, 21, 100–102] The ^1H DOSY spectrum of 6.8 ± 0.5 nm PbSe-OA NCs (Fig. 2.15) showed broad peaks with chemical shifts characteristic of bound oleate and a diffusion coefficient of $(0.75 \pm 0.01) \times 10^{-10} \text{ m}^2 \text{ s}^{-1}$. This contrasts significantly with the diffusion coefficient of free oleic acid of $(7.75 \pm 0.05) \times 10^{-10} \text{ m}^2 \text{ s}^{-1}$ (Fig. 2.16). The measured diffusion coefficient for PbSe-OA corresponds to a hydrodynamic diameter of 10.0 ± 0.5 nm, which agrees well with a 6.8 nm PbSe core and a tightly bound ~ 1.6 nm ligand shell on each side.

The broad alkene resonance at $\delta=5.7$ ppm is well separated from other resonances in the ^1H NMR spectrum and provides an ideal handle for tracking the fate of oleate as ligand stripping progresses. As $\text{BF}_3\text{:Et}_2\text{O}$ was added to the NC dispersion, the broad oleate alkene resonance shifted upfield and decreased in intensity while a sharp resonance at $\delta=5.4\text{--}5.5$ ppm, which I assign to $[\text{OA:BF}_3]^-$, appeared and grew in intensity (Fig. 2.2a). The measured diffusion coefficient of the broad resonance increased only slightly throughout the experiment (from (0.75 ± 0.01) to $(1.20 \pm 0.02) \times 10^{-10} \text{ m}^2 \text{ s}^{-1}$), but the measured diffusion coefficient of the sharp resonance increased from $(1.02 \pm 0.03) \times 10^{-10} \text{ m}^2 \text{ s}^{-1}$ at 0.2 equivalents BF_3 to $(4.43 \pm 0.02) \times 10^{-10} \text{ m}^2 \text{ s}^{-1}$ at 2.3 equivalents BF_3 (Fig. 2.2b and 2.17). This can be explained by oleate reacting with $\text{BF}_3\text{:Et}_2\text{O}$ to form $[\text{OA:BF}_3]^-$ and Et_2O . As the negative charge of $[\text{OA:BF}_3]^-$ is more diffuse than OA^- , $[\text{OA:BF}_3]^-$ is expected to bind much less strongly to the nanocrystal surface. As a result, $[\text{OA:BF}_3]^-$ rapidly exchanges on and off the nanocrystal, and the observed diffusion coefficient is a

weighted average between the bound and unbound states.

As the titration proceeded, $[\text{OA}:\text{BF}_3]^-$ became increasingly liberated from the surface. On the other hand, unreacted oleate remained tightly bound to the NC. As more of the ligand shell was removed, the remaining oleate ligands experienced more configurational entropy (or conformational degrees of freedom), allowing them to reconfigure at the ligand-NC interface. As a result, the hydrodynamic diameter of the NC, as measured by DOSY of the broad resonance at $\delta=5.7$ ppm, decreased from 10.0 ± 0.5 nm (inorganic core + ligand shell) to 6.3 ± 0.3 nm (inorganic core alone) over the course of the titration. Changes in the chemical shift for tightly bound oleate can be explained by changes in the local dielectric environment as neighboring oleate ligands are removed. These results provide strong support that $[\text{OA}:\text{BF}_3]^-$ adducts are exchanging on-and-off the surface of PbSe nanocrystals during the stripping process, thus stabilizing the surface against surface metal cation desorption. Alternate explanations for the sharp peak at $\delta=5.5$ ppm were considered, but found to be inconsistent with our observations. For example, I considered that the sharp resonance at $\delta=5.5$ ppm could be due to the exchange of charge-neutral $\text{Pb}(\text{OA})_2$, which Hens and co-workers observed in the case of PbSe-OA oxidation.^[17] However, I found that $\text{Pb}(\text{OA})_2$ is unstable in the presence of BF_3 , making this hypothesis unlikely (Fig. 2.18). Furthermore, all experiments were carried out in tightly sealed screw-top NMR tubes, which were immediately transferred from a glovebox into the NMR spectrometer in order to avoid

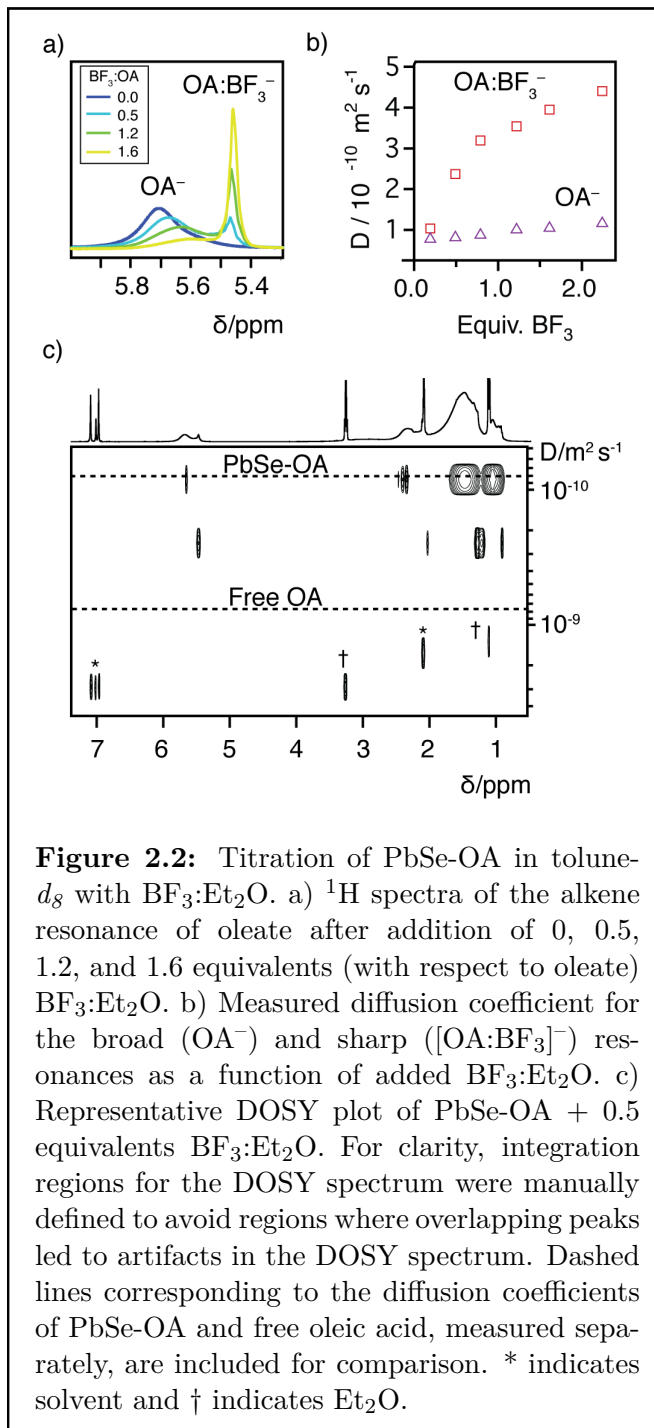


Figure 2.2: Titration of PbSe-OA in toluene- d_8 with $\text{BF}_3:\text{Et}_2\text{O}$. a) ^1H spectra of the alkene resonance of oleate after addition of 0, 0.5, 1.2, and 1.6 equivalents (with respect to oleate) $\text{BF}_3:\text{Et}_2\text{O}$. b) Measured diffusion coefficient for the broad (OA^-) and sharp ($[\text{OA}:\text{BF}_3]^-$) resonances as a function of added $\text{BF}_3:\text{Et}_2\text{O}$. c) Representative DOSY plot of PbSe-OA + 0.5 equivalents $\text{BF}_3:\text{Et}_2\text{O}$. For clarity, integration regions for the DOSY spectrum were manually defined to avoid regions where overlapping peaks led to artifacts in the DOSY spectrum. Dashed lines corresponding to the diffusion coefficients of PbSe-OA and free oleic acid, measured separately, are included for comparison. * indicates solvent and † indicates Et_2O .

oxygen exposure. I also ruled out the possibility that $[\text{OA}:\text{BF}_3]^-$ was merely becoming entangled in the ligand shell rather than exchanging on and off the nanocrystal surface by considering that the diffusion coefficient measured at 2.3 equivalents of added $\text{BF}_3:\text{Et}_2\text{O}$ indicated that the species was still spending some time diffusing with the nanocrystal, despite the almost complete loss of the ligand shell at this point in the titration.

2.4 Origin of the non-coordinating counter-ion and fate of anionic ligands

Support that $\text{BF}_3:\text{Et}_2\text{O}$ -mediated equilibrium-controlled ligand stripping avoids loss of surface excess $\text{Pb}(\text{II})$ was provided by measurement of the PbSe NCs' surface excess $\text{Pb}(\text{II})$ before and after stripping using inductively coupled plasma atomic emission spectroscopy (ICP-AES). As-synthesized 5.8 ± 0.5 nm diameter PbSe-OA NCs gave a $\text{Pb}:\text{Se}$ ratio of 1.24 ± 0.03 , while naked PbSe returned with a 1.23 ± 0.02 ratio of $\text{Pb}:\text{Se}$. This retention of surface excess $\text{Pb}(\text{II})$ during ligand stripping is unique among agents that generate naked PbSe nanocrystals: a $\sim 1:1$ ratio is typically observed when using Meerwein's salt directly, while a 1.15:1 ratio is observed when using 1-ethoxy-*N,N*-dimethylmethaminium tetrafluoroborate.^[25] Moreover, our new $\text{BF}_3:\text{LB}$ approach is the only procedure that yields dispersible naked PbSe , most likely due to the enhanced electrostatic stabilization that follows retention of excess surface $\text{Pb}(\text{II})$. Based on these data, it is then appropriate to describe the composition of naked PbSe nanocrystals as $(\text{Pb}^{2+})_{0.23n}(\text{Y}^-)_{0.46n}(\text{PbSe})_n$ where n is ~ 1600 and Y^- is the counter-ion generated during ligand stripping.^[103]

Given that no exogenous ions of the type Y^- were added to the ligand-stripping solu-

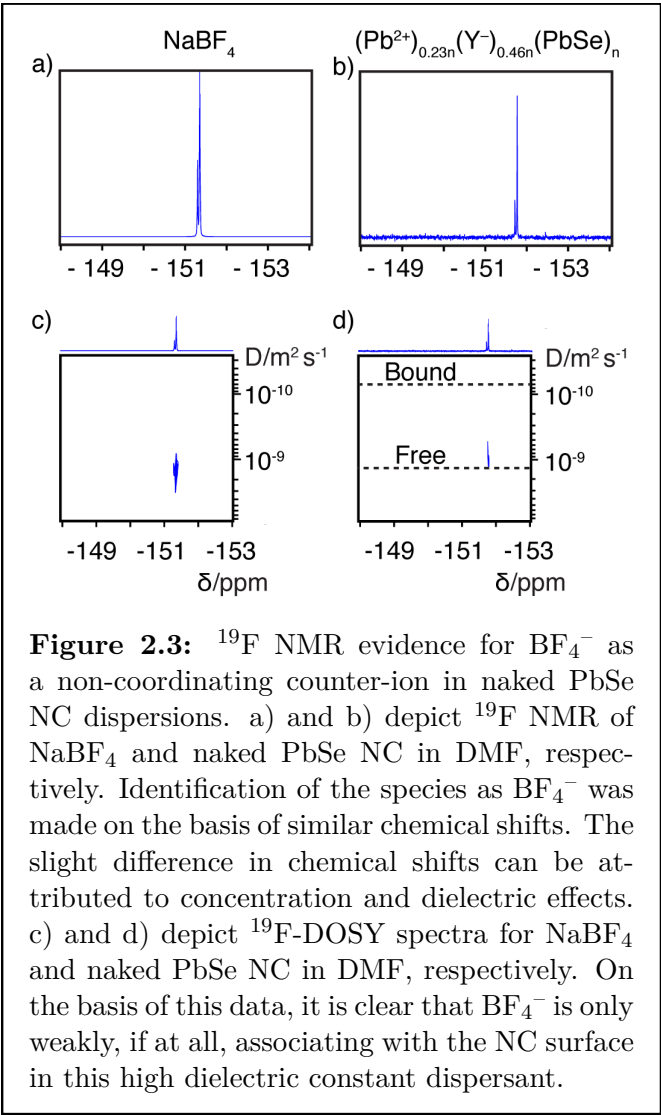


Figure 2.3: ^{19}F NMR evidence for BF_4^- as a non-coordinating counter-ion in naked PbSe NC dispersions. a) and b) depict ^{19}F NMR of NaBF_4 and naked PbSe NC in DMF, respectively. Identification of the species as BF_4^- was made on the basis of similar chemical shifts. The slight difference in chemical shifts can be attributed to concentration and dielectric effects. c) and d) depict ^{19}F -DOSY spectra for NaBF_4 and naked PbSe NC in DMF, respectively. On the basis of this data, it is clear that BF_4^- is only weakly, if at all, associating with the NC surface in this high dielectric constant dispersant.

tion, it was necessary to establish the chemical identity of Y^- and its mechanistic origins as the compensating charge at the cationic naked PbSe NC surface. FT-IR of a thin film of naked PbSe NCs showed a strong peak at 1120 cm^{-1} , suggesting the presence of BF_4^- even though no BF_4^- was added to the ligand-stripping solution. To confirm that BF_4^- was present in the purified dispersions of naked PbSe NCs, ^{19}F NMR was carried out. Strong peaks at $\delta = -151.72$ and -151.77 ppm with a 1:4 ratio in integrated intensity were observed, consistent with isotopic shifts due to bonding of ^{19}F to ^{10}B and ^{11}B , respectively (Fig. 2.3). The assignment of this peak to BF_4^- was made by acquiring the ^{19}F NMR spectrum of NaBF_4 in DMF, and noting a similar chemical shift as that observed for our naked PbSe dispersions (Fig. 2.3a-b). I also noted that BF_4^- in naked PbSe dispersions is only weakly, if at all, associating with the NC surface in DMF (Fig. 2.3c-d).

In order to establish the origins of the formation of BF_4^- , I acquired the ^{19}F NMR spectrum for $\text{BF}_3:\text{Et}_2\text{O}$ in $\text{DMF-}d_7$ (Fig. 2.19). The major chemical species present is the DMF adduct of BF_3 at $\delta = -152.4$ ppm; this adduct accounting for 96% of the fluorine in the system, alongside two minor fluorine-containing species. The chemical shifts of these minor species were $\delta = -150.8$ and -151.8 ppm, and were present in $\sim 1:2$ ratio in integrated intensity. Based on the chemical shift, the peak at $\delta = -151.8$ ppm can be assigned to BF_4^- . These data are consistent with the disproportionation of $\text{DMF}:\text{BF}_3$ to form $[(\text{DMF})_2\text{BF}_2]^+$ and BF_4^- , thus accounting for one possible source of BF_4^- counter-ions in naked PbSe NC dispersions (Fig. 2.4).^[104]

From the view of electroneutrality, the replacement of anionic oleate ligands with non-coordinating BF_4^- counter-ions at the NC surface requires both generation of BF_4^- and either conversion of oleate anions to a neutral species or pairing of oleate with a cationic species (i.e., OA^- with $[(\text{DMF})_2\text{BF}_2]^+$). I sought to understand oleate speciation post-stripping by performing ESI-MS on a reaction mixture of $\text{Pb}(\text{OA})_2$ and $\text{BF}_3:\text{Et}_2\text{O}$ in benzene- d_6 (Fig. 2.5). It is known from previous work that carboxylates can coordinate one or two equivalents of BF_3 , and that carboxylate BF_3 adducts can undergo disproportionation reactions to generate BF_4^- and $[\text{B}(\text{O}_2\text{CR})_n\text{F}_{4-n}]^-$.^[105] In accordance with this known reactivity pathway, ESI-MS indicates that our reaction mixture contains OA^-

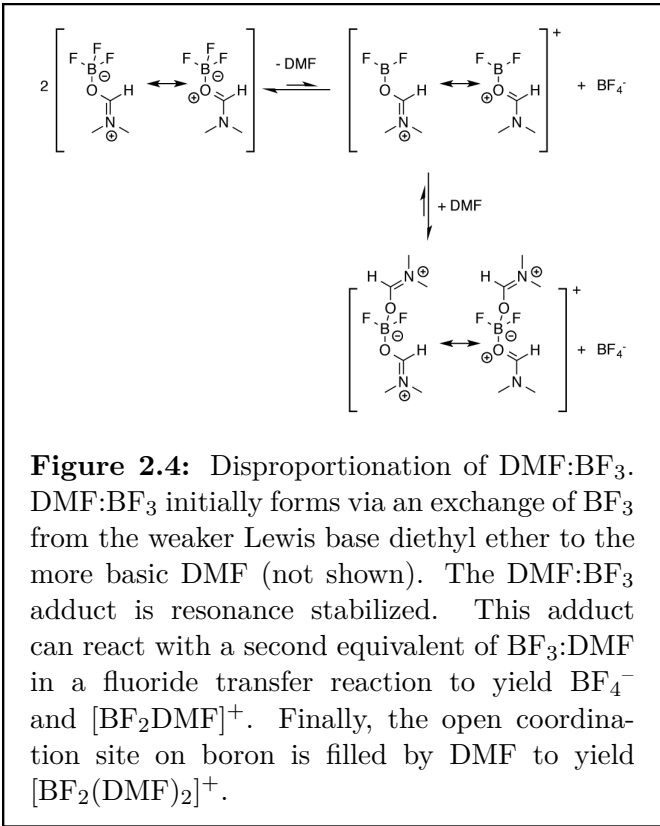
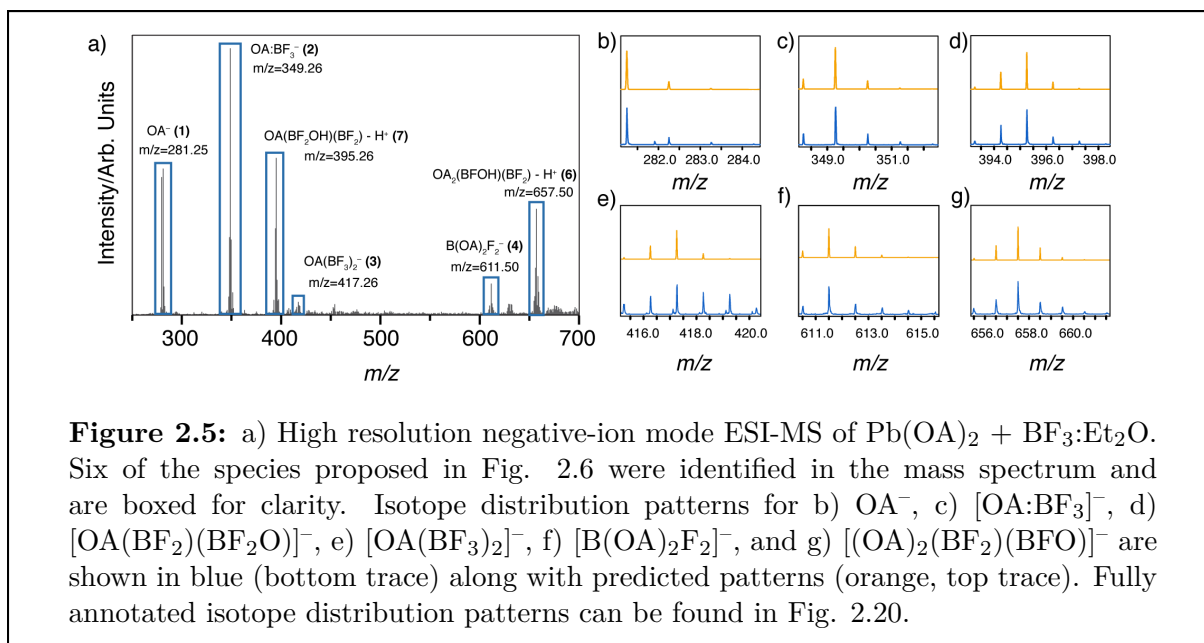
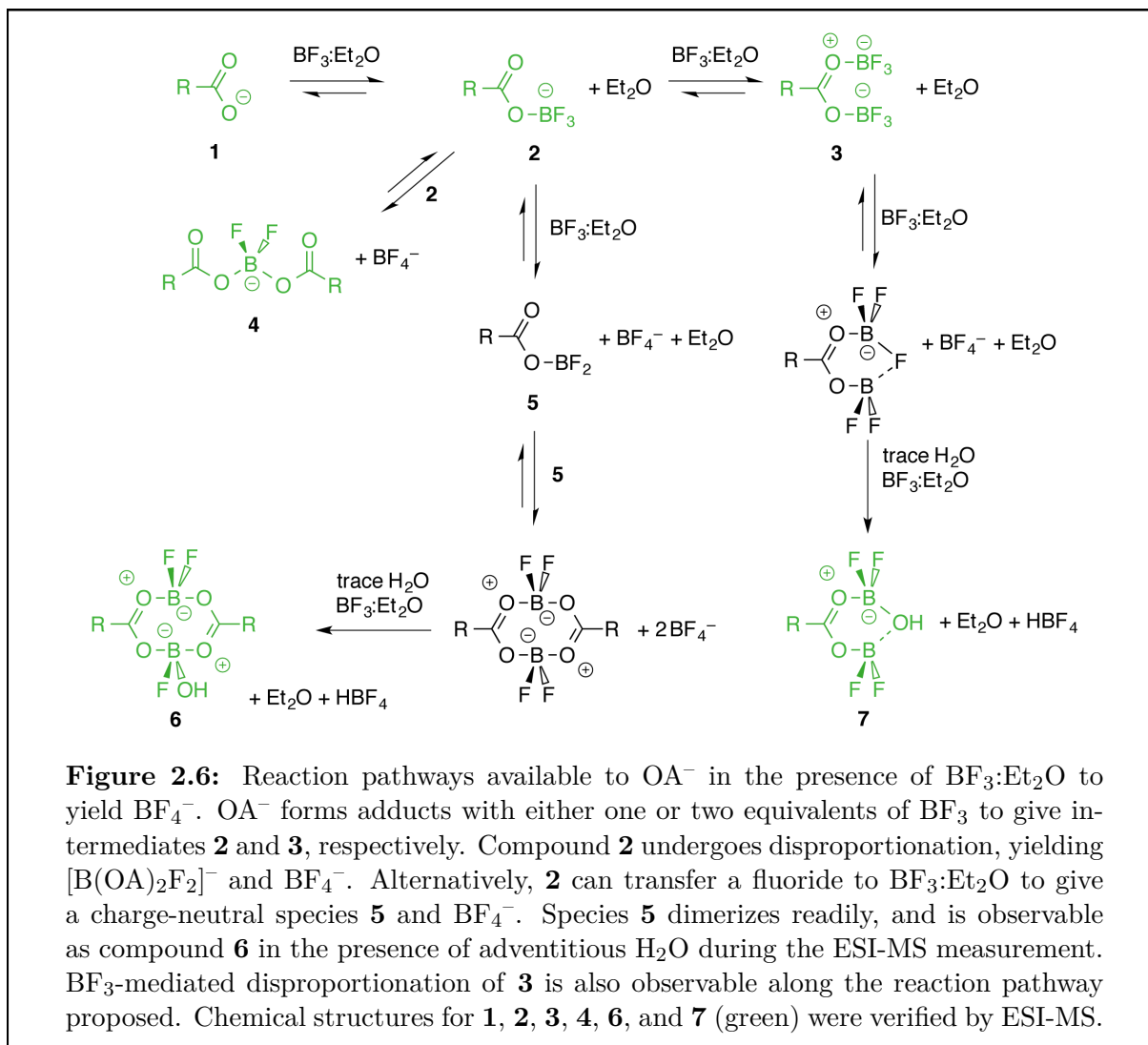


Figure 2.4: Disproportionation of $\text{DMF}:\text{BF}_3$. $\text{DMF}:\text{BF}_3$ initially forms via an exchange of BF_3 from the weaker Lewis base diethyl ether to the more basic DMF (not shown). The $\text{DMF}:\text{BF}_3$ adduct is resonance stabilized. This adduct can react with a second equivalent of $\text{BF}_3:\text{DMF}$ in a fluoride transfer reaction to yield BF_4^- and $[\text{BF}_2\text{DMF}]^+$. Finally, the open coordination site on boron is filled by DMF to yield $[\text{BF}_2(\text{DMF})_2]^+$.



(**1**, $m/z = 281.25$, calc. 281.25),
 $[\text{OA}:\text{BF}_3]^-$ (**2**, $m/z = 349.26$, calc. 349.25), $[\text{OA}(\text{BF}_3)_2]^-$ (**3**, $m/z = 417.26$, calc. 417.26),
 and $[\text{B}(\text{OA})_2\text{F}_2]^-$ (**4**, $m/z = 611.50$, calc. 611.50) (Figs. 2.5 and 2.6). In addition to anionic disproportionation products, I also observe species that result from the hydrolysis of neutral disproportionation products in the presence of adventitious water. For example, fluoride transfer from $[\text{OA}:\text{BF}_3]^-$ (**2**) to $\text{BF}_3:\text{Et}_2\text{O}$ generates BF_4^- and $\text{OA}(\text{BF}_2)$ (**5**), which readily dimerizes to form the neutral $(\text{OA})_2(\text{BF}_2)_2$ species. While this dimer is not directly observable by ESI-MS due to its lack of charge, the deprotonated hydrolysis product, $[(\text{OA})_2(\text{BF}_2)(\text{BFO})]^-$ (**6**, $m/z = 657.50$, calc. 657.51) was observed. The $[\text{OA}(\text{BF}_3)_2]^-$ adduct **3** can also undergo fluoride loss to generate BF_4^- and neutral $\text{OA}(\text{BF}_3)(\text{BF}_2)$. Again, this neutral species is undetectable by ESI-MS, but I observe the deprotonated form of the hydrolysis product, $[\text{OA}(\text{BF}_2)(\text{BF}_2\text{O})]^-$ (**7**, $m/z = 395.26$, calc. 395.26). The transfer of fluoride from BF_3 oleate adducts to excess $\text{BF}_3:\text{Et}_2\text{O}$ provides a pathway for the conversion of anionic oleate ligands into neutral species along with the generation of non-coordinating BF_4^- . It is also worth noting that in addition to $[\text{OA}:\text{BF}_3]^-$, the anionic species formed along this pathway also have the ability to stabilize NC surfaces during the stripping process.



2.5 Applications of cationic naked nanocrystals

The unprecedented access to stable dispersions of cationic naked PbSe NCs allowed us to better control their mesoscale order in thin films and composites, yielding new classes of mesostructured materials with applications as energy conversion materials. For example, thin films of lead chalcogenide NCs are common active layers in Schottky-type solar cells, field effect transistors, NIR photodetectors, and thermoelectrics.^[13, 15, 25, 93, 106–114]

As synthesized (i.e., with ligands intact), they can be assembled into periodic lattices with hexagonal close packing (*hcp*). Where controlled propagation of energy in the film is required for the function of the device, ligand removal can be advantageous. As shown here and elsewhere, order is usually lost upon stripping ligands in thin films (Fig. 2.7 and 2.22).^[13, 115] In addition, cracks and defects can manifest as a result of the dramatic volume change that occurs when organics are liberated. In contrast to the colloidal glasses produced by in-film ligand removal, ordered thin films of naked PbSe can be prepared simply by casting their dispersions directly onto substrates. Apparent cubic packing is evidenced in the top-down SEM images (Figure 2.7d), indicating significant differences in the preferred packing geometry for ligand-coated and ligand-stripped NCs.

To further distinguish packing geometries between the different PbSe NC films, grazing incidence small angle X-ray scattering (GISAXS) was carried out. Both ligand-stripped PbSe NC films in Figure 2.7c and 2.7d showed a decrease in interparticle spacing from ~ 1.3 nm to ~ 0.4 nm, consistent with ligand removal. However, films that were spin-coated from stripped dispersions of PbSe exhibited a tendency towards in-plane ordering as opposed to the isotropic packing observed in films that were stripped in-film (Figure 2.7d and 2.22).

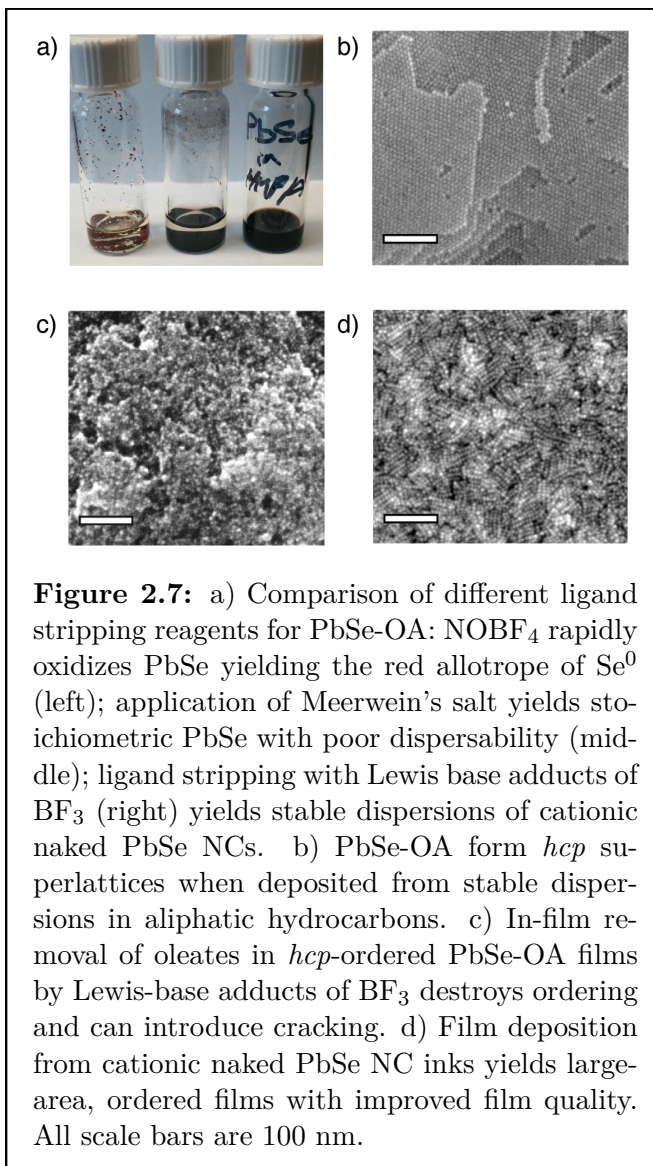


Figure 2.7: a) Comparison of different ligand stripping reagents for PbSe-OA: NOBF₄ rapidly oxidizes PbSe yielding the red allotrope of Se⁰ (left); application of Meerwein's salt yields stoichiometric PbSe with poor dispersability (middle); ligand stripping with Lewis base adducts of BF₃ (right) yields stable dispersions of cationic naked PbSe NCs. b) PbSe-OA form *hcp* superlattices when deposited from stable dispersions in aliphatic hydrocarbons. c) In-film removal of oleates in *hcp*-ordered PbSe-OA films by Lewis-base adducts of BF₃ destroys ordering and can introduce cracking. d) Film deposition from cationic naked PbSe NC inks yields large-area, ordered films with improved film quality. All scale bars are 100 nm.

The observed packing in films deposited from ligand-coated *vs.* ligand-stripped PbSe NCs can arise from: differences in surface energies of exposed facets leading to preferred NC-to-NC orientations^[116]; differences in packing preferences for non-deformable objects (i.e., the naked PbSe) compared to partially-deformable ligand-coated particles^[117]; differences in interaction potentials available to the system to guide the assembly trajectory during solvent evaporation (van der Waals *vs.* electrostatics)^[118]. As such, our work suggests new opportunities to control energy propagation in NC films through their packing in the active layers.

More elaborate mesostructured BCP-NC hybrid architectures were also possible using polystyrene-*block*-poly(*N,N*-dimethylacrylamide) architecture-directing agents.^[81] For example, naked NC inks of PbSe were mixed with architecture-directing BCPs and deposited onto Si substrates by drop-casting or spin-coating to prepare hierarchically ordered composites (Fig. 2.8 and 2.23). Notably,

no further thermal or solvent vapor treatment of the films was required to establish order. As measured by GISAXS, these composites exhibited an in-plane periodicity of 45 nm, with a peak width at half maximum of 0.008 \AA^{-1} . These new materials were only accessible thanks to the improved control over surface chemistry granted by our new chemical approach, and the availability of naked NC inks of PbSe opens the door to creating a wide variety of new and interesting mesoscale architectures that have been impossible in the past.

2.6 Conclusions

The mechanistic insights gained in this work provide a much-needed framework for rationalizing the successes and failures of different chemical approaches for removing surface-bound ligands from nanocrystals while maintaining colloidal dispersability. I hypothesized that earlier approaches based on irreversible severing of NC-ligand bonds failed to main-

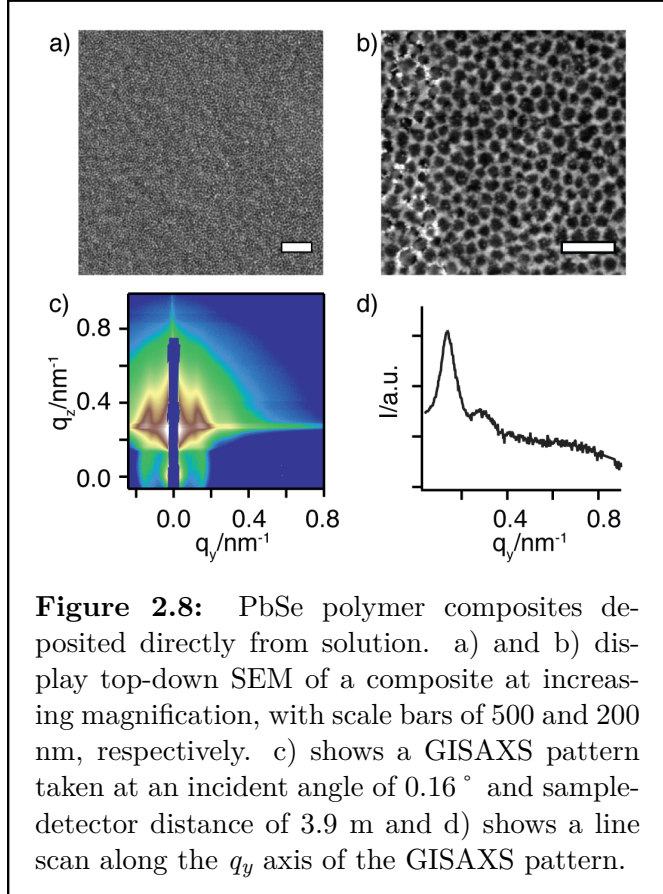


Figure 2.8: PbSe polymer composites deposited directly from solution. a) and b) display top-down SEM of a composite at increasing magnification, with scale bars of 500 and 200 nm, respectively. c) shows a GISAXS pattern taken at an incident angle of 0.16° and sample-detector distance of 3.9 m and d) shows a line scan along the q_y axis of the GISAXS pattern.

tain colloidal dispersability for sensitive compositions due to a lack of surface stabilization and concomitant desorption of excess metal cations from the NC surface. To address this shortcoming, I proposed the use of reversible Lewis acid-base chemistry to generate physisorbed anionic species that stabilize the NC surface until coordinating solvent is able to re-passivate the surface. Using PbSe NC as a model system, I demonstrated that anionic BF_3 adducts of surface-bound ligands exchanged on-and-off the NC surface, providing stabilization. Furthermore, I showed that NCs stripped under equilibrium control maintained colloidal stability and did not suffer from the excess surface metal desorption that can be problematic when using some irreversible ligand stripping reagents. As a result, ligand stripping under equilibrium control represents a powerful new class of reactions for modifying the surface chemistry of colloidal NC while maintaining colloidal stability.

I leveraged this additional control to prepare previously unobtainable mesostructured NC films and polymer-NC composites with high mass loadings of PbSe. Notably, these composites did not require any further thermal or solvent-vapor treatment to establish order, which simplifies their processing for end-use applications including photovoltaics, thermoelectrics, and NIR photodetectors. These new materials are expected to yield insights into the role of architecture on electronic, excitonic, and thermal transport in mesostructured materials and composites.

2.7 Supporting information

2.7.1 Nanocrystal syntheses

Synthesis of oleate-passivated lead selenide nanocrystals (PbSe-OA)

Lead selenide nanocrystals were synthesized under an inert atmosphere following slightly modified reported procedures.^[119] Briefly, selenium shot (960 mg, 12.2 mmol) was added to TOP (8.64 g, 23.3 mmol) in a 40 mL septum capped vial and stirred overnight in a nitrogen glovebox prior to the addition of diphenylphosphine (84 mg, 0.45 mmol). Separately, in a 100 mL three-necked flask, lead(II) oxide (1.34 g, 6 mmol), oleic acid (4.24 g, 15 mmol), and 1-octadecene (23.4 mL) was placed under vacuum at room temperature 15 min and then at 110 °C for 1 h to dry and degas the solution. After solution became colorless and transparent, the temperature was raised to 180 °C at which point the TOP-Se solution was rapidly injected. After this TOP-Se injection, the reaction temperature dropped to ~150 °C and was kept at this temperature for the desired reaction time (5 min gave PbSe nanocrystals with ~ 7 nm diameter). The reaction was cooled in a water bath. The nanocrystals were then purified by precipitation three times from hexanes using first ethanol (1×) and then acetone (2×) to give 460 mg purified NC (1.2 mmol (PbOA)_{0.2}PbSe, 24% yield).

Synthesis of copper selenide nanocrystals (Cu_{2-x}Se)

Copper selenide nanocrystals were synthesized under an inert atmosphere following slightly modified reported procedures.^[120] Briefly, selenium powder (94.8 mg, 1.2 mmol) was added to 1-octadecene (9 mL) and oleylamine (6 mL) in a 50 mL three-necked flask and placed under vacuum at room temperature and 110 °C for 15 min and 1 h, respectively to dry and degass the solution. Afterwards, the Se solution was placed under nitrogen flow and raised to 310 °C. The solution was orange and transparent. Separately, in a 25 mL three-necked flask, CuCl (198 mg, 2 mmol), oleylamine (2 mL), and 1-octadecene (3 mL) were placed under vacuum at 110 °C for 15 min to dry and degas the solution. The solution was light green and transparent. Next, the copper-containing solution was rapidly injected into the Se-containing solution and the reaction temperature dropped to ~285 °C. The reaction temperature was allowed to recover to 300 °C and was kept at this temperature for 20 min before cooling in a water bath. The particles were then purified by precipitation three times from hexanes/toluene (50% *v/v*) using ethanol.

Synthesis of nickel nanocrystals (Ni)

Nickel nanocrystals were synthesized under an inert atmosphere following slightly modified standard procedures.^[121] Briefly, nickel(II) 2,4-pentanedionate hydrate (84.7 mg, 0.33 mmol) was added to TOP (1 mL) in a 40 mL septum capped vial and in a nitrogen glovebox and then sonicated for 10 min to form a green/blue solution. In a separate 25 mL

three-necked flask, oleylamine (10 mL) was placed under vacuum at room temperature and 110 °C for 15 min and 1 h, respectively to dry and degas the solvent. The oleylamine was cooled to RT prior to the injection of the Ni-TOP solution. The reaction temperature was raised at a rate of 10 °C min⁻¹ to 250 °C and allowed to react for 30 min. The reaction was cooled in a water bath. The particles were then purified by precipitation three times from hexanes/toluene (50% *v/v*) using ethanol.

Synthesis of manganese oxide nanocrystals (Mn₃O₄)

Manganese oxide nanocrystals were synthesized in air following established procedures.^[122] Briefly, manganese acetate (513 mg, 3.0 mmol), stearic acid (1.71g, 6.0 mmol), and oleylamine (9.9 mL, 30 mmol) were dissolved in xylene (45 mL) in a 250 mL two neck flask with redox condenser and heated to 90 °C with stirring. Water (3 mL) was rapidly injected and the solution turned from clear dark brown to cloudy and light brown. The reaction temperature was held at 90 °C for 3 h, followed by cooling to room temperature. All solids were removed from the reaction mixture by centrifugation, and 350 mL ethanol was added to precipitate Mn₃O₄ nanocrystals. The nanocrystals were purified by precipitation three times from hexanes using acetone.

Synthesis of zinc oxide nanocrystals (ZnO)

Zinc oxide nanocrystals were synthesized in air following slightly modified procedures.^[123, 124] Briefly, potassium hydroxide (902 mg, 16 mmol) was dissolved in methanol (150 mL) in a 500 mL round-bottom flask. The solution was heated to 60 °C with stirring and held

at this temperature for 30 min. Next, a stock solution of zinc acetate dihydrate (1.757 g, 8.0 mmol) in methanol (50 mL) was added to the potassium hydroxide solution. The reaction was allowed to proceed for 2 h at 60 °C, after which time the mixture was allowed to cool to RT naturally. The reaction mixture volume was reduced to 50 mL under reduced pressure at 40 °C. Zinc oxide nanocrystals were precipitated by adding 5 equivalents of hexanes and 1 equivalent of isopropanol followed by centrifugation. The nanocrystals were redispersed in the minimal volume of methanol, and the precipitation and redispersion steps were repeated twice. On the final redispersion step the nanocrystals were redispersed in chloroform (3 mL) containing 375 µL oleylamine and 121 µL oleic acid. The nanocrystals were precipitated with acetone and purified by precipitation three times from hexanes using acetone.

Synthesis of titanium dioxide nanocrystals (TiO₂)

TiO₂ nanocrystals were synthesized under an inert atmosphere following established procedures.^[125] Briefly, oleic acid(35.0 g, 124 mmol) was dried under vacuum at 120 °C for 60 min in a 100 mL 3-neck flask. The temperature was reduced to 90 °C and the flask was filled with nitrogen. Titanium tetraisopropoxide (1.5 mL, 5.1 mmol) was rapidly

injected to yield a clear, yellow solution. After 5 minutes, a stock aqueous solution of trimethylamine-*N*-oxide (2 M, 5 mL, 10 mmol) was injected, at which point the reaction mixture turned white and cloudy. The reaction was held at 90 °C with stirring for 5 hours and allowed to cool to RT naturally. The nanocrystals were precipitated by adding 120 mL ethanol. The nanocrystals were recovered by centrifugation and purified three times by precipitation from hexanes using acetone.

2.7.2 Ligand stripping procedure

Activated DMF was prepared in a nitrogen glovebox by adding $\text{BF}_3:\text{Et}_2\text{O}$ (20 μL , 0.16 mmol) to 500 μL DMF and mixing vigorously. Next, 500 μL of a stock solution of nanocrystals in hexanes (5–10 mg/mL) was added to the activated DMF and mixed vigorously. Toluene (3.5 mL) was then added to induce mixing of the two layers and precipitation of stripped nanocrystals, which were redispersed in DMF. The resulting naked nanocrystal dispersion was purified by multiple washes with hexanes and precipitation from DMF with toluene.

2.7.3 In-Situ NMR

A known amount of PbSe-OA was dried under vacuum and redispersed in toluene- d_8 . The amount of oleate in the system was determined by quantitative NMR using 1,4-dioxane as an internal standard and 45 s interscan delays. Diffusion ordered spectroscopy (DOSY) was carried out at room temperature using standard bipolar convection compensating pulses. The diffusion delay, Δ , was set to 200 ms and the gradient pulse length, δ , was set to achieve at least 90% signal attenuation between 95% and 5% gradient strength. For the BF_3 titration experiment, the gradient pulse length was held at 5 ms, but for other experiments it varied from 1–2 ms. The gradient strength was varied between 5 and 95% of the calibrated maximum gradient strength of 51.1 G cm^{-1} in 16 steps. The resulting data was processed in the Bruker Topspin and Bruker Dynamics Center software packages, where it was fit to the appropriate form of the Stejskal-Tanner equation.

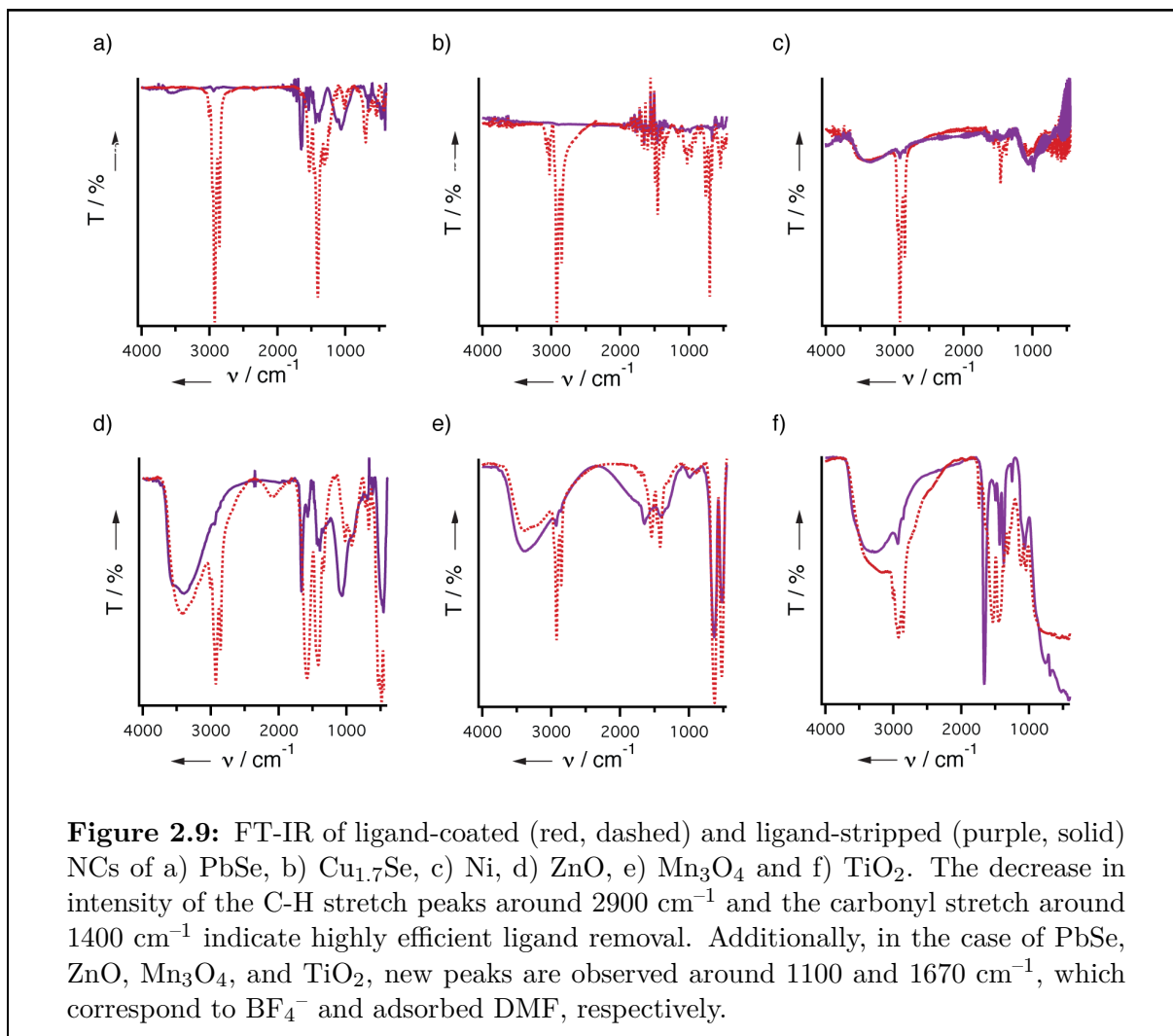
2.7.4 ESI-MS

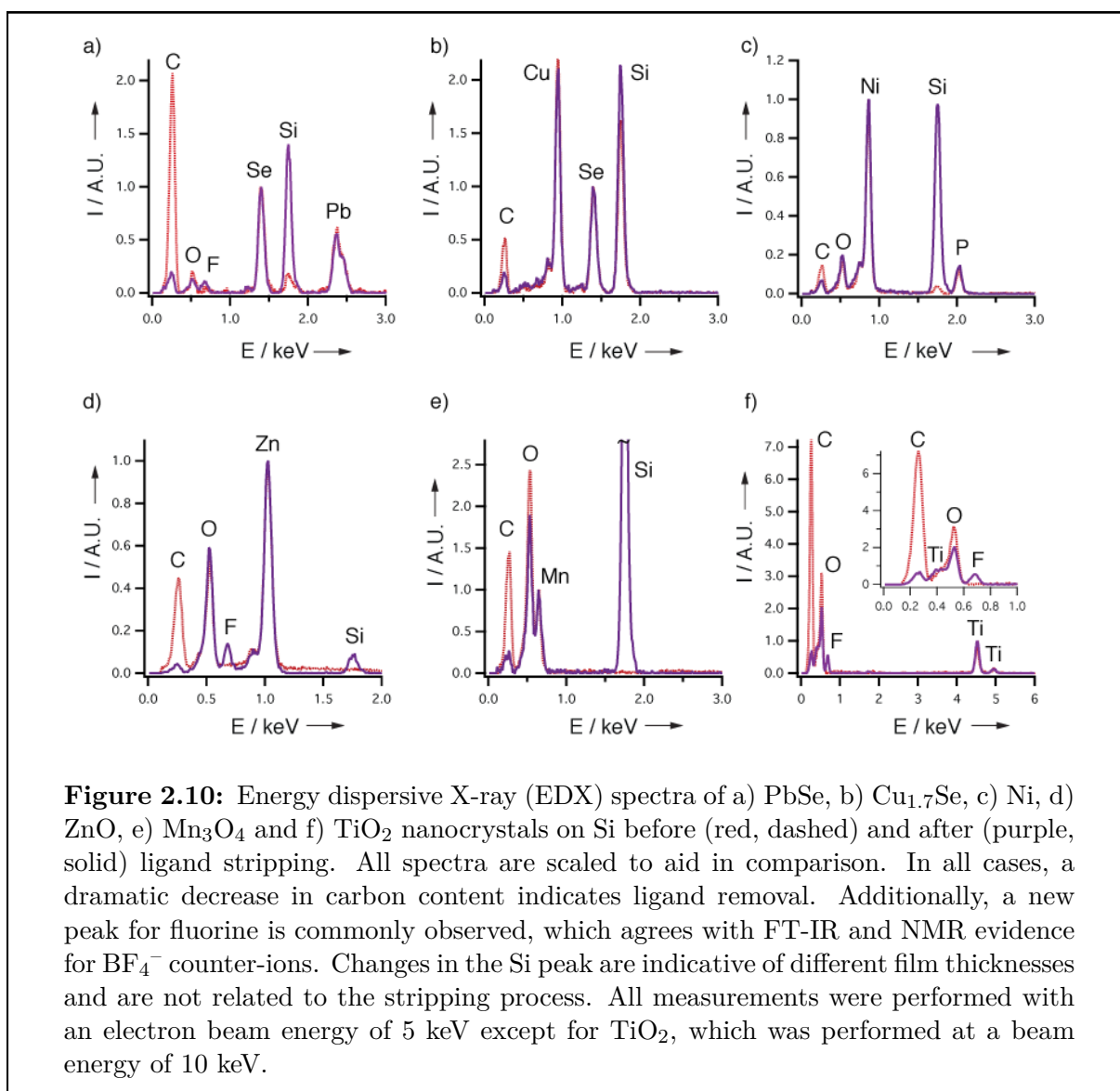
A reaction mixture of $\text{Pb}(\text{OA})_2$ and $\text{BF}_3:\text{Et}_2\text{O}$ was prepared by dissolving $\text{Pb}(\text{OA})_2$ (3 mg, 4 μmol) in 700 μL benzene- d_6 and adding $\text{BF}_3:\text{Et}_2\text{O}$ (8 μmol). For improved ionization efficiency, the reaction mixture was diluted 5-fold with dry acetonitrile to prepare the final ESI-MS sample. ESI-MS was run in negative-ion mode.

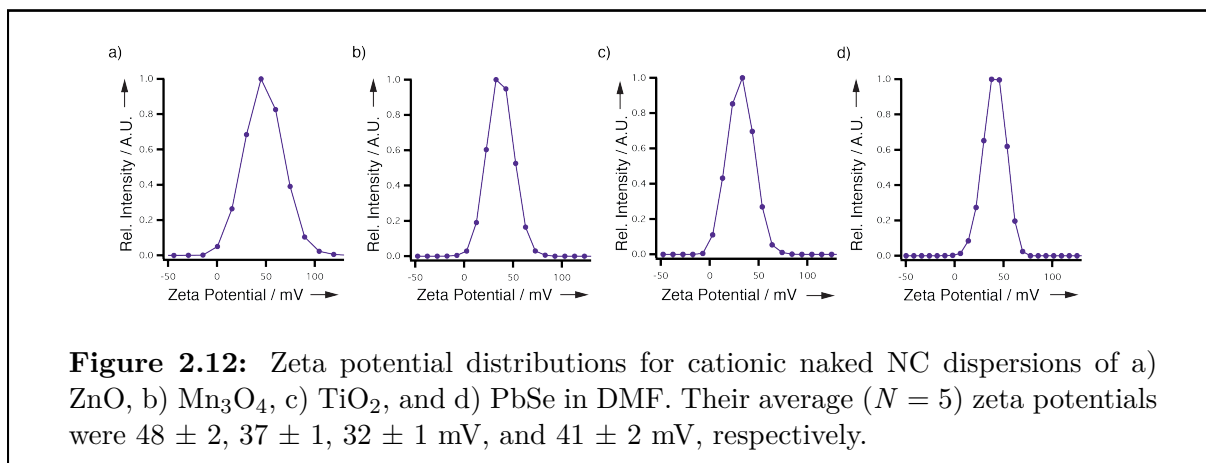
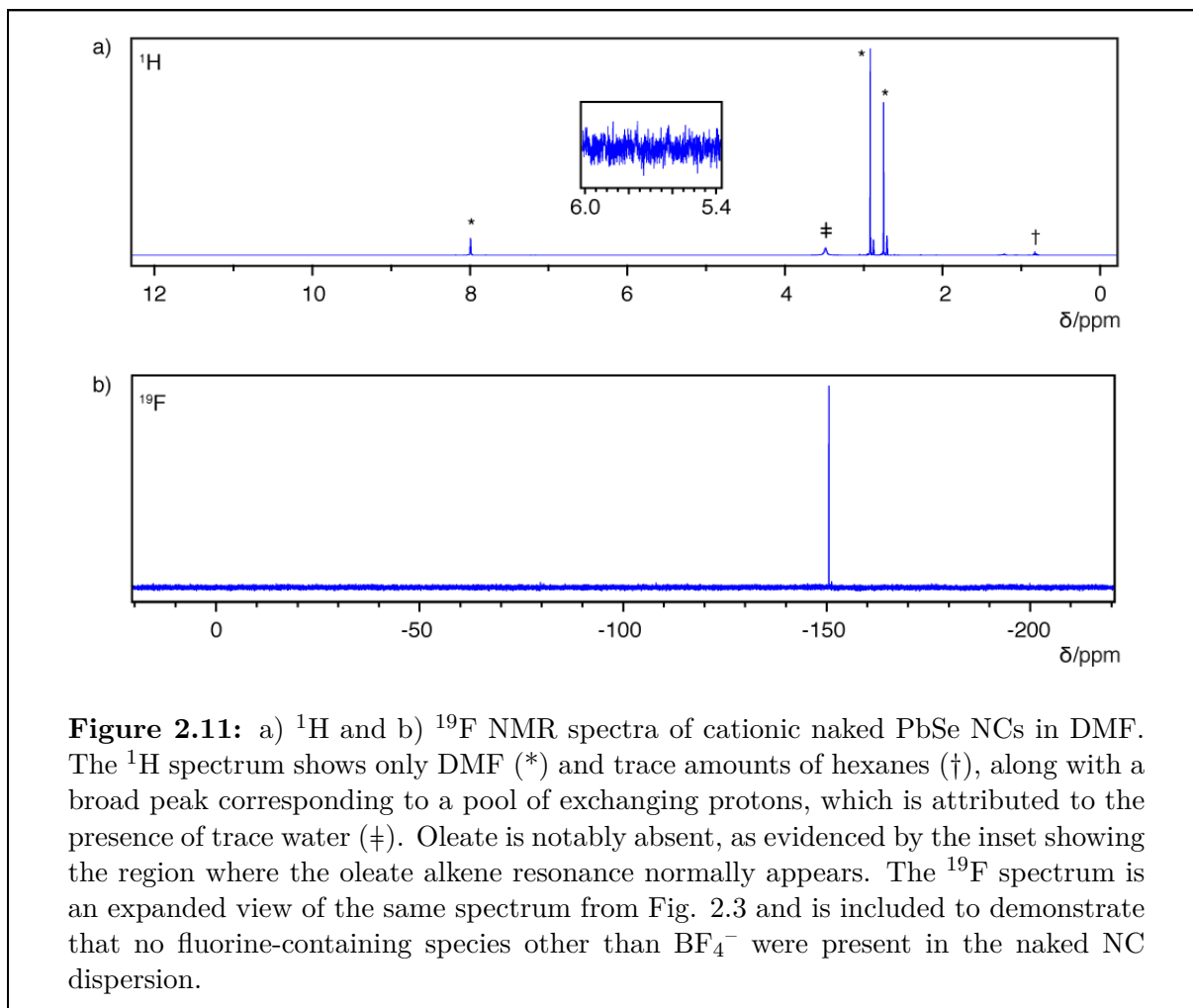
2.7.5 Preparation of naked nanocrystal thin films and polymer composites

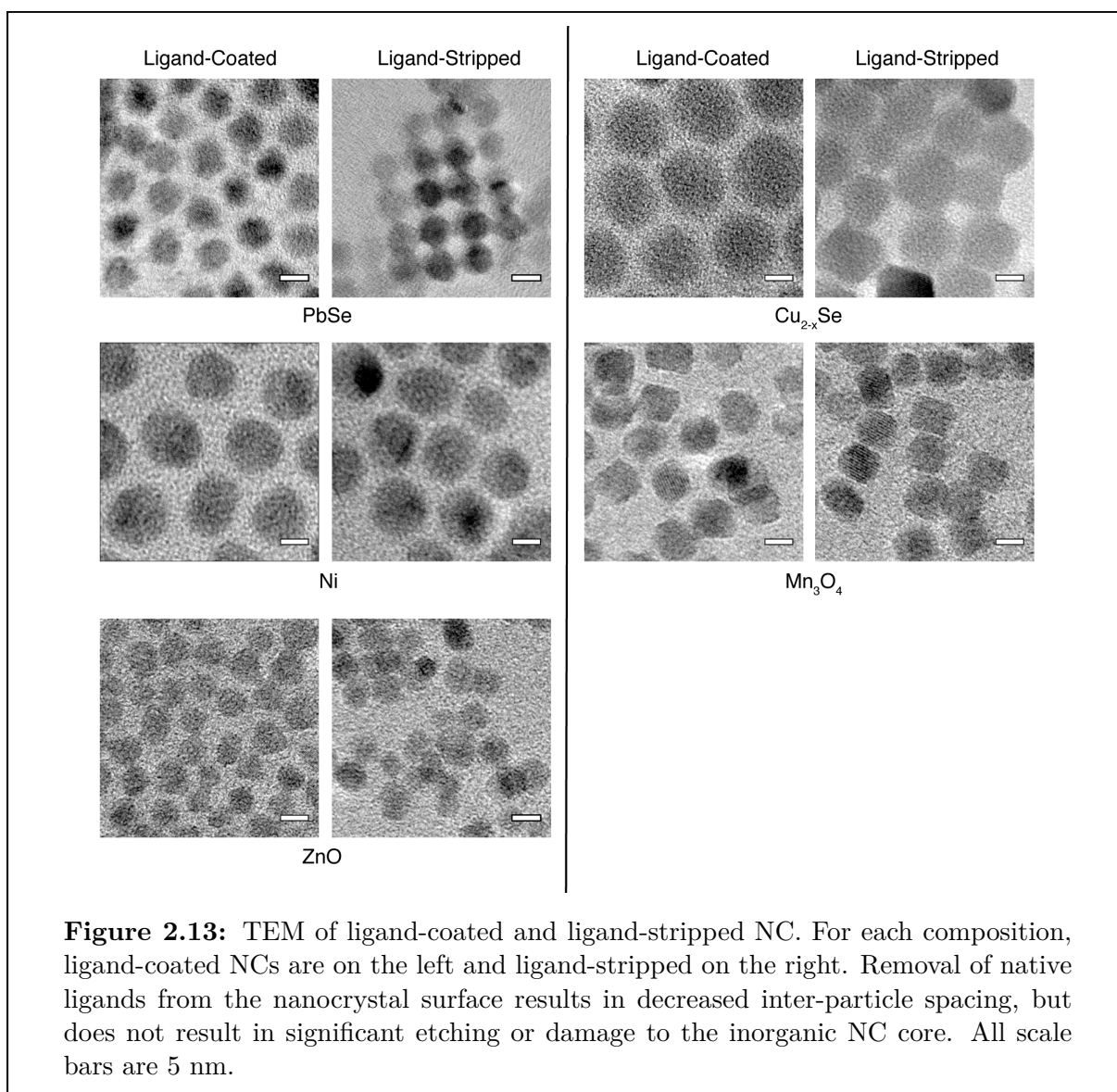
Thin films of PbSe-OA were prepared by spin-coating a solution of PbSe-OA in 1:1 hexane:octane (v/v) onto a silicon wafer. To strip the NC film in the solid state, the film was dipped into a solution of $\text{BF}_3:\text{Et}_2\text{O}$ (50 μL) in HMPA (1 mL) and rinsed with hexanes. Ordered thin-films of naked PbSe NC could be prepared by spin-coating a solution ($\sim 10 \text{ mg mL}^{-1}$) of naked PbSe NC directly onto a silicon wafer. Architecture-directing 20kDa-60kDa PS-*b*-PDMA block co-polymers were prepared as described by us elsewhere^[81] and dissolved in DMF to form a stock solution at a concentration of 50 mg mL^{-1} . Separately, a 30 mg mL^{-1} stock solution of naked PbSe NC in DMF was prepared. The stock solutions were mixed along with excess DMF to yield a solution with a final concentration of 10 mg mL^{-1} polymer and $3\text{--}10 \text{ mg mL}^{-1}$ NC, which was dropcast directly onto a Si wafer to produce ordered polymer-NC composites.

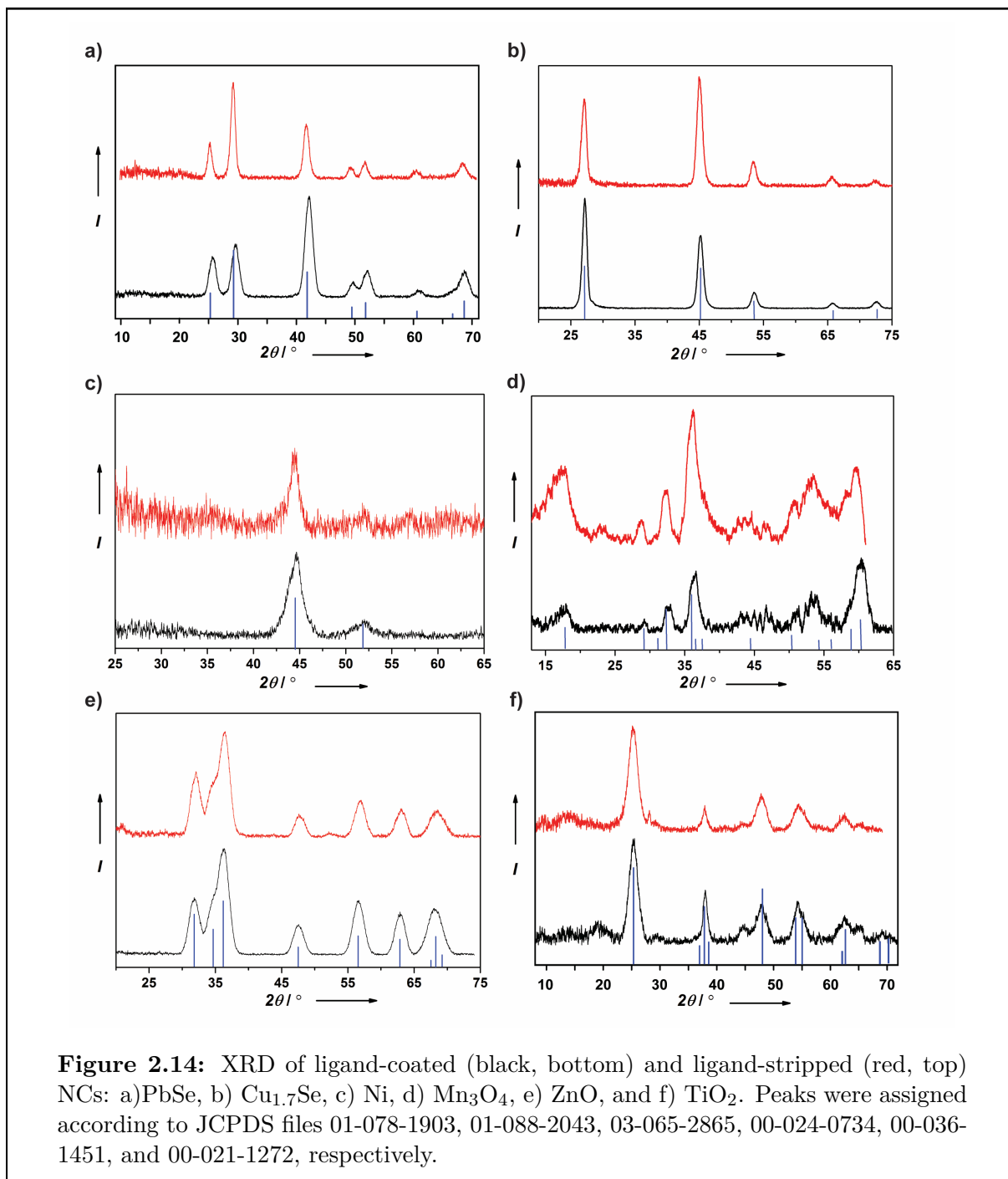
2.7.6 Additional figures

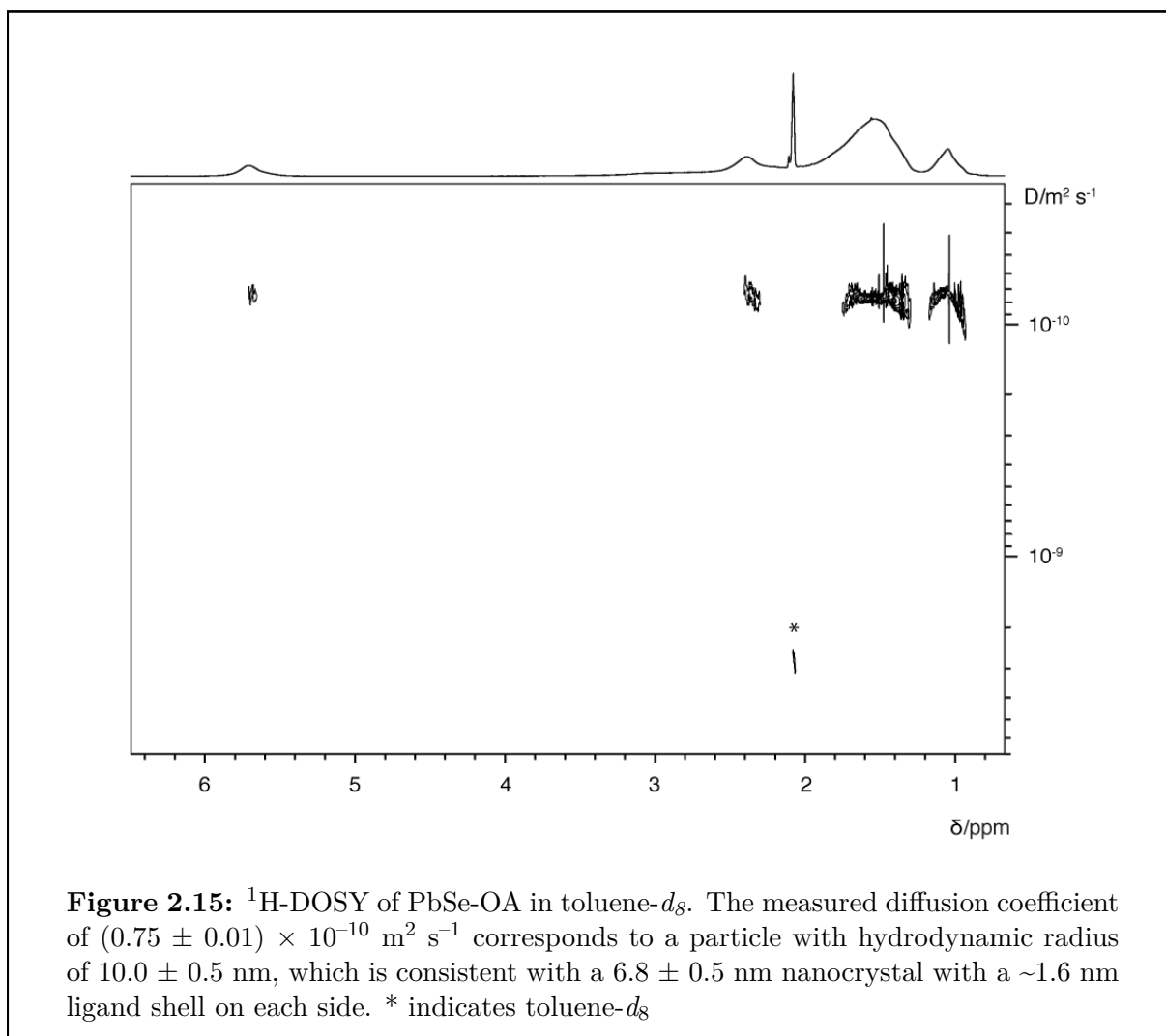












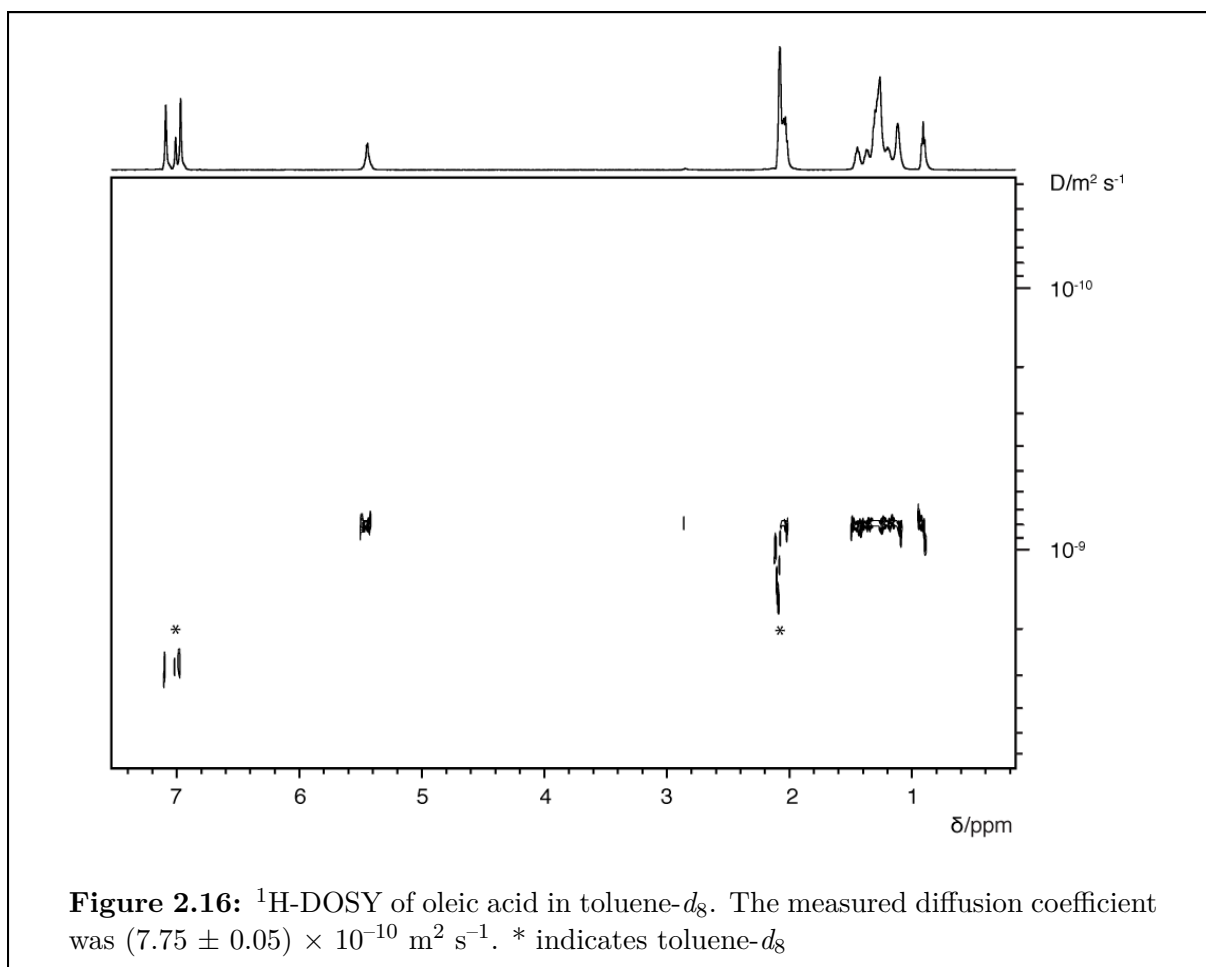
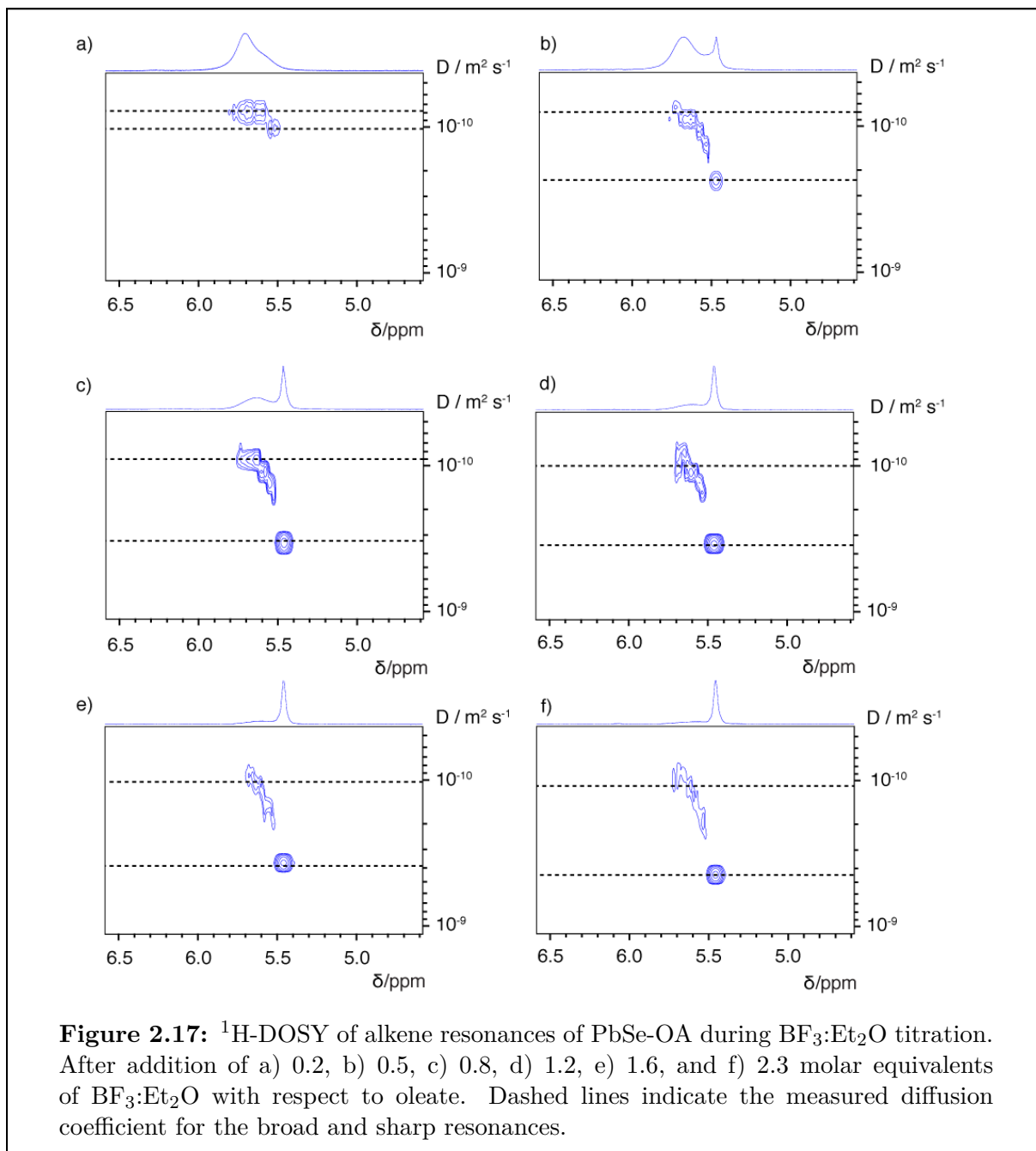
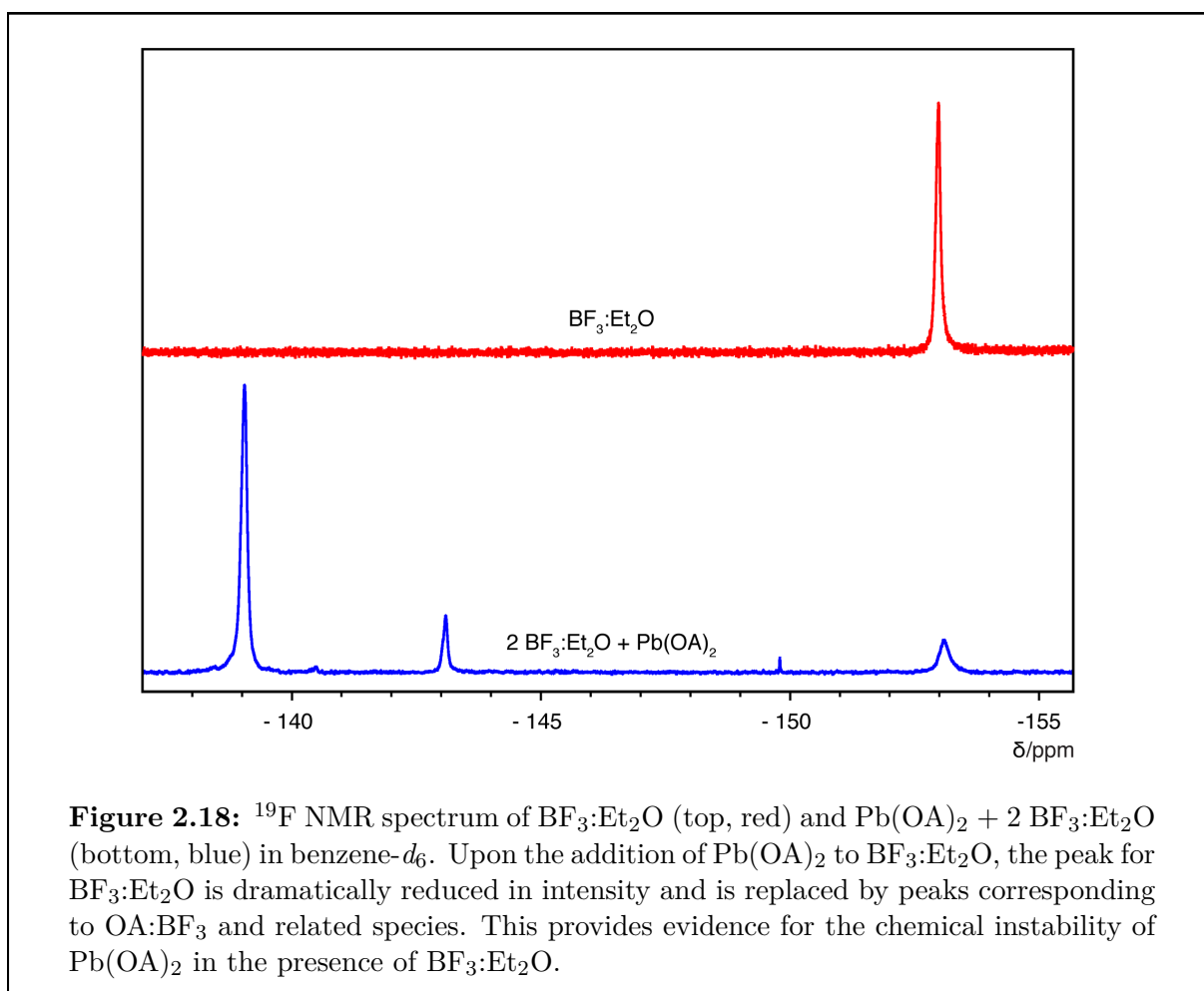


Figure 2.16: ^1H -DOSY of oleic acid in $\text{toluene-}d_8$. The measured diffusion coefficient was $(7.75 \pm 0.05) \times 10^{-10} \text{ m}^2 \text{ s}^{-1}$. * indicates $\text{toluene-}d_8$





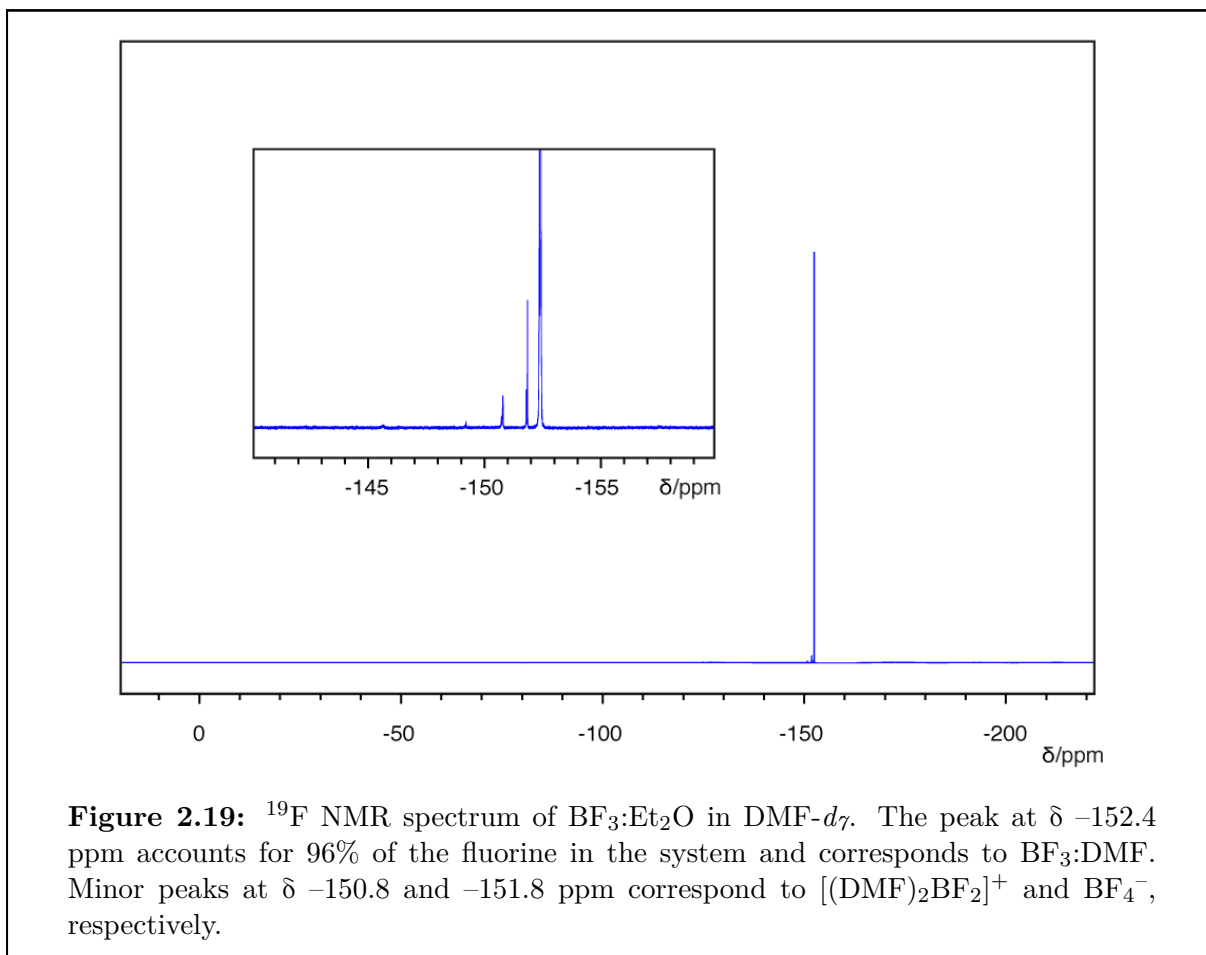
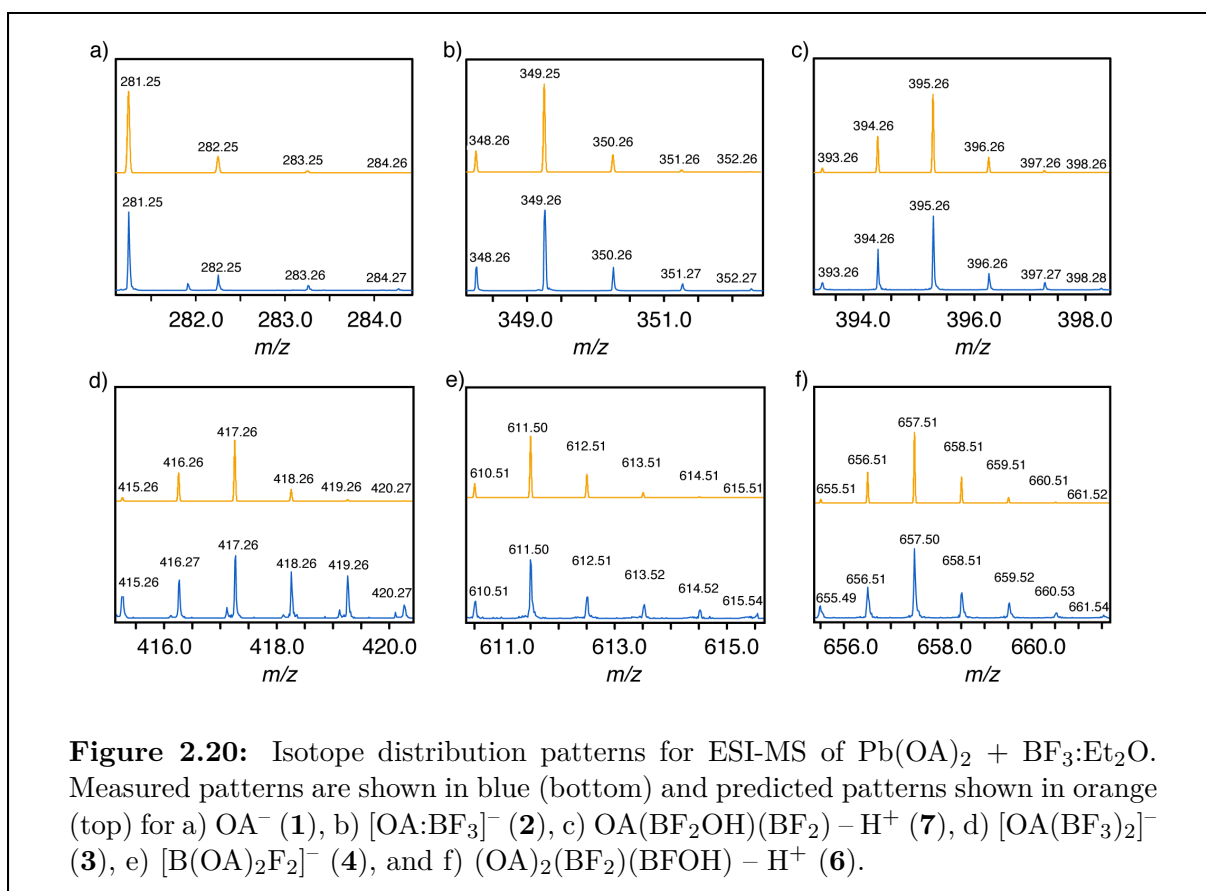
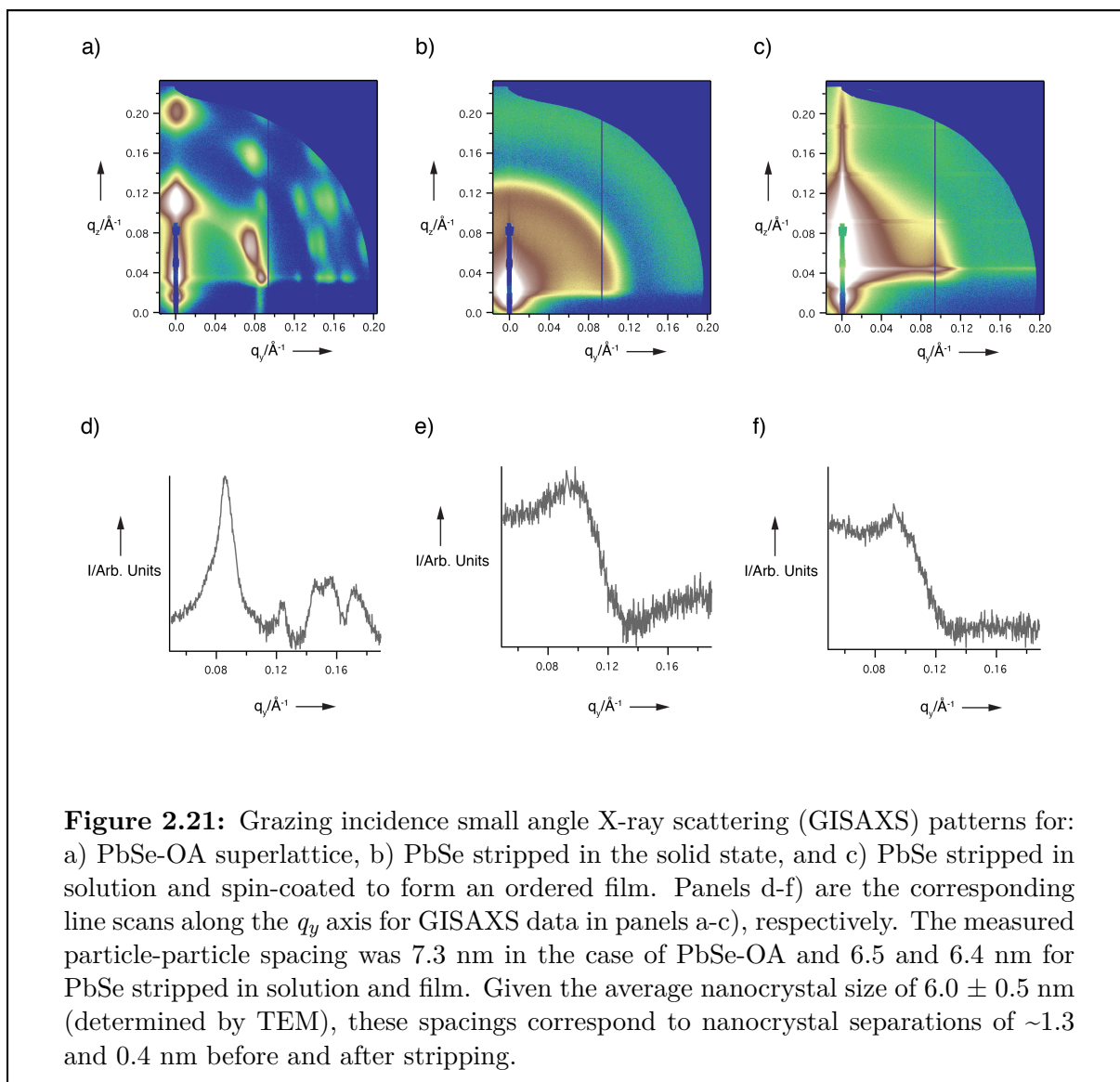


Figure 2.19: ^{19}F NMR spectrum of $\text{BF}_3:\text{Et}_2\text{O}$ in $\text{DMF-}d_7$. The peak at $\delta -152.4$ ppm accounts for 96% of the fluorine in the system and corresponds to $\text{BF}_3:\text{DMF}$. Minor peaks at $\delta -150.8$ and -151.8 ppm correspond to $[(\text{DMF})_2\text{BF}_2]^+$ and BF_4^- , respectively.





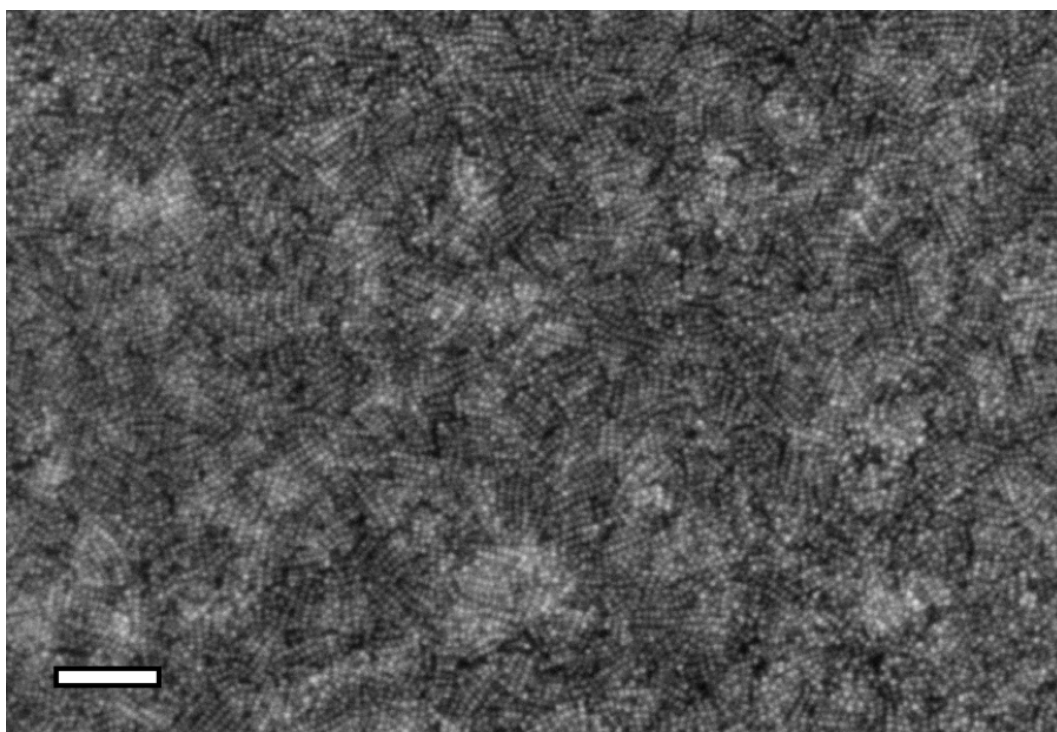


Figure 2.22: SEM of ligand-stripped PbSe thin-film deposited from solution: an enlarged field of view of the data presented in Fig. 2.7d. Scale bar is 100 nm.

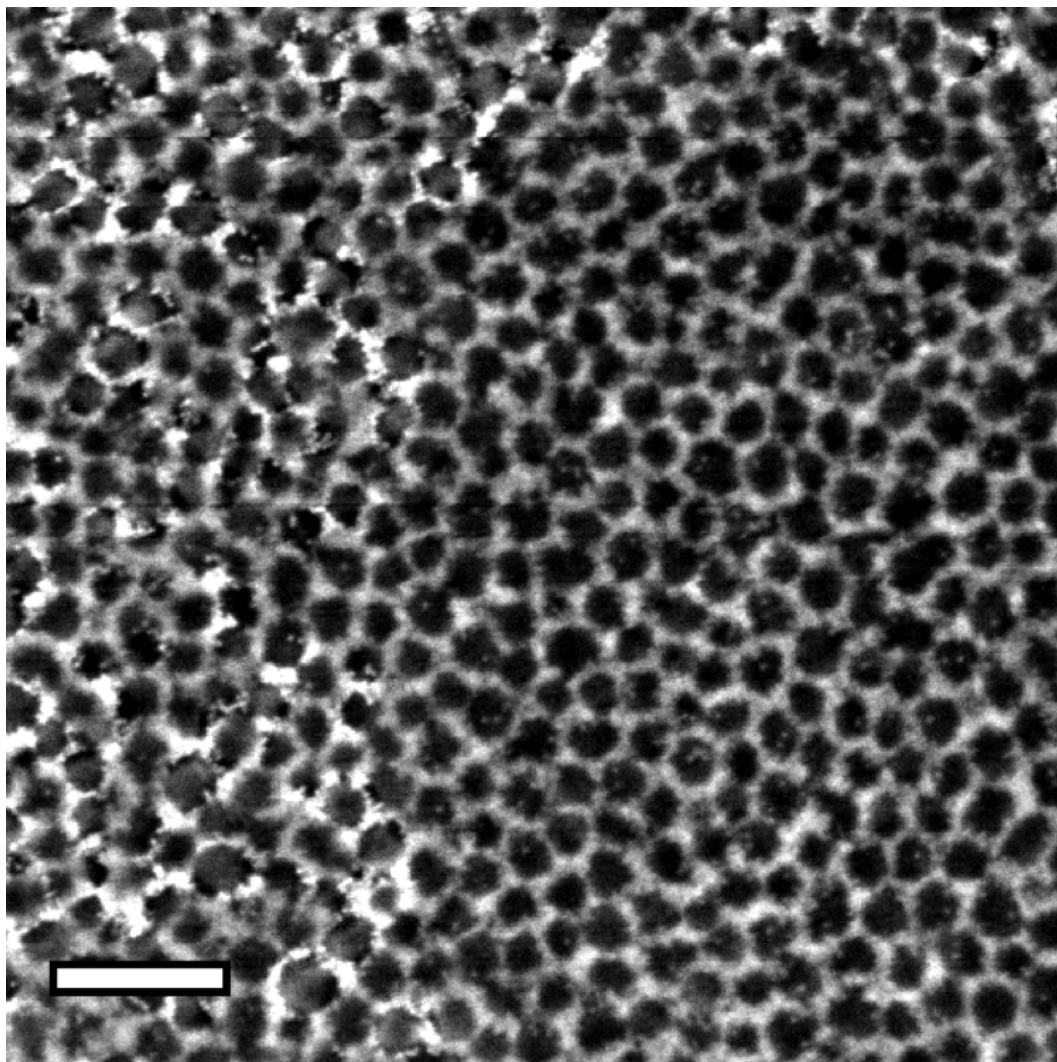


Figure 2.23: SEM of a ligand-stripped PbSe-block copolymer mesostructured composite: an enlarged field of view of the data presented in main text Fig. 2.8b. Scale bar is 200 nm.

2.8 Acknowledgements

I thank N. Su and T. Williams for supplying Ni nanocrystals and block copolymer architecture-directing agents, respectively, A. Hexemer for assistance with GISAXS, P. Frischmann for assistance with ESI-MS, and L. Gerber for helpful discussions. All work with PbSe, TiO₂, ZnO, and Mn₃O₄ was performed by S. E. Doris, C. Li, A. W. Wills, and B. A. Helms. C. Li and B. A. Helms were supported by the Joint Center for Energy Storage Research, an Energy Innovation Hub funded by the U.S. Department of Energy, Office of Science, Office of Basic Energy Sciences. S. E. Doris was supported by the Department of Defense through the National Defense Science & Engineering Graduate Fellowship program. J. J. Lynch and J. J. Urban carried out all experiments with Ni and Cu_{1.7}Se, acknowledging support from the AFOSR MURI program under FA9550-12-1-0002. Portions of the work – including nanocrystal synthesis, characterization, and chemical transformations thereof – were carried out as User Projects at the Molecular Foundry, which is supported by the Office of Science, Office of Basic Energy Sciences, of the U.S. Department of Energy under Contract No. DE-AC02-05CH11231. GISAXS was carried out at Beamline 7.3.3 of the Advanced Light Source, which is supported by the Director of the Office of Science, Office of Basic Energy Sciences, of the U.S. Department of Energy under the same contract.

Chapter 3

A Polysulfide-Blocking Microporous Polymer Membrane Tailored for Hybrid Li–Sulfur Flow Batteries

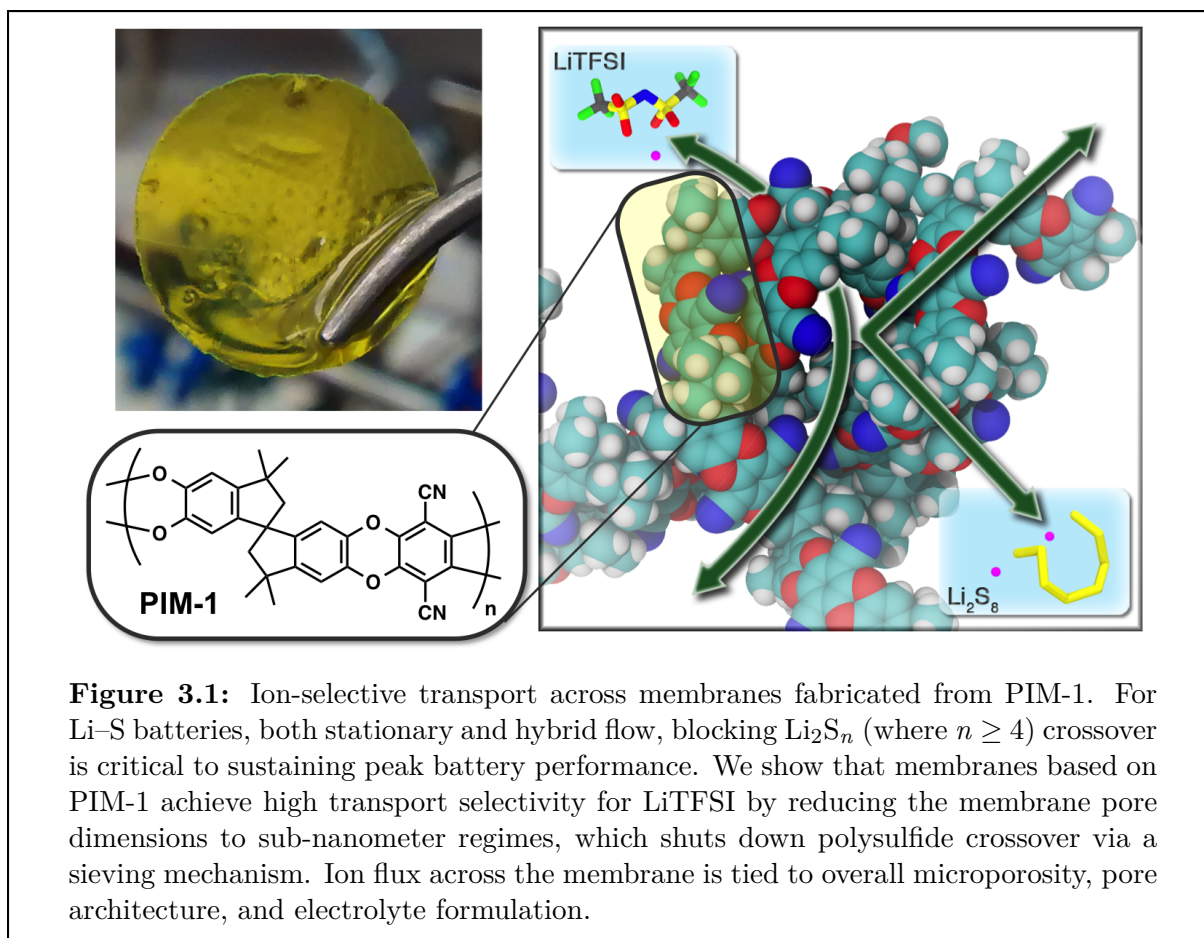
Reproduced with permission from *Nano Lett.* **2015**, *15*(9), 5724–5729.
Copyright 2015 American Chemical Society.

3.1 Introduction and prior art

Membranes (or separators) are critical for ionic conduction and electronic isolation in many electrochemical devices. For cell architectures that utilize redox-active species that are dissolved, dispersed, or suspended in electrolyte—from fuel cells^[126–128] (FCs) to redox flow batteries^[5, 40, 129–134] (RFBs)—it is also imperative that the membrane prevent active material crossover that would otherwise contribute to device shorting, electrode fouling, or irrevocable loss in capacity. Unfortunately, commercial battery separators, which feature shape-persistent mesopores, are freely permeable to most active materials used in RFBs.^[135] Alternative membrane separators have thus far relied heavily on variants of aqueous single-ion conductors, e.g., Nafion[®],^[43, 136, 137] which may ultimately restrict the use of certain types of flowable electrodes. Considerably less attention has been paid to size-sieving as a mechanism to achieve membrane selectivity, although success in this regard would allow greater flexibility in battery chemistries. Despite the wide availability of porous materials^[138] that might serve effectively as membrane components—including zeolites,^[47] metal organic frameworks,^[48–50] covalent organic frameworks,^[139] carbon nanotubes,^[51–53] cyclic peptide nanotubes,^[140–142] and microporous polymers^[54, 55]—rational design rules for achieving ion-selective transport via sieving in flow battery membranes have not been established.

Guided by theoretical calculations, I apply here polymers of intrinsic microporosity (PIMs) as a membrane platform for achieving high-flux, ion-selective transport in non-aqueous electrolytes. These polymers are synthesized in a single step and easily cast into large-area sheets with well-controlled pore structure and pore chemistry (Fig. 3.1).^[58, 59, 143–145] The unique micropore architecture of PIMs arises primarily from two molecular characteristics: 1) PIMs do not feature rotating bonds along their backbone; and 2) they incorporate rigid sharp bends into at least one of the constituent monomers at regular intervals along the polymer chain. Both features contribute to frustrated packing of polymer chains in the solid state.^[146] As a result, PIMs are amorphous yet exhibit high intrinsic microporosity (< 2 nm) and high surface area (300 – 1500 m² g⁻¹).^[147–149] The open pore architecture of PIMs suggested to us that they might be uniquely positioned for selective species transport in electrochemical devices via sieving.

I highlight here new opportunities for PIMs to serve as ion-selective membranes in RFBs,^[150–156] using lithium-sulfur (Li-S) as a model battery chemistry. Here the lithium anode is stationary and separated, by the membrane, from the flowable sulfur-containing catholyte.^[151, 155] This RFB features a high theoretical specific energy capacity of 1,670 mAh g⁻¹ of S and operating voltage that exceeds 2.0 V.^[30, 33, 157–162] While these are desirable characteristics, this battery chemistry suffers from low Coulombic efficiency and rapid capacity fade when lithium polysulfides (PS) diffuse to and react with the metal anode surface. Strategies seeking to mitigate PS crossover in Li-S batteries have included the use of sacrificial anode-protecting additives (e.g., LiNO₃),^[163–166] single-ion conducting membranes,^[136, 137] conductive interlayers,^[166–168] permselective barriers,^[169] and even polysulfide adsorbates.^[170–174] Nonetheless, continuous Li consumption upon cycling re-



mains a problem. My demonstration here that PIM membranes block PS crossover, while allowing ions in the supporting electrolyte to traverse the membrane with minimal impedance, indicates a direct solution to the PS crossover problem is feasible; I also show dramatically improved battery performance when PIM membranes are in place, rather than conventional battery separators.

3.2 Molecular dynamics simulations of solvated polysulfides

To inform the rational design of a membrane platform capable of achieving high transport selectivity for supporting electrolyte (Lithium bis(trifluoromethane)sulfonimide, LiTFSI) *vs.* PS in Li-S RFBs, we carried out molecular dynamics (MD) simulations of each species' solvated structures in different etheral solvents – diglyme (G2), triglyme (G3), and tetraglyme (G4) – as these are commonly used in Li-S RFBs.^[175–177] The sim-

ulated effective sizes of these solvated complexes were determined by the radii of gyration (R_g) of the solute and the first solvation shell. These shells were typically composed of two solvent molecules, as exemplified by the average snapshots shown in Figure 3.2a. We also calculated the size of elemental sulfur, which exhibits no explicit solvent coordination in our simulations. For this singular case, we determined a size for S_8 using its atoms' van der Waals solvent-excluded radii. Our determinations of R_g provide size-ranges for selective ion transport (Fig. 3.2b). As the primary contributors to the shuttling currents are lithium polysulfides Li_2S_n where $n \geq 4$, the membrane pore dimensions should be smaller than 1.2–1.7 nm in order to achieve ion-selective transport.

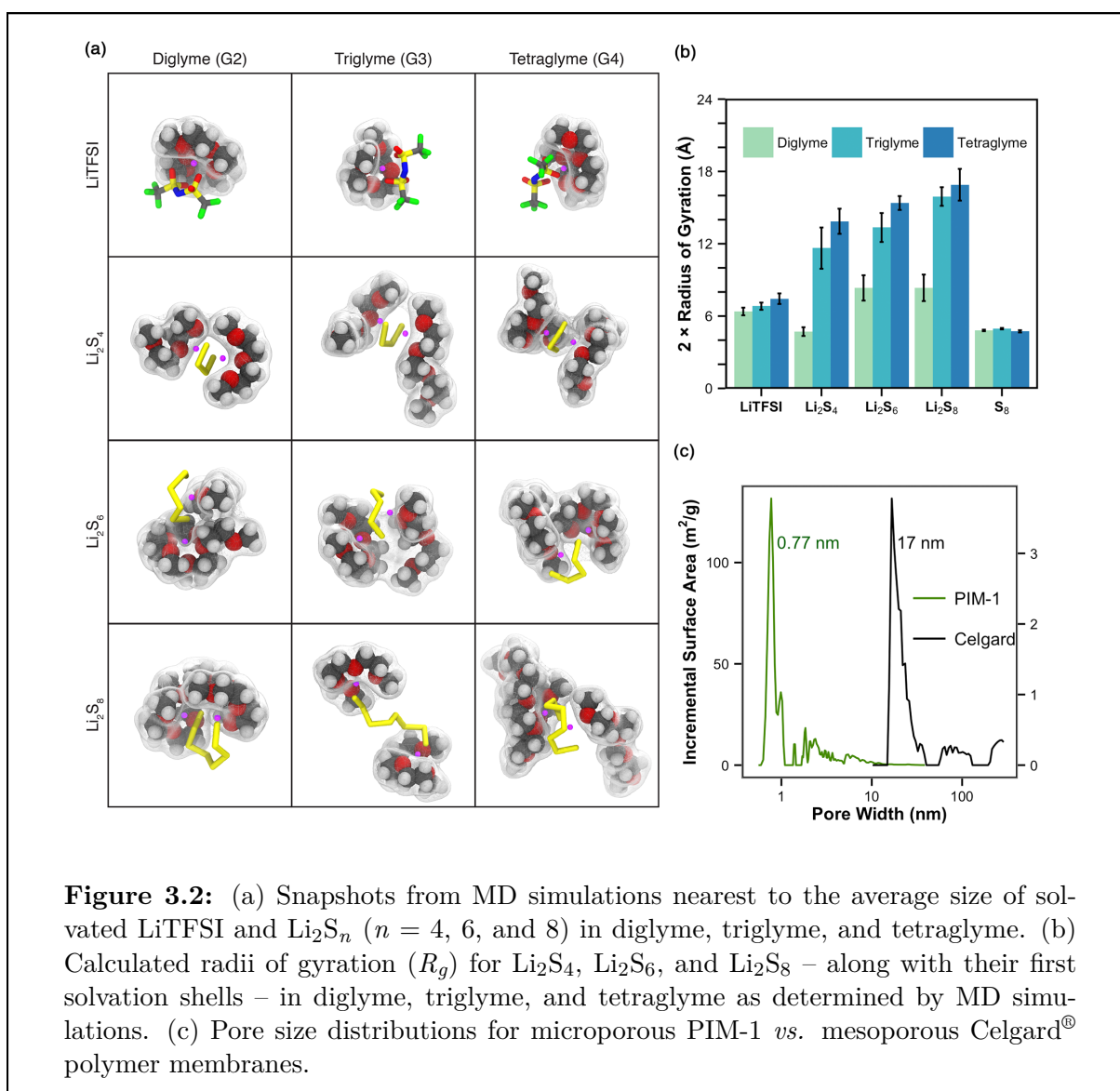


Figure 3.2: (a) Snapshots from MD simulations nearest to the average size of solvated LiTFSI and Li_2S_n ($n = 4, 6, \text{ and } 8$) in diglyme, triglyme, and tetraglyme. (b) Calculated radii of gyration (R_g) for Li_2S_4 , Li_2S_6 , and Li_2S_8 – along with their first solvation shells – in diglyme, triglyme, and tetraglyme as determined by MD simulations. (c) Pore size distributions for microporous PIM-1 *vs.* mesoporous Celgard® polymer membranes.

3.3 Transport of supporting electrolyte and active material in PIM-1 membranes

Directed by our MD simulations, we identified PIM-1^[58] as a possible PS-blocking membrane material for Li-S hybrid flow cells. PIM-1 is the progenitor of a family of non-networked ladder polymers that are mechanically^[178] and thermally^[179] robust; pertinent to their use here, their pore dimensions are sub-nm. PIM-1 was synthesized (200 kg mol⁻¹) on a multi-gram scale from inexpensive, commercially available monomers and cast from solution into flexible free-standing membranes (~10 μm thick) (Figures 3.1 and 3.5). We determined the specific surface area (795 m² g⁻¹) and pore size distribution of PIM-1 using nitrogen adsorption isotherms (Figure 3.2c). PIM-1 membranes had a nominal pore size of 0.77 nm, which is ideal for selective transport of LiTFSI and PS blocking. This stands in stark contrast with commercially available Celgard[®] 2325, which has a much larger pore size of 17 nm: far too large for size-selective transport (Figure 3.2c). Celgard[®] 2325 and similar mesoporous polymer separators^[135] are commonly used in Li-S cells and serve as a useful benchmark for new membrane materials.^[180] A total porosity of ~25% was determined for PIM-1 membranes using ellipsometric porosimetry, which is comparable to the porosity of Celgard[®] 2325. As PIM-1 membranes are expected to swell to a degree upon introduction of electrolyte, this determina-

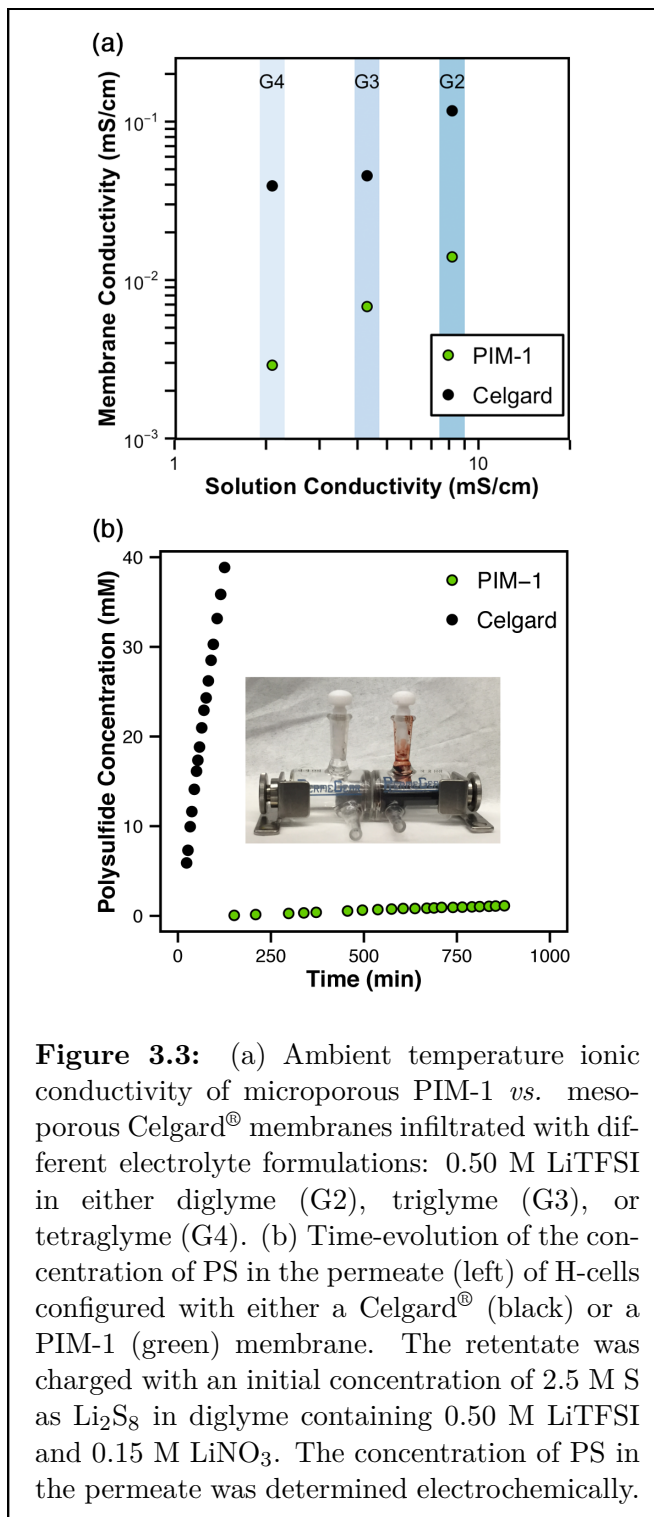


Figure 3.3: (a) Ambient temperature ionic conductivity of microporous PIM-1 *vs.* mesoporous Celgard[®] membranes infiltrated with different electrolyte formulations: 0.50 M LiTFSI in either diglyme (G2), triglyme (G3), or tetraglyme (G4). (b) Time-evolution of the concentration of PS in the permeate (left) of H-cells configured with either a Celgard[®] (black) or a PIM-1 (green) membrane. The retentate was charged with an initial concentration of 2.5 M S as Li₂S₈ in diglyme containing 0.50 M LiTFSI and 0.15 M LiNO₃. The concentration of PS in the permeate was determined electrochemically.

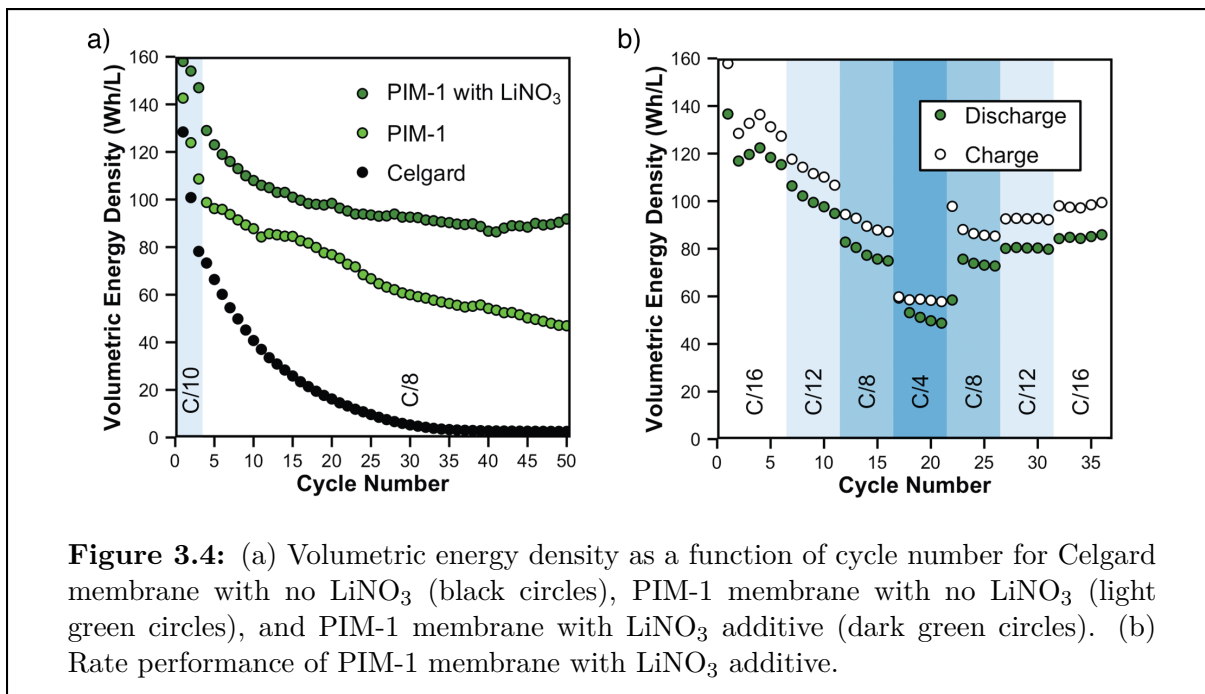
tion should be considered a lower limit to the available free volume.

I hypothesized that during battery operation the free volume in PIM-1 (and PIMs generally) would become swollen and infiltrated with electrolyte, creating an ionically percolating solution-phase conductive network. As a result, ion flux would be solely carried by (and be dependent on) the solution conductivity within the pores; polymer chain dynamics, which are orders of magnitude slower, would no longer dictate the membrane’s ionic conductivity. To test this hypothesis, we evaluated PIM-1’s membrane ionic conductivities in glymes of different oligomer lengths—diglyme (G2), triglyme (G3) and tetraglyme (G4)—containing 0.50 M LiTFSI. We noted a strong correlation between the membrane ionic conductivity and the bulk solution ionic conductivity^[181] of the electrolyte (Fig. 3.3a). These results indicate that the ion current is indeed carried by the infiltrating electrolyte, as predicted. This behavior was also observed in Celgard[®] separators (Fig. 3.3a). By comparing the membrane ionic conductivities for Celgard[®] and PIM-1, we found that reducing the pore dimensions from 17 nm to 0.77 nm, respectively, only decreased membrane ionic conductivity ten-fold. We also found that electrolytes based on diglyme provided the highest membrane ionic conductivity for both platforms, and was thus chosen as the supporting electrolyte for all subsequent experiments.

To quantify the polysulfide-blocking ability of PIM-1 *vs.* Celgard[®], I performed membrane crossover experiments in H-cells configured with dissolved PS (2.5 M S as Li₂S₈ in diglyme containing 0.50 M LiTFSI and 0.15 M LiNO₃) on the retentate side and PS-free electrolyte on the permeate side (Fig. 3.3b, inset). The concentration of PS over time was then monitored electrochemically on the permeate side using either cyclic voltammetry or square wave voltammetry, where current could be correlated to concentration of PS via a calibration curve (Figures 3.6 and 3.7). Using an initial rate approximation, the diffusion coefficient of PS across the membrane was calculated to be $6.8 \times 10^{-8} \text{ cm}^2 \text{ s}^{-1}$ for Celgard[®] and $1.3 \times 10^{-10} \text{ cm}^2 \text{ s}^{-1}$ for PIM-1 (~500-fold reduction). This is compelling evidence that PS are screened by a size-sieving mechanism within PIM-1’s ionically-percolating micropore network, as hypothesized. This PS-blocking ability comes at minimal expense to overall membrane ionic conductivity compared to Celgard[®], thus highlighting the value in guiding membrane design through careful examination of the solvated structures of ions *vs.* redox active species in the electrolyte.

3.4 Improved capacity retention for batteries with PIM-1 membranes

Given the outstanding PS-blocking ability of the PIM-1 membrane, their performance in Li-S batteries was tested employing soluble sulfur catholytes. To do so, Swagelok cells were assembled with Li-metal anodes, polysulfide catholytes (2.5 M S as Li₂S₈ in diglyme containing 0.50 M LiTFSI) and Celgard[®] or PIM-1 membranes. Lithium anodes were scraped to reveal a fresh surface prior to cell assembly. Seeking to isolate the membrane’s influence on mitigating PS shuttling currents, LiNO₃ additives were deliberately avoided



in the electrolyte formulation. Moreover, to improve sulfur utilization, 5 wt% Ketjenblack was employed as an embedded current collector in the catholyte.^[153, 180] Three break-in cycles at C/10 were used to equilibrate PIM-1's membrane microenvironments before cycling at a C/8 rate. Overall, higher capacity fade was observed for both types of cells during the break-in due to the ample time allowed for polysulfide shuttling. The Li-S cells configured with Celgard[®] membranes exhibited a drastic capacity fade from ~150 Wh L⁻¹ after the break-in cycles to less than 20 Wh L⁻¹ within the first 20 cycles, all at a C/8 rate. In contrast, batteries configured with PIM-1 membranes exhibited higher capacity at all cycles, sustaining 50 Wh L⁻¹ at the end of 50 cycles (Figure 3.4a). The performance of PIM-1 membranes was further improved with the addition of LiNO₃ as an anode-protecting additive, with a sustained capacity of approximately 100 Wh L⁻¹ after 50 cycles (Figure 3.4a) and stable cycling at rates as high as C/4 (Figure 3.4b). These results represent improvements in capacity retention over related work with Li-S flow cells, particularly in the absence of LiNO₃, and highlight the possibility for combining our membrane approach with other strategies to mitigate the effects of polysulfide crossover.^[166, 182]

3.5 Conclusions and future work

Redox flow batteries present unique opportunities for low-cost, multi-hour energy storage—but also limitations. In order for RFBs to mature as a deployable technology, their

longevity should be greatly improved for battery chemistries offering high-power performance. Toward that end, we highlighted the transport needs for membranes employed in non-aqueous Li-S cells, where the cathode was formulated as an energy-dense, flowable solution of polysulfides with Ketjenblack as an embedded current collector. We showed that rational principles for membrane design emerge from molecular dynamics simulations of the solvated structures of S_8 , Li_2S_n ($n = 8, 6, \text{ or } 4$), and LiTFSI in different electrolytes, and more specifically, that their calculated radius of gyration places an upper limit of 1.2–1.7 nm on the pore dimensions required for polysulfide blocking. Indeed, I showed that membranes processed from polymers of intrinsic microporosity exhibited unprecedented blocking characteristics for soluble polysulfides owing to their sub-nm pore dimensions. This blocking ability led to significantly improved device performance with respect to capacity fade and other important metrics. Given that the pore size, pore chemistry, and overall porosity for PIM membranes are tunable using molecular engineering and polymer processing, the membrane’s transport characteristics can be tailored to suit a broad spectrum of electrochemical devices, including stationary batteries and fuel cells. Our success suggests a revolution in ion-transporting membranes is within reach.

3.6 Supporting information

3.6.1 Materials and methods

Ionic conductivity measurements

Soaked membranes were sandwiched between two stainless steel blocking electrodes. Potentiostatic electrochemical impedance spectroscopy (PEIS) was used with 50 mV AC bias scanning from 1 MHz to 100 mHz. The high frequency x -axis intercept is taken to be the resistance of the membrane. The membrane conductivity was then calculated taking into account the cell geometry.

Crossover experimental methods

Crossover measurements were made by placing respective membranes between the cell halves of a PermeGear Side-Bi-Side diffusion cell. Next, to the retentate side of the cell was added 2.5 mL of supporting electrolyte (0.15 M LiNO₃, 0.5 M LiTFSI in diglyme) and 2.5 mL of 2.5 M Li₂S₈ electrolyte was added to the permeate side. In this case, due to the presence of lithium as a reference electrode, LiNO₃ was necessary to prevent the reaction of polysulfides with the lithium. Crossover was determined by cyclic voltammetry and square wave voltammetry measurements of the permeate side of the cell. Cyclic voltammetry allowed concentrations between 5.0–60 mM to be measured while square wave voltammetry allowed for measurements of concentrations ranging from 0.20–1.0 mM. Given the different rates of crossover between the two materials, both techniques were necessary as the Celgard[®] crossover was too fast to be measured accurately with the SWV, and the PIM crossover was too slow to be measured in a convenient time frame with CV. A glassy carbon disc electrode (1 mm) was obtained from BAS Inc. (West Lafayette, IN), polished before use and used as the working electrode. Lithium metal was used as the reference and counter electrodes. A calibration curve for each electrochemical technique was obtained by measuring the current as a function of concentration for a set of known concentration polysulfide solutions (Figures 3.6 and 3.7). The concentration of polysulfide *vs.* time for the crossover measurements was then calculated using the linear equation determined from the calibration curves.

Battery cycling

Cathode slurry was spread evenly into the cathode well. Lithium chip was punched using a 7/16-inch bore and pressed onto the anode. Due to the safety concern of dendrite formation, membranes were sandwiched between two Celgard[®] layers to isolate them from the lithium polysulfide slurry and the lithium anode surface. The tri-layer membrane was then pressed in between the two electrodes to assemble a Swagelok battery.

3.6.2 Computational methods

First-principles molecular dynamics simulations

The S_8 /LiTFSI/Li₂S_{*n*}-TEGDME systems were simulated using a modified version of the mixed Gaussian and plane wave code^[183] CP2K/Quickstep^[184]. We employed a triple- ζ basis set with two additional sets of polarization functions (TZV2P)^[185] and a 320 Ry plane-wave cutoff. The unknown exchange-correlation potential is substituted by the revised PBE generalized gradient approximation^[186, 187], and the Brillouin zone is sampled at the Γ -point only. Interactions between the valence electrons and the ionic cores are described by norm-conserving pseudopotentials^[188, 189]. The Poisson problem is tackled using an efficient Wavelet-based solver.^[190] We overcome the poor description of the short-range dispersive forces within the PBE-GGA exchange-correlation functional by employing the DFTD3 empirical corrections of Grimme *et al.*^[191] In order to equilibrate the systems, we performed 10 ps of NPT dynamics, using a Nose-Hoover thermostat (temperature damping constant of 100 fs) and an Anderson barostat (pressure damping constant of 2 ps). Snapshots of the system were saved every step. The snapshot with a volume closest to the average of the last 5 ps of MD was then selected as input for an additional 20 ps simulation in the constant volume, constant temperature (canonical or NVT) ensemble.

Structural analysis

We estimated the “size” of the solvated lithium polysulfide species as the sum of two terms: 1) the radius of gyration of the solute (R_{gyr}) and 2) the size of the glyme solvation shell. All structural analyses were performed for every 10 snapshots from the last 20 ps of the NVT AIMD simulations (4,000 for each system). The R_{gyr} was computed as

$$R_{gyr} = \sqrt{\frac{1}{M} \sum_i m_i (r_i - r_{cm})^2}$$

where M is the total mass of the solute, R_{cm} is the center of mass and the sum is over all r_i atoms in the solute.

The solvation environment around each dissolved polysulfide was obtained calculating the Li-glyme (oxygen atom) and S-glyme pair distribution functions (PDF) from the last 20 ps NVT MD simulation. The 1st solvation shell was obtained from the minimum in the PDF after the first peak, and the number of solvent molecules obtained by simple integration.

3.6.3 Additional figures

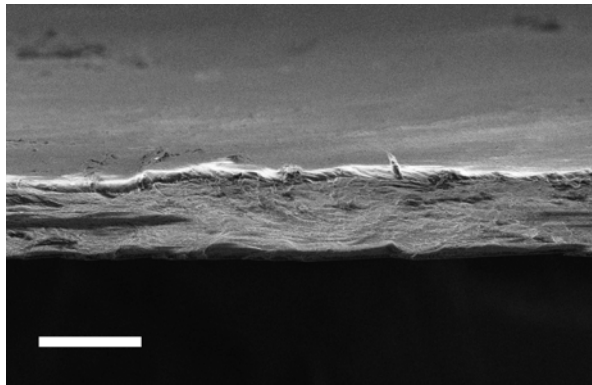


Figure 3.5: Cross-sectional scanning electron micrograph of a free-standing PIM-1 membrane. The scale bar is 10 μm .

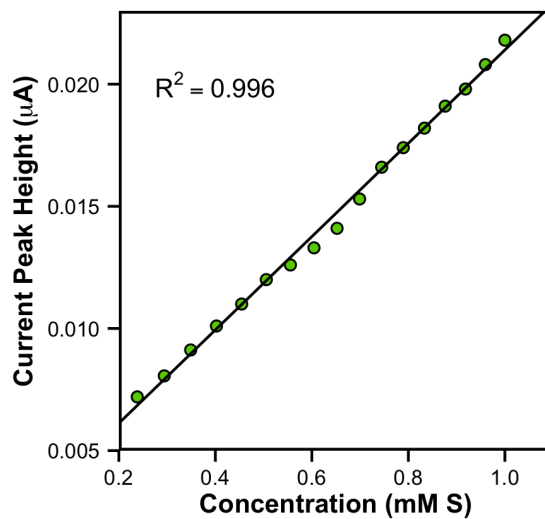


Figure 3.6: Calibration curve of current *vs.* concentration obtained via square wave voltammetry for the lower concentration regime.

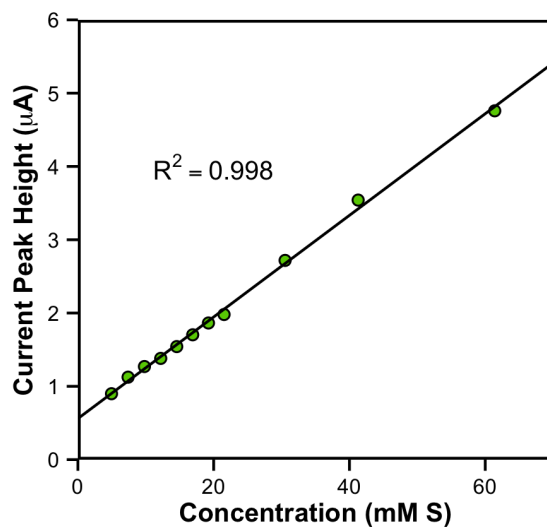


Figure 3.7: Calibration curve of current *vs.* concentration obtained via cyclic voltammetry for the higher concentration regime.

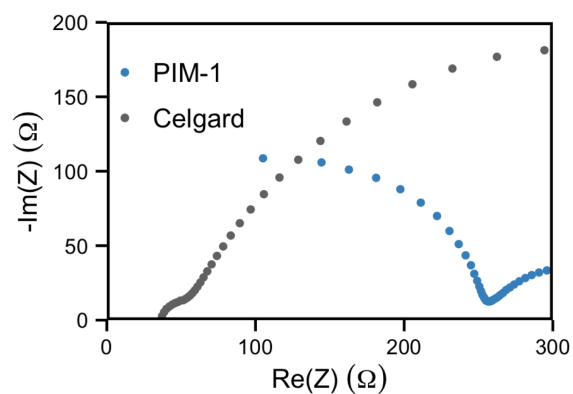
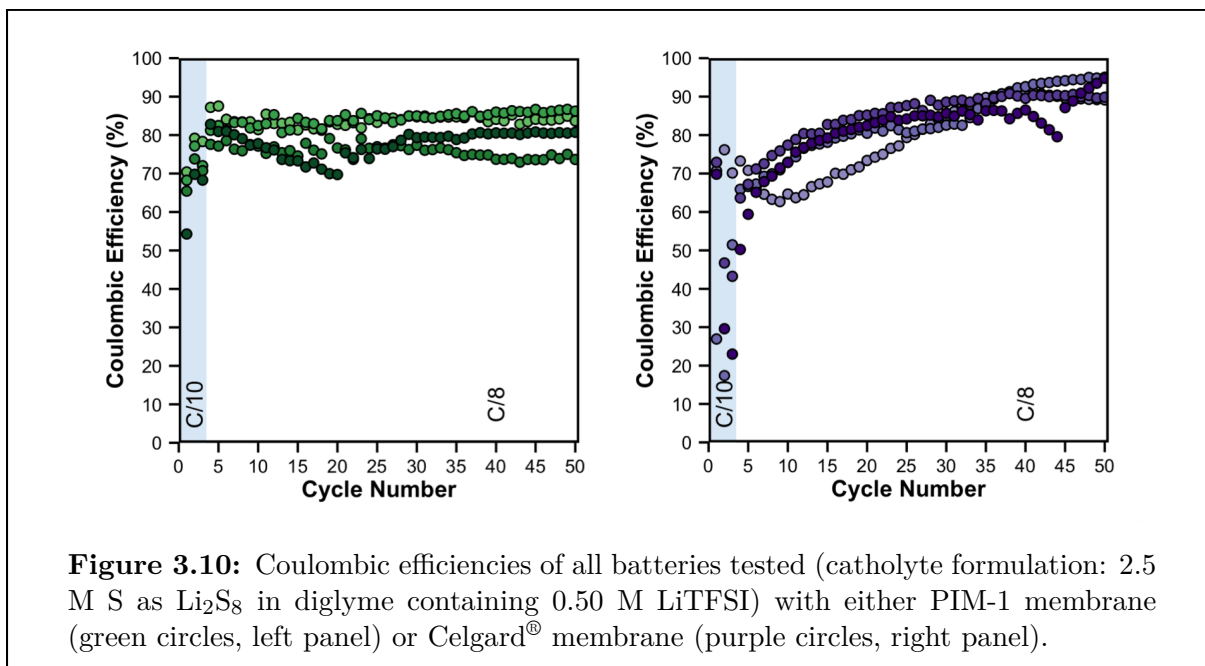
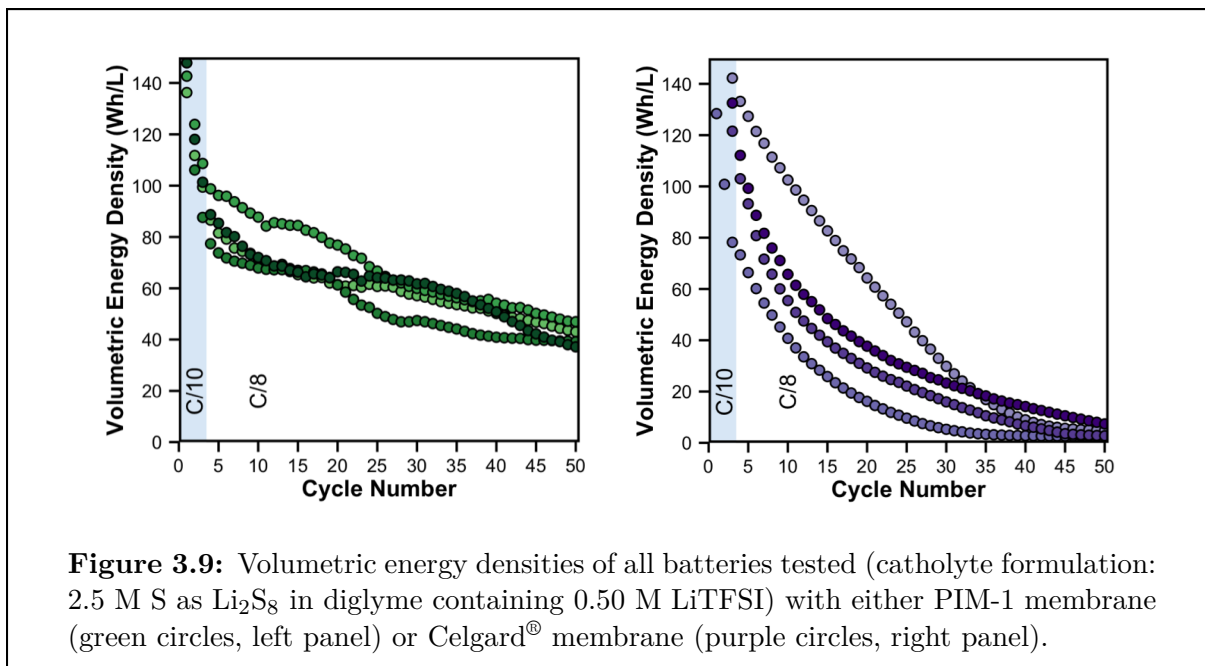
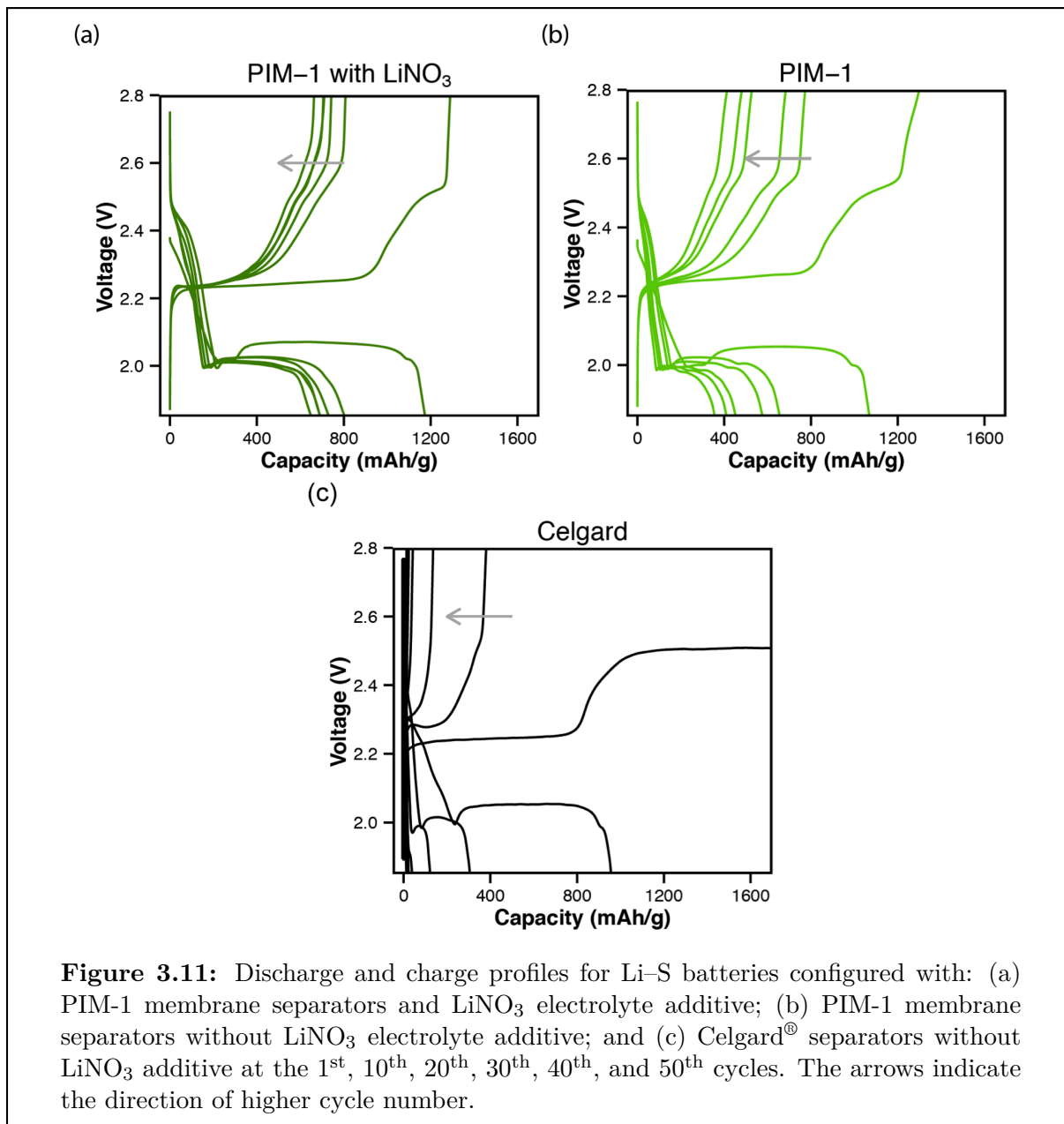
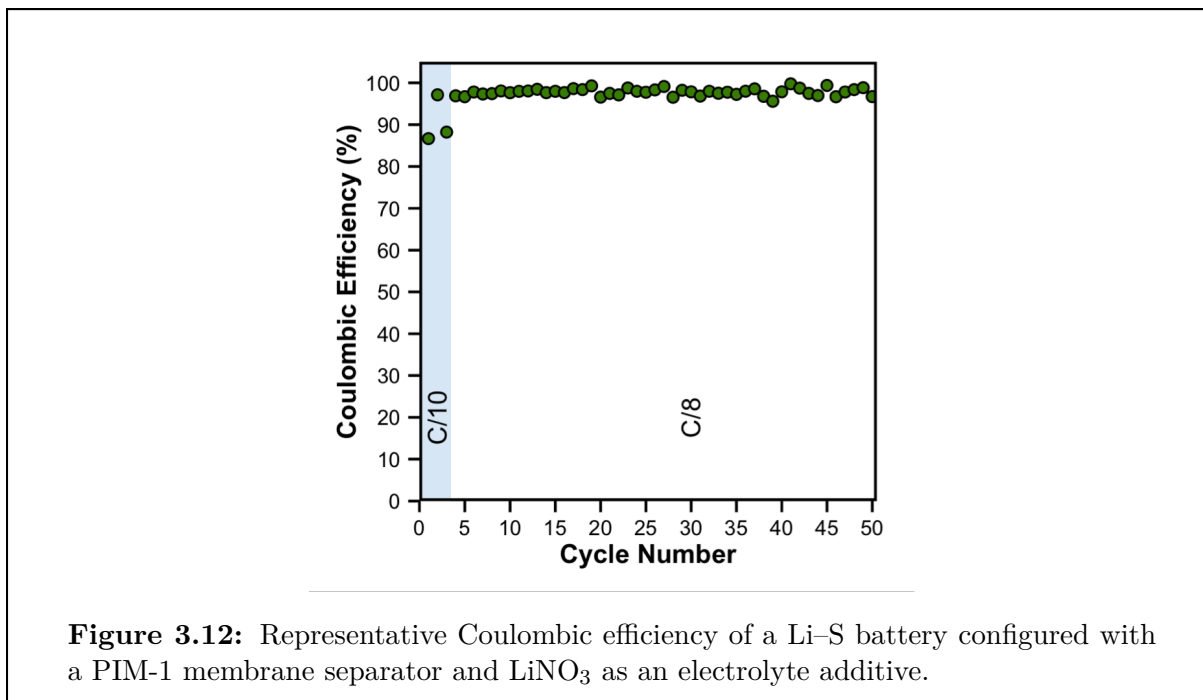


Figure 3.8: Electrochemical impedance spectroscopy (EIS) of Li-S cells configured with PIM-1 and Celgard[®] as membranes, respectively. The membrane ionic conduction kinetics are represented by the sizes of high-frequency semicircles, which are 20.1 Ω and 215.1 Ω for Celgard[®] and PIM-1, respectively.







3.6.4 Acknowledgements

This chapter is the result of a collaboration between myself, C. Li, A.L. Ward, T.A. Pascal, D. Prendergast, and B.A. Helms, and I am thankful to all my co-authors for their help with this work. We thank D. Sun for assistance with nitrogen adsorption experiments, A. Bondaz for assistance with ellipsometric porosimetry. E. Wong, S. Ferreira, P. Chavez, B. Smith, D. Li for electrode fabrication, as well as P. Frischmann and L. C. H. Gerber for helpful discussions. C. Li, A. L. Ward, and B. A. Helms were supported by the Joint Center for Energy Storage Research, an Energy Innovation Hub funded by the U.S. Department of Energy, Office of Science, Office of Basic Energy Sciences. S. E. Doris was supported by the Department of Defense through the National Defense Science & Engineering Graduate Fellowship program. D.P. and T.A.P. acknowledge support from the Batteries for Advanced Transportation Technologies program, administered by the Assistant Secretary for Energy Efficiency and Renewable Energy, Office of Vehicle Technologies of the U.S. Department of Energy under Contract DE-AC02-05CH11231. Portions of the work—including polymer synthesis and characterization, molecular dynamics simulations, polymer processing, membrane crossover experiments, and Li-S battery performance—were carried out as User Projects at the Molecular Foundry, which is supported by the Office of Science, Office of Basic Energy Sciences, of the U.S. Department of Energy under Contract No. DE-AC02-05CH11231. The computational portion of this work used resources of the National Energy Research Scientific Computing Center, a DOE Office of Science User Facility supported by the Office of Science of the U.S. Department of Energy under the same contract.

Chapter 4

Understanding and Controlling the Chemical Evolution and Polysulfide-Blocking Ability of Lithium–Sulfur Battery Membranes Cast from Polymers of Intrinsic Microporosity

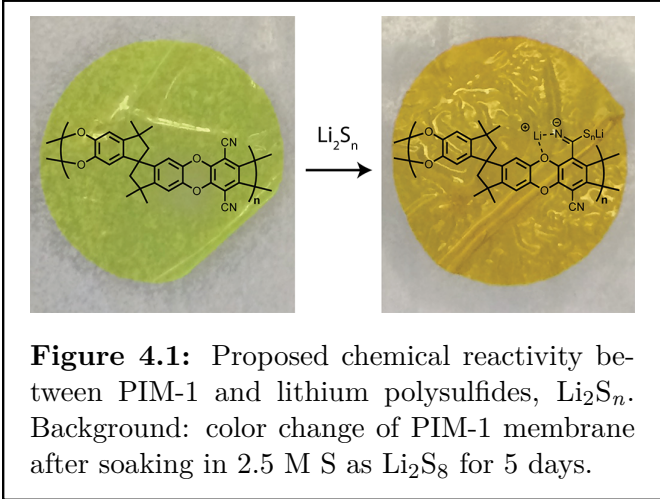
Reproduced from *J. Mater. Chem. A*, **2016**, *4*, 16946–16952 with permission from the Royal Society of Chemistry and all co-authors.

4.1 Introduction and prior art

Batteries rely on separators or membranes to electrically isolate the negative and positive electrodes while allowing ionic current to flow between them. For batteries with solid-state electrodes (e.g., Li-ion or lithium–sulfur batteries), mesoporous polymer separators often serve this purpose.^[135] On the other hand, batteries that use soluble active-materials (e.g., redox-flow batteries or lithium–polysulfide batteries) require more advanced membranes capable of blocking active-species crossover while allowing counter-ions to pass.^[5, 30, 192]

To this end, a number of membrane materials for selective lithium-ion transport in non-aqueous electrolytes have been proposed, including lithiated Nafion[®],^[42, 43] solid polymer electrolytes,^[44] Li-ion conducting glasses,^[41] and polymers of intrinsic microporosity (PIMs).^[56] These membranes must maintain their active-species blocking ability to ensure long battery lifetimes and high efficiency, even if those active-species are highly reactive. Despite the importance of membrane stability, little is known about the effect of chemical reactivity on transport selectivity for these membranes. Here I use size-selective, polysulfide-blocking membranes cast from PIM-1, a polymer of intrinsic microporosity, as a model system for understanding the design rules needed to stabilize their performance as ion-selective membranes for lithium–sulfur (Li–S) and lithium–polysulfide (Li–PS) batteries.

Li–S and Li–PS batteries are attractive technologies due to the high specific capacity (1675 mAh g⁻¹) and low cost of sulfur.^[31–36] The reduction of sulfur (S₈) to lithium sulfide (Li₂S) proceeds through several intermediates, including highly soluble lithium polysulfides—Li₂S_{*n*}, where 4 ≤ *n* ≤ 8—that can diffuse across the cell and react with the anode, leading to the well-known shuttle effect. This shuttling effect is known to decrease cell lifetime and efficiency.^[193–195] To address the polysulfide crossover problem, we recently reported size-selective membranes based on polymers of intrinsic microporosity (PIMs) that block polysulfide crossover while allowing Li-ion transport.^[56] PIMs are unique in that they have permanent microporosity due to frustrated packing of polymer chains in the solid state.^[54, 55, 58, 59, 143, 179] This property makes PIMs both highly permeable and well suited as size-selective membranes because the pore size can be carefully chosen to block active-species crossover while allowing facile Li⁺ transport. Despite these promising characteristics, little is known about their chemical stability in batteries or the impact of polymer reactivity on polymer structure and transport behavior over long periods of time.



During the operation of both Li–S and Li–PS batteries, Li_2S_n are in direct contact with the membrane. Li_2S_n are both nucleophilic and reducing to many organics with low-lying LUMOs.^[160, 196] I hypothesized that electrophilic 1,4-dicyanooxanthrene functionalities in PIM-1 might be prone to nucleophilic attack by Li_2S_n , forming lithiated thioamides (Fig. 4.1). To that end, I noted during post-mortem analysis of cycled Li–PS batteries that PIM-1 membranes changed in color from bright yellow to orange, suggesting a chemical reaction had indeed taken place. In addition to the color change, membranes that were soaked in polysulfide solution were subsequently insoluble in chloroform, while membranes that were soaked in solvent or electrolyte retained their chloroform solubility. Neither the product of that transformation nor its impact on PIM-1’s transport selectivity was immediately known. Thus, I carried out detailed chemical analyses of the reaction products using a variety of spectroscopic methods—including *in situ* FT-IR and NMR spectroscopy—and was able to link local changes in PIM-1’s pore chemistry to changes in macroscale pore architecture and related transport selectivity. With that knowledge, I was subsequently able to prevent these undesirable changes in pore architecture by cross-linking PIM-1 membranes, yielding robust membranes that retained their selectivity for at least 95 h in the presence of high concentrations of reactive lithium polysulfides.

4.2 Concentration-Dependent crossover behavior

In order to understand the effect of chemical reactivity on the selectivity of PIM-1 membranes, I conducted long-term tests (i.e., for periods longer than 12 h, as had been investigated previously) of the polysulfide-blocking ability of PIM-1. During these measurements, I found that the effective diffusion coefficient (D_{eff}) of Li_2S_n through PIM-1 membranes was not constant; instead, it gradually increased over time.

To understand whether this change in polysulfide blocking was related to the proposed chemical reaction with Li_2S_n or an unrelated membrane degradation mechanism, I studied the crossover rate systematically as a function of Li_2S_n concentration in contact with the membrane. These measurements were carried out by placing a PIM-1 membrane of known thickness and area between two compartments of electrolyte. One of these compartments (the retentate) contained an initial concentration (C_0) of Li_2S_n , while the other initially contained none (the permeate). The concentration of Li_2S_n in the permeate compartment was then measured as a function of time. The concentration of Li_2S_n in the permeate compartment at any time (in mol L^{-1}) is given by:

$$C_{\text{permeate}}(t) = \frac{A \int_0^t J(t) dt}{V_{\text{permeate}}}$$

where J is the flux across the membrane in $\text{mmol cm}^{-2} \text{ s}^{-1}$, A is the membrane cross-sectional area in cm^2 , and V_{permeate} is the permeate compartment volume in mL. The flux of Li_2S_n across the membrane is given by Fick’s first law. For short time periods when a

small fraction of the active material has crossed through the membrane, the flux is given by:

$$J(t \approx 0) = D_{eff} \frac{C_0}{l}$$

where D_{eff} is the effective diffusion coefficient of Li_2S_n through the membrane in $\text{cm}^2 \text{s}^{-1}$, C_0 is the initial concentration of Li_2S_n in the retentate in mol L^{-1} , and l is the membrane thickness in cm. Thus, the concentration of active species in the permeate is described by:

$$C_{permeate}(t) = \frac{D_{eff} C_0 A}{l V_{permeate}} t$$

and D_{eff} of Li_2S_n through the membrane can be calculated from the slope of this plot (see Section B.1 and Fig. 4.8).

For an ideal membrane that does not react with Li_2S_n or degrade otherwise, D_{eff} should be small and should not change with time. We observed that for $C_0 = 0.20 \text{ M S}$ as Li_2S_8 , D_{eff} decreased from 1.2×10^{-9} to $6.4 \times 10^{-10} \text{ cm}^2 \text{s}^{-1}$ during the first 15 h of the crossover experiment (Fig. 4.2). This decrease was followed by a gradual increase to $7.9 \times 10^{-10} \text{ cm}^2 \text{s}^{-1}$ after 80 h. At higher C_0 , the increase in D_{eff} with time was much sharper. For instance, with $C_0 = 0.50 \text{ M S}$, D_{eff} increased from 6.3×10^{-10} to $2.0 \times 10^{-9} \text{ cm}^2 \text{s}^{-1}$ after 50 h. For $C_0 = 0.80 \text{ M}$ and 1.0 M , D_{eff} had a lower initial value of $3.9 \times 10^{-10} \text{ cm}^2 \text{s}^{-1}$ followed by a sharp increase to $2.0 \times 10^{-9} \text{ cm}^2 \text{s}^{-1}$ after only 18 h. Thus, at high polysulfide concentrations in the electrolyte, the membrane's polysulfide-blocking ability degraded, with faster degradation at higher sulfur concentrations. This concentration dependence implies that the degradation in membrane performance is due to a chemical reaction. Since the ion-selectivity of these membranes is tied to their pore size and size-distribution, this trend points towards a change in the pore structure that is a direct consequence of the chemical reactivity of the polymer membrane.

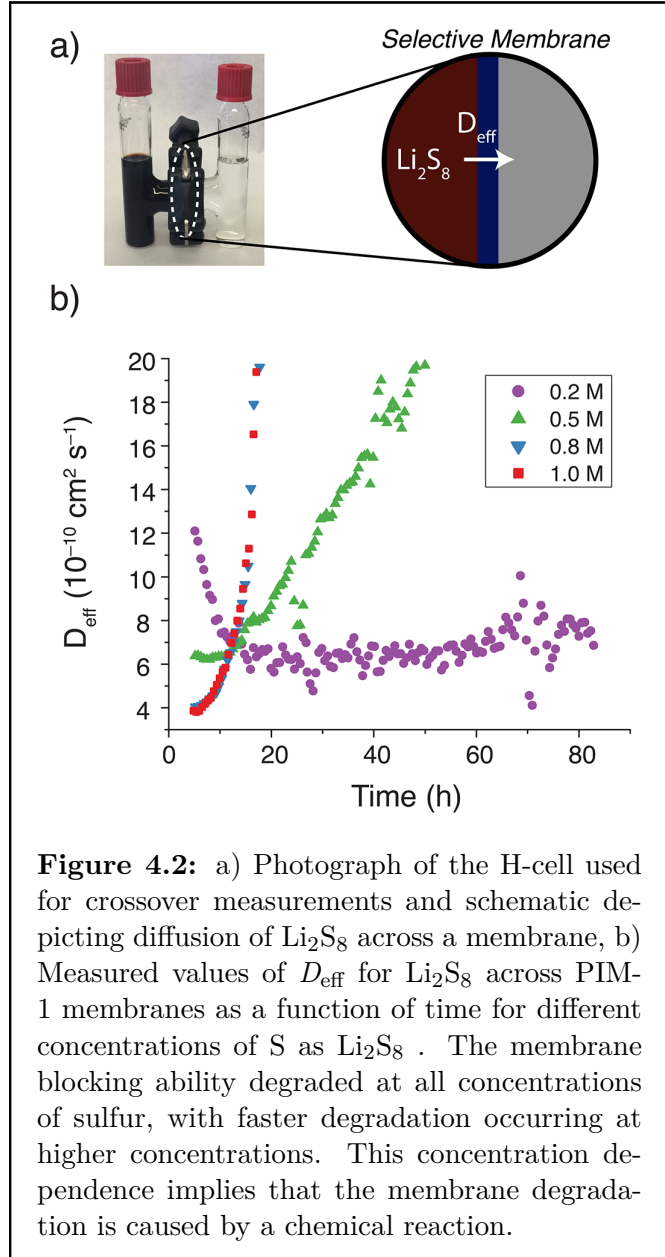


Figure 4.2: a) Photograph of the H-cell used for crossover measurements and schematic depicting diffusion of Li_2S_8 across a membrane, b) Measured values of D_{eff} for Li_2S_8 across PIM-1 membranes as a function of time for different concentrations of S as Li_2S_8 . The membrane blocking ability degraded at all concentrations of sulfur, with faster degradation occurring at higher concentrations. This concentration dependence implies that the membrane degradation is caused by a chemical reaction.

4.3 Verification of reaction pathway with a model compound

To verify the proposed reactivity pathway of PIM-1 with NMR and mass spectrometry in typical battery solvents^[197, 198] that PIM-1 is insoluble in, model compound **1** was synthesized and allowed to react with excess Li_2S_8 in 1:1 (*v/v*) THF-*d*₈:diglyme (Fig. 4.3). In the presence of 20 equiv. Li_2S_8 , ^1H -NMR shows complete conversion of the model compound into several different species of lithiated thioamides **2**, all of which have one unreacted nitrile group (Fig. 4.3b, Figs. 4.9–4.11). This distribution of products was expected, as it is well known that Li_2S_n in solution exist as a variety of species with different chain lengths.^[158, 199] Negative-ion mode high-resolution electrospray ionization mass spectrometry (ESI-MS) provided further evidence for the conversion of the nitrile group in the model compound to a lithiated thioamide. The most intense peak in the ESI-MS spectrum corresponded to $[\mathbf{1} + \text{SH}]^-$ (m/z obsd. 485.12, calc. 485.15), which forms from hydrolysis of the proposed species in the presence of adventitious water. Smaller peaks corresponding to species where both nitrile groups reacted to give $[\mathbf{1} + \text{Li}_3\text{S}_n]^-$ were also observed, where $n = 5$ (m/z obsd. 633.04, calc. 633.08), 6 (m/z obsd. 665.01, calc. 665.05), 7 (m/z obsd. 696.99, calc. 697.03), and 8 (m/z obsd. 728.96, calc. 729.00), providing strong evidence for the conversion of **1** to **2** (Fig. 4.3c–d, Figs. 4.12–4.13).

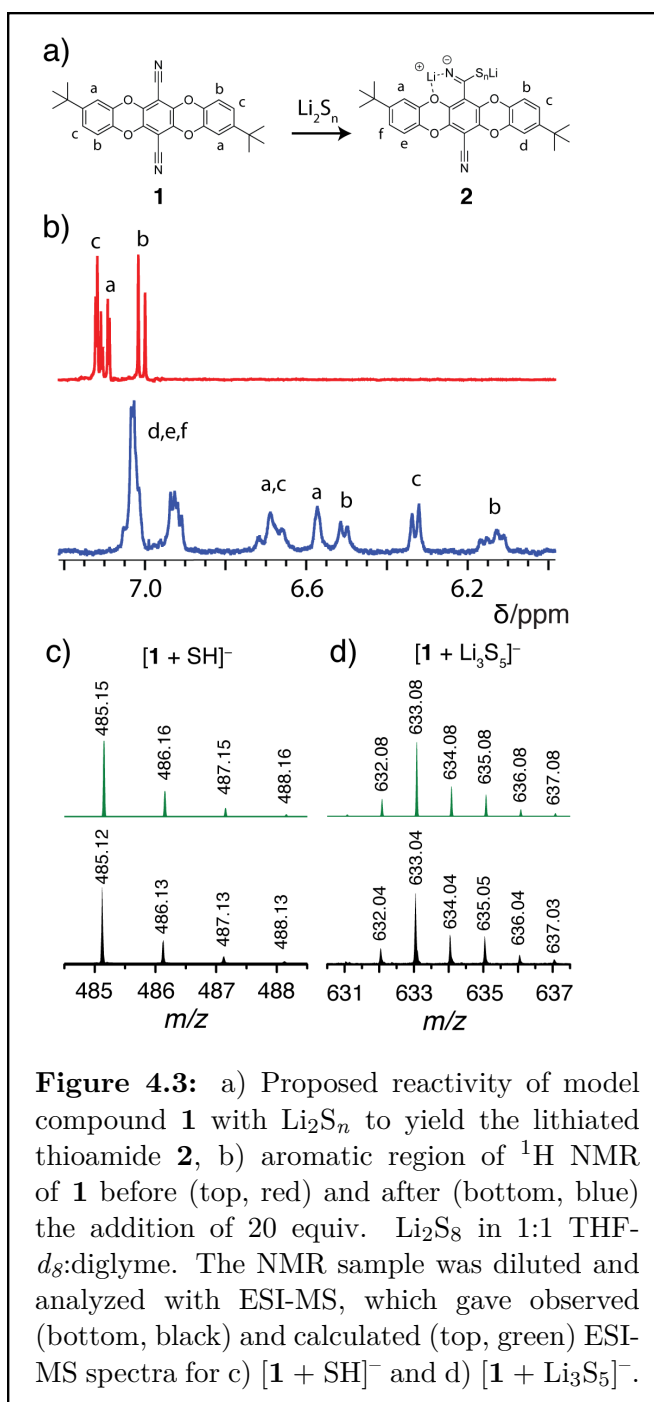


Figure 4.3: a) Proposed reactivity of model compound **1** with Li_2S_n to yield the lithiated thioamide **2**, b) aromatic region of ^1H NMR of **1** before (top, red) and after (bottom, blue) the addition of 20 equiv. Li_2S_8 in 1:1 THF-*d*₈:diglyme. The NMR sample was diluted and analyzed with ESI-MS, which gave observed (bottom, black) and calculated (top, green) ESI-MS spectra for c) $[\mathbf{1} + \text{SH}]^-$ and d) $[\mathbf{1} + \text{Li}_3\text{S}_5]^-$.

4.4 *In-Situ* FT-IR of PIM-1 membranes

Having established the likelihood of reactivity of the nitrile groups of PIM-1 with the aid of **1**, I sought to measure the extent and rate of this reaction with *in situ* FT-IR spectroscopy. A thin film of PIM-1 was deposited on a polished silicon ATR probe that was immersed in 1.0 M S as Li_2S_8 in electrolyte. The intensity of the nitrile stretch at 2239 cm^{-1} slowly decreased in intensity to 92% of its initial value after 22.5 h (Fig. 4.4). Concomitantly, new stretches at 2221 and 1579 cm^{-1} appeared and grew in intensity. The stretch at 2221 cm^{-1} is attributable to unreacted nitrile groups *para* to the newly formed thioamide, while the stretch at 1579 cm^{-1} is consistent with the thioamide functional group.^[200] This pattern of reactivity, with only one of the nitriles in the 1,4-dicyanooxanthrene group reacting, is commonly observed in 1,4-cyanoarenes.^[201–205] After 22.5 h, the polysulfide solution was removed and replaced with electrolyte, and the new peaks persisted, indicating that the chemical reaction is not reversible in the presence of electrolyte (Fig. 4.14).

The time-scale for conversion of nitrile groups on PIM-1 to lithiated thioamides is similar to the time-scale of increased crossover rates (Fig. 4.2), providing compelling evidence that the change in membrane active-species blocking ability is due to its chemical evolution. Further evidence for this hypothesis was provided by repeating the *in situ* FT-IR experiment in the presence of 0.2 M S as Li_2S_8 . As expected, the chemical reaction was slower, with the nitrile peak only decreasing to 97% of its initial value after 22.5 h (Fig. 4.15). These experiments show that changes in membrane chemical reactivity are directly correlated to changes in membrane selectivity, with larger extents of conversion of nitrile

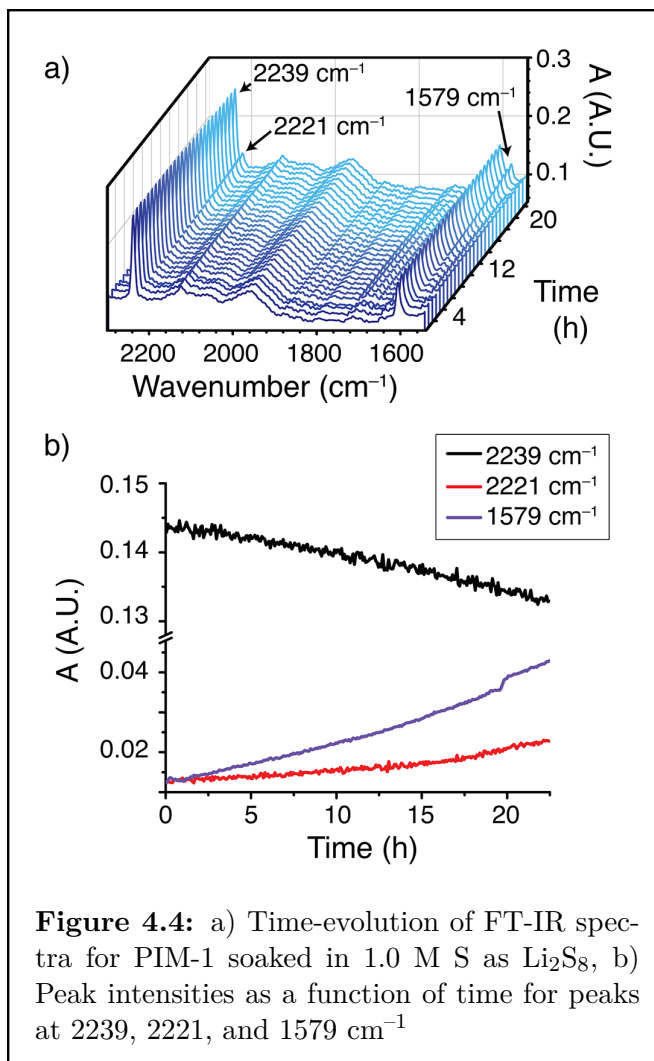
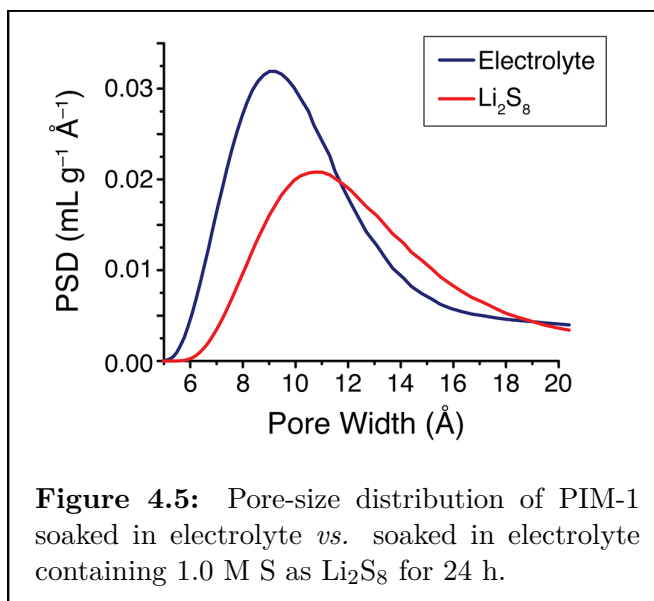


Figure 4.4: a) Time-evolution of FT-IR spectra for PIM-1 soaked in 1.0 M S as Li_2S_8 , b) Peak intensities as a function of time for peaks at 2239 , 2221 , and 1579 cm^{-1}

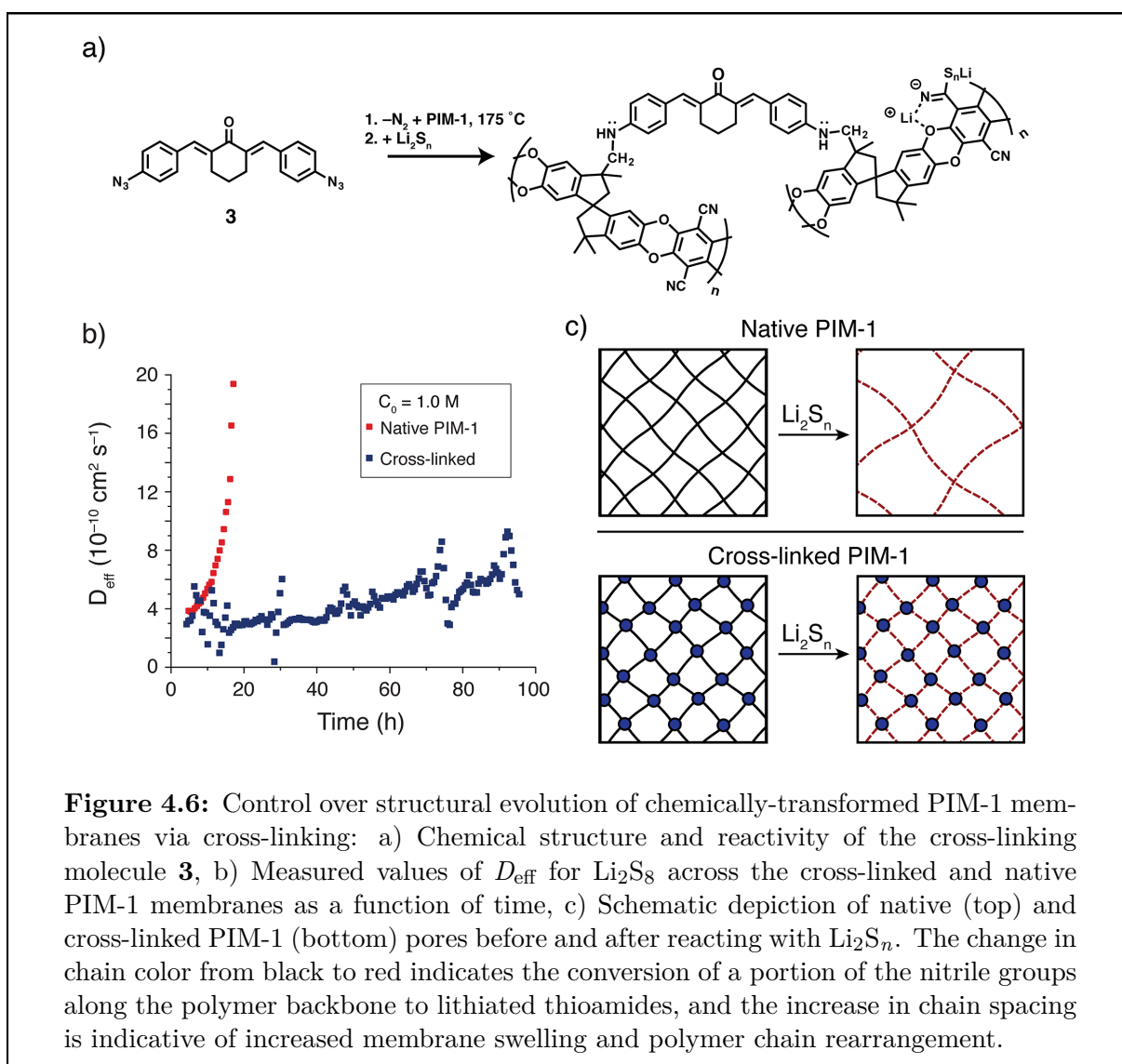
to lithiated thioamide corresponding to lower membrane selectivity.

4.5 Nitrogen adsorption of PIM-1 membranes

On the basis of model compound studies, *in situ* FT-IR, and concentration-dependent crossover, it is clear that PIM-1 reacts with lithium polysulfides and that this reactivity correlates with decreased polysulfide-blocking ability. In order to understand how the chemical reactivity of PIM-1 leads to a change in polysulfide blocking, I used nitrogen adsorption experiments to relate changes in polymer chemistry to changes in the pore structure of the membrane. PIM-1 membranes were soaked in electrolyte or electrolyte containing 1.0 M S as Li_2S_8 , washed thoroughly, and dried under vacuum at 120 °C for 19 h. Ni-



trogen adsorption isotherms were measured at 77 K, and pore size distributions were calculated. Both isotherms were characterized by high nitrogen uptake at very low pressures that is typical of microporous materials, as well as pronounced hysteresis that is commonly observed for PIMs.^[206] The unreacted PIM-1 membranes had a typical pore width of 9 Å, which is consistent with reported values (Fig. 4.5, Fig. 4.16).^[179] In contrast, the reacted PIM-1 membranes had larger pores with a typical width of 11 Å. These results suggest that the reacted PIM-1 packs less efficiently than PIM-1 in the solid state due to the presence of lithiated thioamide appendages. This change in polymer structure explains the decreased polysulfide-blocking ability of PIM-1 after soaking in solutions of lithium polysulfides. In addition to changes in the dry polymer structure after reaction with lithium polysulfides, it is also possible that the proposed reactivity effects the solvation of polymer chains, thus further altering the structure of the polymer in its swollen state.



4.6 Cross-Linking of PIM-1 to prevent chemically-induced changes in pore architecture

In order to prevent this undesirable chemically induced change in membrane pore-architecture and the resulting decrease in active-species blocking-ability, I sought to lock the membrane into its initial pore architecture via cross-linking. To accomplish this, 0.1 molar equivalents of cross-linker **3** (Fig. 4.6a) were added to the membrane-casting solutions. Upon heating the membranes to 175 °C under vacuum, the azide groups of **3** are converted to reactive nitrenes, which insert into C-H bonds in PIM-1 and cross-link the membrane (Fig. 4.6a).^[145] The cross-linking reaction was monitored by FT-IR, which showed complete disappearance of the azide peak at 2110 cm⁻¹ after heating for 7.5 h, indicating that the cross-linker reacted completely (Fig. 4.17). The resulting membranes were insoluble in chloroform, with a gel fraction of greater than 95%, providing further evidence for extensive cross-linking.

In order to test the hypothesis that cross-linking would prevent chemically-induced changes in pore architecture and membrane selectivity, I measured the time-dependence of D_{eff} of Li₂S_n through 10% cross-linked PIM-1 and noted a dramatic difference in membrane selectivity between cross-linked and native PIM-1 membranes (Fig. 4.6b). In the presence of 1.0 M S as Li₂S₈, D_{eff} of Li₂S_n through native PIM-1 membranes increased from 3.9 × 10⁻¹⁰ to 2.0 × 10⁻⁹ cm² s⁻¹ in 18 h. In contrast, D_{eff} of Li₂S_n for 10% cross-linked PIM-1 under the same conditions only increased slightly, from 3.0 × 10⁻¹⁰ to 7.0 × 10⁻¹⁰ cm² s⁻¹ over 95 h. This difference in long-term membrane selectivity is not due to a decrease in membrane reactivity compared to native PIM-1, as the FT-IR spectrum of cross-linked PIM-1 treated with Li₂S_n also contains peaks corresponding lithiated thioamides (Fig. 4.18). Instead, I attribute the dramatic improvement in long-term crossover behavior for cross-linked PIM-1 to a decrease in membrane swelling and polymer chain rearrangement upon reaction with Li₂S_n (Fig. 4.6c). This explanation is further supported by electrolyte uptake measurements. After soaking PIM-1 membranes in 1.0 M S as Li₂S₈ in electrolyte for 24 h, native PIM-1 membranes took up 140 ± 11% of their own mass in the solution, while the cross-linked membranes took up only 117 ± 8%. Thus, the cross-linked PIM-1 membranes swell significantly less than native PIM-1 membranes after reacting with Li₂S_n.

Ultimately, my results highlight the importance of understanding the effect of membrane chemical reactivity on its selectivity and durability of its ion-transporting abilities. By cross-linking PIM-1, an undesirable increase in membrane swelling and concomitant decrease in selectivity can be avoided, even in the presence of reactive active-species. Furthermore, despite this dramatic improvement in the membrane's active-species blocking ability, the ionic conductivity of the membrane only decreased slightly, from 5.9 × 10⁻³ for native PIM-1 to 1.8 × 10⁻³ mS cm⁻¹ for 10% cross-linked PIM-1 (Fig. 4.19), meaning that enhanced blocking ability is not coming at the expense of ion conduction.

4.7 Lithium–Sulfur batteries incorporating native and cross-linked PIM-1 membranes

Finally, to test the performance of native and cross-linked PIM-1 membranes in Li–S batteries, we assembled coin cells (CR2032) with a lithium anode and a Ketjen-black/Li₂S₈ cathode^[180] separated by either native or cross-linked PIM-1 membranes. To demonstrate the polysulfide-blocking ability of the PIM-1 membranes, LiNO₃ was not added to the electrolyte, as LiNO₃ would mask the negative effects of the polysulfide-shuttle until it was completely consumed. The galvanostatic discharge curves (Fig. 4.7)

are typical of Li–S cells, with an initial high-voltage plateau corresponding to the reduction of S₈ to Li₂S_{*n*}, a region with decreasing voltage corresponding to the reduction of higher-order polysulfides to lower-order polysulfides, and a low-voltage plateau corresponding to the electro-deposition of Li₂S. The voltage of this lower plateau was the same for cells with native and cross-linked PIM-1 membranes, indicating that the slightly lower ionic conductivity of the cross-linked membranes does not limit the cell voltage or capacity at a rate of C/16 (where a rate of 1C corresponds to the current required to discharge the full theoretical capacity of the battery in 1h). In fact, the first-discharge capacity of the cells with cross-linked PIM-1 membranes was slightly higher (1153 *vs.* 1090 mAh g⁻¹), consistent with the improved polysulfide-blocking ability of cross-linked PIM-1 membranes. This improved polysulfide-blocking ability resulted in less polysulfide shuttling

and sulfur loss to the anode, which manifested in improved cycling performance and Coulombic efficiency (Fig 4.20). Clearly, cross-linked PIM-1 membranes out-perform native PIM-1 membranes in Li–S cells due to their improved polysulfide-blocking ability.

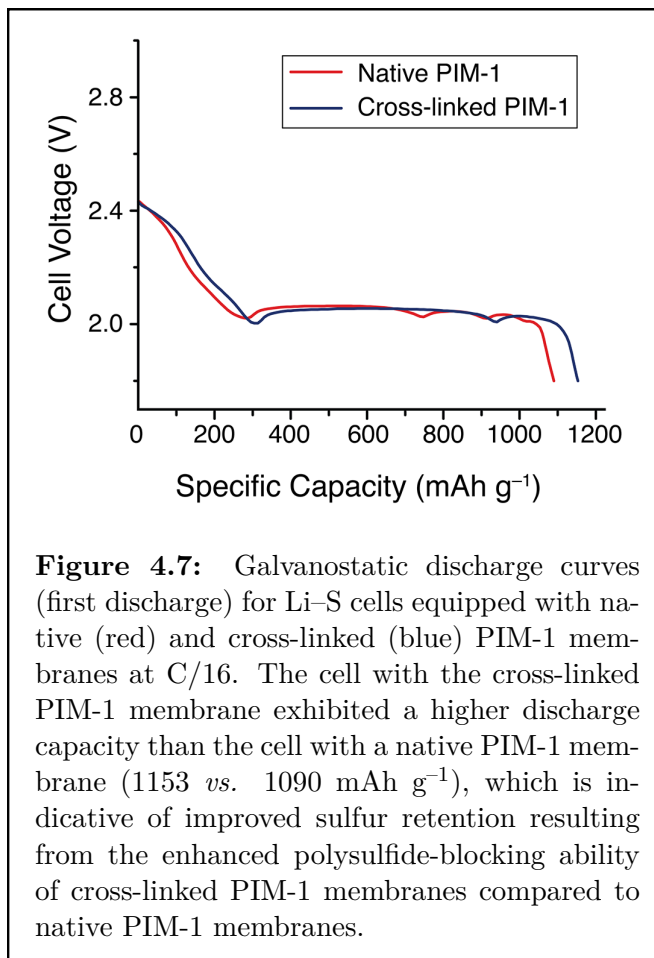


Figure 4.7: Galvanostatic discharge curves (first discharge) for Li–S cells equipped with native (red) and cross-linked (blue) PIM-1 membranes at C/16. The cell with the cross-linked PIM-1 membrane exhibited a higher discharge capacity than the cell with a native PIM-1 membrane (1153 *vs.* 1090 mAh g⁻¹), which is indicative of improved sulfur retention resulting from the enhanced polysulfide-blocking ability of cross-linked PIM-1 membranes compared to native PIM-1 membranes.

4.8 Conclusions

Membranes capable of sustainably blocking active-species crossover are critical for the implementation of next-generation batteries. However, relatively little is known about how selective membranes evolve in the presence of highly reactive active species. In this work, I systematically studied the chemical evolution of a promising membrane material (PIM-1) in the presence of dissolved lithium polysulfides and found that the nitrile groups on the polymer backbone react with lithium polysulfides to form lithiated thioamides. This change in chemical structure of the polymer led to a change in the membrane's pore architecture, causing a decrease in active-species blocking ability. After gaining this insight, I mitigated this undesirable chemically induced change in pore structure by cross-linking the membranes. The resulting cross-linked membranes maintained favorable ionic conductivities while exhibiting dramatically improved long-term active-species blocking ability. The insights gained in this work regarding the relationship between membrane chemical reactivity and selectivity are critical for developing membranes for next-generation energy storage devices, including Li-S and non-aqueous redox-flow batteries.

4.9 Supporting information

4.9.1 Materials and methods

Synthesis of PIM-1

PIM-1 with molecular weight 200 kg mol^{-1} was synthesized as described elsewhere.^[56, 179] Briefly, a mixture of anhydrous potassium carbonate (8.3 g, 60 mmol), 3,3,3',3'-tetramethyl-1,1'-spirobisindane-5,5',6,6'-tetrol (6.8 g, 20 mmol) and tetrafluoroterephthalonitrile (4.0 g, 20 mmol) in dry DMF was stirred at 65 °C for 4 d. On cooling, the mixture was added to water and the crude product collected by filtration. Repeated precipitations from a concentrated solution of polymer in chloroform into methanol yielded 8.90 g (19.3 mmol, 97% yield) of the fluorescent yellow polymer (PIM-1).

Synthesis of model compound 1

Model compound **1** was synthesized as described elsewhere.^[207] Briefly, an oven-dried 40 mL septum-capped vial was charged with a stir bar, 4-*tert*-butylcatechol (997 mg, 6 mmol), tetrafluoroterephthalonitrile (600 mg, 3 mmol), and dry DMF (13 mL). The mixture was stirred for several minutes to give a transparent orange solution. Next, potassium carbonate (871 mg, 6.3 mmol) was added, and the mixture was heated to 70 °C under nitrogen for 25 h. The resulting suspension was added to 100 mL water, filtered, and rinsed with water and acetone. Finally, the product was dried at reduced pressure overnight to yield 1.306 g (2.9 mmol, 96% yield) of **1** as a bright yellow powder. ¹H (CDCl₃, 500 MHz): δ 7.03 (dd, 2H, $J_{HH} = 8.2, 2.2$ Hz, ArH), 7.02 (d, 2H, $J_{HH} = 2.1$ Hz, ArH), 6.92 (d, 2H, $J_{HH} = 8.2$ Hz, ArH), 1.29 (s, 18H, CH₃).

Membrane preparation

Free-standing membranes were prepared by drop-casting 12.5 mg mL⁻¹ solutions of PIM-1 in chloroform into Teflon-coated wells under a crystallization dish. Cross-linked membranes were cast in the same way from 12.5 mg mL⁻¹ solutions of PIM-1 in chloroform with 0.1 equivalents of cross-linker per polymer repeat unit. The membranes were then heated under vacuum at 175 °C for 7.5 h to complete the cross-linking reaction. After casting, the membranes were further dried under vacuum and soaked in electrolyte for at least 6 h.

4.9.2 Crossover measurement and analysis

A PIM-1 membrane of known thickness (typically 8–12 μm) was placed between two halves of an H-cell (obtained from Adams & Chittenden Scientific Glass, Berkeley, CA) with an aperture diameter of 1.6 cm and sealed in place with a chemically resistant O-ring. One half of the H-cell (the retentate) was charged with 12 mL of Li₂S₈ in electrolyte,

while the other half (the permeate) was charged with the same volume of electrolyte with no Li_2S_8 . Both compartments were stirred to ensure homogeneity. Every 20–30 min, the stirring was stopped and the concentration was measured electrochemically by acquiring a CV at 100 mV s^{-1} from 2.00 V to 3.00 V *vs.* Li/Li^+ (with a glassy carbon working electrode and lithium foil counter/reference electrode). The peak anodic current was related to polysulfide concentration with a calibration curve (Fig. 4.8).

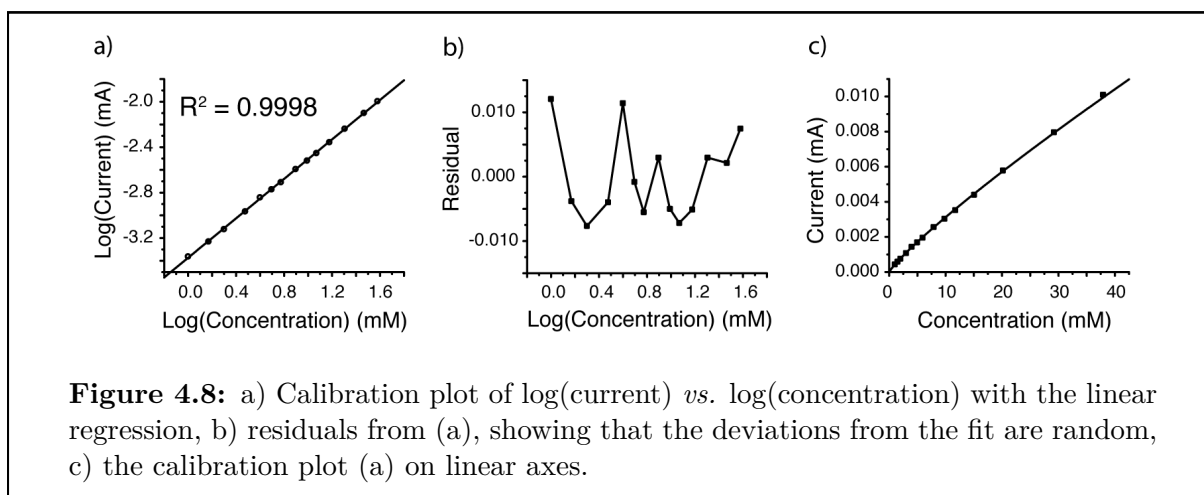


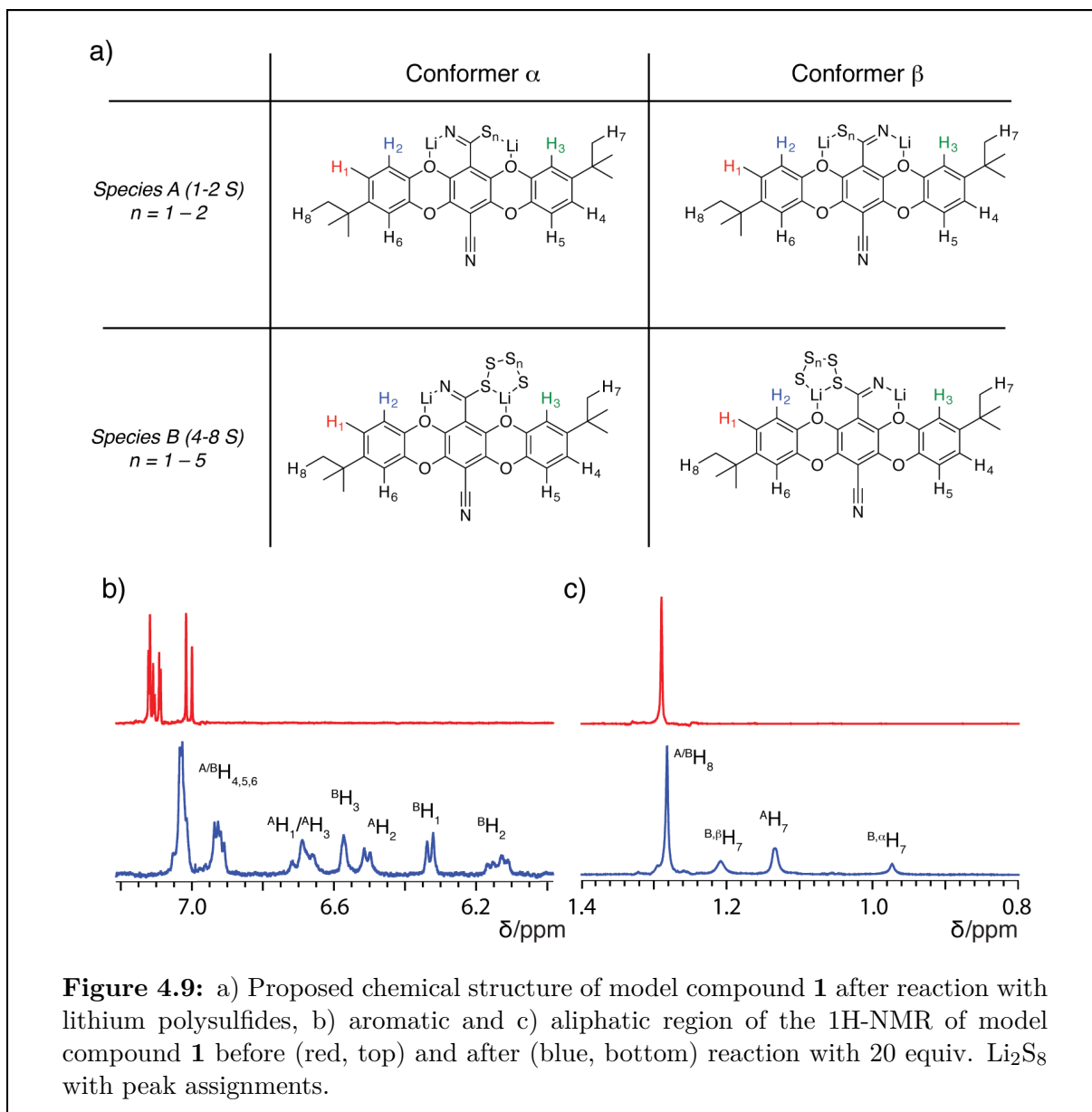
Table 4.1: Known concentration, calculated concentration from the calibration curve, and the percent difference for all points on the calibration curve.

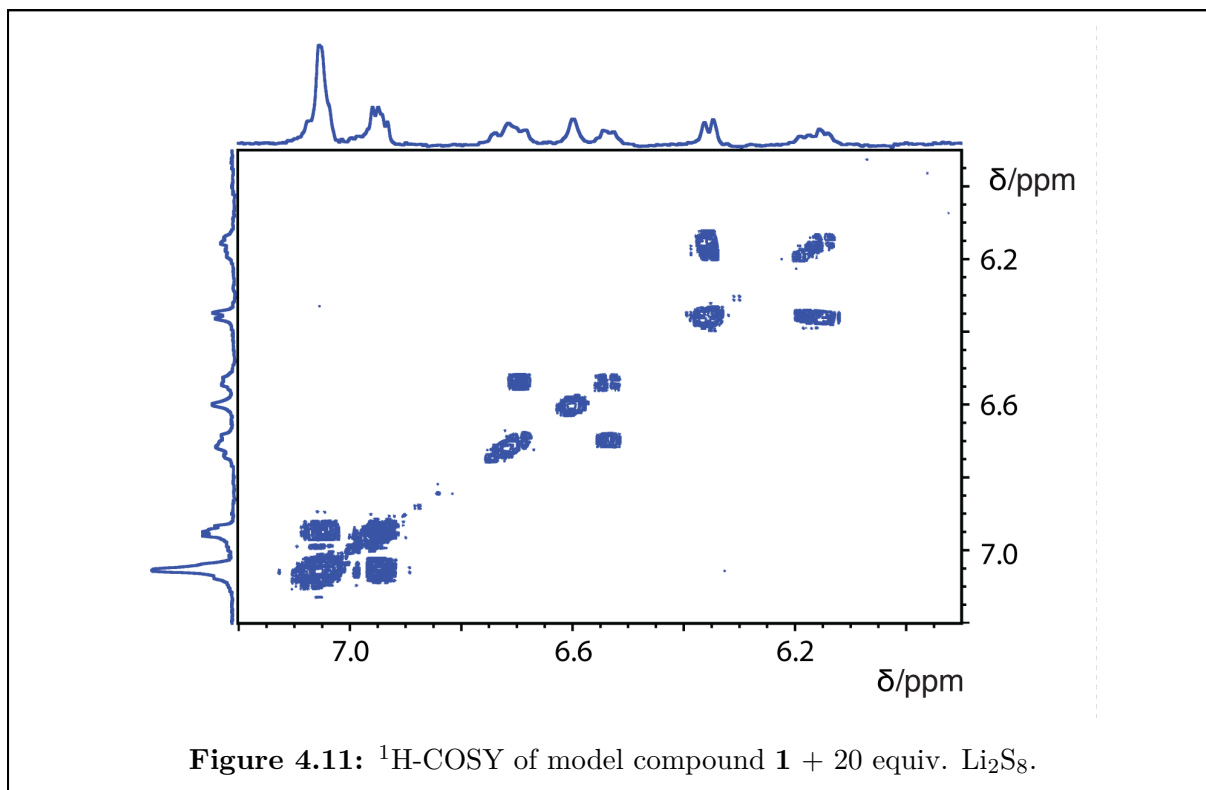
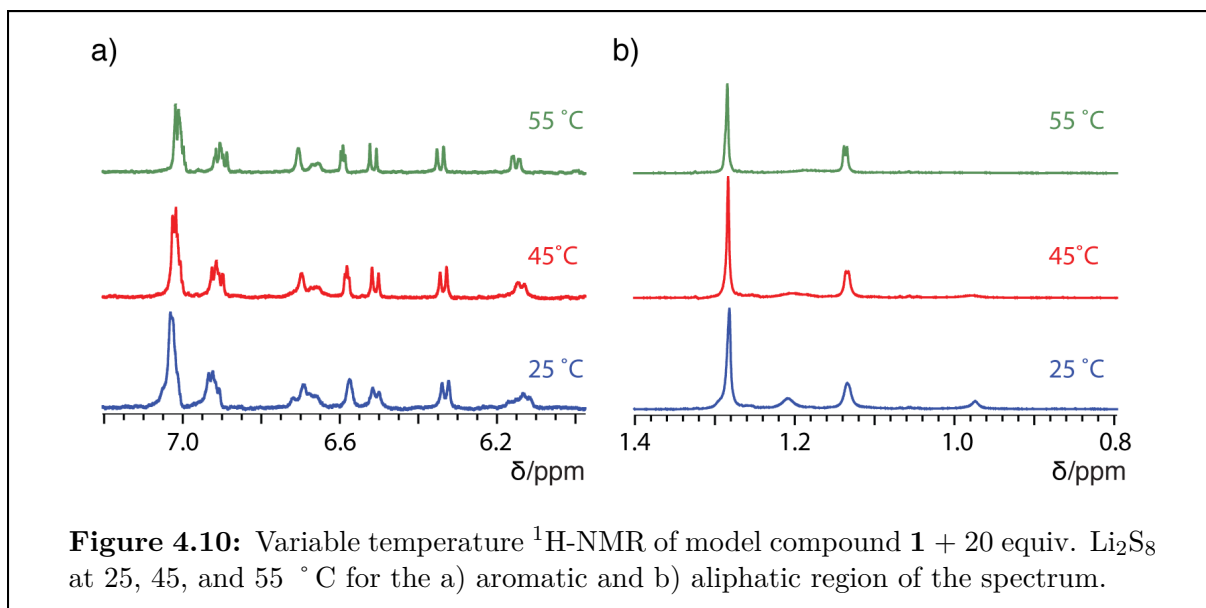
Actual Conc. (mM)	Calc. Conc. (mM)	Difference (%)
0.998	1.030	3.3
1.478	1.463	-1.0
1.992	1.952	-2.0
2.982	2.951	-1.0
3.968	4.090	3.1
4.950	4.939	-0.2
5.929	5.843	-1.5
7.874	7.936	0.8
9.804	9.675	-1.3
11.719	11.498	-1.9
15.034	14.832	-1.3
20.154	20.313	0.8
29.190	29.357	0.6
37.893	38.651	2.0

4.9.3 Characterization of chemically transformed model compound

Assignment of $^1\text{H-NMR}$ of reacted model compound

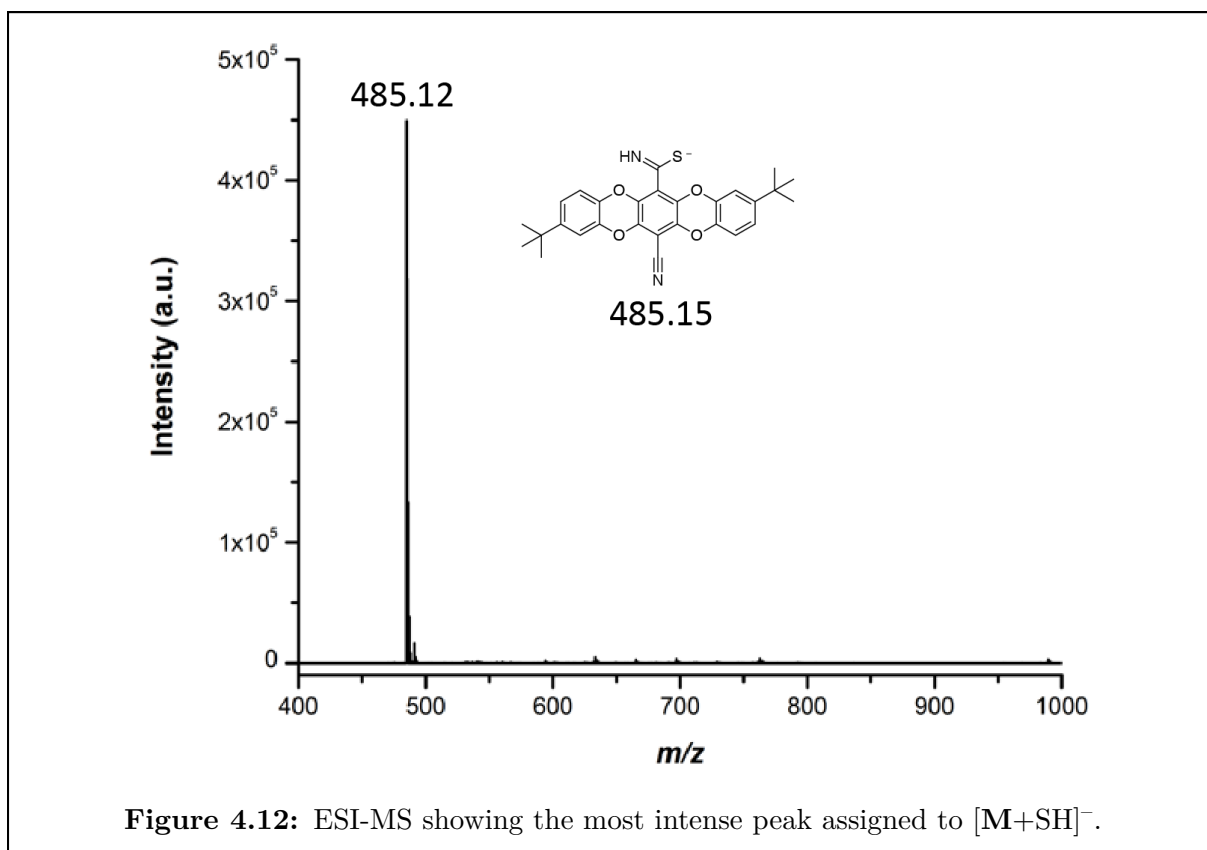
Solutions of lithium polysulfides are well known to consist of numerous species.^[158, 199] Therefore, a number of lithiated thioamides are expected to result from the reaction of model compound **1** with Li_2S_8 . The aliphatic region of the ^1H NMR spectrum of **1** + 20 Li_2S_8 has one sharp singlet at 1.28 ppm and three broad singlets at 1.21, 1.13, and 0.97 ppm with relative integration of the sharp singlets to broad singlets of 1:1. The sharp singlet, which is within 0.02 ppm of the unreacted compound resonance, is attributable to *tert*-butyl groups on the opposite side of the molecule from the reacted nitrile group (Fig. 4.9a, proton 8). The broad peaks correspond to *tert*-butyl groups close to the reacted nitrile, and can be assigned to two separate species: one where the rotation around the C–CN bond is unhindered, and another where the rotation is hindered. We hypothesized that for lithiated thioamides containing more than 3 sulfur atoms (species B in Fig. 4.9), the unbound terminal sulfur atom can chelate lithium along with the neighboring oxygen, thus hindering rotation about the C–CN bond. As a result, the protons from the *tert*-butyl groups in the α and β conformers are chemically distinct, with peaks at 1.21 and 0.97 ppm. As temperature was increased to 55 °C (Fig. 4.10), these peaks broadened as is typical before coalescence, which supports this assignment. On the other hand, lithiated thioamides with fewer sulfur atoms cannot chelate lithium in the same way, and so they have less hindered rotation about the C–CN bond, leading to one broad peak at 1.13 ppm for the signal average between the α and β conformers. As expected, this peak did not broaden as temperature is increased. The multiplets from 7.1 to 6.9 ppm are similar in chemical shift to the multiplets in the unreacted model compound and can be assigned to protons 4, 5, and 6. This is further supported by the relative integration of the peaks, with the multiplets from 7.1 to 6.9 ppm having a relative integration of 3, equivalent to the total integral from 6.8 to 6.1 ppm. The remaining peaks were readily assigned on the basis of $^1\text{H-COSY}$ (Fig. 4.11) and integration data. H_3 protons were assigned based on the absence of *o*-coupling and the absence of $^1\text{H-COSY}$ cross-peaks, with the upfield peak assigned to the more shielded proton of species B. Pairs of multiplets corresponding to H_1 and H_2 were assigned based on $^1\text{H-COSY}$ cross-peaks, with the upfield pair assigned to species B and the more upfield of each pair of multiplets assigned to proton 2.

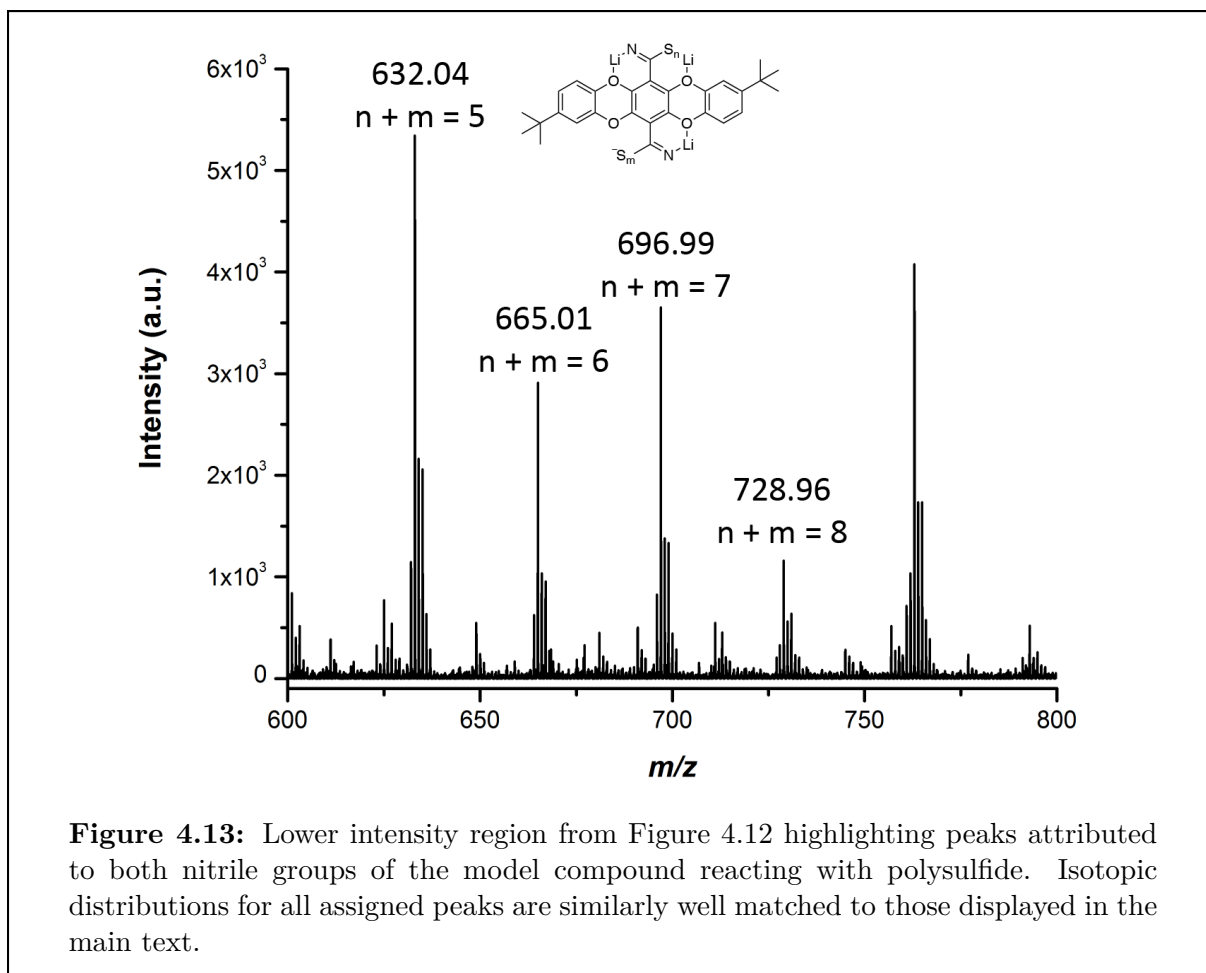




ESI-MS of reacted model compound

An 8 mM solution of **1** in 1:1 diglyme:THF- d_8 was treated with 20 equivalents of Li_2S_8 in the same solvent mixture. After 10 days mixing to ensure complete equilibration, the solution was diluted to 8×10^{-6} M in **1**. To avoid contamination/decomposition of the reacted model compound with water and oxygen, the syringe and capillary of the ESI-MS instrument were purged with dry, air-free THF immediately prior to analysis. The ESI-MS was operated in negative mode with an injection rate of $5 \mu\text{L min}^{-1}$.





4.9.4 Characterization of chemically transformed PIM-1

FT-IR of PIM-1 in the presence of lithium polysulfides

PIM-1 was drop-cast onto the polished silicon ATR probe of the spectrometer from a 12.5 mg mL^{-1} solution in chloroform, which was dipped into electrolyte blanketed under nitrogen. A stock solution of Li_2S_8 in electrolyte was injected to yield a sulfur concentration of 1.0 M or 0.2 M, as appropriate. The resulting solution was stirred under nitrogen and spectra were acquired every 5 min. Peak heights as shown in Fig. 4.4b were measured from a 2-point baseline.

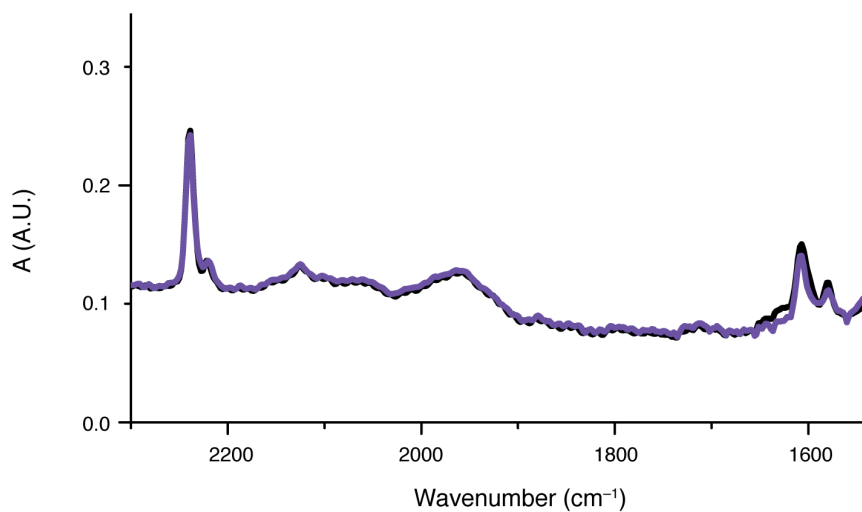


Figure 4.14: FT-IR of PIM-1 after soaking in 1.0 M S as Li₂S₈ in electrolyte for 22.5 h (black) and after replacing the Li₂S₈ solution with fresh electrolyte and soaking for an additional 8.5 h (violet).

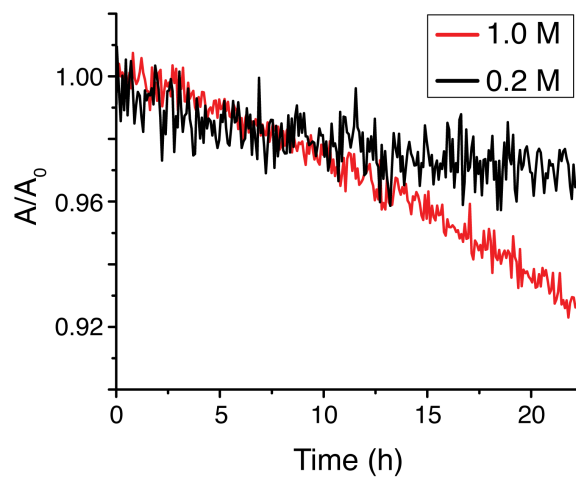
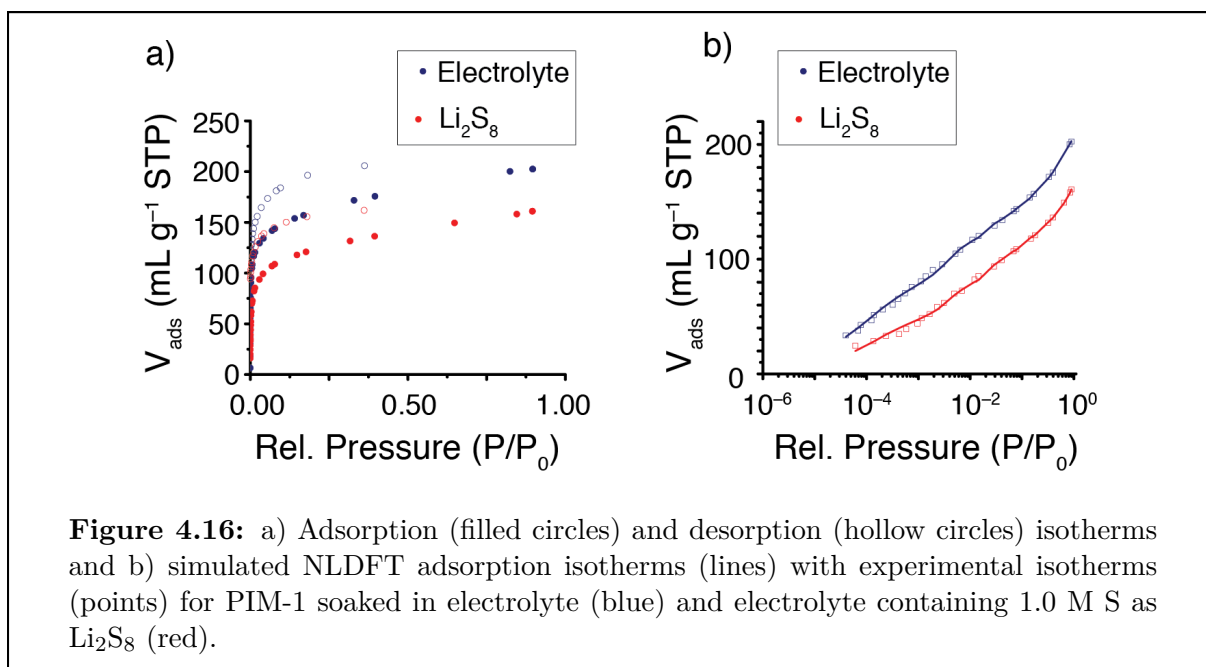


Figure 4.15: Normalized intensity of the nitrile stretch at 2239 cm⁻¹ of PIM-1 in the presence of 0.2 M (black) and 1.0 M (red) S as Li₂S₈.

Gas adsorption measurements of PIM-1

PIM-1 was soaked in electrolyte or electrolyte containing 1.0 M S as Li_2S_8 for 24 h, followed by washing with and soaking in diglyme for a total of 26 h. Finally, the membranes were washed with glyme, dried under vacuum at room temperature for 70 h, and dried under vacuum at 120°C for 19 h before measurement. Pore size distributions were calculated from adsorption isotherms using the SAIEUS software package with a heterogeneous surfaces NLDFT model.^[208, 209]



FT-IR of cross-linked PIM-1

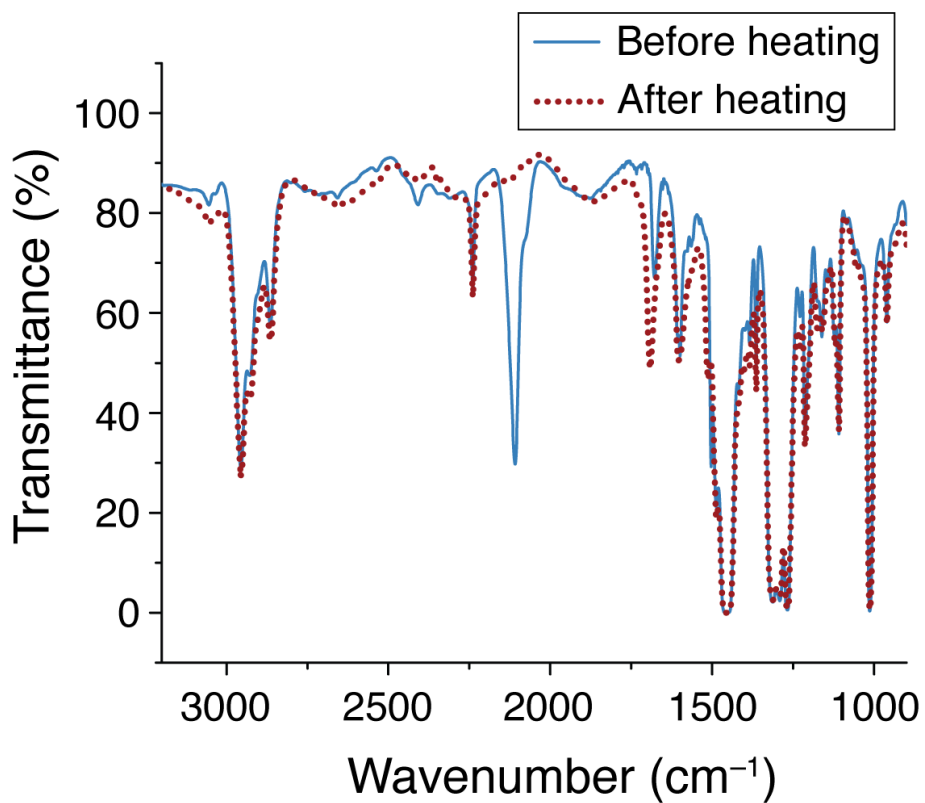


Figure 4.17: FT-IR spectra of membranes cast from PIM-1 with 0.1 molar equivalents of cross-linker **3** before (blue, solid) and after (red, dotted) heating at 175 °C for 7.5 h. Complete disappearance of the azide peak at 2110 cm⁻¹ indicates complete reaction of the cross-linker.

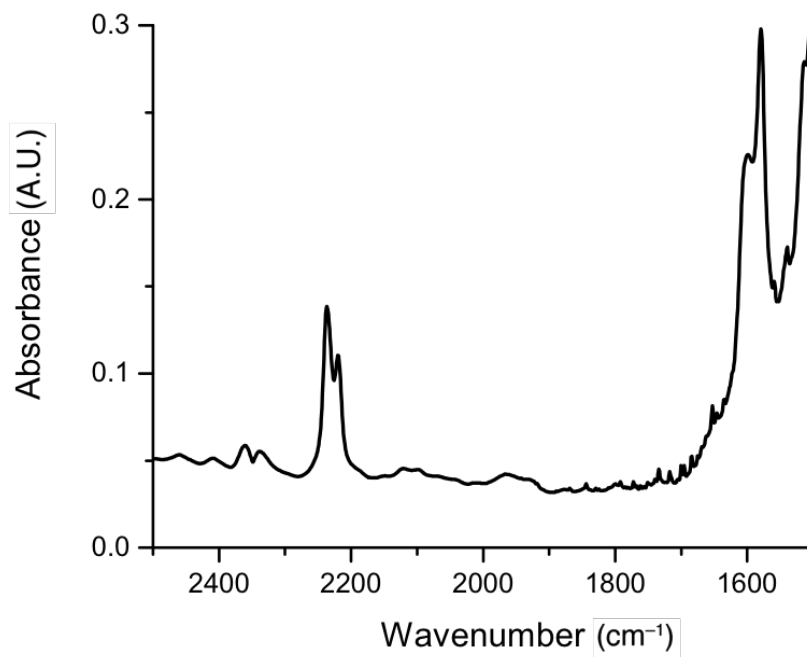


Figure 4.18: FT-IR spectrum of cross-linked PIM-1 membrane soaked in 1.0 M S as Li_2S_8 in electrolyte for 24 h. The appearance of new peaks at 2221 and 1579 cm^{-1} indicates conversion of nitrile groups to lithiated thioamides.

4.9.5 Ionic conductivity of PIM-1 membranes

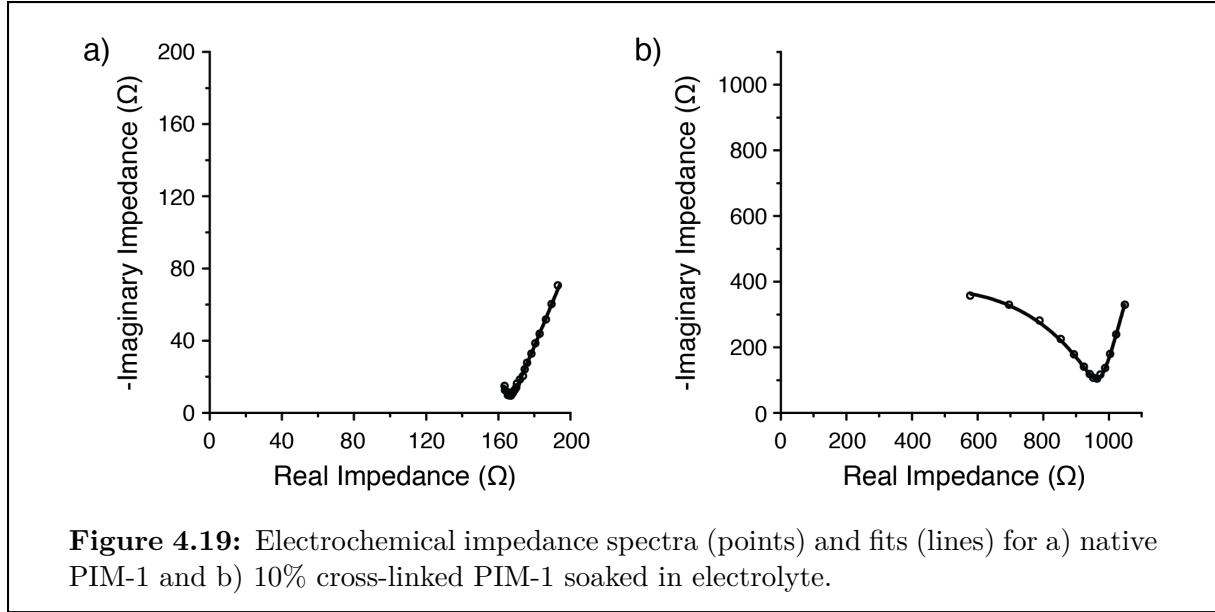


Table 4.2: Fitting parameters from Fig. 4.19.

Sample	Membrane Thickness (μm)	Q_{DL} ($\text{Fs}^{\alpha-1}$) [α]	Q_{M} ($\text{Fs}^{\alpha-1}$) [α]	R_{M} (Ω)	χ^2
Native PIM-1	11	$(18 \pm 2) \times 10^{-6}$ [0.75]	$(2 \pm 1) \times 10^{-9}$ [0.93]	165 ± 1	0.130×10^{-3}
Cross-linked PIM-1	20	$(2 \pm 1) \times 10^{-6}$ [0.84]	$(7 \pm 1) \times 10^{-9}$ [0.83]	967 ± 1	0.171×10^{-3}

4.9.6 Li-S battery assembly and testing

Preparation of the cathode

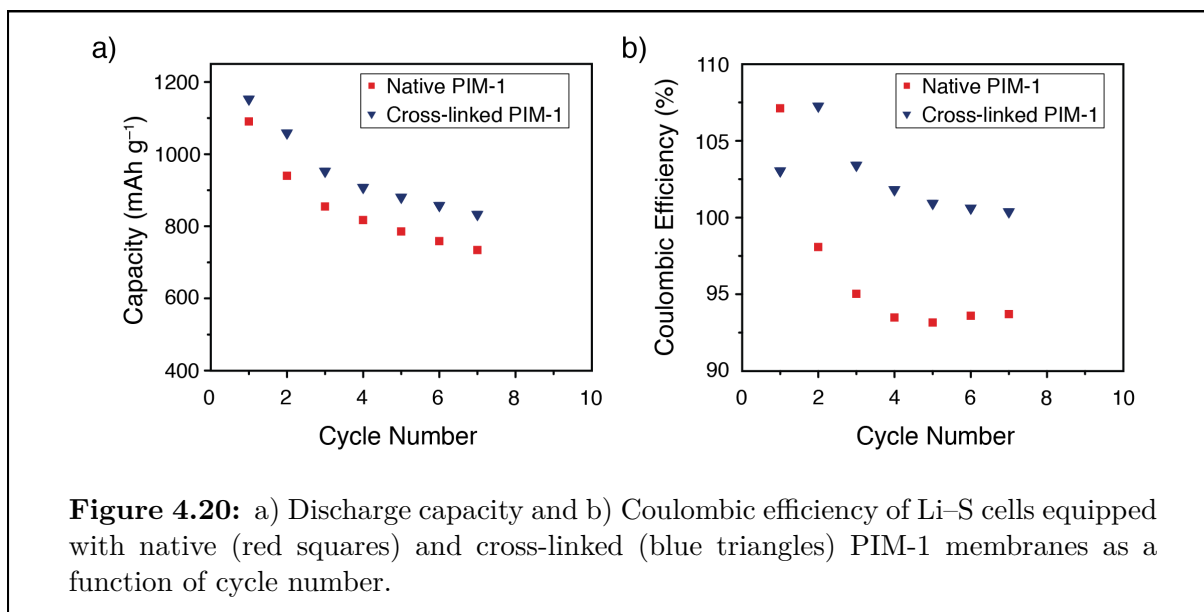
All battery electrolyte was 0.5 M LiTFSI in diglyme (with no added LiNO_3). A slurry of Ketjen-black/ Li_2S_8 was prepared by adding 30.8 mg Ketjen-black to 500 μL 1.0 M S as Li_2S_8 in electrolyte and sonicating for 30 min. Approximately 20 mg of the resulting slurry, which contained 5% *w/w* conductive Ketjen-black, was then added to a carbon nanofiber paper disk^[210] (1.13 cm^2 , $\sim 2\text{mg}$), which served as the sulfur cathode.

Cell assembly

CR2032 coin cells were used for all battery tests. The anode was a lithium disk with a diameter of 15 mm and thickness of 750 μm . The anode was covered with one layer of Celgard[®] 2400 followed by a 10 μm native or cross-linked PIM-1 membrane. Finally, the cathode was added to the top of this stack and the cell was sealed. All membranes were soaked in electrolyte overnight before use.

Battery cycling

The cells were galvanostatically cycled at a C/16 rate with voltage cut-offs of 1.8 and 2.8 V. The rate was set relative to 1C, which is the required current to charge or discharge the full theoretical capacity of the battery in 1h ($1.675 \text{ A g}^{-1} \text{ S}$). The discharge capacity of the cell with cross-linked PIM-1 dropped to 833 mA h g^{-1} after 7 cycles, which is about 72.2% of the initial capacity (Fig. 4.20a). At the same time, the discharge capacity of the cell with native PIM-1 decreased to 734 mA h g^{-1} , which is only 67.3% of the initial capacity. Thus, cross-linked PIM-1 achieves better capacity retention when applied in Li-S batteries. Furthermore, the Coulombic efficiency of the cells containing cross-linked PIM-1 membranes was higher than the cells with native PIM-1 membranes (100.4 *vs.* 93.7 % after 7 cycles, Fig. 4.20b). These improvements in Coulombic efficiency and cycle-life are a direct consequence of the improved polysulfide-blocking ability of cross-linked PIM-1.



4.9.7 Acknowledgements

We thank L. Maserati and D. Britt, C. Li and L. Gerber for assistance with nitrogen adsorption measurements, polymer synthesis and helpful discussions, respectively. S.E. Doris was supported by the Department of Defense through the National Defense Science & Engineering Graduate Fellowship program. A.L. Ward, P.D. Frischmann, L. Li and B.A. Helms were supported by the Joint Center for Energy Storage Research, an Energy Innovation Hub funded by the U.S. Department of Energy, Office of Science, Office of Basic Energy Sciences. Portions of the work—including polymer synthesis and characterization, polymer processing, and membrane crossover experiments—were carried out as User Projects at the Molecular Foundry, which is supported by the Office of Science, Office of Basic Energy Sciences, of the U.S. Department of Energy under Contract No. DE-AC02-05CH11231.

Chapter 5

Redox-Switchable Microporous Polymer Membranes that Extend the Cycle-Life of Lithium-Sulfur Batteries

Reproduced with permission from unpublished work in preparation.

5.1 Introduction and prior art

Membranes play a critical role in many battery technologies, where they serve to electronically isolate the anode from the cathode and allow the battery's working ion to diffuse between them.^[135, 211] For battery chemistries that involve active materials that are either dissolved, dispersed, or suspended in electrolyte, membranes must also prevent active-material crossover; failure to do so leads to low round-trip energy efficiency and in some cases unacceptable capacity fade.^[5, 30, 192] This is particularly problematic in lithium-sulfur (Li-S) batteries, where inefficiencies and instabilities arise when soluble polysulfides—intermediates in the electrochemical interconversion of S_8 and Li_2S —cross over and incur a shuttling current or irreversibly react with the lithium-metal anode.^[33–36, 193–195]

Here I show that these shortcomings are alleviated in the Li-S battery when its membrane is rationally configured from redox-switchable polymers of intrinsic microporosity (PIMs) (Figure 5.1).^[54, 55, 58, 59, 143] Key to my success is the adaptation of the membrane's transport selectivity for the battery's working ion *in operando*. More specifically, I leverage the reducing environment of the sulfur cathode to chemically transform a charge-neutral and size-selective PIM membrane into a lithiated and anionic PIM membrane with enhanced polysulfide-rejecting properties. The design of these new adaptive PIM membranes was computationally guided using a materials genome,^[60, 61, 212] where candidate monomer segments were screened for their susceptibility to reduction by polysulfides (i.e., a reduction potential

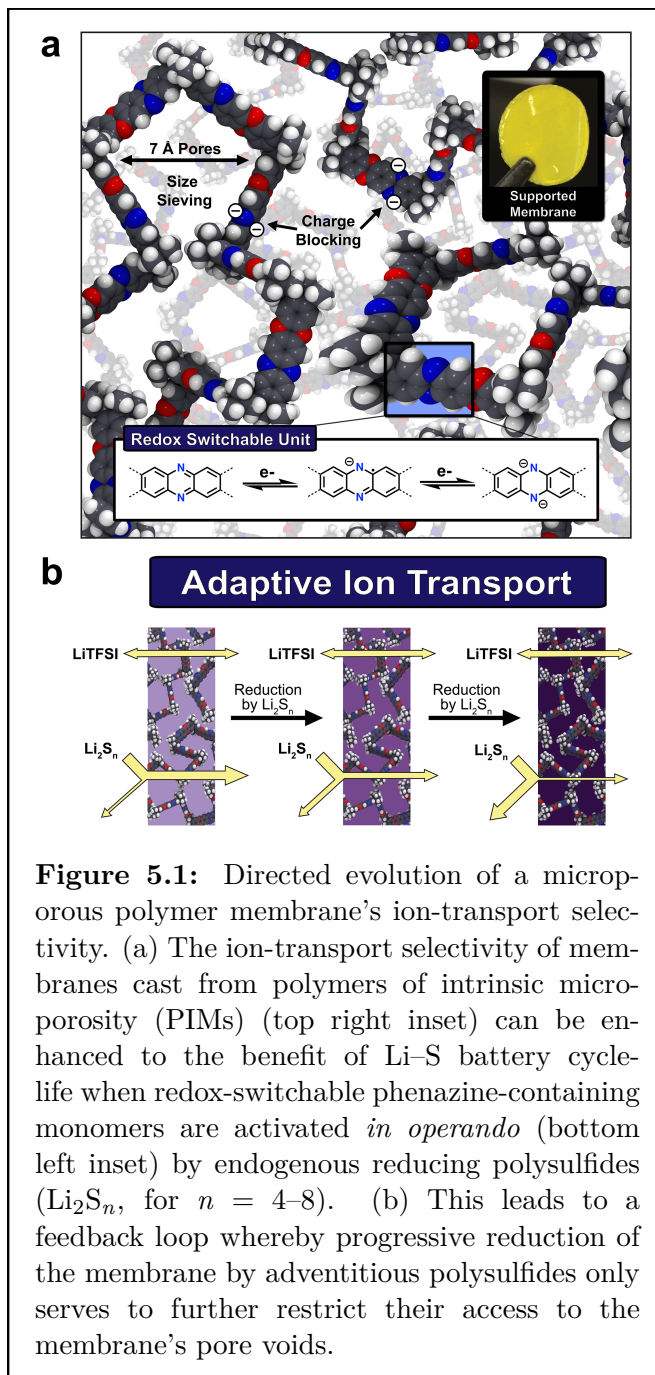


Figure 5.1: Directed evolution of a microporous polymer membrane's ion-transport selectivity. (a) The ion-transport selectivity of membranes cast from polymers of intrinsic microporosity (PIMs) (top right inset) can be enhanced to the benefit of Li-S battery cycle-life when redox-switchable phenazine-containing monomers are activated *in operando* (bottom left inset) by endogenous reducing polysulfides (Li_2S_n , for $n = 4-8$). (b) This leads to a feedback loop whereby progressive reduction of the membrane by adventitious polysulfides only serves to further restrict their access to the membrane's pore voids.

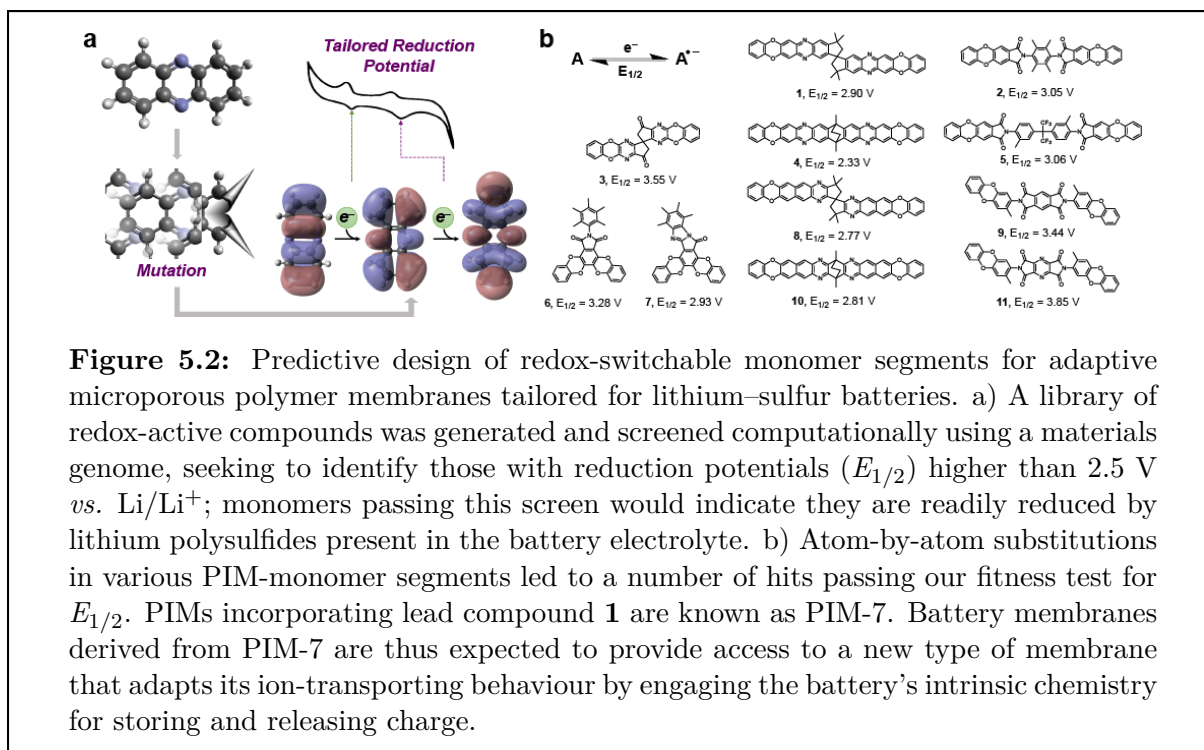
and a reduction potential

above 2.5 V *vs.* Li/Li⁺). I experimentally validated these predictions and was further able to demonstrate that progressive reduction and lithiation of the PIM membrane by polysulfides slows polysulfide diffusive permeability from 1.7×10^{-10} to 9.2×10^{-11} cm² s⁻¹—an impressive 570-fold improvement over non-selective Celgard separators^[135]—without significantly impacting the membrane’s ionic conductivity ($\sigma = 5 \times 10^{-3}$ mS cm⁻¹ at 298 K). We also showed that by blocking polysulfide crossover, the Coulombic efficiency and cycle-life of Li–S cells greatly improves—most notably in the absence of lithium-anode protecting additives.^[163–165, 213] The stability of the lithium metal anode under these conditions is unprecedented, and highlights the unexpected and exciting new opportunities afforded by responsive redox-active polymers, and ultimately adaptive membranes, in advanced battery technology development.

PIMs are a compelling and versatile platform to understand structure-transport relationships in microporous polymer membranes. Transport outcomes are rationalized on the basis of membrane porosity and pore architecture and their relation to the species interacting with the membrane.^[54, 55, 58, 59, 143, 214] The membrane’s structural characteristics are dictated by polymer chain-packing relationships^[146, 215, 216] and these packing relationships are ultimately determined by monomer segments within polymer chains,^[54, 55, 59] polymer processing techniques used to cast the membrane,^[144, 217, 218] and membrane-electrolyte interactions.^[56] In the past, PIMs have advanced as membranes with passive, non-transformable architectures; these membranes are overwhelmingly used for selective gas transport.^[54, 55, 58, 59, 143] In the context of a Li–S battery, however, a myriad of chemical transformations can take place.^[158, 162, 177, 219–221] Therefore, we reasoned that PIM membranes need not be inactive; instead, they might serve as adaptive components whose microporous architectures are switchable, dynamic, and tailored at the molecular level to respond to local chemical cues within the battery’s electrolyte—in this case lithium polysulfides (Li₂S_{*n*}, for *n* = 4–8), which are endogenous to Li–S batteries. The ability of these new PIM membranes to adapt and sustain their polysulfide-blocking ability in operando is unusual and offers advantages over traditional approaches based on single-ion conducting membranes^[43, 136, 137] and other permselective barriers^[169, 222–224] whose beneficial properties are ultimately transient. The origin of this transience is tied to the use of anode-protecting additives in the electrolyte (e.g., LiNO₃), which are consumed until exhausted and their stabilizing effects are lost thereafter.^[163–165, 213]

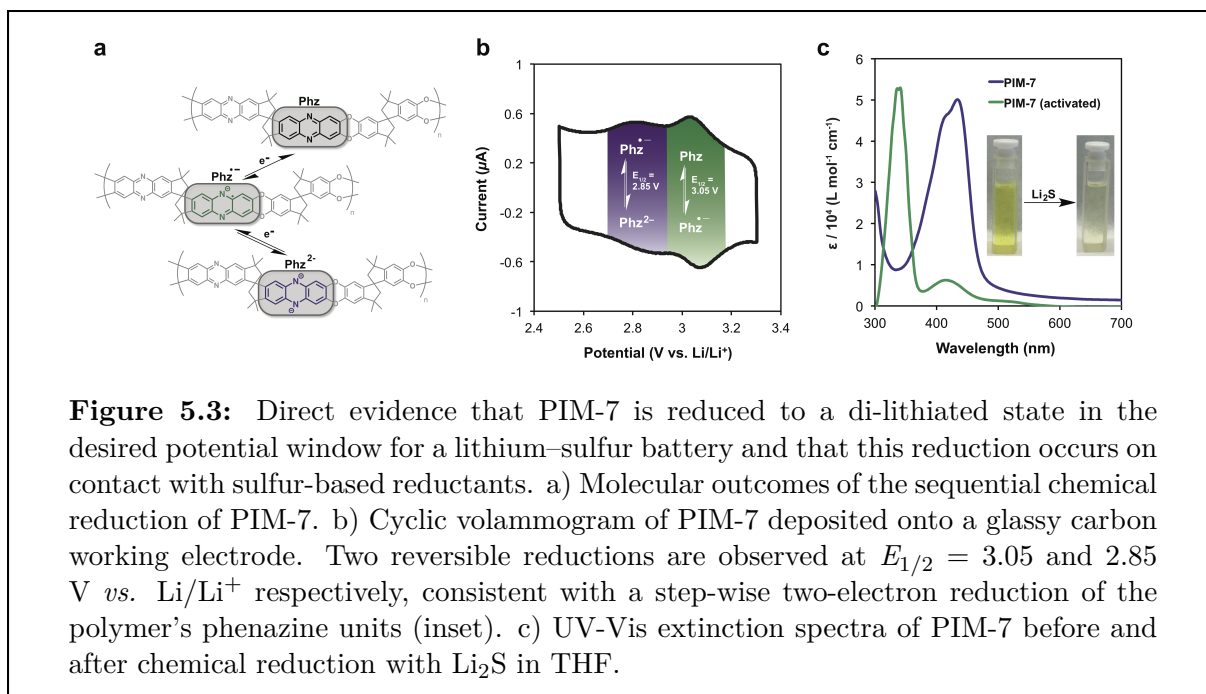
5.2 Computational screening of monomers for redox-switchable behavior

To confer adaptive transport behaviors to PIM membranes, we screened a library of candidate monomer segments for switchable redox properties—and more specifically, for a reduction potential ($E_{1/2}$) higher than 2.5 V *vs.* Li/Li⁺. The library design focused on phenazines (e.g., **1** & **4**), 1*H*-isoindole-1,3(2*H*)-diones (e.g., **2**, **5**, & **6**), pyrazines (e.g., **3**), *H*-isoindolo[2,1-*a*]benzimidazol-11-ones (e.g., **7**), benzo[*g*]quinoxalines (e.g., **8**



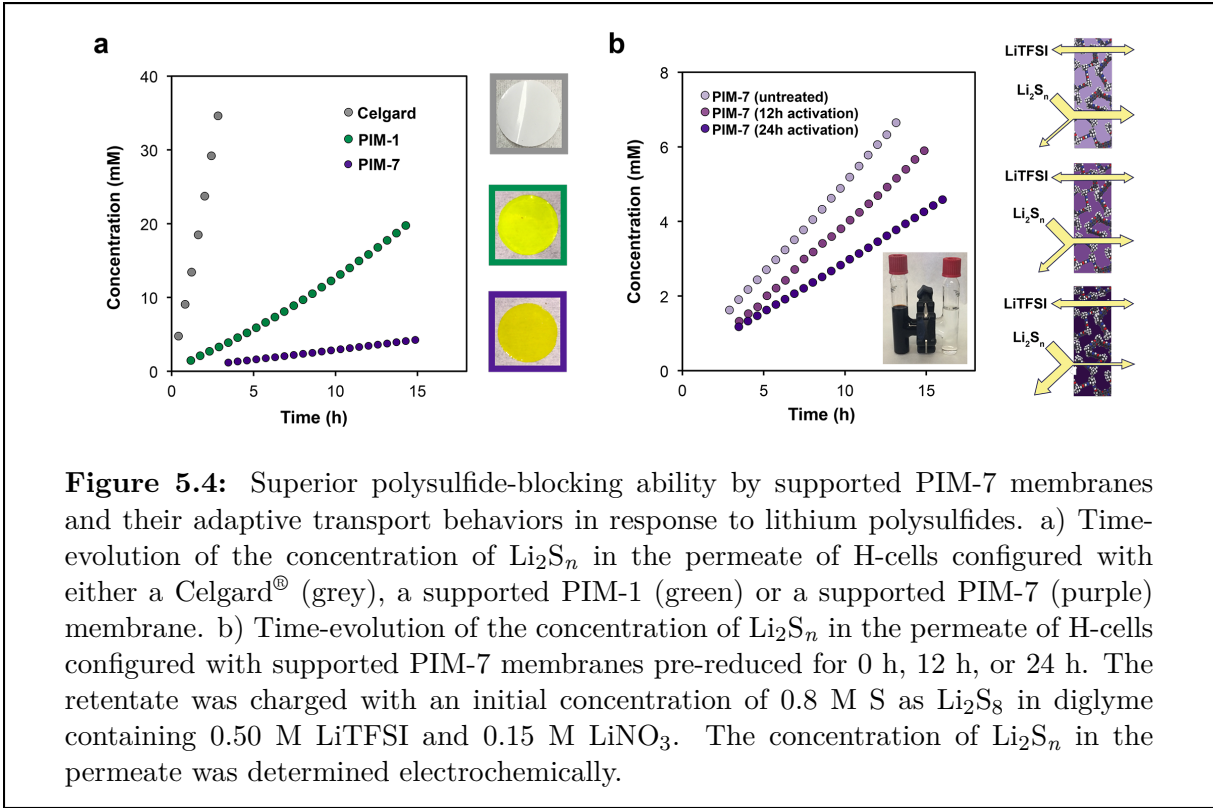
& **10**), benzo[1,2-c:4,5-c']dipyrrole-1,3,5,7(*2H,6H*)-tetrone (e.g., **9**), and dipyrrolo[3,4-b:3',4'-e]pyrazine-1,3,5,7(*2H,6H*)-tetrone (e.g., **11**)—all of which in principle could be reduced and lithiated at oxygen or at nitrogen centers upon interaction with Li_2S_n . For example, members of the library containing 1*H*-isoindole-1,3(*2H*)-dione substituents are predicted to be reduced by polysulfides to their lithiated radical anions, while others containing diazaheterocycles were designed to undergo sequential reductions to a closed-shell dianionic (and di-lithiated) state, in some cases driven by re-aromatization (e.g., **1** & **4**). The molecular structure and reduction potential of the PIM membrane segments were predicted using density functional theory.^[225, 226] As lithium cations can bind to any of the electronegative heteroatoms in the monomer segments, the most favorable binding site was identified by comparing the DFT-predicted energy of all possible $\text{Li}^+\text{-O/N}$ binding configurations. The reduction potential ($E_{1/2}$) was then predicted by calculating the adiabatic electronic affinity of the segments in the delithiated state.^[60, 61] Structure relaxation and energy evaluation were carried out using the M08-SO functional,^[227] while solvent effects were captured by the IEF-PCM model,^[228] where the dielectric constant value was set to the experimentally determined value of 9.0 for the battery electrolyte (Figure 5.13). All DFT calculations were performed using the Q-Chem software package.^[229] Many candidates in the library passed our screen (Figure 5.2b); to discriminate between hits, we hypothesized that closed-shell dianionic outcomes may provide more chemical stability long-term, and thus our focus turned to monomers containing phenazines. Charge-neutral

PIMs derived from phenazine-containing monomer segment **1** (calculated $E_{1/2} = 2.90$ V for the 1st reduction and 2.28 V for the 2nd reduction *vs.* Li/Li⁺) are known as PIM-7;^[143, 230] however, the redox-active character of these polymers has not been reported previously nor has their ion-transporting ability as a membrane.



5.3 Adaptive transport of lithium polysulfides through PIM-7 membranes

To validate our predictions, we first synthesized PIM-7 via step-growth polymerization in 78% yield and M_n of 80 kg mol^{-1} . Care was taken to adapt the synthetic methodology to afford PIM-7 with high molecular weight as needed to cast flexible membranes (see section 5.6). With high molecular weight PIM-7 in hand, we then carried out cyclic voltammetry (CV) on the polymer drop-cast onto a glassy carbon working electrode. PIM-7 exhibited two reversible reduction peaks at $E_{1/2} = 3.05$ and 2.85 V *vs.* Li/Li⁺, consistent with the reduction of the phenazine unit to the radical anion followed by the reduction to the dianionic species (Figure 5.3a). We noted that while the first reduction was within the range predicted by the genome screen, the second was not. We were able to resolve this incongruity in part by taking into account solvent effects using the SMD solvation model,^[231] which addresses solute-solvent dispersion interactions that are lacking in the currently available IEF-PCM model. Within this context, we calculated



$E_{1/2} = 3.31$ V for the 1st reduction and 2.75 V for the 2nd reduction (*vs.* Li/Li^+) for **1**. In parallel, we also demonstrated experimentally that PIM-7 could be chemically reduced when introduced to a solution of Li_2S . The optical signatures of PIM-7 in its charge neutral and di-anionic state were readily distinguished by UV-Vis spectroscopy (Figure 5.3b), with wavelength-shifts in the extinction maxima of 440 nm to 330 nm consistent with increased electron density of the polymer in its reduced state. Taken together, these results confirmed that PIM-7 membranes will become negatively charged and lithiated in the reducing environment of the Li-S battery as predicted from the computational screen.

Ion-Selective membranes were prepared by casting PIM-7 as a thin layer on a mesoporous Celgard[®] support using a wire-wound rod coating process.^[232] This method afforded uniform, 2 μm -thick coatings of PIM-7 on the flexible polymer support as evidenced by cross-sectional SEM (Figure 5.15). The packing of polymer chains for PIM-7 in the dry state yields an average pore size of 0.70 nm for the membrane.^[143] This size regime is predicted to be ideal for sieving polysulfides by size in battery electrolyte.^[56] In order to confirm that PIM-7 selective layers block polysulfide crossover, I carried out crossover measurements using native supported PIM-7 membranes of a known area and thickness placed between two compartments of a diffusion cell (*i.e.*, an H-cell). The H-cell was configured with dissolved Li_2S_n (0.8 M S as Li_2S_8 in diglyme containing 0.50 M LiTFSI and 0.15 M LiNO_3) on the retentate side and Li_2S_n -free electrolyte on the

permeate side (Figure 5.4a, and the cell shown in the inset of Figure 5.4b). The migration of Li_2S_n to the permeate side was then monitored for up to 15 h using CV, where the concentration of polysulfides could be directly related to the measured peak current in the CV using a calibration curve determined separately for a 1–50 mM concentration regime for Li_2S_n (Figure 5.16). I carried out the same experiments on un-modified Celgard[®] separators, which are known to be poorly selective for Li_2S_n (negative control), and for PIM-1 on Celgard, which has been reported by us^[56] to provide selectivity but not adaptability (positive control). From these data, I was able to calculate effective diffusive permeabilities ($D_{\text{eff,membrane}}$) of Li_2S_n through Celgard[®] and PIM on Celgard layered hybrid membranes. After measuring $D_{\text{eff,membrane}}$ for Celgard[®] alone, I was able to extract the effective diffusive permeability of Li_2S_n through the PIM selective layer, $D_{\text{eff,selective}}$, from $D_{\text{eff,membrane}}$ of Li_2S_n through the layered membranes (see section B.1). This analysis returned $D_{\text{eff,selective}}$ values of : $D_{\text{eff}} = 5.2 \times 10^{-8} \text{ cm}^2 \text{ s}^{-1}$ for Celgard[®]; $4.3 \times 10^{-10} \text{ cm}^2 \text{ s}^{-1}$ for PIM-1 on Celgard[®]; and $1.7 \times 10^{-10} \text{ cm}^2 \text{ s}^{-1}$ for PIM-7 on Celgard[®] without any Li_2S_n pretreatment. Thus, PIM-7 represents the best size-selective membrane for blocking Li_2S_n crossover to date, with diffusive permeabilities for Li_2S_n that are 2.5 and 306-fold lower than PIM-1 and Celgard, respectively.

I next sought to understand the impact of polysulfide-driven reductive chemical transformations on the polysulfide-blocking ability of PIM-7 membranes over time. To do so, PIM-7 membranes were bathed in concentrated solutions of Li_2S_n (1.0 M S as Li_2S_8 in diglyme containing 0.50 M LiTFSI and 0.15 M LiNO_3) for a prescribed period, either 12 h or 24 h, and then rinsed with and soaked in fresh electrolyte. The crossover data showed that PIM-7’s polysulfide-blocking ability is enhanced as the phenazine units are progressively reduced over time by Li_2S_n (Figure 5.4b). From these data, we were also able to quantify the evolutionary changes in Li_2S_n diffusive permeability from the baseline of $1.7 \times 10^{-10} \text{ cm}^2 \text{ s}^{-1}$ for PIM-7 on Celgard in its initial state, to $1.4 \times 10^{-10} \text{ cm}^2 \text{ s}^{-1}$ after 12 h and $9.2 \times 10^{-11} \text{ cm}^2 \text{ s}^{-1}$ after 24 h of chemical transformation. Extended application of Li_2S_n beyond 24 h did not appear to further enhance the membrane’s polysulfide-blocking ability. We attribute this effect to the slow diffusion of polysulfides through the membrane and the feedback loop associated with the reduced form of the membrane further retarding the migration of additional polysulfides. Thus, the membrane adapts its transport behavior and sustains these functions indefinitely; indeed, supported PIM-7 membranes demonstrated a stable crossover rate for at least 2 d. Advantageously, while the polysulfide-blocking character of supported PIM-7 membranes was enhanced upon increasing reduction of the phenazine subunits, the membrane ionic conductivity remained largely unchanged at $5 \times 10^{-3} \text{ mS cm}^{-1}$ (Figure 5.17).

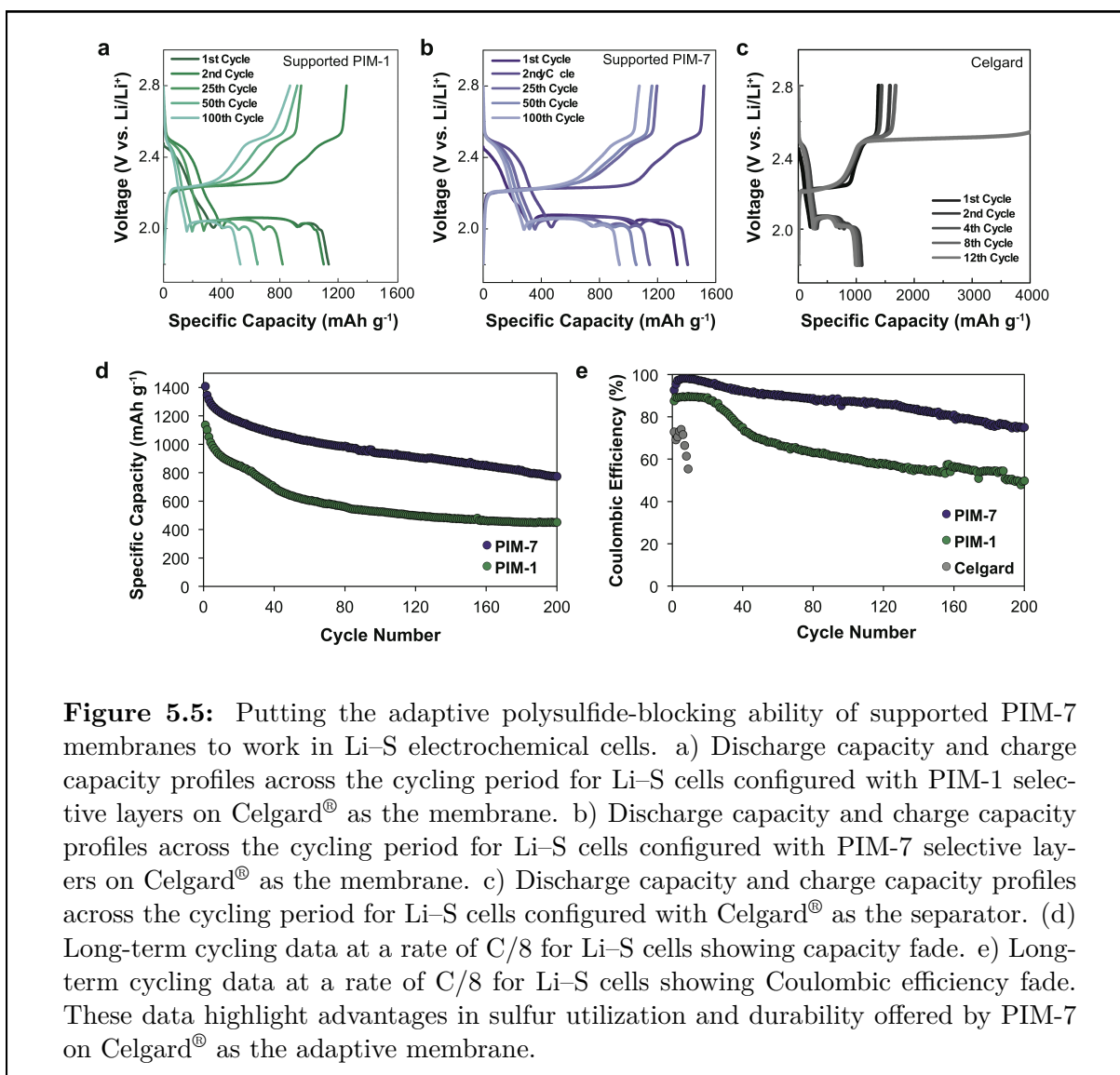


Figure 5.5: Putting the adaptive polysulfide-blocking ability of supported PIM-7 membranes to work in Li-S electrochemical cells. a) Discharge capacity and charge capacity profiles across the cycling period for Li-S cells configured with PIM-1 selective layers on Celgard[®] as the membrane. b) Discharge capacity and charge capacity profiles across the cycling period for Li-S cells configured with PIM-7 selective layers on Celgard[®] as the membrane. c) Discharge capacity and charge capacity profiles across the cycling period for Li-S cells configured with Celgard[®] as the separator. (d) Long-term cycling data at a rate of C/8 for Li-S cells showing capacity fade. e) Long-term cycling data at a rate of C/8 for Li-S cells showing Coulombic efficiency fade. These data highlight advantages in sulfur utilization and durability offered by PIM-7 on Celgard[®] as the adaptive membrane.

5.4 Improved cycle-life in lithium sulfur batteries using PIM-7 membranes

The superior polysulfide blocking ability of adaptive PIM-7 membranes over non-selective Celgard[®] and passively-selective PIM-1 membranes had a profound effect on the sulfur utilization, energy efficiency, and cycle-life of Li-S batteries. Here we assembled Li-S coin cells using a dissolved polysulfide cathode, whereby a semi-solid ink containing Li_2S_n (1.0 M S as Li_2S_8 in diglyme containing 0.50 M LiTFSI) and Ketjen-black (5% *w/w*) was introduced to a high surface-area carbon nanofiber current collector.^[157, 180, 210, 220] In this configuration, a high concentration of polysulfides is in direct contact with the membrane; this presents the most aggressive fitness test for the membrane constructs. All coin cells were tested using electrolytes that were devoid of LiNO_3 as an anode-protecting additive; in doing so, the Coulombic inefficiencies associated with the polysulfide shuttle can only be improved upon by an ion-selective membrane. All cells were galvanostatically cycled between 1.8–2.8 V at a C/8 rate for up to 200 cycles. Cells assembled with non-selective Celgard[®] separators (negative control) were prone to Coulombic (and energy) inefficiencies associated with the manifestation of a polysulfide shuttle as has been previously reported.^[163–165, 193, 213] In particular, charging these cells required increasingly more energy with each cycle, and an infinite charge was observed at cycle 12 and for all cycles thereafter (Figure 5.5c). Beyond cycle 12, several days were required to fully recharge cells configured with Celgard[®]; the sulfur utilization on discharge was $\sim 1000 \text{ mA h g}^{-1}$ for the limited number of cycles achievable over a several-months period of observation. On the other hand, Li-S cells assembled with passively-selective PIM-1 membranes on Celgard[®] (positive control, Figure 5.5a) were significantly more effective at arresting the polysulfide shuttle; no infinite-charge regime was observed and the energy required to fully charge these cells was sustainably low. The sulfur utilization of these cells ($\sim 1100 \text{ mA h g}^{-1}$ after the second-cycle discharge) was on par with cells assembled with Celgard[®], as was the capacity fade in the first few cycles; however, the cycle-life of these cells was significantly extended to 200 cycles. The specific capacity of PIM-1 cells at the end of 200 cycles was 451 mA h g^{-1} with a capacity fade of 0.302% per cycle. In contrast to cells assembled with either Celgard[®] alone or PIM-1 on Celgard[®], those assembled with adaptive membranes consisting of PIM-7 on Celgard[®] (Figure 5.5) were most effective at preventing the polysulfide shuttle. The initial Coulombic efficiency and thus energy efficiency of these cells was high (92.6%, compared to 87.5 % for PIM-1 on Celgard[®] and 72.9 % for Celgard[®] alone). We also noted that these cells gave markedly improved sulfur utilization, with a specific capacity of 1407 mA h g^{-1} ($\sim 20\%$ enhancement over both Celgard[®] and PIM-1 on Celgard[®], and 88% of theoretical); this is consistent with their chemically-evolved ability to better sequester the polysulfides to the sulfur cathode. Cells assembled with PIM-7 on Celgard[®] were able to sustain capacities of 774 mA h g^{-1} (55% of initial) over 200 cycles, with a capacity fade of 0.225% per cycle.

5.5 Conclusions and future work

The emerging view from our work is that macromolecular design strategies for ion-selective polymer membranes are primed for a paradigm-shift. It is now possible to use the redox environment of an electrochemical cell to chemically transform the structure and architecture of the membrane across multiple length scales in a manner that enhances the transport selectivity of the membrane. The negative feedback loop associated with polysulfides reacting with PIM-7's phenazine subunits and then encountering restrictions in their access to deeper pore voids is both unusual and powerful in preventing the polysulfide shuttle. To that point, past work in ion-selective membranes would suggest that it is not possible to enhance the selective transport properties of the membrane without negatively impacting membrane conductivity. Our success in this regard highlights the power of directed evolution in defining new properties in ion-transporting membrane materials. In future schemes, we see the predictive design strategies, led by materials genomics as outlined here, as essential for tailoring the switching ability to a specific battery chemistry. PIMs manifest as a universal platform to address crossover problems across a variety of battery architectures, whether solid-state and solution-based electrodes are employed. PIM membranes, adaptive and otherwise, therefore stand to significantly advance the field of electrochemical energy storage for aviation, transportation, and the grid.

5.6 Supporting information

5.6.1 Materials and methods

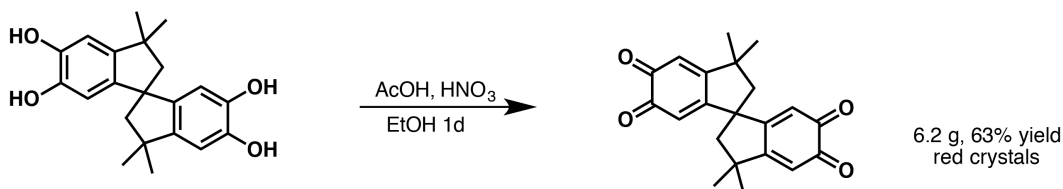
Synthesis of PIM-1

High molecular-weight PIM-1 was synthesized as described elsewhere.^[56, 179] Briefly, a mixture of anhydrous K_2CO_3 (16.6 g, 120 mmol), 3,3,3',3'-tetramethyl-1,1'-spirobisindane-5,5',6,6'-tetrol (7.07 g, 20 mmol), and 2,3,5,6-tetrafluoroterephthalonitrile (4.00 g, 20 mmol) in dry *N,N*-dimethylformamide (200 mL) was stirred at 65 °C for 4 d. On cooling, the mixture was added to water and the crude product collected by filtration. Repeated precipitations from a concentrated solution of polymer in chloroform into methanol gave the fluorescent yellow polymer in good yield (7.36 g, 80%) and whose physical attributes were consistent with previous reports. 1H NMR ($CDCl_3$, 500 MHz) δ 6.81 (br, 2H), 6.42 (br, 2H), 2.33 (br, 2H), 2.17 (br, 2H), 1.36 (br, 6H), 1.31 (br, 6H) ppm. THF-SEC: $M_w = 386,030$; $M_n = 136,014$; PDI = 2.84.

Synthesis of PIM-7

We found that the previously reported synthesis for PIM-7 and precursors^[230] **A** and **B** did not yield consistent results to provide materials pure enough to give PIM-7 of high enough molecular weight for our purposes. A modified procedure for the synthesis of PIM-7 and its precursors is given below (Schemes 5.1–5.3).

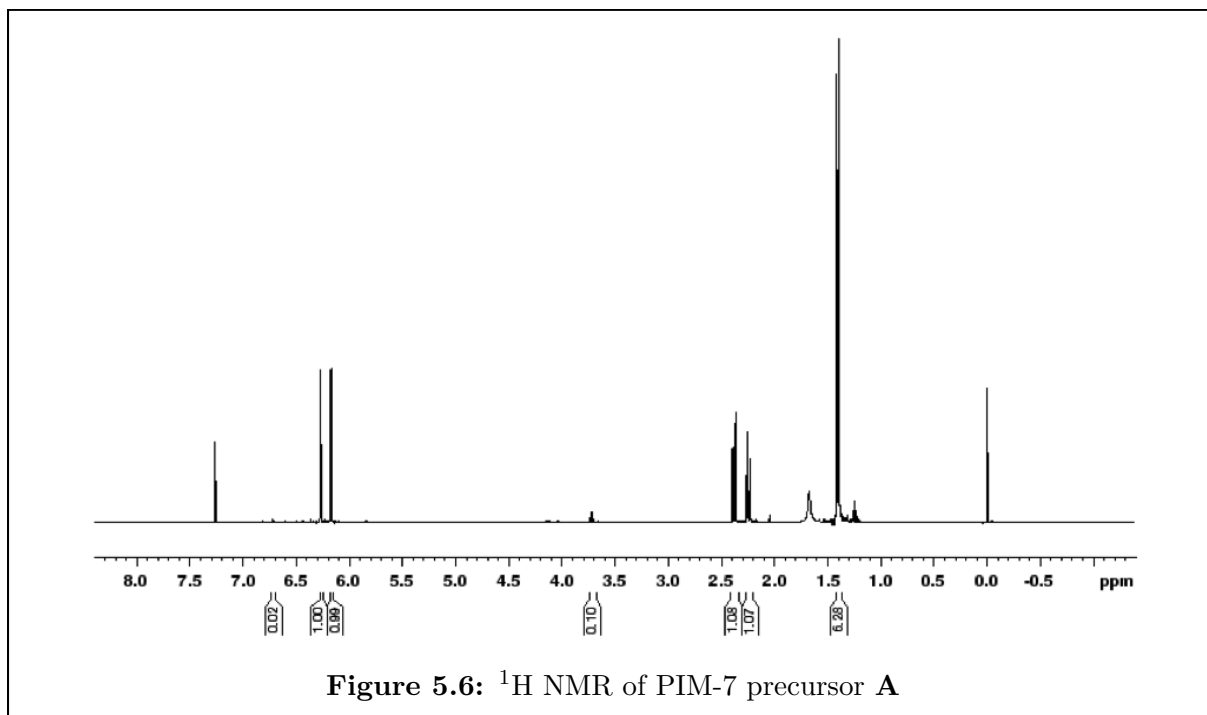
Scheme 5.1: Synthesis of PIM-7 precursor **A**

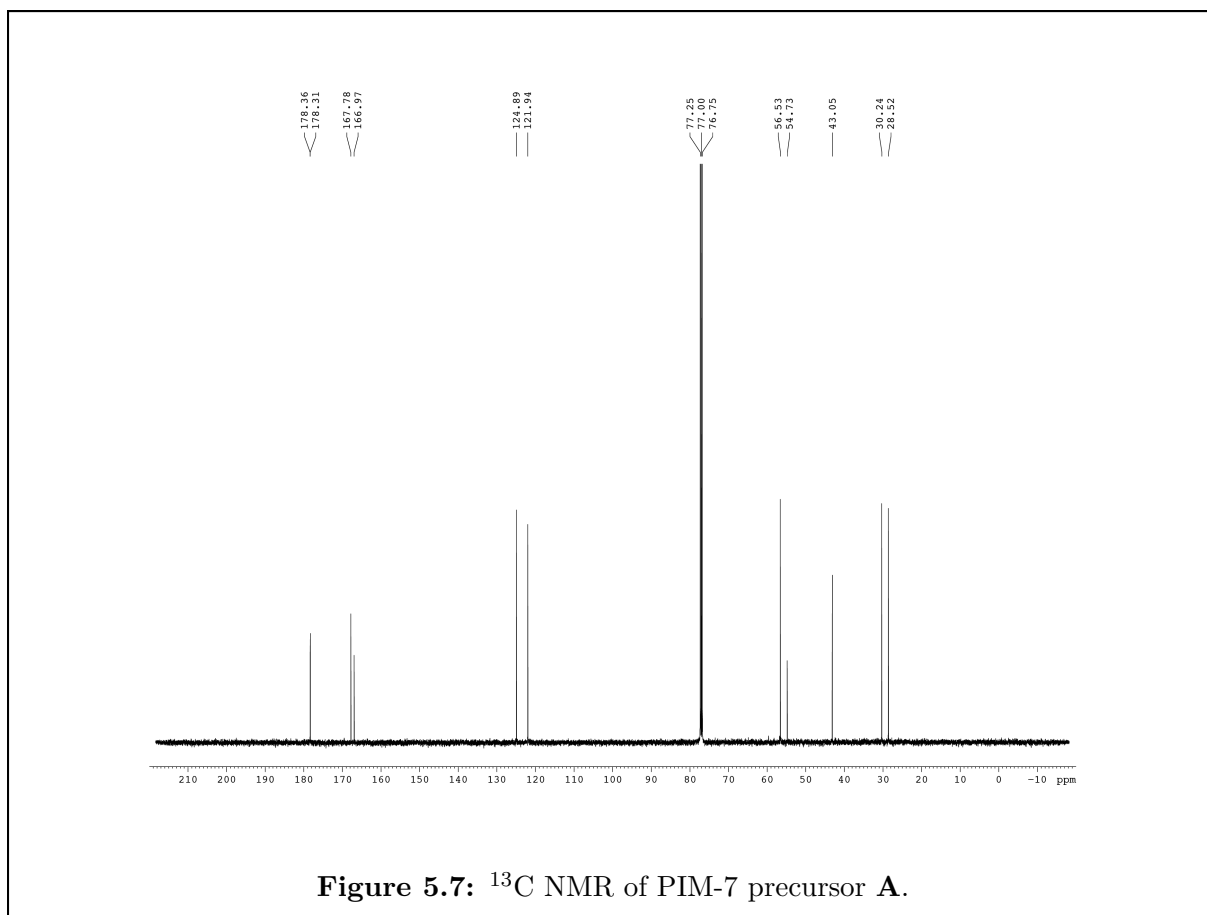


Synthesis of PIM-7 Precursor **A**

To a cooled solution (0 °C) of 3,3,3',3'-tetramethyl-1,1'-spirobisindane-5,5',6,6'-tetrol (10 g, 29 mmol) in EtOH (150 mL) was added acetic acid (7.0 mL, 122 mmol) dropwise, followed by fuming nitric acid (10 mL, 252 mmol) to give a dark red suspension. The reaction mixture was stirred at 0 °C for 2 h, warmed to room temperature and stirred for 12 h. The reaction mixture was filtered and washed with DI water (3×50 mL) and EtOH (3×50 mL) to yield the product **A** as red crystals (6.2 g, 63% yield). 1H NMR (500 MHz, $CDCl_3$): see Figure 5.6. ^{13}C NMR (125 MHz, $CDCl_3$): δ 178.36, 128.31, 167.78, 166.97, 124.89, 121.94, 56.53, 54.73, 43.05, 30.24, 28.52 ppm (Figure 5.7). 1H - ^{13}C HSQC NMR ($CDCl_3$): see Figure 5.8. HRMS(ESI): Calcd. 359.1254 ($C_{21}H_{20}O_4Na$).

Found 359.1251. Anal. calcd for $C_{21}H_{20}O_4$: C, 74.98; H, 5.99. Found: C, 73.75; H, 6.14 (suggesting a 3:1 molar ratio of the expected product to adventitious H_2O).





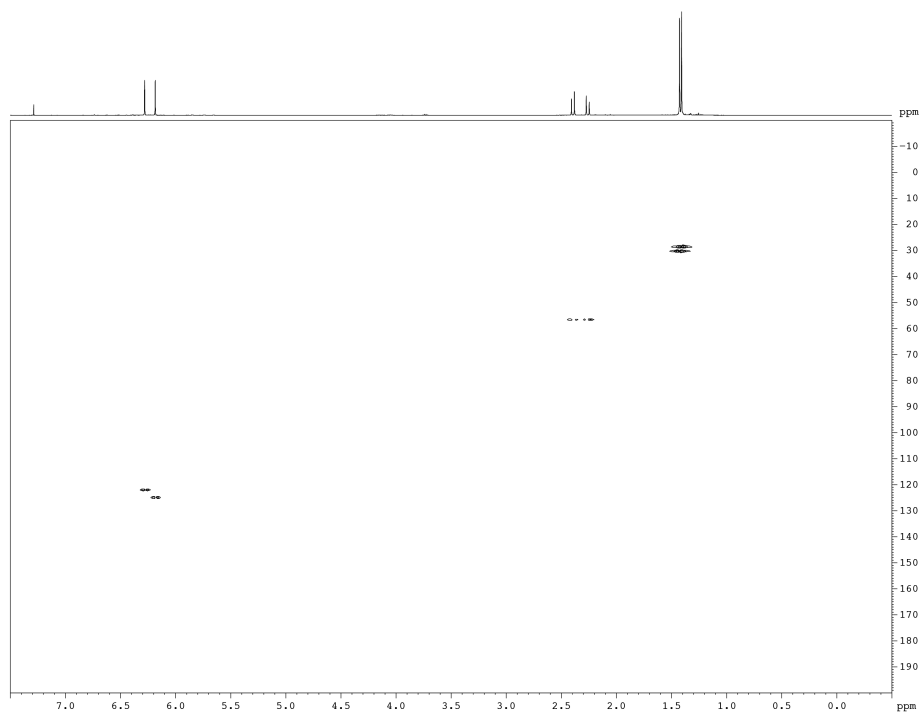
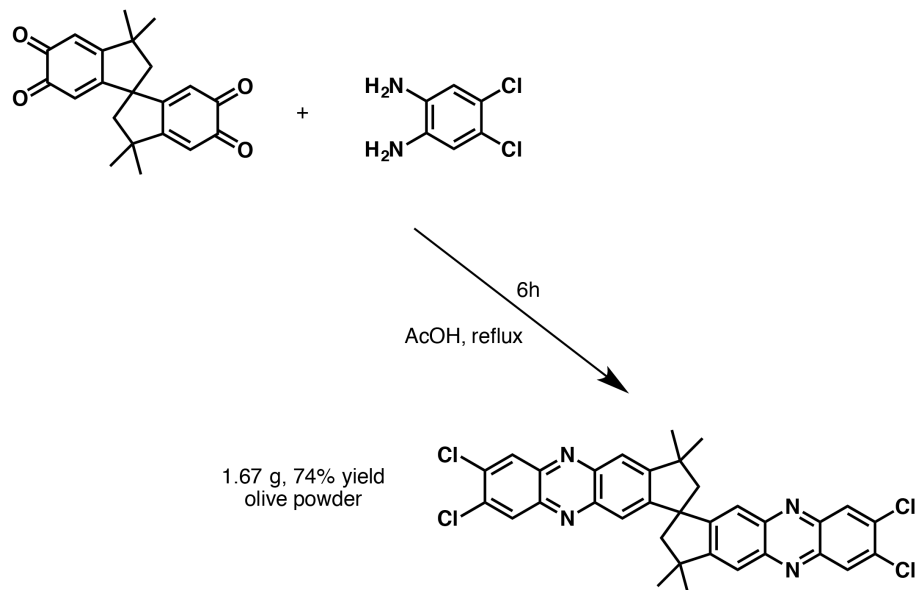
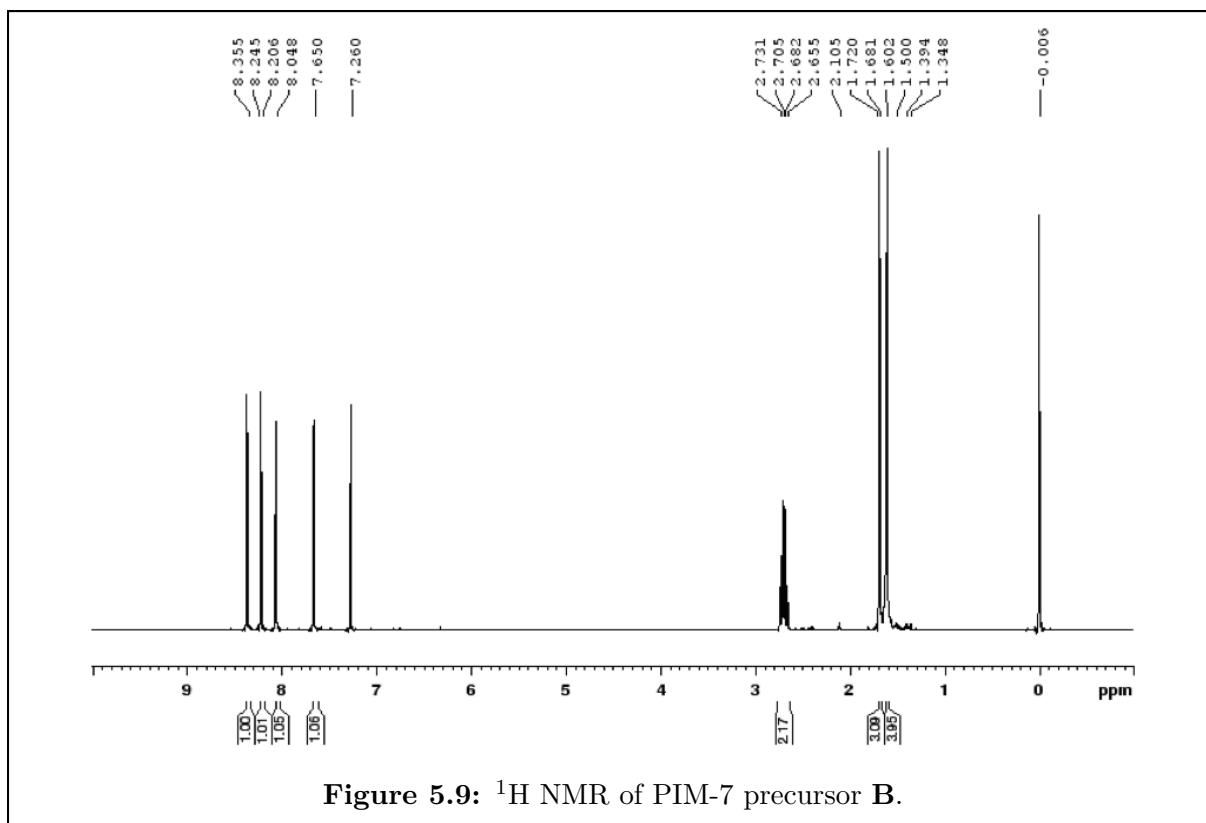


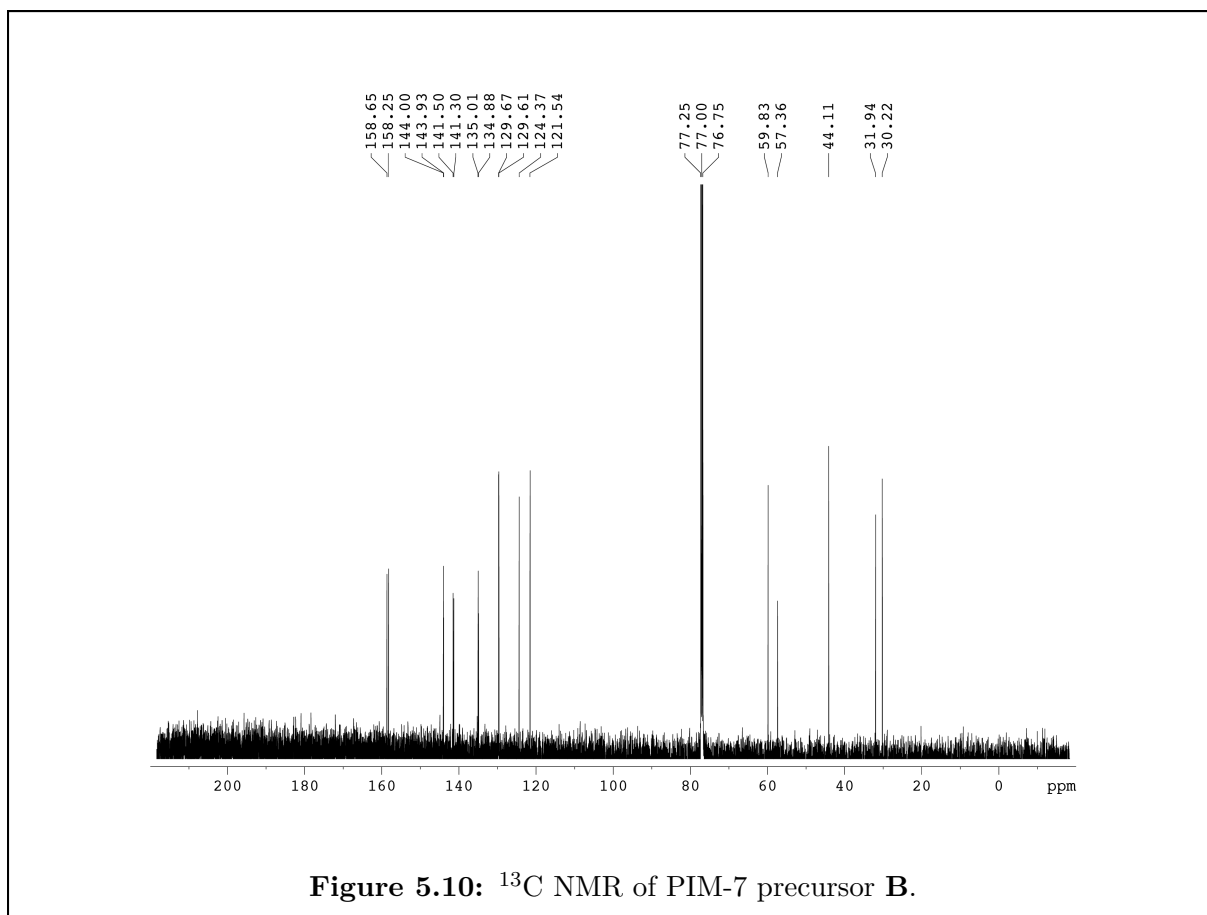
Figure 5.8: ^1H - ^{13}C HSQC NMR of PIM-7 precursor **A**.

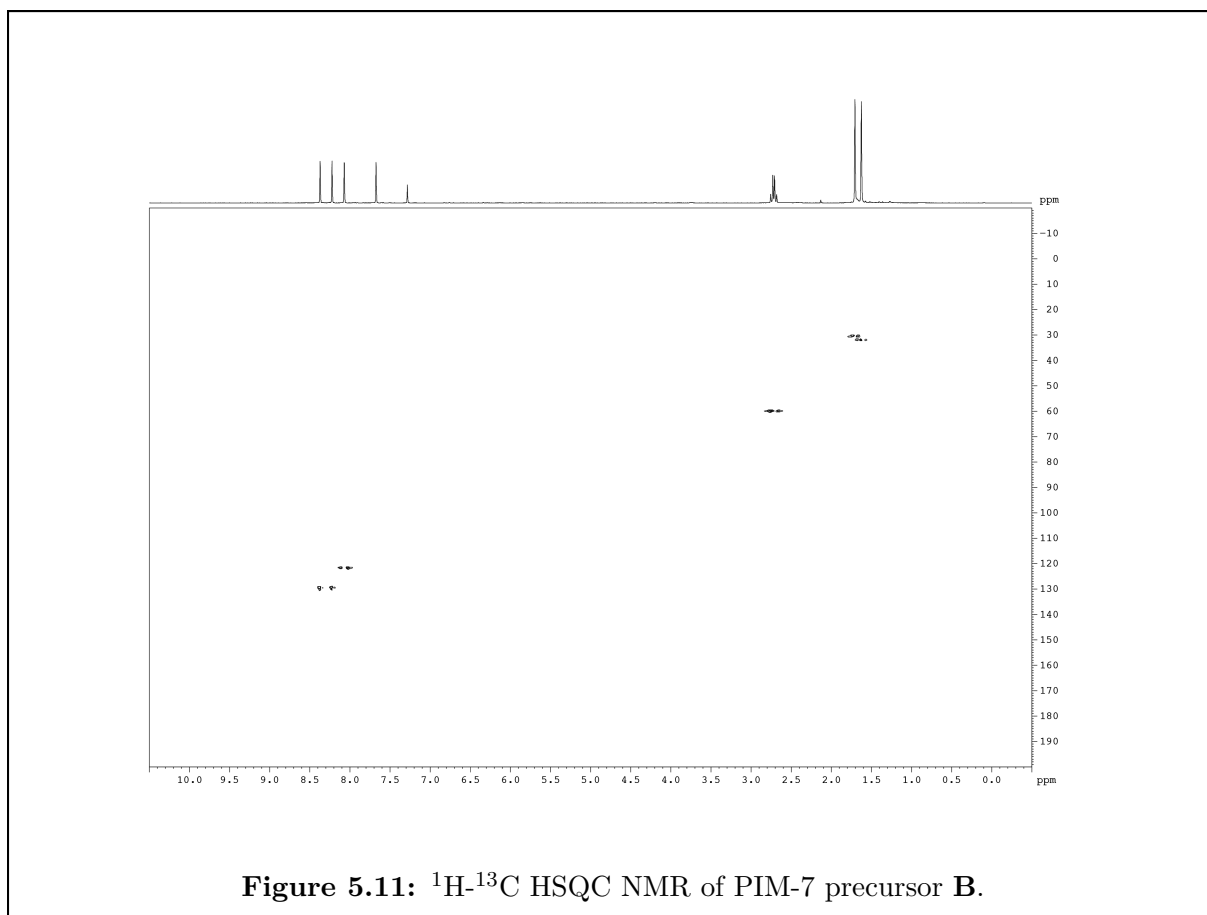
Scheme 5.2: Synthesis of PIM-7 precursor **B**.

Synthesis of PIM-7 Precursor **B**

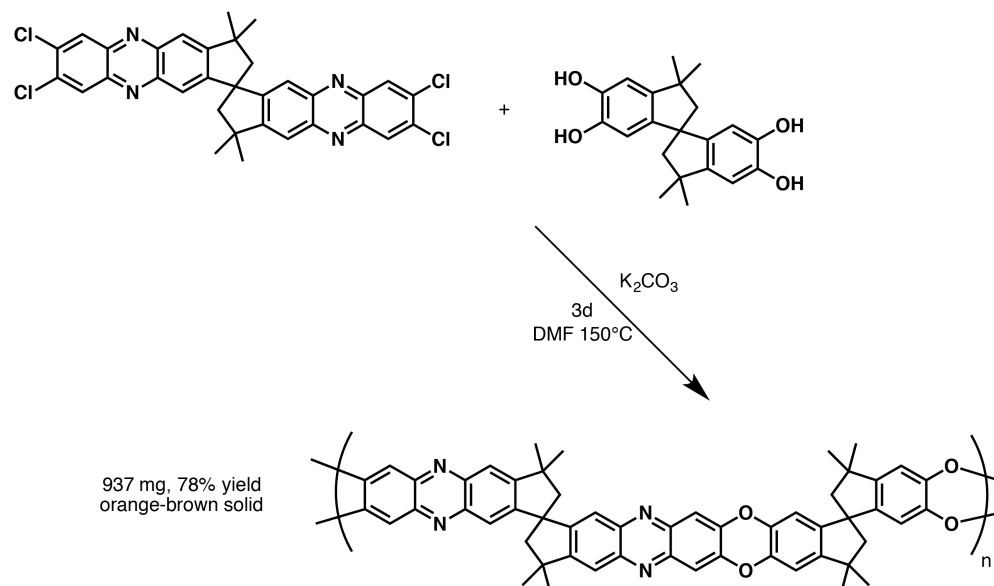
To a solution of **A** (1.19 g, 4 mmol) in 100 mL of acetic acid was added 4,5-dichloro-*o*-phenylenediamine (2.5 g, 14 mmol) to give a dark solution. The reaction mixture was heated to 120 °C for 3 h. After cooling, the reaction mixture was filtered and the resulting solid was washed with acetic acid (3 × 50 mL), DI water (3 × 50 mL), and EtOH (3 × 50 mL). The solid was then washed with warm toluene (3 × 50 mL) to yield the product **B** as a yellow-green solid (1.67 g, 74% yield). ¹H NMR (500 MHz, CDCl₃): see Figure 5.9. ¹³C NMR (125 MHz, CDCl₃): δ 158.65, 158.25, 144.00, 143.93, 141.50, 141.30, 125.01, 134.88, 129.67, 129.61, 124.37, 121.54, 59.83, 57.36, 44.11, 31.94, 30.22 ppm (see Figure 5.10). ¹H-¹³C HSQC (CDCl₃): see Figure 5.11. HRMS(ESI): Calcd 617.0828 (C₃₃H₂₅N₄C₁₄). Found 617.0831. Anal. calcd for C₃₃H₂₄C₁₄N₄: C, 64.10; H, 3.91; N, 9.06. Found: C, 62.58; H, 3.96; N, 8.59 (suggesting a 1:1 molar ratio of the expected product to adventitious H₂O).





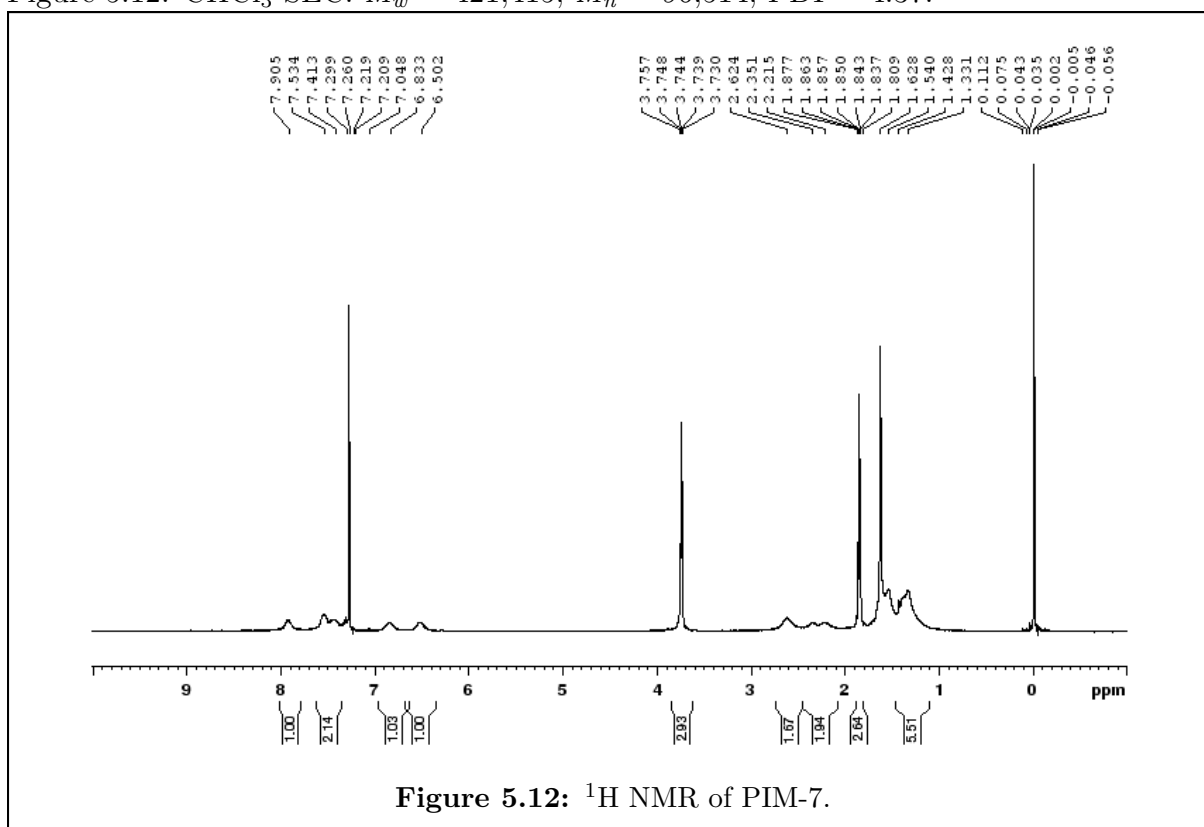


Scheme 5.3: Synthesis of PIM-7.



Synthesis of PIM-7

To a solution of 3,3,3',3'-tetramethyl-1,1'-spirobisindane-5,5',6,6'-tetrol (495 mg, 1 mmol), 18-crown-6 (358 mg, 1 mmol), and **B** (900 mg, 1 mmol) in 25 mL dry DMF was added anhydrous K_2CO_3 (1.2 g, 9 mmol) to give a green suspension. The reaction mixture was stirred at 150 °C for 3 d. On cooling, the mixture was added to 500 mL of 1% HCl and the solid collected by filtration. The solid was washed with DI (3×200 mL) and MeOH (3×200 mL). The solid was dissolved in 10 mL of chloroform, filtered through glass wool, and added dropwise to 300 mL MeOH. The precipitation was repeated to yield PIM-7 as an orange-brown solid (937 mg, 78% yield). 1H NMR (500 MHz, $CDCl_3$): see Figure 5.12. $CHCl_3$ -SEC: $M_w = 421,415$; $M_n = 96,514$; PDI = 4.37.



Membrane Preparation

Thin films of both PIM-1 and PIM-7 supported on Celgard[®] 2325 were prepared using an Elcometer 4340 Automatic Film Applicator. Solutions of PIM-1 (50 mg mL^{-1}) or PIM-7 (70 mg mL^{-1}) were prepared in chloroform. The PIM solution ($70 \mu\text{L}$) was deposited on the surface of the Celgard 2325 and applied as a thin film with an Elcometer wire-wound rod with a wet film height specification of $20 \mu\text{m}$. The thickness of the PIM layer was confirmed using cross-sectional SEM. (Figs. 5.14 and 5.15)

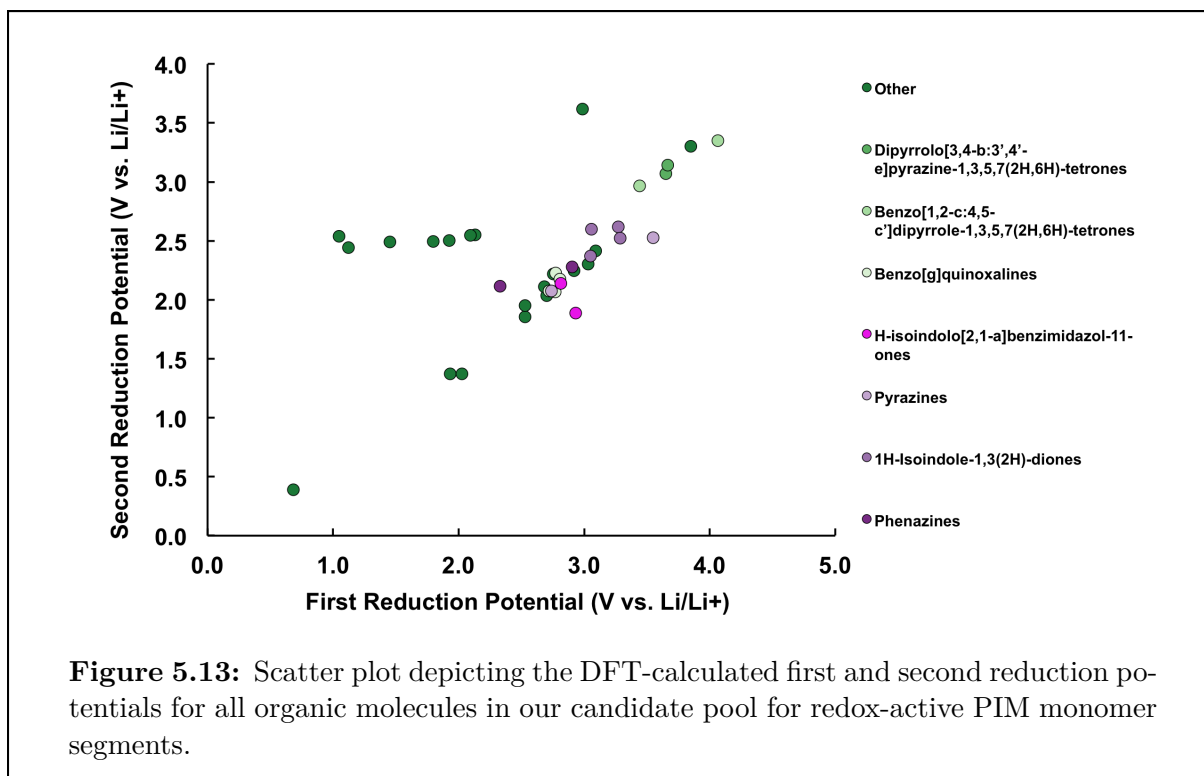
Battery Cycling

The battery cycling tests were carried out with CR2032 coin cells. The anode was a lithium chip (750 μm thickness), which was cut into a disk with the diameter of 15 mm. The polysulfide-KB slurry (~ 20 mg) was loaded on a carbon nanofiber paper disk (1.13 cm^2 , ~ 2 mg), which served as the sulfur cathode. The separator used was Celgard[®] 2325, PIM-1 supported on Celgard[®] 2325, or PIM-7 supported on Celgard[®] 2325. The PIM-7 supported on Celgard[®] 2325 membrane was soaked in the polysulfide solution 24 h before use. The electrolyte was made of 0.5 M LiTFSI in diglyme without any LiNO_3 added. The galvanostatic discharge and charge tests were conducted with a BioLogic VMP3 potentiostat within the voltage range of 1.8–2.8 V.

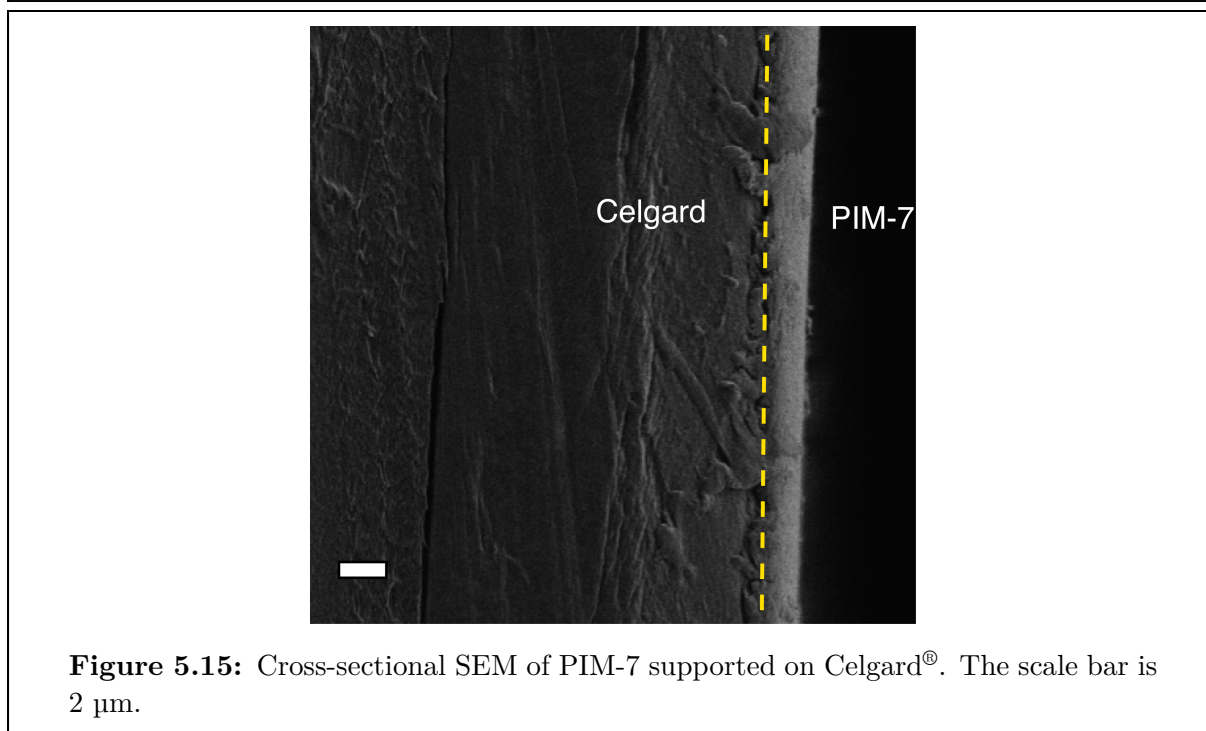
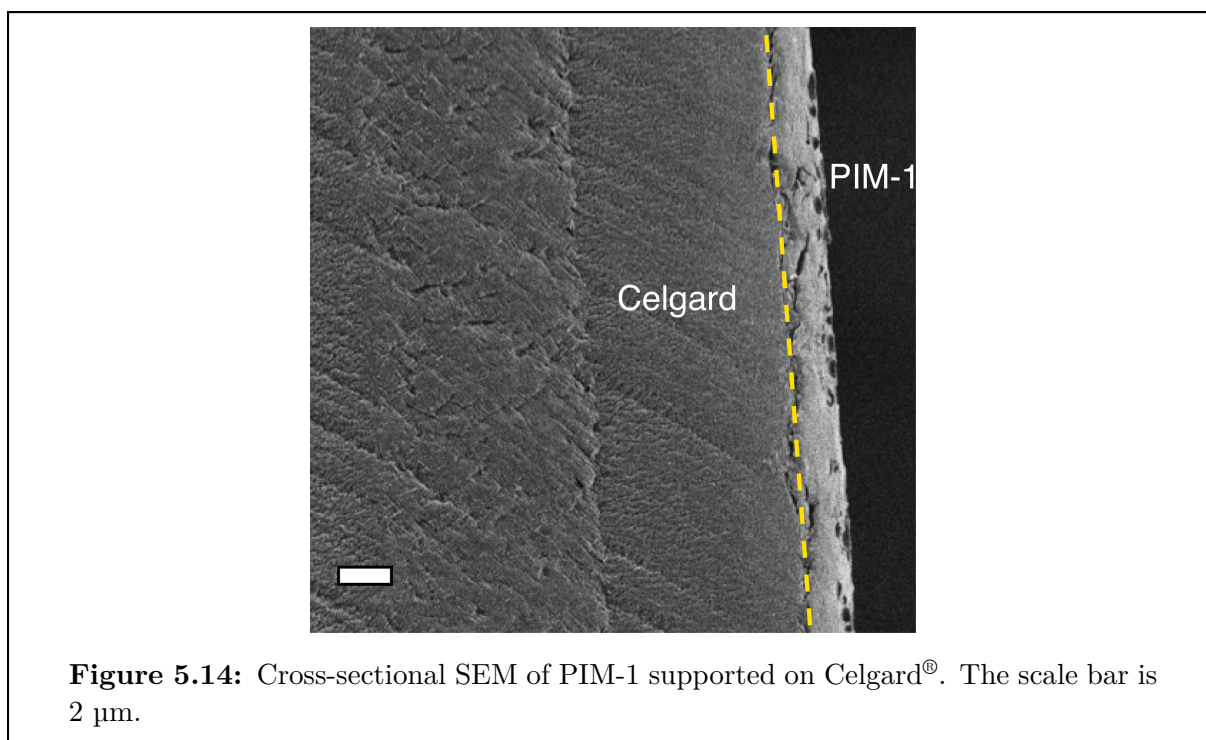
5.6.2 Materials genome screening for PIM reactivity

A researcher-generated library of model compounds was used as a starting point for Materials Genome screens of redox-active PIM segments. This library of model compounds was subject to analysis using density functional theory (DFT).^[225, 226] All DFT calculations were performed using the Q-Chem software package.^[229] In our screens, we focused our attention on identifying the electrochemical potential ranges (*vs.* Li/Li^+) where PIM monomer segments could be reduced and lithiated. In that Li^+ can bind to any number of electronegative heteroatoms in the PIM monomer segments, generally through either nitrogen or oxygen atoms, we were careful to identify the most favorable binding site by comparing the DFT-predicted energy of all possible Li^+ -O/N binding configurations.

With this information, we were then able to calculate the reduction potentials ($E_{1/2}$) by comparing to the adiabatic electronic affinity of the segments in their non-reduced (and delithiated) state^[60, 61] to the absolute reduction potential of a reference electrode (Li/Li^+). We carried out structure relaxation and energy evaluation using the M08-SO functional.^[227] Solvent effects were captured by the IEF-PCM model,^[228] where the dielectric constant value was set to the experimentally determined value of 9.0 for the battery electrolyte. For high ranking candidates (e.g., model compound **1**, shown in Figure 5.2b), the solvent effects were further refined using the SMD solvation model^[231] to address the solute-solvent dispersion interaction, which was lacking in the currently available IEF-PCM model. All predicted reduction potentials are shown in Figure 5.13.



5.6.3 Scanning electron microscopy of PIM-1 and PIM-7 selective layers on Celgard[®]



5.6.4 Polysulfide crossover measurements and analysis

A PIM-1 or PIM-7 membrane of known thickness (typically 2 μm) supported on Celgard[®] was placed between two halves of an H-cell with an aperture diameter of 1.6 cm and sealed in place with a chemically resistant O-ring. One half of the H-cell (the retentate) was charged with 12 mL of Li_2S_8 in electrolyte, while the other half (the permeate) was charged with the same volume of electrolyte with no Li_2S_8 . Both compartments were stirred to ensure homogeneity. Every 20–30 min, the stirring was stopped and the concentration was measured electrochemically by acquiring a CV at 100 mV s^{-1} from 2.00 V to 3.00 V *vs.* Li/Li^+ . The peak anodic current was related to polysulfide concentration (C) with a calibration curve (Fig. 5.16). From this data, D_{eff} was calculated as described in section B.1. The subscripts selective, Celgard, and composite refer to the PIM portion of the membrane, Celgard portion of the membrane, and the full composite membrane, respectively.

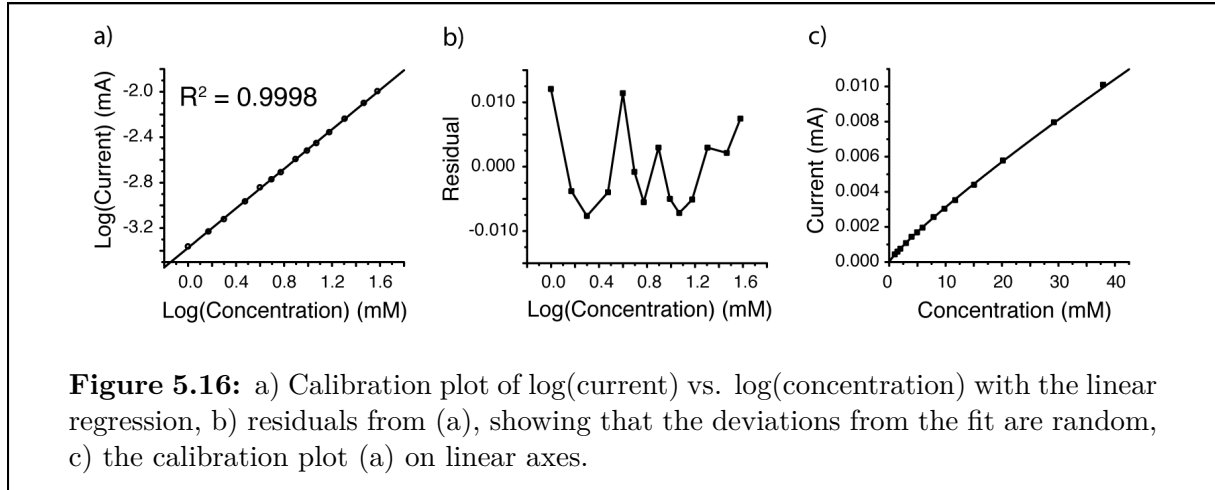
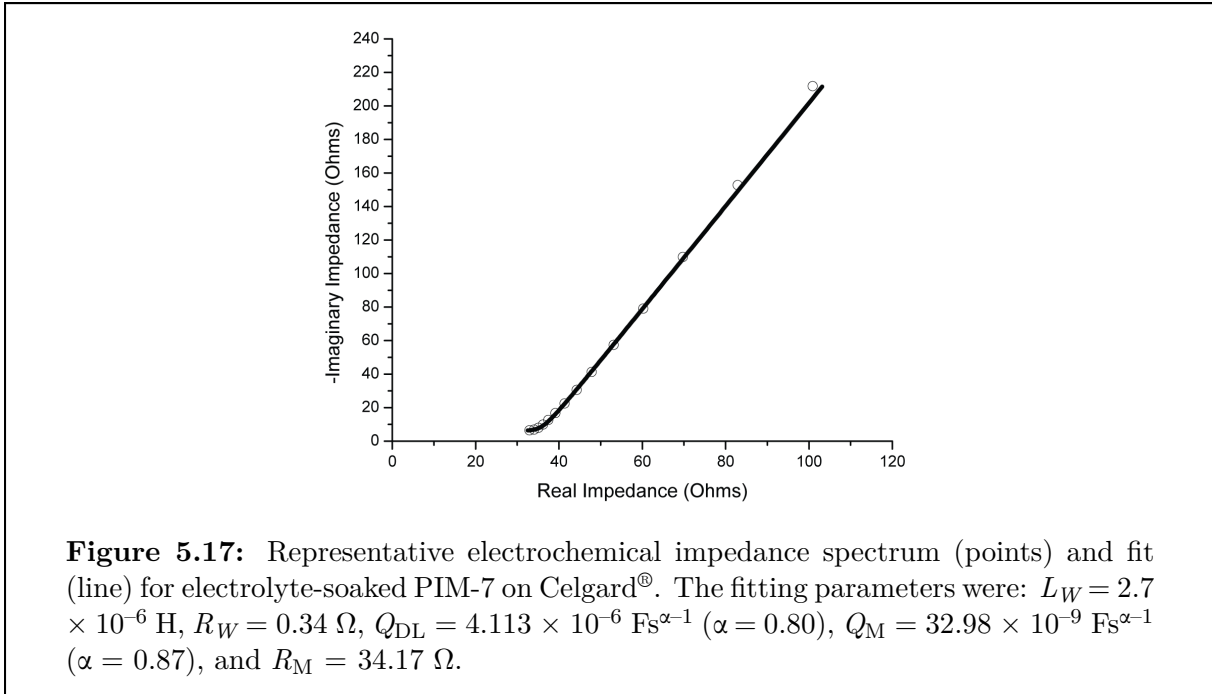


Table 5.1: Calculated effective diffusion coefficients for Li_2S_8 through Celgard, PIM-1 on Celgard, and PIM-7 on Celgard.

Membrane	Soaking time (h)	$D_{\text{eff,composite}} \text{ (cm}^2 \text{ s}^{-1}\text{)}$	$D_{\text{eff,selective}} \text{ (cm}^2 \text{ s}^{-1}\text{)}$
Celgard	0	$(5.2 \pm 0.4) \times 10^{-8}$	N/A
PIM-1 on Celgard	0	$(5.3 \pm 0.4) \times 10^{-9}$	$(4.3 \pm 0.3) \times 10^{-10}$
PIM-7 on Celgard	0	$(2.2 \pm 0.2) \times 10^{-9}$	$(1.7 \pm 0.1) \times 10^{-10}$
	12	$(1.8 \pm 0.1) \times 10^{-9}$	$(1.4 \pm 0.1) \times 10^{-10}$
	24	$(1.2 \pm 0.1) \times 10^{-9}$	$(9.2 \pm 0.7) \times 10^{-11}$

5.6.5 Electrochemical impedance spectroscopy during membrane evolution

The ionic conductivity of supported PIM-7 membranes was measured before and after soaking in a solution of Li_2S_8 (for 24 h) by electrochemical impedance spectroscopy (EIS) as described in section B.2. The membrane resistance, R_M , consists of the Celgard and PIM resistances in series. The resistance of the PIM layer can be calculated by subtracting the measured resistance of Celgard ($R_{M,\text{Celgard}} = 13 \text{ } \Omega$) from the composite membrane resistance. The average measured conductivity for PIM-7 before soaking in a solution of Li_2S_8 was $(7 \pm 2) \times 10^{-3} \text{ mS cm}^{-1}$, while the average measured conductivity after soaking for 24 h in Li_2S_8 was $(5 \pm 3) \times 10^{-3} \text{ mS cm}^{-1}$ (see Figure 5.17).



5.6.6 Acknowledgements

This chapter is the result of a collaboration between myself, A.L. Ward, L. Li, M.A. Hughes Jr., X. Qu, K.A. Persson, and B.A. Helms, and I am thankful to all my co-authors for their help with this work. A.L.W., X.Q., K.A.P., and B.A.H. were supported by the Joint Center for Energy Storage Research, an Energy Innovation Hub funded by the U.S. Department of Energy, Office of Science, Office of Basic Energy Sciences. S.E.D. was supported by the Department of Defense through the National Defense Science & Engineering Graduate Fellowship program. M.J.H. was supported in part by the U.S. Department of Energy, Office of Science, Office of Workforce Development for Teachers and Scientists

(WDTS) under the Science Undergraduate Laboratory Internships Program (SULI). Portions of the work—including polymer synthesis and characterization, polymer processing, membrane testing, and Li-S battery testing—were carried out as a User Project at the Molecular Foundry, which is supported by the Office of Science, Office of Basic Energy Sciences, of the U.S. Department of Energy under Contract No. DE-AC02-05CH11231. The computational portion of this work used resources of the National Energy Research Scientific Computing Center, a DOE Office of Science User Facility supported by the Office of Science of the U.S. Department of Energy under the same contract. The Materials Project (BES DOE Grant No. EDCBEE) is acknowledged for infrastructure and algorithmic support.

Chapter 6

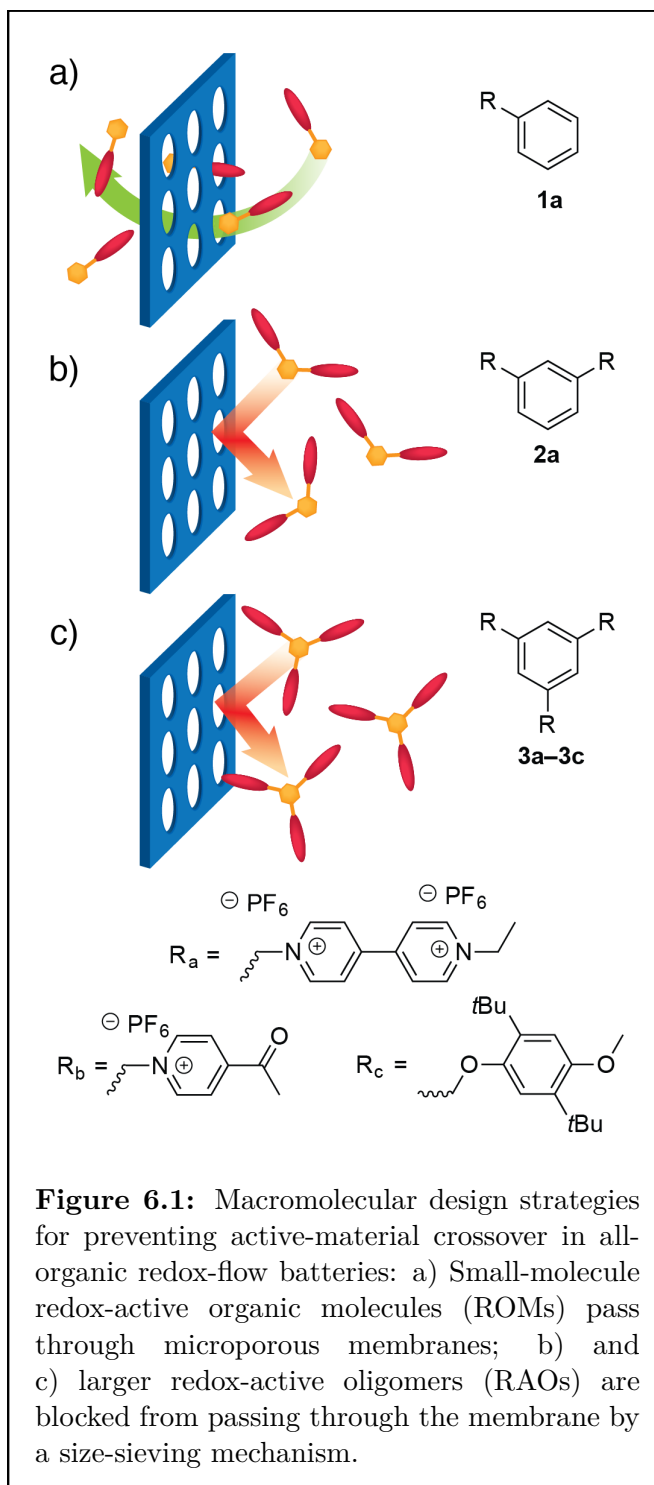
Macromolecular Design Strategies for Preventing Active-Material Crossover in Non-Aqueous All-Organic Redox-Flow Batteries

Reproduced with permission from unpublished work in preparation.

6.1 Introduction and prior art

All-Organic redox-flow batteries are well positioned to offer low-cost, multi-hour electrochemical energy storage at large scale in line with targets for grid modernization.^[5, 37–40] During flow-battery operation, solutions of redox-active organic molecules (ROMs) in a non-aqueous electrolyte are circulated through the negative and positive electrode compartments of an electrochemical cell. These compartments are electronically isolated from each other by a separator or ion-conducting membrane.^[135, 155] In order to maximize cycle-life and efficiency, it is imperative to block ROMs from migrating between electrode compartments during cycling while also maintaining facile transport of the working ion.^[192]

Here I show how this is achieved through macromolecular design principles advanced and applied to ROMs and ion-selective membranes derived from polymers of intrinsic microporosity (PIMs) (Fig. 6.1). In contrast with traditional mesoporous battery separators, membranes derived from PIMs feature permanent micropores that in principle allow working-ion conduction while blocking the crossover of larger active-materials.^[54, 56–59] Indeed, I found that the effective diffusion coefficient (D_{eff}) for small-molecule ROMs (e.g., **1a**) through PIM-1 membranes decreased 40-fold compared to a Celgard[®] separator with ~20 nm pores. Additional gains in blocking ability (470-fold) were obtained by chemically cross-

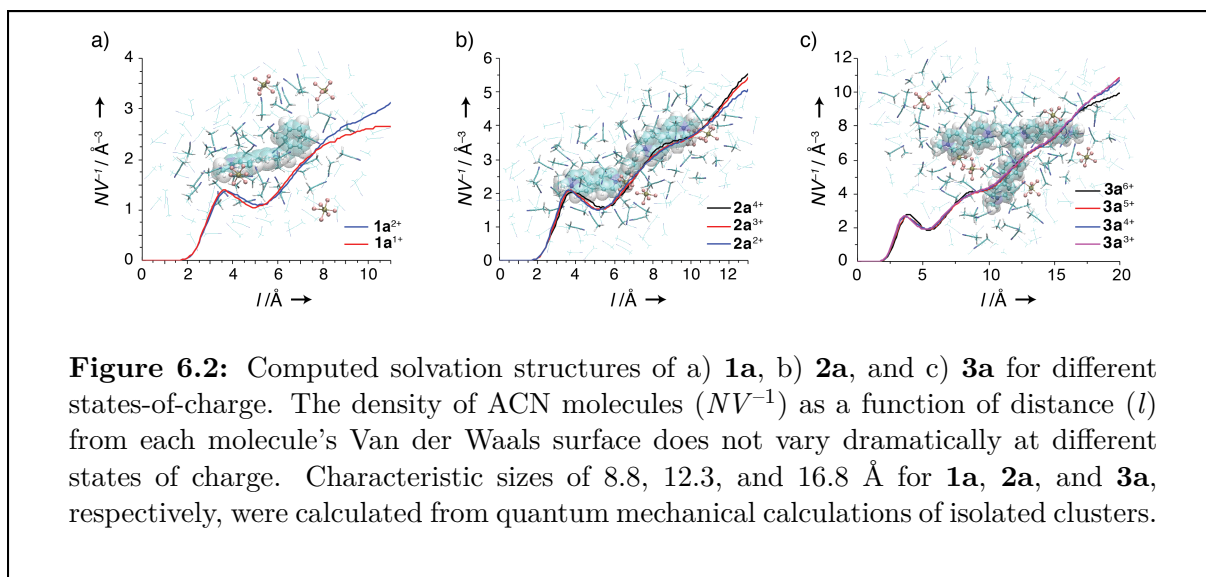


linking PIM-1 membranes, which restricted pore swelling in electrolyte. While these gains alone are impressive, I hypothesized that simply increasing the effective size of the ROM (e.g., through oligomerization) would provide active-materials that were larger than the PIM membrane’s pore-size exclusion limit and thereby enable active-material blocking through a size-sieving mechanism. Indeed, by increasing slightly the molecular dimensions from 8.8 to 12.3 Å through oligomerization, D_{eff} fell below my experimental limit of quantification, with an estimated upper-bound of $3.4 \times 10^{-11} \text{ cm}^2 \text{ s}^{-1}$ (Fig. 6.2). Despite this dramatic 9,000-fold improvement in membrane blocking ability relative to Celgard[®], PIM-1 membranes retained high ionic conductivities of at least 0.4 mS cm^{-1} (compared to 2.2 mS cm^{-1} for Celgard[®]). Furthermore, I found that sieving oligomeric organic active materials by size with PIM membranes was general to different ROM chemistries (e.g., **3b** and **3c**) in a variety of battery electrolytes (e.g., ACN, PC, DME, etc.), highlighting the generality of this approach.

Breaking with convention, the advances reported here provide an important counterpoint to: 1) single-component electrodes paired with ceramic membranes, which are expensive and difficult to scale;^[41] 2) thick macroporous separators paired with mixed-electrode formulations (i.e., anolytes and catholytes present in both electrode compartments), which lead to Coulombic inefficiencies and short cycle-life;^[233, 234] and 3) mesoporous separators paired with concentrated solutions of redox-active polymers, which are difficult to pump through electrochemical cells at high molecular weight and at all states-of-charge.^[235–239] Our strategy to implement ROM oligomerization, as opposed to polymerization, should also serve to retain the facile charge transfer kinetics that are characteristic of ROM monomers, which is essential for power quality and high active-material utilization.^[240]

6.2 Computational prediction of the solvated structures of organic redox-active molecules and oligomers

To quantitatively inform the critical size regime for ROM-blocking by a size-selective polymer membrane, we designed a series of viologen-based redox-active oligomers (RAOs) (**1a–3a**, Fig. 6.1) and studied their solvated structures computationally in acetonitrile (ACN) using a combination of ab initio quantum mechanical studies and classical molecular dynamics simulations (see section 6.7, Figs. 6.5–6.9, Tables 6.1–6.2). Our RAO design was structurally minimal, with redox-active viologens serving as pendants to a central mesitylene core (Fig. 6.1). We were interested in understanding active-material solvation at different states of charge (SOCs), as changes in solvation may affect the crossover behavior during cell cycling. We found that ACN molecules are preferentially oriented at solvent-viologen interfaces, with electron-rich nitriles stabilizing the cationic viologen pendants at all SOCs. For each redox-active oligomer, we calculated the average number



of ACN molecules as a function of distance from the molecule's Van der Waals surface (Fig. 6.2) and found that the ROM solvation shells do not change significantly at different SOCs. This implies that membranes that are blocking to active-materials at one SOC will also block their crossover as the battery is cycled and the SOC changes. Furthermore, ACN molecules in the solvation shell are only weakly associated with the ROMs, and the solvation of ROMs in ACN does not lead to significant changes in conformation with respect to isolated geometries. Therefore, the hydrodynamic radii and associated volumes of ROMs were computed from quantum mechanical calculations of isolated clusters. Characteristic sizes for viologen monomer (**1a**), dimer (**2a**) and trimer (**3a**) were 8.8, 12.3, and 16.8 Å, respectively. These results suggest that polymer membranes whose pore dimensions were maintained below 1.2 nm are likely to block the viologen dimer and trimer; considerably smaller pores would be required to sieve the monomer.

6.3 Controlling the active-material crossover rate by manipulating molecular size

To validate the theoretical predictions of a critical size-regime for ROM-blocking, we synthesized the viologen-based ROM monomer (**1a**, 84%), dimer (**2a**, 80%), and trimer (**3a**, 69%) by a simple displacement reaction involving *N*-ethyl-4,4'-bipyridinium hexafluorophosphate and benzyl bromide, 1,3-bis(bromomethyl)benzene, and 1,3,5-tris(bromomethyl)benzene, respectively. Cyclic voltammetry of each compound showed that **1a**, **2a**, and **3a** are reversibly reduced at -0.75 V *vs.* Ag/Ag⁺ (Fig. 6.10, Table 6.3). This low reduction potential along with the high solubility of each species in ACN is promising for their use as energy dense anolytes in all-organic redox flow batteries.^[37]

The crossover behavior for each RAO/membrane pairing was quantified by measuring the effective diffusion coefficient (D_{eff}) of each ROM or RAO through different membranes (Fig. 6.3, Figs. 6.11–6.12, see section 6.7 for details). Membrane blocking-ability was quantified by comparing each ROM or RAO's diffusion coefficient through the membrane (D_{eff}) to its diffusion coefficient through solution (D_{sol}). For the non-selective Celgard[®] membrane, high values for D_{eff} of $(5.4 \pm 0.4) \times 10^{-7}$, $(3.1 \pm 0.3) \times 10^{-7}$, and $(2.2 \pm 0.2) \times 10^{-7}$ cm² s⁻¹ for **1a**, **2a**, and **3a**, respectively, were measured. These measured values of D_{eff} are only 30-fold lower than D_{sol} for each species, indicating that the blocking-ability of Celgard[®] is equally poor for **1a**, **2a**, and **3a**. PIM-1 membranes, which feature nanometer-sized pores, significantly outperformed Celgard[®], with **1a**, **2a**, and **3a** diffusing through the membrane 1,280, 11,600, and 32,900-fold slower, respectively, than through solution (Fig. 6.3b). This dramatic improvement in membrane blocking-ability upon reducing the pore size from approximately 20 nm to less than 1 nm, along with the improved membrane blocking-ability for larger RAOs, is indicative of size-selective sieving of active-materials. However, our theoretical calculations of the sizes of **2a** and **3a** imply that both should be completely blocked by PIM-1 membranes. We hypothesized that swelling of the PIM-1 membranes in electrolyte increases the average pore size above the 0.9 nm pores present in dry membranes,^[144] thus allowing some crossover of the larger RAOs.

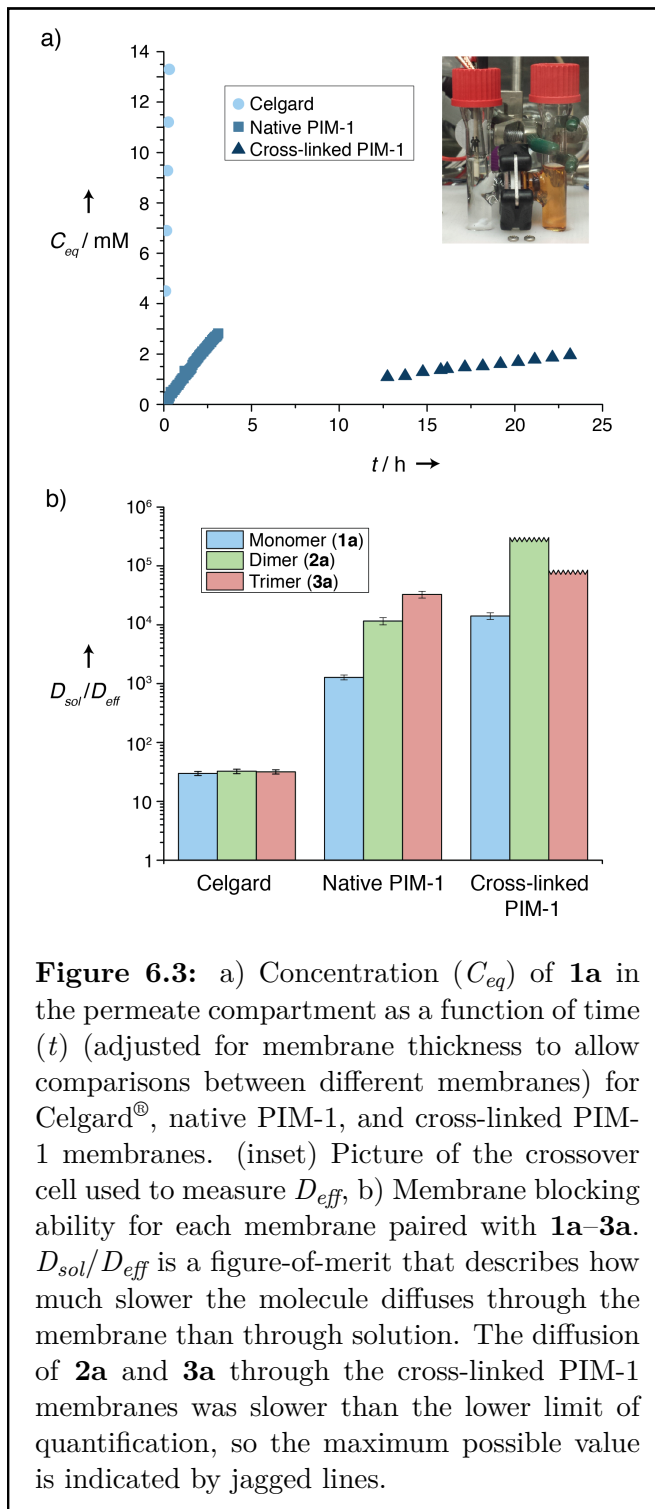


Figure 6.3: a) Concentration (C_{eq}) of **1a** in the permeate compartment as a function of time (t) (adjusted for membrane thickness to allow comparisons between different membranes) for Celgard[®], native PIM-1, and cross-linked PIM-1 membranes. (inset) Picture of the crossover cell used to measure D_{eff} , b) Membrane blocking ability for each membrane paired with **1a–3a**. D_{sol}/D_{eff} is a figure-of-merit that describes how much slower the molecule diffuses through the membrane than through solution. The diffusion of **2a** and **3a** through the cross-linked PIM-1 membranes was slower than the lower limit of quantification, so the maximum possible value is indicated by jagged lines.

6.4 Further improvement in crossover rate by controlling membrane pore size and degree of swelling

By cross-linking PIM-1, the degree of swelling is controllable, and the membrane pore size is further constricted. Cross-linking was accomplished by casting solutions of PIM-1 containing the cross-linking agent 2,6-bis(4-azidobenzylidene)-cyclohexanone. The dry membranes were then heated to 175 °C under vacuum to convert the azide groups of the cross-linking agent to reactive nitrenes, which insert into C-H bonds on the polymer and cross-links the membranes (Fig. 6.13).^[57, 145] Cross-linked PIM-1 membranes exhibited the best active-species blocking-ability observed to date, with **1a** diffusing through the membrane 14,200-fold slower than through solution, and **2a** and **3a** diffusing slower than the limit of quantification (297,000 and 85,000-fold slower, respectively, than through solution). This unprecedented 9,000-fold improvement in blocking ability (with respect to Celgard[®]) came at minimal cost to ionic conductivity, with cross-linked PIM-1 membranes only 5-fold less conductive than Celgard (0.4 *vs.* 2.2 mS cm⁻¹, see Fig. 6.14).

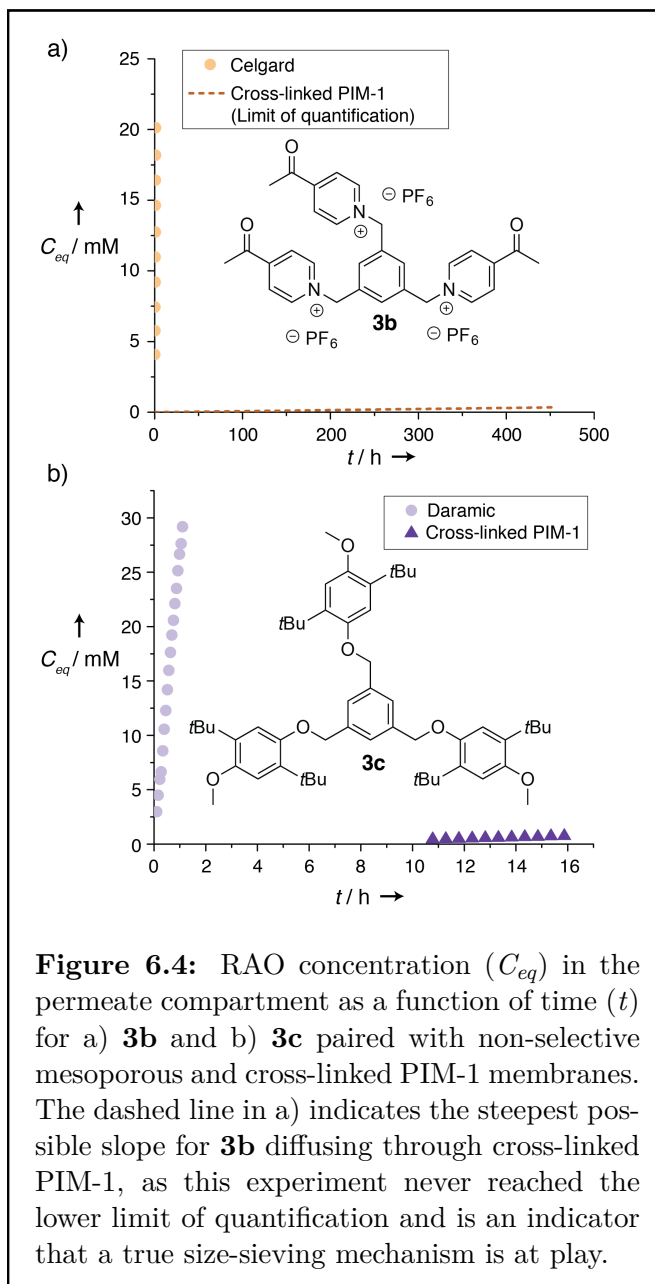


Figure 6.4: RAO concentration (C_{eq}) in the permeate compartment as a function of time (t) for a) **3b** and b) **3c** paired with non-selective mesoporous and cross-linked PIM-1 membranes. The dashed line in a) indicates the steepest possible slope for **3b** diffusing through cross-linked PIM-1, as this experiment never reached the lower limit of quantification and is an indicator that a true size-sieving mechanism is at play.

6.5 Oligomerization as a generalizable strategy

To demonstrate that oligomerization is a generalizable approach to blocking ROM crossover in all-organic non-aqueous redox flow batteries, we synthesized trimeric RAOs based on acylpyridinium hexafluorophosphate (**3b**, 89%) and DB3 (**3c**, 90%) redox-active pendant groups. Monomeric forms of these RAOs have been identified as promising candidates for non-aqueous redox-flow batteries, although their crossover through the battery membrane remains an issue.^[38, 39] Consistent with these reports, cyclic voltammetry showed evidence for reversible reduction of **3b** at -1.40 V *vs.* Ag/Ag⁺ in 0.1 M TBAPF₆/propylene carbonate. Likewise, **3c** underwent reversible oxidation at 0.56 V *vs.* Ag/Ag⁺ in 0.1 M TBAPF₆/dimethoxyethane. Both **3b** and **3c** were blocked by cross-linked PIM-1 membranes, with **3b** diffusing through the membrane slower than the lower limit of quantification of 1.0×10^{-11} cm² s⁻¹ and **3c** diffusing through the membrane with $D_{eff} = (8.1 \pm 0.7) \times 10^{-10}$ cm² s⁻¹ (Fig. 6.4). This corresponds to 6,800 and 460-fold improvements in the crossover rate of **3b** and **3c**, respectively, when compared to their diffusion through non-selective mesoporous separators. Clearly, oligomerization provides a straightforward path to preparing a wide variety of RAOs that are effectively blocked by microporous polymer membranes.

6.6 Conclusions and future work

Macromolecular design of both membranes and active-species is a powerful approach for solving the crossover problem in all-organic redox-flow batteries. Here I showed how computational chemistry informs the design space for ROM oligomers, or RAOs, and that by pairing RAOs with RAO-blocking microporous PIM membranes, active material crossover is reduced by nearly four orders of magnitude with respect to commercially available battery separators with negligible decreases in ionic conductivity. ROM oligomerization was demonstrated for several redox-active motifs, including those that serve as either negative or positive electrode materials in redox-flow batteries. In all cases, RAO crossover was effectively blocked when constituted as flowable electrodes in a variety of battery solvents, including acetonitrile, propylene carbonate, and 1,2-dimethoxyethane. These promising results point the way forward towards the design of new classes of RAOs and membranes for all-organic redox-flow batteries, along with their incorporation in next-generation redox-flow battery prototypes.

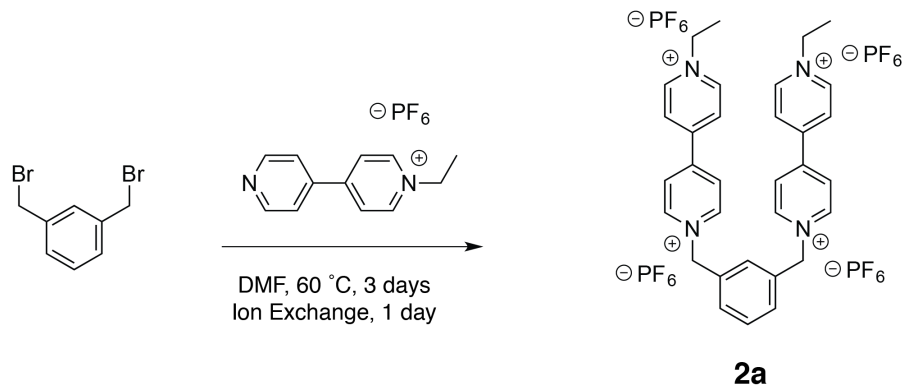
6.7 Supporting information

6.7.1 Materials and methods

For experiments with ROM and RAOs **1a–3a**, electrolyte refers to 0.1 M LiPF₆ in acetonitrile. For experiments with RAOs **3b** or **3c**, electrolyte refers to 0.1 M tetrabutylammonium hexafluorophosphate in propylene carbonate or 1,2-dimethoxyethane, respectively. *N*-ethyl-4,4'-bipyridinium hexafluorophosphate and viologen monomer (**1a**) were synthesized using reported protocols.^[235]

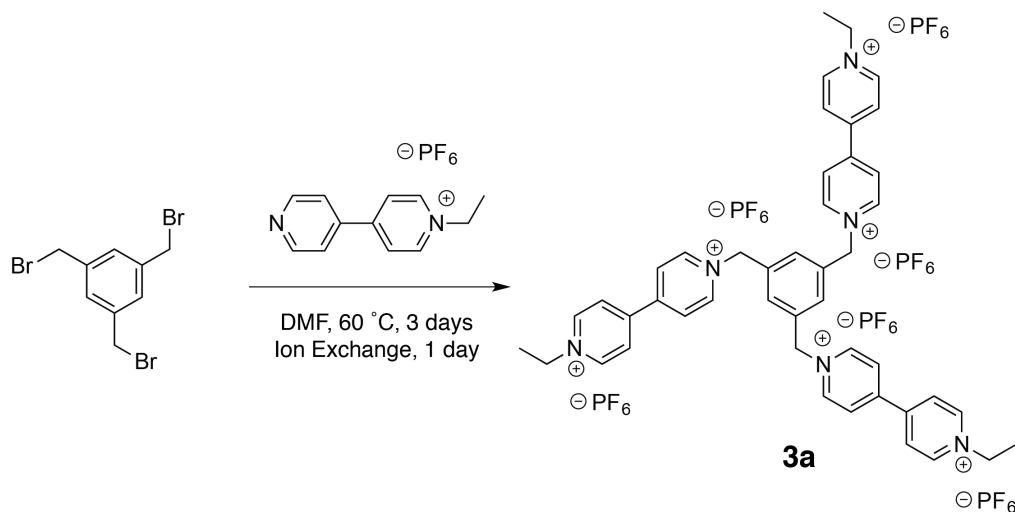
Synthesis of *N*-ethyl-4,4'-bipyridinium hexafluorophosphate

N-ethyl-4,4'-bipyridinium hexafluorophosphate was synthesized as described previously.^[235] Briefly, ethyl iodide (5.12 mL, 64.0 mmol, 1.0 equiv) was added to a solution of 4,4-bipyridine (10.0 g, 64.0 mmol, 1.0 equiv) in DCM (50 mL). As the reaction progressed, an orange solid precipitated from solution. The mixture was stirred for 24 h at RT, and additional orange solid was precipitated from solution by adding diethyl ether. The solid was isolated by filtration and rinsed with DCM/ether (1:1 *v/v*). The solid was then dissolved in a minimum volume of water and ammonium hexafluorophosphate (53.0 g, 325 mmol, 5.0 equiv) was added portion-wise. As ammonium hexafluorophosphate was added, a beige solid precipitated out of solution. The resulting mixture was stirred for 24 h, and the solid was isolated by filtration, followed by rinsing with water, methanol, and ether. The resulting solid was dried under vacuum for 24 h to yield *N*-ethyl-4,4'-bipyridinium hexafluorophosphate (6.27 g, 30% yield, 2 steps) as a beige solid.

Scheme 6.1: Synthesis of **2a**

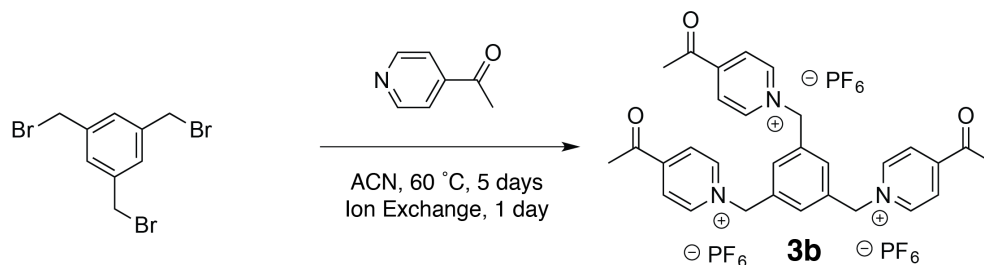
Synthesis of viologen dimer (**2a**)

1,3-Bis(bromomethyl)benzene (2.5 g, 9.47 mmol, 1.0 equiv) was reacted with *N*-Ethyl-4,4'-bipyridinium hexafluorophosphate (12.5 g, 37.9 mmol, 4 equiv) in DMF. The solution was then allowed to reach 60 °C and stirred at this temperature for 3 days. Solids precipitated out as the reaction progressed. The mixture was added to diethyl ether, and the solids filtered and rinsed with additional diethyl ether. The solids were then dissolved in a minimal amount of acetonitrile/water (1:4, *v/v*) and ammonium hexafluorophosphate (10 equiv) in a minimal amount of water was added portion wise. The resulting mixture was stirred for 24 h. Acetonitrile was removed under reduced pressure and water was added to the mixture to further precipitate out the solid. The solid was filtered out and rinsed with water, methanol, and diethyl ether. The product was dried under vacuum for 24 h to yield the viologen dimer, **2a** (8.0 g, 80%, 2 steps) as a white powder. ¹H NMR (500 MHz, CD₃CN) δ=8.96 – 8.91 (m, 8H), 8.41 – 8.38 (m, 8H), 7.61 – 7.60 (m, 4H), 5.84 (s, 4H), 4.68 (q, *J* = 7.5 Hz, 4H), 1.65 ppm (t, *J* = 5 Hz, 6H); ¹³C NMR (125 MHz, CD₃CN) δ=151.7, 150.9, 146.8, 146.5 (t, *J* = 8.1 Hz), 146.4, 134.9, 131.9, 131.8, 131.5, 128.5, 128.3, 65.2, 58.8, 16.6 ppm; HRMS (ESI-TOF): *m/z* for C₃₂H₃₄F₁₈N₄P₃ (M-PF₆)⁺ calculated 909.1709, found 909.1667.

Scheme 6.2: Synthesis of **3a**

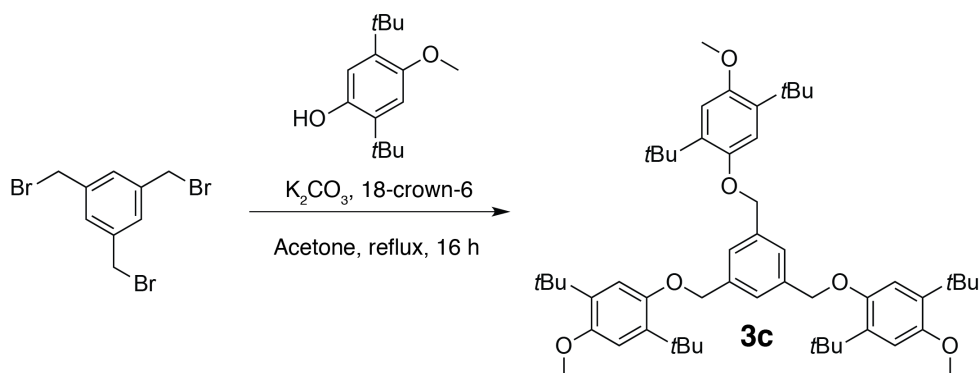
Synthesis of viologen trimer (**3a**)

1,3,5-tris(bromomethyl)benzene (3.37 g, 9.46 mmol, 1.0 equiv) was reacted with *N*-ethyl-4,4'-bipyridinium hexafluorophosphate (10.0 g, 30.28 mmol, 3.2 equiv) in DMF. The solution was then allowed to reach 60 °C and stirred at this temperature for 3 days. Solid precipitated out as the reaction progressed. The mixture was added to diethyl ether, and the solid was filtered out and rinsed with additional diethyl ether. The solid was then dissolved in a minimal amount of acetonitrile/water (1:4, *v/v*) and ammonium hexafluorophosphate (10 equiv) in a minimal amount of water was added portion wise. The resulting mixture was stirred for 24 h. Acetonitrile was removed under reduced pressure and water was added to the mixture to further precipitate out the solid. The solid was filtered out and rinsed with water, methanol, and diethyl ether. The solid was dried under vacuum for 24 h to yield the viologen trimer, **3a** (10.3 g, 69%, 2 steps) as a white powder. ^1H NMR (500 MHz, CD_3CN) δ = 8.92 (d, J = 10 Hz, 12H), 8.41 – 8.37 (m, 12H), 7.67 (s, 3H), 5.84 (s, 6H), 4.68 (q, J = 7.5 Hz, 6H), (t, J = 7.5 Hz, 9H) 1.65 ppm; $^{13}\text{C}\{^1\text{H}\}$ NMR (125 MHz, CD_3CN) δ = 152.0, 151.0, 147.0, 146.6, 136.2, 133.1, 128.7, 128.4, 64.9, 59.0, 16.8 ppm; HRMS (ESI): m/z for $\text{C}_{45}\text{H}_{48}\text{N}_6\text{PF}_6^{5+}$ ($\text{M} - 5\text{PF}_6^-$) $^{5+}$ calculated 163.4711, found 163.4710; m/z for $\text{C}_{45}\text{H}_{48}\text{N}_6\text{P}_2\text{F}_{12}^{4+}$ ($\text{M} - 4\text{PF}_6^-$) $^{4+}$ calculated 240.5801, found 240.5798; m/z for $\text{C}_{45}\text{H}_{48}\text{N}_6\text{P}_3\text{F}_{18}^{3+}$ ($\text{M} - 3\text{PF}_6^-$) $^{3+}$ calculated 369.0950, found 369.0945; Anal. Calc'd for $\text{C}_{45}\text{H}_{48}\text{N}_6\text{P}_6\text{F}_{36}$: C, 35.04; H, 3.14; N, 5.45; Found: C, 34.92; H, 3.21; N, 5.34.

Scheme 6.3: Synthesis of **3b**

Synthesis of acylpyridinium trimer (**3b**)

4-Acetylpyridine (10.0 g, 83 mmol, 4.0 equiv) was added to a solution of 1,3,5-tris(bromomethyl)benzene (7.4 g, 21 mmol, 1.0 equiv) in acetonitrile (100 mL). The solution was stirred at 60 °C for 5 days. A precipitate formed, and was filtered and rinsed with diethyl ether. The solid was then dissolved in acetonitrile and water, and ammonium hexafluorophosphate (21.0 g, 130 mmol, 6.2 equiv) was added. The mixture was stirred overnight. Acetonitrile was removed under reduced pressure, and the solid was filtered off, dissolved in a minimal amount of acetonitrile, and precipitated by adding excess water with vigorous stirring. This process was repeated once more, followed by rinsing the solid with methanol (2 \times) and diethyl ether. The product was dried overnight to yield 17 g of the acylpyridinium trimer, **3b** (89%, over 2 steps). Further purification of **3b** was carried out by dissolving the crude mixture in a minimal amount of acetonitrile and then filtering away the dark-colored solids. Water was added to the filtrate and the mixture was cooled at 4 °C to precipitate **3b** as a tan solid, which was isolated by filtration. The product was washed with methanol (50 mL) and diethyl ether (50 mL) before drying in vacuo. ^1H NMR (500 MHz, $\text{DMSO-}d_6$) δ =9.28 (d, J = 7 Hz, 6H), 8.55 (d, J = 7 Hz, 6H), 7.62 (s, 3H), 5.90 (s, 6H), 2.76 (s, 9H) ppm; $^{13}\text{C}\{^1\text{H}\}$ NMR (125 MHz, $\text{DMSO-}d_6$) δ =160.6, 149.0, 146.6, 135.8, 126.4, 62.8, 27.4 ppm; HRMS (ESI): m/z for $\text{C}_{30}\text{H}_{30}\text{O}_3\text{N}_3^{3+}$ ($\text{M} - 3\text{PF}_6^-$) $^{3+}$ calculated 160.0757, found 160.0755; m/z for $\text{C}_{30}\text{H}_{30}\text{O}_3\text{N}_3\text{PF}_6^{2+}$ ($\text{M} - 2\text{PF}_6^-$) $^{2+}$ calculated 312.5959, found 312.5955; m/z for $\text{C}_{30}\text{H}_{30}\text{O}_3\text{N}_3\text{P}_2\text{F}_{12}^+$ ($\text{M} - \text{PF}_6^-$) $^+$ calculated 770.1565, found 770.1554; Anal. Calc'd for $\text{C}_{30}\text{H}_{30}\text{P}_3\text{F}_{18}\text{N}_3\text{O}_3$: C, 39.36; H, 3.30; N, 4.59; Found: C, 39.23; H, 3.48; N, 4.49.

Scheme 6.4: Synthesis of **3c**

Synthesis of DB3 trimer (**3c**)

To a solution of 2,5-di-*tert*-butyl-4-methoxyphenol (7.80 g, 33 mmol), 1,3,5-tris(bromomethyl)benzene (3.57 g, 10 mmol), and 18-crown-6 (871 mg, 1.0 mmol) in acetone (50 mL) was added freshly pulverized, oven-dried potassium carbonate (6.83 g, 49.5 mmol) while stirring vigorously. The reaction mixture was heated at reflux for 16 h, cooled, and then the solids filtered; the solids were then washed with dichloromethane (3×50 mL). The filtrate was concentrated in vacuo. The crude product was dissolved in diethyl ether (150 mL), which was then extracted with aqueous sodium hydroxide (15% *w/w*) (3×50 mL), water (1×50 mL), and brine (1×50 mL). The ethereal layer was dried over magnesium sulfate, which was removed by filtration. After concentrating the ethereal layer in vacuo, the product was recrystallized from ethanol/dichloromethane to yield **3c** as colorless needles (7.44 g, 90%). 1H NMR (500 MHz, $CDCl_3$) δ =7.52 (s, 3H), 6.89 (s, 3H), 6.85 (s, 3H), 5.10 (s, 6H), 3.81 (s, 9H), 1.37 (s, 27H), 1.32 (s, 27H) ppm; $^{13}C\{^1H\}$ NMR (125 MHz, $CDCl_3$), δ =152.4, 151.3, 138.9, 136.8, 136.5, 125.8, 113.1, 111.9, 71.4, 56.1, 34.9, 34.8, 30.2, 30.0 ppm; HRMS (ESI): *m/z* for $C_{54}H_{78}O_6^+$ (M) $^+$ calculated 822.5793, found 822.5792; Anal. Calc'd for $C_{54}H_{78}O_6$: C, 78.79; H, 9.55; Found: C, 78.81; H, 9.60.

Synthesis of PIM-1

PIM-1 with molecular weight, $M_W = 386$ kg mol $^{-1}$ ($M_N = 136$ kg mol $^{-1}$, PDI= 2.8) was synthesized as described elsewhere.^[56, 57, 179] Briefly, a mixture of anhydrous potassium carbonate (8.3 g, 60 mmol), 3,3,3',3'-tetramethyl-1,1'-spirobisindane-5,5',6,6'-tetrol (6.8 g, 20 mmol) and 2,3,5,6-tetrafluoroterephthalonitrile (4.0 g, 20 mmol) in dry DMF was stirred at 65 °C for 4 d. On cooling, the mixture was added to water and the crude product collected by filtration. Repeated precipitations from a concentrated solution of polymer in chloroform into methanol yielded 8.90 g (19.3 mmol, 97% yield) of the fluorescent yellow polymer (PIM-1).

Membrane preparation

PIM-1 was dissolved in chloroform at a concentration of 12.5 mg mL⁻¹. PIM-1 membranes were cast by depositing 1 mL of solution into 3.5 cm diameter Teflon wells. The solvent was left to evaporate under an evaporation dish under ambient pressure for 5 h or until dryness. The films were further dried in vacuo overnight. Crosslinked PIM-1 membranes were prepared by adding 0.1 molar equivalents of 2,6-bis(4-azidobenzylidene)-cyclohexanone to the casting solution. Once dried, the crosslinked films were activated by heating in a vacuum oven at 175 °C for 7.5 h. The dried films were used as cast and Celgard[®] 2325 membranes were punched into 1 and 3/16 inch circles. All membranes were soaked in electrolyte overnight before use.

6.7.2 Computational methods

Computational methodology

The systematic study of solvation structures of ROMs at different states of charge was performed in two steps. In the first step, the quantum mechanical study of small molecular clusters (isolated molecules) of ROMs (**1a**, **2a**, **3a**), ACN and PF₆⁻ at $T=0$ K was carried out. First, we calculated the optimal molecular configurations of the ROMs with and without counter-ions and solvent (ACN) molecules. Next we evaluated charge distributions, and performed HOMO/LUMO orbital analysis (Figures 6.5–6.7). The effects of the finite temperature and condensed liquid phase on the ROMs solvation in ACN were accounted for by the use of classical MD. Generalized Amber force fields^[241] (GAFF) were used for solute and solvent molecules as well as for counter-ions. GAFF charges on nitrogen atoms underestimate the effects of the polarity of the ROM molecules. The comparison between the GAFF charge scheme and the charges obtained from ab initio is shown in Tables 6.1–6.2. In our simulations we used GAFF force field parameters in combination with Mulliken partial charges derived from ab initio calculations for the optimized geometry of ROMs. The free energy profiles were computed using the metadynamics technique.^[242, 243] For the study of solvated structures of ROMs/ACN we calculated pair radial distribution functions (rdf) obtained with an algorithm adapted for non-spherical objects. Instead of taking the center of the mass of the ROM molecule as a reference point for rdf, the algorithm explicitly evaluates the distribution of distances from each atom of the ROM molecule to the solvent molecules (center of the mass of ACN or a particular atom in the solvent molecule, e.g., N) and averages them over the MD trajectory.

Quantum chemistry calculations

Optimized geometries, relative energies, and molecular orbitals were calculated with the DFT TeraChem package.^[244] As suggested in the previous extensive computational studies of aprotic ionic liquids, for ROMs/ACN systems in our calculations we used B3LYP5-D3 functional with the 6-311++G** basis set^[245] in combination with the third

version of Grimme’s empirical dispersion correction.^[191] We used the L-BFGS geometry optimization method^[246] with the termination criterion for the maximum energy gradient component of 4.5×10^{-4} au. Wave function convergence threshold was set as 3.0×10^{-5} . Two-electron integral threshold was set as 1.0×10^{-12} , and the basis set linear dependency threshold was of 1.0×10^{-4} . Partial charges were computed using the full NBO and Mulliken analysis. For the open shell molecules unrestricted Kohn-Sham orbitals were computed.

Molecular dynamics calculations

Classical molecular dynamics (MD) simulations were conducted on the solutions (ROMs in ACN)—with PF_6^- ions added accordingly to attain zero total charge—using the LAMMPS simulation package.^[247] Long-range electrostatic interactions were treated within the particle-mesh Ewald (PME) method with a cutoff distance 1.0 nm with grid spacing in k -space of 10^{-5} . A cut-off of 1.0 nm with a spline from 0.9 to 1.0 nm was used for Lennard-Jones interactions. The relaxation of the initial structures was performed in two steps, first using steepest descent with a convergence criterion of 10^{-4} kcal mol⁻¹ for energies and 10^{-4} kcal mol⁻¹ Å⁻¹ for forces. The systems were first heated to 298 K in the canonical ensemble (NVT). To remove any “memory” effects, the systems were first melted at 400 K and then annealed back to 298 K three times (with 2 ns each step). Then, isothermal-isobaric (NPT, $P=1$ atm, $T=298$ K) simulations were performed for 2 ns (2 fs time step) to obtain the correct density using a Nose/Hoover temperature thermostat and Nose/Hoover pressure barostat.^[248, 249] Afterwards, the NVT simulations were performed ($T=298$ K) for 1 ns (2 fs time step) to equilibrate and sample the properties of interest. Structural properties were obtained from 10 ns MD simulation runs with an integration time step 1 fs in NVT ensemble. We ran several parallel simulations of solvated **1a**, **2a** and **3a** at different concentrations. For **1a**, $C_{ROM}=0.03$ –0.1 M with a box size of $4 \times 4 \times 4$ nm. For **2a**, $C_{ROM}=0.02$ –0.1 M with a box size of $6 \times 6 \times 6$ nm. For **3a**, $C_{ROM}=0.01$ –0.05 M with a box size of $8 \times 8 \times 8$ nm.

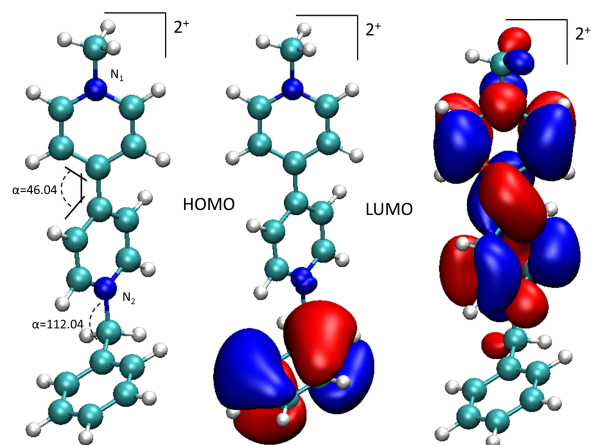


Figure 6.5: Viologen monomer (**1a**) at 2+ state of charge and optimal configurations of its HOMO and LUMO orbitals.

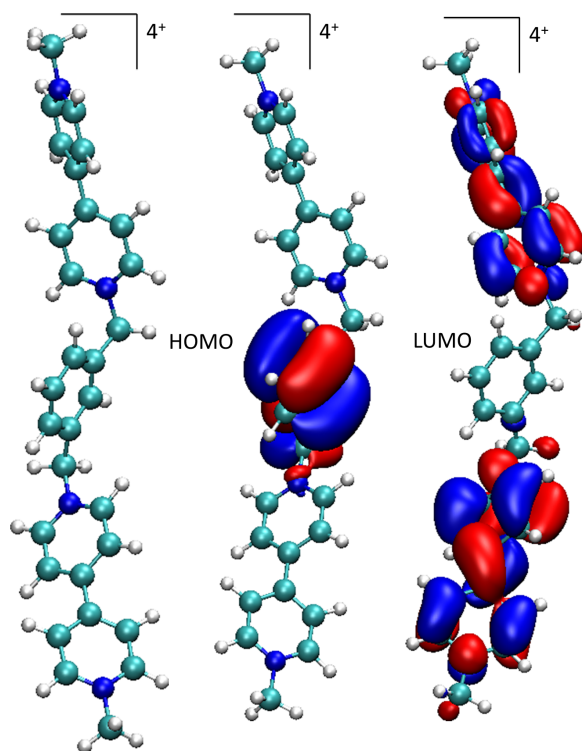


Figure 6.6: Viologen dimer (**2a**) at 4+ state of charge and optimal configurations of its HOMO and LUMO orbitals.

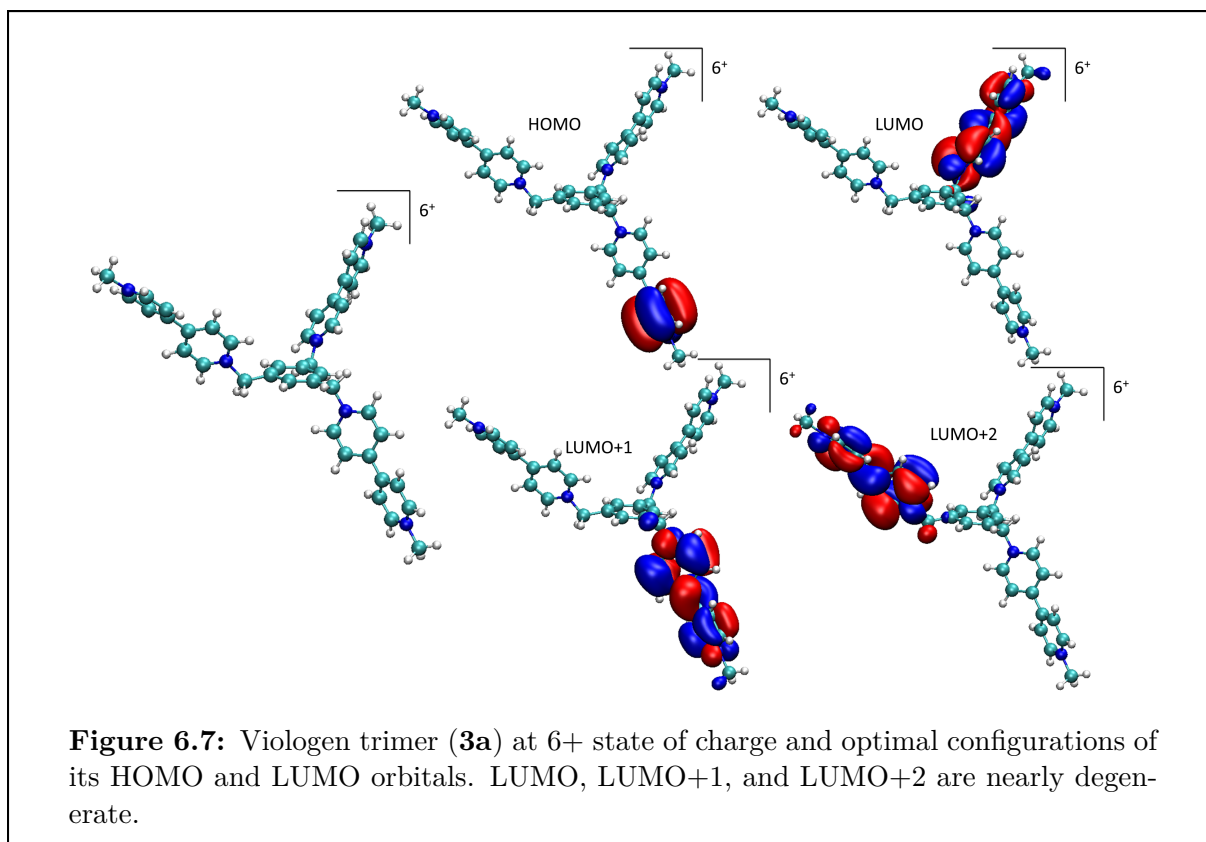


Table 6.1: Comparison between two charge schemes: GAFF *vs.* Mulliken charges from ab initio DFT calculations: **1a** at two different states of charge

GAFF		Mulliken		
1a¹⁺	1a²⁺	1a¹⁺	1a²⁺	
-0.086	-0.015	-0.085	-0.138	C
-0.216	-0.232	-0.167	-0.123	C
0.053	0.083	0.073	0.042	C
-0.206	-0.219	-0.167	-0.123	C
-0.115	-0.067	-0.085	-0.014	C
0.211	0.193	0.026	0.055	N
0.187	0.234	0.174	0.229	H
0.121	0.233	0.161	0.203	H
0.124	0.231	0.161	0.203	H
0.188	0.237	0.174	0.229	H
-0.141	-0.118	-0.026	-0.016	C
-0.205	-0.2	-0.208	-0.125	C
0.048	0.049	0.065	0.023	C
-0.177	-0.177	-0.208	-0.125	C
-0.188	-0.175	-0.026	-0.016	C
0.305	0.296	0.091	0.055	N
0.2	0.234	0.145	0.232	H
0.129	0.217	0.166	0.198	H
0.129	0.219	0.166	0.198	H
0.193	0.277	0.145	0.232	H
-0.29	-0.256	-0.124	0.0546	C
0.228	0.275	0.114	0.112	H
0.139	0.182	0.114	0.112	H
0.0085	-0.095	0.0222	-0.2	C
-0.097	-0.094	-0.074	-0.101	C
-0.152	-0.138	-0.129	-0.119	C
-0.125	-0.132	-0.148	-0.069	C
-0.136	-0.134	-0.129	-0.119	C
-0.133	-0.11	-0.074	-0.101	C
0.134	0.145	0.161	0.141	H
0.173	0.204	-0.128	0.166	H
0.174	0.201	0.555	0.169	H
0.174	0.193	-0.128	0.166	H
0.131	0.144	0.161	0.141	H
-0.347	-0.352	0.0089	-0.042	C
0.218	0.232	0.074	0.116	H
0.186	0.252	0.074	0.116	H
0.161	0.181	0.744	0.116	H

Table 6.2: Comparison between two charge schemes: GAFF *vs.* Mulliken charges from ab initio DFT calculations: acetonitrile and PF_6^-

Mulliken	GAFF	
ACN	ACN	
0.206	0.2087	C
-0.438	-0.376	N
-0.29	-0.05	C
0.1734	0.0707	H
0.1734	0.0707	H
0.1734	0.0707	H
PF₆ (1-)	PF₆ (1-)	
0.6483	1.2416	P
-0.275	-0.374	F
-0.275	-0.374	F
-0.275	-0.374	F
-0.275	-0.374	F
-0.275	-0.374	F
-0.275	-0.374	F

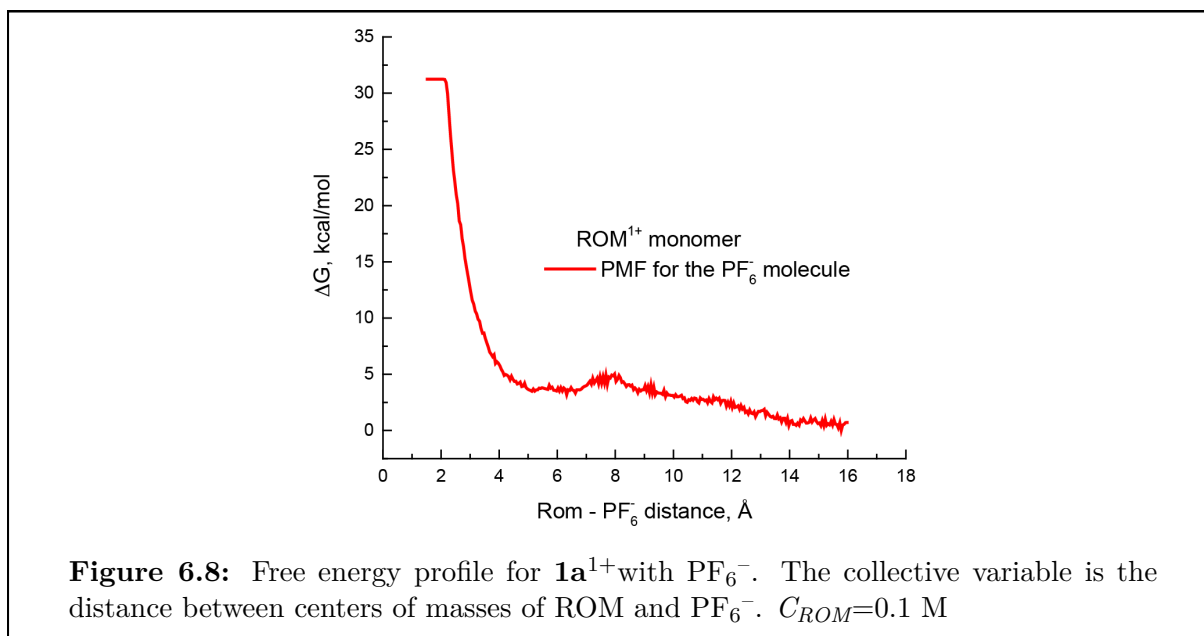


Figure 6.8: Free energy profile for $\mathbf{1a}^{1+}$ with PF_6^- . The collective variable is the distance between centers of masses of ROM and PF_6^- . $C_{ROM}=0.1$ M

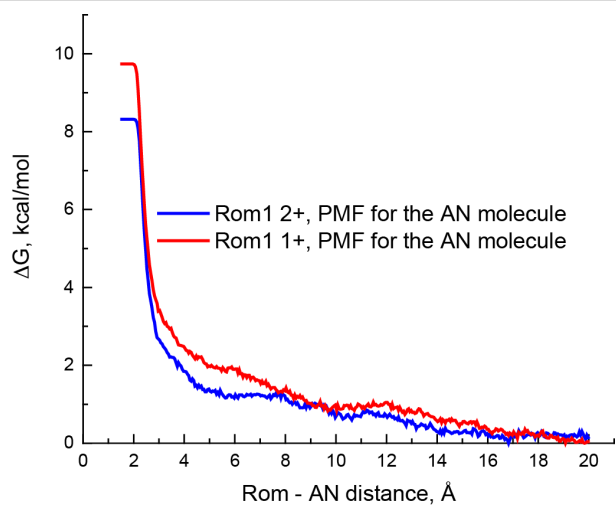


Figure 6.9: Free energy profiles for $1\mathbf{a}^{1+}$ and $1\mathbf{a}^{2+}$ with ACN. The collective variable is the distance between centers of masses of ROM and ACN. $C_{ROM}=0.1$ M

6.7.3 Electrochemical properties of ROM and RAOs

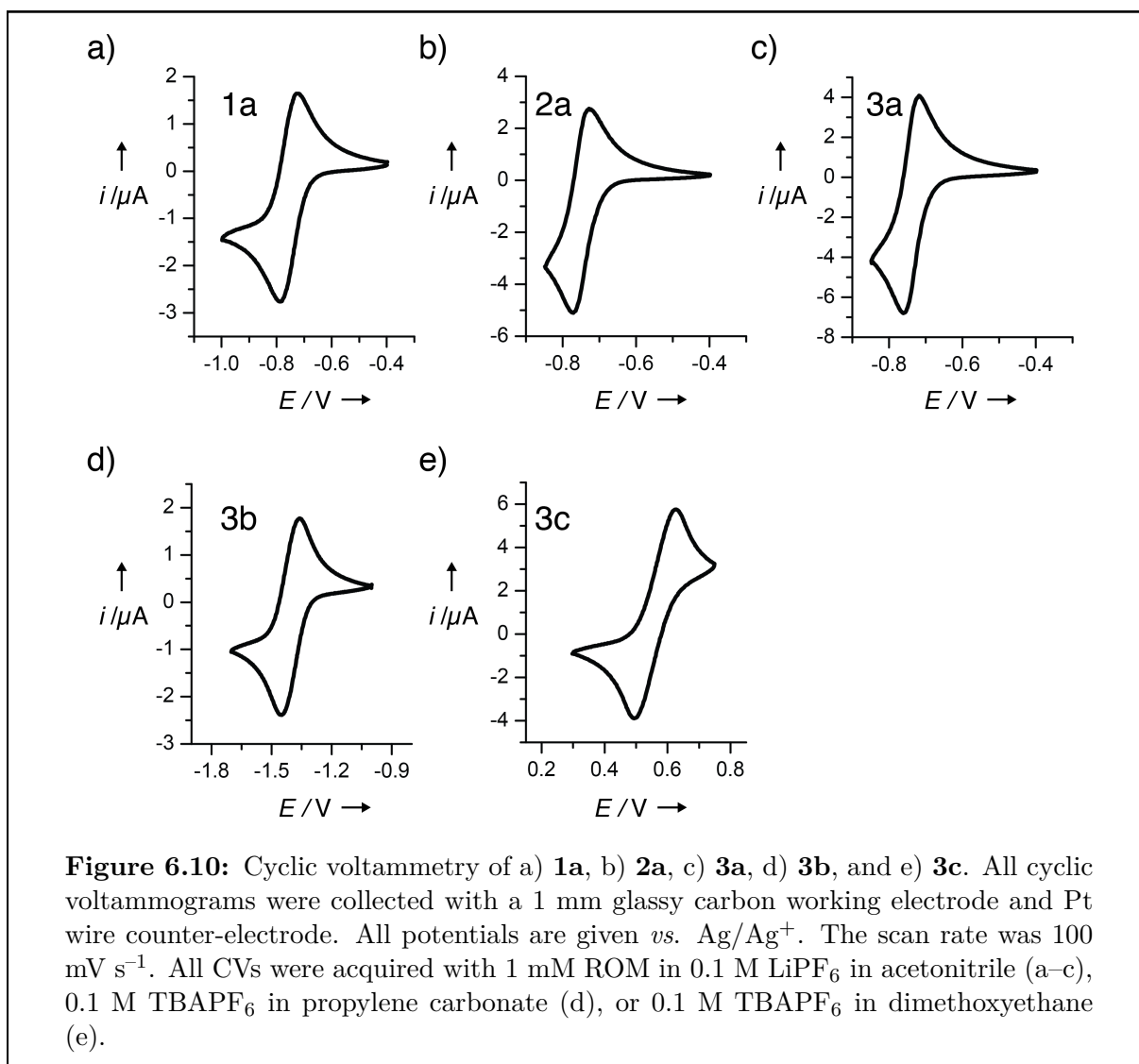


Table 6.3: Redox potentials of ROM and RAOs **1a–3c** calculated from CVs acquired with: $C_{\text{ROM}}=1 \text{ mM}$ and $\nu = 100 \text{ mV s}^{-1}$

Molecule	Electrolyte	$E_{1/2}$ (V <i>vs.</i> Ag/Ag^+)	ΔE_p (mV)
Viologen monomer (1a)	0.1 M LiPF_6 in ACN	-0.756	58
Viologen dimer (2a)	0.1 M LiPF_6 in ACN	-0.752	38
Viologen trimer (3a)	0.1 M LiPF_6 in ACN	-0.742	39
Acylpyridinium trimer (3b)	0.1 M TBAPF_6 in PC	-1.404	88
DB3 trimer (3c)	0.1 M TBAPF_6 in DME	0.562	124

6.7.4 Crossover measurements and analysis

A membrane of known thickness (typically 10–25 μm) was placed between two halves of an H-cell with an aperture diameter of 1.6 cm and sealed in place with a chemically resistant O-ring. One half of the H-cell (the retentate) was charged with 10 mL of 0.100 M ROM monomer (**1a**), 0.050 M dimer (**2a**), or 0.033 M trimer (**3a**, **3b**, or **3c**) in electrolyte, while the other half (the permeate) was charged with the same volume of electrolyte with no ROM (or RAO). For viologen-based ROM and RAOs (**1a–3a**), the salt concentration in the permeate was increased to 0.250, 0.225, and 0.215 M for the monomer, dimer, and trimer experiments, respectively, in order to minimize the initial osmotic pressure difference between the two compartments. Similarly, for acylpyridinium trimer **3b**, the salt concentration in the permeate was increased to 0.166 M. Both compartments were stirred to ensure homogeneity. Every 5–60 min, the stirring was stopped and the concentration of ROM or RAO in the permeate was measured electrochemically by acquiring a CV at 100 mV s^{-1} from -0.40 to -0.85 V (for **1a**, **2a**, and **3a**), -1.00 to -1.70 V (for **3b**), or 0.30 to 0.75 V (for **3c**) *vs.* Ag/Ag^+ . The peak cathodic (for **1a**, **2a**, **3a**, and **3b**) or anodic (for **3c**) current was related to ROM concentration with a calibration curve (Fig. 6.11 and Table 6.4). Equivalent concentration (C_{eq}) refers to the concentration of ROM or RAO that would be observed with a 10 μm membrane and $C_0 = 0.1$ M. This allows for easier visual comparison of crossover experiments performed with different membrane thicknesses

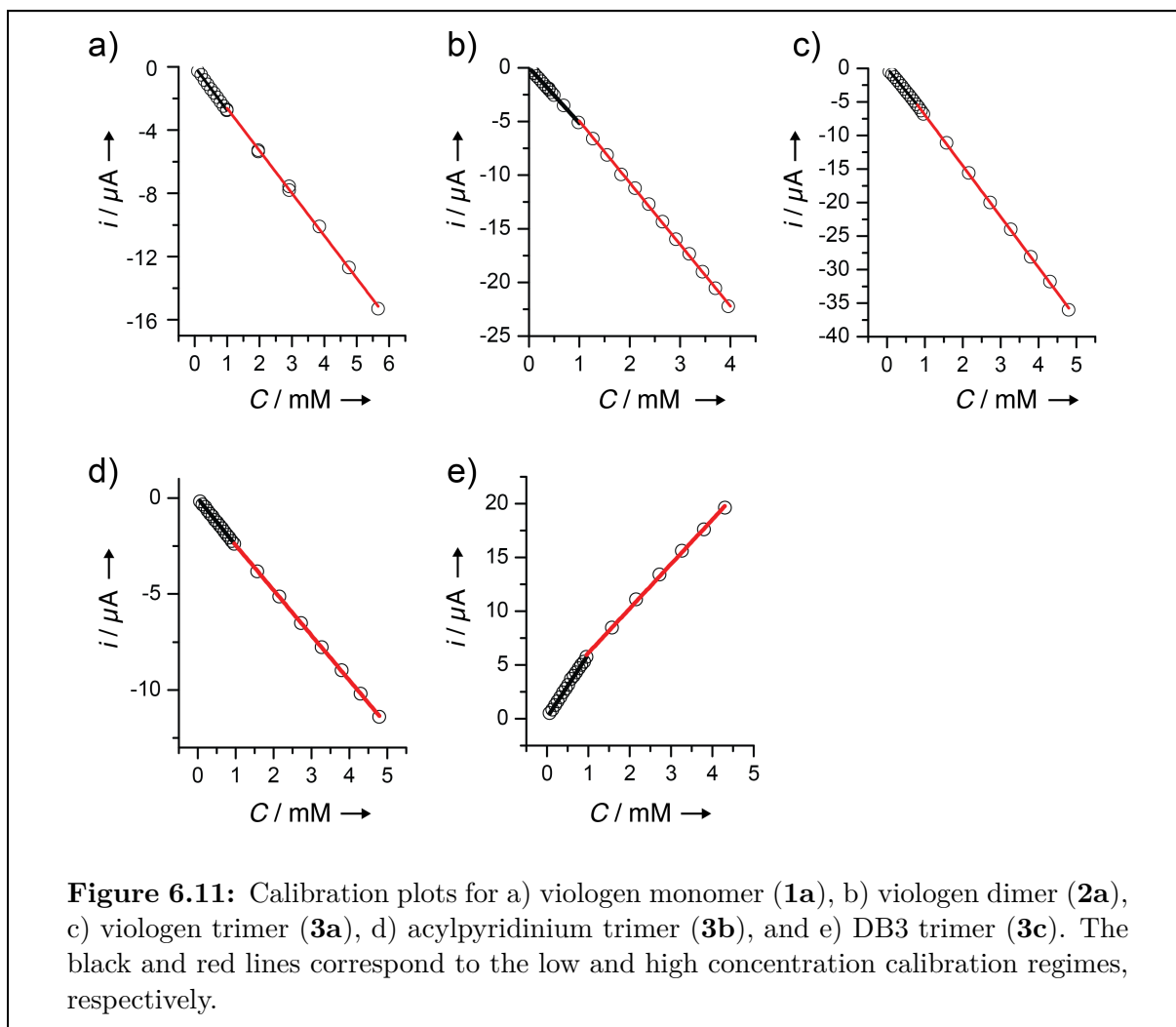


Table 6.4: Calibration curve parameters and fitting errors for each viologen ROM and RAO

Molecule	Slope (mA/mM)	Intercept (mM)	R ²
Viologen-based ROM and RAOs			
1a (low conc.)	$(-2.77 \pm 0.02) \times 10^{-3}$	$(0 \pm 2) \times 10^{-5}$	0.9993
1a (high conc.)	$(-2.69 \pm 0.05) \times 10^{-3}$	$(0 \pm 2) \times 10^{-4}$	0.9986
2a (low conc.)	$(-5.18 \pm 0.04) \times 10^{-3}$	$(2 \pm 2) \times 10^{-5}$	0.9992
2a (high conc.)	$(-5.76 \pm 0.05) \times 10^{-3}$	$(8 \pm 2) \times 10^{-4}$	0.9992
3a (low conc.)	$(-6.85 \pm 0.06) \times 10^{-3}$	$(2 \pm 3) \times 10^{-5}$	0.9993
3a (high conc.)	$(-7.57 \pm 0.04) \times 10^{-3}$	$(6 \pm 1) \times 10^{-4}$	0.9998
Acylpyridinium-based RAOs			
3b (low conc.)	$(-2.46 \pm 0.02) \times 10^{-3}$	$(-1 \pm 1) \times 10^{-5}$	0.9994
3b (high conc.)	$(-2.34 \pm 0.01) \times 10^{-3}$	$(-11 \pm 3) \times 10^{-5}$	0.9999
DB3-based RAOs			
3c (low conc.)	$(5.89 \pm 0.06) \times 10^{-3}$	$(10 \pm 3) \times 10^{-5}$	0.9988
3c (high conc.)	$(4.14 \pm 0.05) \times 10^{-3}$	$(20 \pm 2) \times 10^{-4}$	0.9991

Limit of quantification

As the salt concentration between the retentate and permeate equalizes, an osmotic pressure difference builds between the two compartments. This induces osmotic flow of solvent from the permeate into the retentate, thus rendering measurements after this time invalid due to competing convection and diffusion in opposite directions. In acetonitrile, this solvent movement was never observed for times < 36 hours, so the lower limit of quantification for D_{eff} is set by this time and the minimum quantifiable ROM concentration. In propylene carbonate, this solvent movement wasn't observed even after 1 week, so the lower limit of quantification for D_{eff} is set by the duration of the experiment.

Summary of crossover measurements

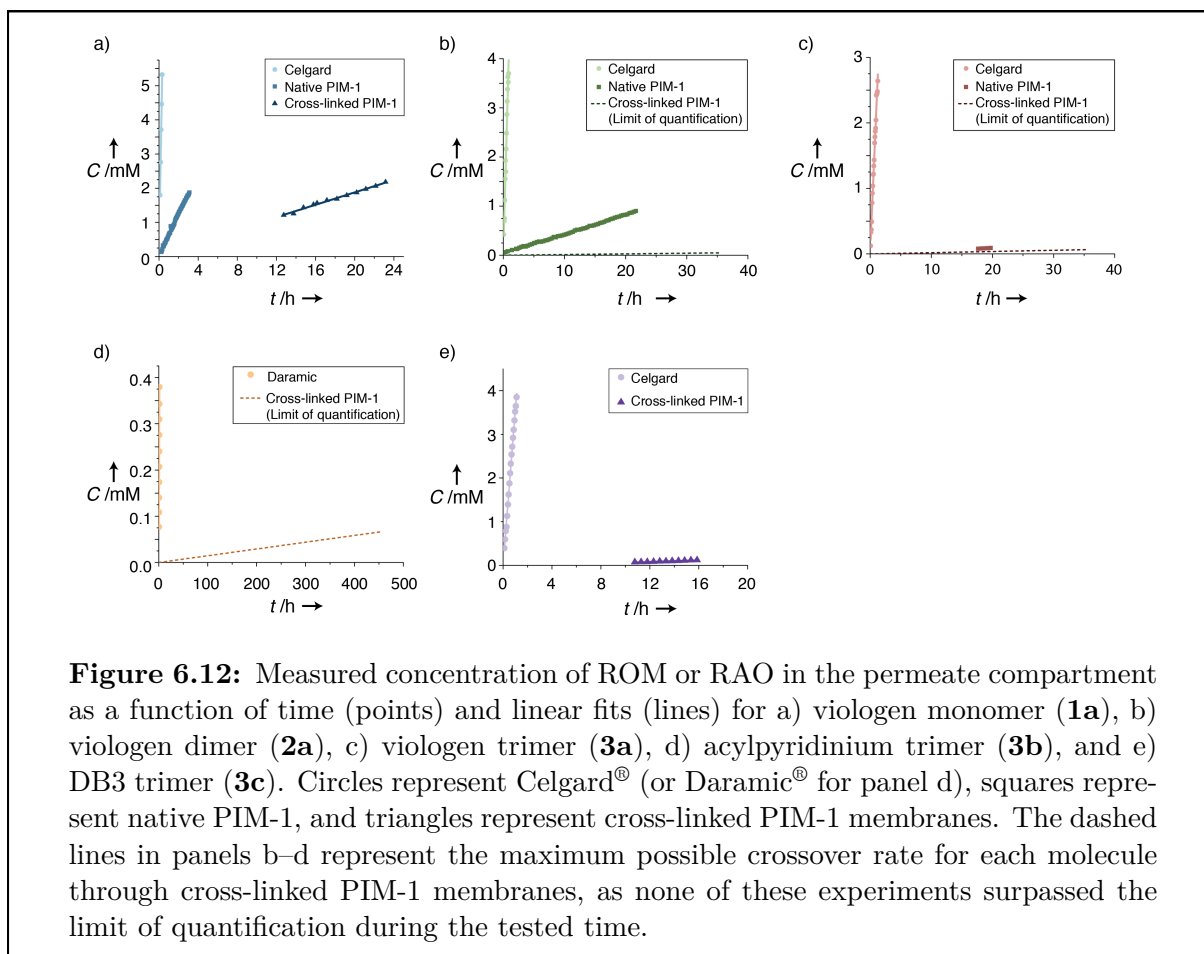


Table 6.5: Measured values for D_{eff} (in $\text{cm}^2 \text{s}^{-1}$) for all membrane/ROM pairings. * indicates that D_{eff} was below the limit of quantification, so the reported value is an upper-bound for D_{eff} . † indicates that the measurement was performed with Daramic[®] instead of Celgard[®] due to poor wetting of Celgard[®] with propylene carbonate.

	Celgard	Native PIM-1	Cross-linked PIM-1
Viologen-based ROM and RAOs			
Monomer (1a)	$(5.4 \pm 0.4) \times 10^{-7}$	$(1.3 \pm 0.1) \times 10^{-8}$	$(1.1 \pm 0.1) \times 10^{-9}$
Dimer (2a)	$(3.1 \pm 0.3) \times 10^{-7}$	$(9 \pm 1) \times 10^{-10}$	3.4×10^{-11} *
Trimer (3a)	$(2.2 \pm 0.2) \times 10^{-7}$	$(2.1 \pm 0.3) \times 10^{-10}$	8.4×10^{-11} *
Acylpyridinium-based RAOs			
Trimer (3b)	$(2.6 \pm 0.2) \times 10^{-7}$ †	–	1.0×10^{-11} *
DB3-based RAOs			
Trimer (3c)	$(3.7 \pm 0.3) \times 10^{-7}$	–	$(8.1 \pm 0.7) \times 10^{-10}$

Calculation of D_{sol} for viologen ROM and RAOs 1a–3a

The size and shape of viologen monomer (**1a**), dimer (**2a**), and trimer (**3a**) can be described by the smallest oblate spheroid that encompasses all of the atoms in each relaxed chemical structure. The predicted diffusion coefficient (D_{sol}) of these spheroids can be calculated using a modified form of the Stokes-Einstein equation^[250] that takes into account the non-spherical shape of these molecules, as well as the ratio between solute and solvent size:

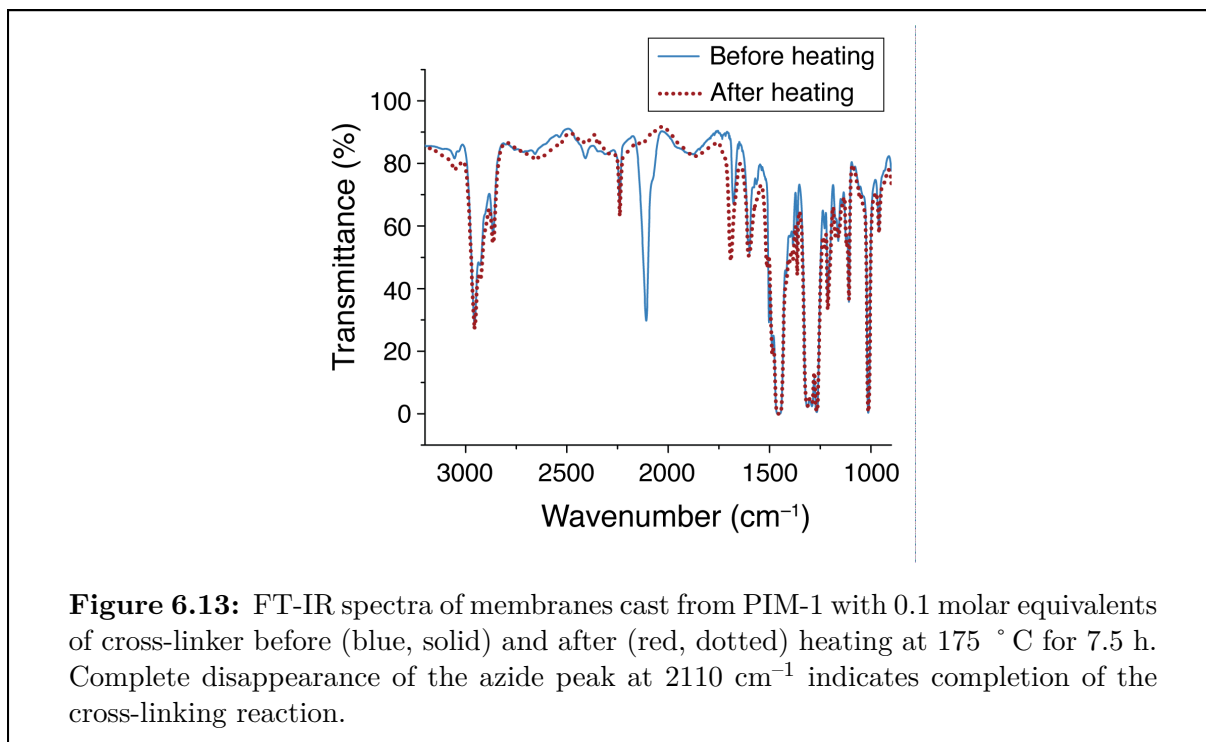
$$D_{sol} = \frac{kT}{c(r_{sol}, r_H) f_s(a, b) \pi \eta r_H}$$

where D_{sol} is the molecule's diffusion coefficient in solution in $\text{m}^2 \text{s}^{-1}$, k is the Boltzmann constant, T is the temperature in K, $c(r_{sol}, r_H)$ is a correction factor for molecules that are similar in size to the solvent,^[251] $f_s(a, b)$ is a correction factor for non-spherical molecules,^[252] η is the solvent's viscosity in Poise, and r_H is the molecule's hydrodynamic radius in m. For large, spherical molecules, the product $cf_s = 6$, yielding the Stokes-Einstein equation.

Table 6.6: Dimensions and volume of the oblate spheroids that encompass the calculated structures of **1a**, **2a**, and **3a**, along with the calculated Stokes-Einstein (assuming spherical shape and small solvent size) and modified Stokes-Einstein (using the known shape and solvent size) diffusion coefficients in acetonitrile.

Species	a axis (Å)	c axis (Å)	Volume (Å ³)	Stokes- Einstein D_{sol} (cm ² s ⁻¹)	Modified Stokes- Einstein D_{sol} (cm ² s ⁻¹)
Monomer (1a)	3.75	6	353.4	1.5×10^{-5}	1.6×10^{-5}
Dimer (2a)	4.38	12.25	984.4	1.0×10^{-5}	1.0×10^{-5}
Trimer (3a)	12.25	3.94	2476.6	7.6×10^{-6}	7.1×10^{-5}

6.7.5 Characterization of cross-linked PIM-1 membranes



6.7.6 Membrane ionic conductivity

Membrane ionic conductivity was measured as described in section B.2 using electrochemical impedance spectroscopy.

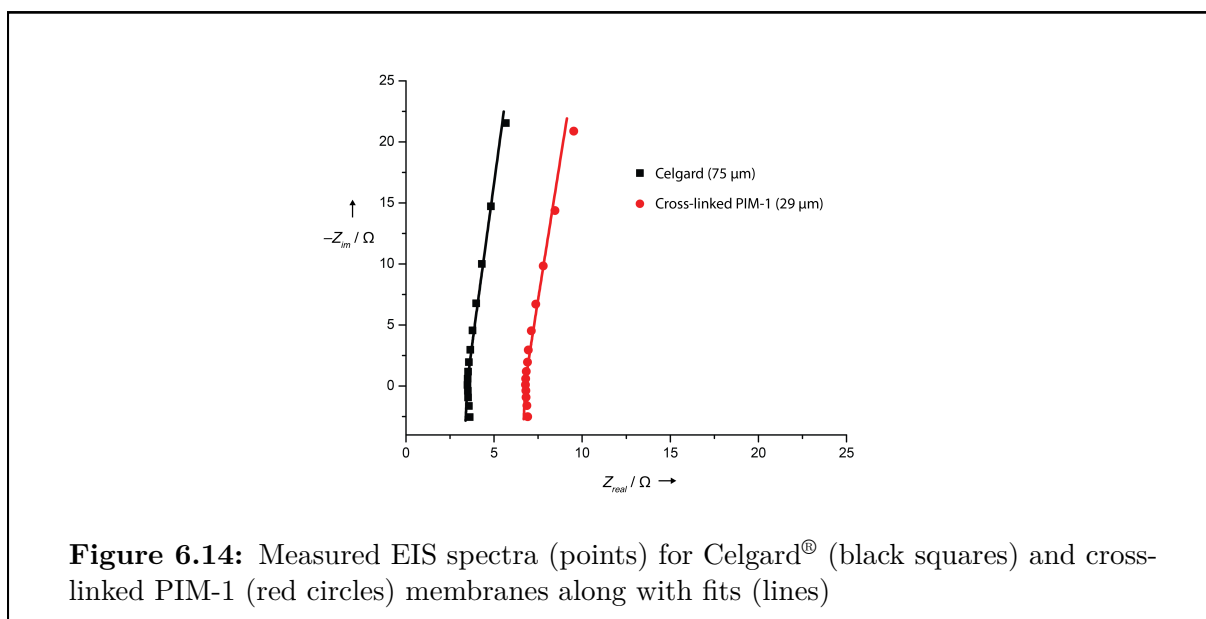


Table 6.7: Fitting parameters for EIS spectra

Membrane	Membrane Thickness (μm)	Q_{DL} ($\text{Fs}^{\alpha-1}$) [α]	Q_M ($\text{Fs}^{\alpha-1}$) [α]	R_M (Ω)	σ (mS cm^{-1})
Celgard [®] (3 \times)	75	11.9×10^{-6} [0.94]	35.5×10^{-9} [1.00]	3.086	2.15
Cross-linked PIM-1 (3 \times)	29	13.3×10^{-6} [0.93]	10.5×10^{-9} [1.00]	6.371	0.40

6.7.7 Acknowledgements

This chapter is the result of a collaboration between myself, A.L. Ward, A. Baskin, P.D. Frischmann, N. Gavvalapalli, E. Chénard, C.S. Sevov, D. Prendergast, J.S. Moore, and B.A. Helms, and I am thankful to all my co-authors for their help with this work. We thank C. Li and L. Maserati for samples of PIM-1. We thank D. Loudermilk from the UIUC School of Chemical Sciences Graphic Services Facility for assistance in the preparation of Fig. 1. A.L.W., A.B., P.D.F., N.G., E.C., C.S.S., D.P., J.S.M., and B.A.H. were supported by the Joint Center for Energy Storage Research, an Energy Innovation Hub funded by the U.S. Department of Energy, Office of Science, Office of Basic Energy Sciences. S.E.D. was supported by the Department of Defense through the National Defense Science and Engineering Graduate Fellowship program. Portions of this work, including polymer synthesis and characterization, crossover measurements, and electrochemical experiments were carried out as user projects at the Molecular Foundry, which is supported by the Office of Science, Office of Basic Energy Sciences of the U.S. Department of Energy under contract no. DE-AC02-05CH11231. The computational portion of this work was supported by a user project at the Molecular Foundry and its computer cluster (Vulcan), managed by the High Performance Computing Services Group at Lawrence Berkeley National Laboratory (LBNL), and by the computing resources of the National Energy Research Scientific Computing Center, LBNL, both of which are supported by the Office of Science of the U.S. Department of Energy under Contract DE-AC02-05CH11231.

Chapter 7

Supramolecular Perylene Bisimide-Polysulfide Gel Networks as Nanostructured Redox Mediators in Dissolved Polysulfide Lithium-Sulfur Batteries

Reproduced with permission from *Chem. Mater.* **2015**, *27*(19), 6765–6770. Copyright 2015 American Chemical Society.

7.1 Introduction and prior art

A renaissance in electrochemical energy storage is underway, fueled both by demand and by the burgeoning field of nanotechnology.^[30, 253] Within this context, organic and polymeric nanomaterials are gaining prominence for their ability to impart novel functions in energy storage devices including self-healing character,^[254] overcharge protection,^[255] and adaptive charge transport.^[256] The modular character and the precision with which they can be prepared continue to advance our understanding of structure-property relationships in polymer electrolytes,^[257, 258] ion-selective membranes and separators,^[141, 259] charge-storage materials,^[235, 260–264] and binders.^[256] Enhancing charge transport in devices by exerting control over component architectures across multiple length scales remains an outstanding challenge in the field. Here we advance supramolecular design principles^[265–267] for the programmed self-assembly of π -conjugated molecules that enable us to coassemble molecular redox mediators and charge-storing inorganic materials into flowable, redox-active 3-D gels. To showcase our nanostructured redox mediator concept, I have investigated the charge-transporting properties of these soft supramolecular gels in lithium-sulfur (Li-S) batteries (Figure 7.1a). Related organogels composed of molecular semiconductors assembled into nanofiber morphologies^[268–270] have shown interesting properties for electrical conductivity,^[271–273] electroluminescence,^[274] colorimetric sensing,^[275] photoinduced charge separation,^[276] light-harvesting,^[277] and photosensitization of H₂-evolving catalysts.^[278] Nonetheless, the application of organic π -gelators in electrochemical energy storage is unexplored.

My focus on Li-S batteries as a test-bed for this concept is tied to their potential to deliver low-cost, energy-dense storage that is scalable for both transportation and grid-scale applications.^[33] Nevertheless, persistent hurdles to commercialization of Li-S batteries remain. For example, a well-known polysulfide (PS) shuttle reaction, where soluble Li₂S_{*n*} (*n* = 4, 6, and 8) cross the separator and react with the Li-metal anode, contributes to a short cycle life.^[279, 280] Creative solutions addressing PS crossover in solid-state Li-S secondary cells have focused on trapping PS within nanostructured scaffolds.^[35, 36, 281–283] In parallel, interest in dissolved PS catholytes is rapidly growing,^[284–287] where high PS solubility and fast reaction kinetics are advantageous to battery performance. The discovery of LiNO₃ as an anode protecting additive^[163, 288] has allowed sulfur catholyte formulations to be optimized for flow battery architectures; for example, the electronic charge transport and sulfur utilization are greatly enhanced using nano-carbon (e.g., Ketjen-black) suspensions as embedded current collectors, which increase the effective surface area of the electrode.^[180, 182]

To understand the factors influencing rate performance and sulfur utilization in Li-S cells employing flowable sulfur catholytes, I turned my attention to redox mediators,^[289] and in particular to π -conjugated organic molecules, which can be tailored to lower barrier heights for charge transfer across electrolyte-current collector interfaces. Inspired by the dynamic reconfigurability of the Ketjen-black suspensions in facilitating charge transport in those catholytes, I hypothesized that redox mediators would likewise benefit from a 3-D

networked architecture in the electrolyte, which would allow charge transport to proceed via self-exchange along the supramolecular assemblies (i.e., via a hopping mechanism). My success in this regard lays new foundations for designing flowable electrodes with adaptive charge-transporting and charge-storing properties. These characteristics are desirable for redox flow battery applications (i.e., long-duration, grid-scale energy storage), where the rheology of the network is subject to molecular-level control and where the network can self-heal when disrupted during intermittent flow pulses.^[290] Depending on the redox chemistry of the mediator, there are further opportunities to halt electron transport at the voltage extrema used to cycle the battery, thereby offering overcharge or overdischarge protection.

7.2 Design criteria of supramolecular redox mediator and electrochemical validation of the high-throughput computational platform

Two principal design criteria were considered in search of a redox-active π -gelator tailored for operation in a Li-S battery: 1) the redox chemistry of the molecular π -gelator needs to match with the charge/discharge potential of a Li-S battery (2.5 V *vs.* Li/Li⁺ for dissolved PS) to enable charge transport during cycling; and 2) to maintain pathways for electronic percolation, the molecular structure of the mediator must provide sustainable non-covalent interactions for nanowire formation at various states of charge that are not disrupted by high salt or PS concentrations.

To accelerate materials discovery with respect to the first design criterion, we developed a high-throughput computational platform to screen π -gelator candidates based on electron affinity (E_{ea}) and ionization potential (E_i).^[60, 61] A mixed density functional theory and polarizable continuum model approach was applied to address geometry optimization, solvation free energy, and electronic energy in a dielectric continuum medium. The screened molecular library spanned several classes of organogelators, and the wide distribution of calculated E_i *vs.* E_{ea} emphasizes the value of the high-throughput platform in streamlining the materials discovery process (Figure 7.1b and Table 7.1).

As a proof of concept demonstration, we focused on the 2.5 V soluble long-chain PS redox couple attributed to $S_8 \rightarrow Li_2S_4$ to avoid complicating phase transformations associated with precipitation of insulating Li_2S .^[279, 280] Precipitation of active material is a well-known driver of capacity fade in redox flow batteries, and increased cycle life and power have been achieved by limiting discharge to the soluble long-chain PS regime.^[285, 286] Of the 85 structures screened (Figures 7.1b and 7.5–7.6), perylene bisimide (PBI) emerged as a leading candidate due to its calculated $E_{ea} = 2.53$ V *vs.* Li/Li⁺ closely matching the S_8/S_4^{2-} redox couple. In addition, PBIs are an established class of n -type semiconductor known for self-assembly into π -stacks, reversible redox chemistry, and synthetic accessibility – all desired features for a supramolecular redox mediator.^[291, 292]

With respect to the second design criterion, PBI **1** was designed and synthesized to serve as a redox mediator capable of assembling into extended supramolecular networks to help facilitate charge transport in soluble PS catholytes (Figure 7.1a, synthetic details found in section 7.6.1). The oligoethylene glycol imide substituents of **1** impart solubility in electrolyte while maintaining a π -surface accessible for π -stacking.

Our high-throughput computational platform predicted an E_{ea} value of 2.47 V *vs.* Li/Li⁺ for a model compound closely related to **1** (PBI **1** in Figure 7.6). We validated the theoretical prediction by measuring cyclic voltammograms of **1** in tetraethylene glycol dimethyl ether (TEGDME) with lithium bis(trifluoromethanesulfonyl)imide (LiTFSI) and LiNO₃ as supporting electrolyte. A reversible redox wave was observed at 2.53 V *vs.* Li/Li⁺ (Figures 7.1c and 7.8), confirming the accuracy of the calculations to within 60 mV and establishing **1** as electrochemically active in the range of soluble PS.

Comparing cyclic voltammograms of **1**, Li₂S₈, and **1** + Li₂S₈ (Figure 7.1c) confirms that **1** serves as a redox mediator for soluble long-chain PS. The two redox waves for Li₂S₈ centered at 2.5 and 2.1 V are attributed to the processes S₈ → S₄²⁻ and S₄²⁻ → S²⁻, respectively.^[160, 293, 294] Introduction of **1** to the Li₂S₈ solution results in a 4-fold increase in current density at the 2.5 V redox wave, roughly twice the summation of the PS and PBI **1** redox couples measured in isolation. This provides evidence that **1** is serving as a redox mediator for increased charge transfer to and from long-chain PS species in solution.

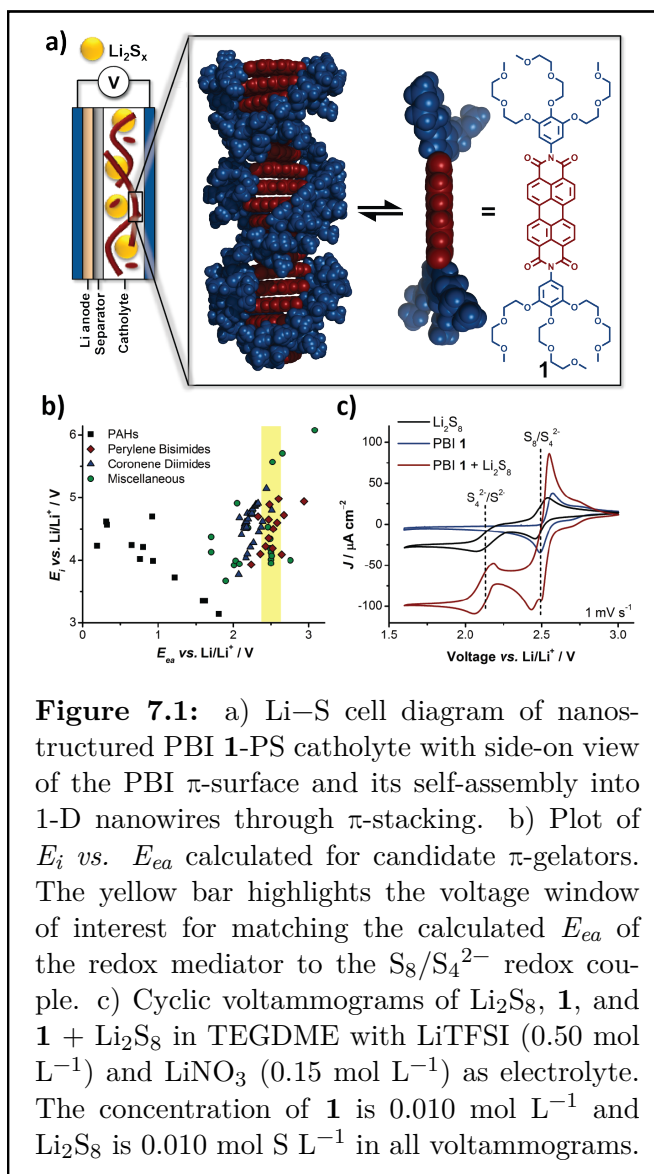


Figure 7.1: a) Li–S cell diagram of nanostructured PBI **1**-PS catholyte with side-on view of the PBI π -surface and its self-assembly into 1-D nanowires through π -stacking. b) Plot of E_i *vs.* E_{ea} calculated for candidate π -gelators. The yellow bar highlights the voltage window of interest for matching the calculated E_{ea} of the redox mediator to the S₈/S₄²⁻ redox couple. c) Cyclic voltammograms of Li₂S₈, **1**, and **1** + Li₂S₈ in TEGDME with LiTFSI (0.50 mol L⁻¹) and LiNO₃ (0.15 mol L⁻¹) as electrolyte. The concentration of **1** is 0.010 mol L⁻¹ and Li₂S₈ is 0.010 mol S L⁻¹ in all voltammograms.

7.3 Characterization of PBI self-assembly and PBI-PS gel morphology

To verify that **1** assembles into nanostructured redox mediators in battery electrolyte, the self-assembly of **1** was studied by UV-vis spectroscopy in TEGDME containing 0.50 mol L^{-1} LiTFSI. PBI **1** exhibited dramatic spectroscopic changes as the concentration was increased from 1.4×10^{-6} to $1.5 \times 10^{-3} \text{ mol L}^{-1}$ due to π -stacking into extended nanowire aggregates (Figure 7.2a).^[291, 292] The increase in optical density above 550 nm with increasing concentration was used to quantify the strength of self-assembly. Fitting the spectroscopic changes to an isodesmic self-assembly model yielded an association constant of $K_a = 6.1 \pm 0.3 \times 10^{-4} \text{ L mol}^{-1}$. From this determination of K_a , number (N) and weight (N_W) average aggregate sizes of 55 and 108, respectively, are calculated for a 0.048 mol L^{-1} solution of **1**. Based on N , N_W , a typical pistacking distance of 0.35 nm, and the 3.1 nm end-to-end length of **1**, an average cylindrical primary aggregate size of 20–40 nm in length by 3 nm in diameter was estimated. Catholyte solutions containing 2.5 mol S L^{-1} as Li_2S_8 and 0.048 mol L^{-1} PBI (5.0% *w/w*) in TEGDME with LiTFSI

(0.50 mol L^{-1}) and LiNO_3 (0.15 mol L^{-1}) were prepared. Despite extensive aggregation of **1** in electrolyte, it remained highly soluble, and no gelation was observed. Within 5 min of mixing **1** with Li_2S_8 a deep purple gel developed and then remained soft but stable to inversion. A picture of Li_2S_8 , **1**, and **1** + Li_2S_8 in electrolyte depicts the unique rheology of the **1** + Li_2S_8 catholyte (Figure 7.2b). The color change distinguishing solutions of **1** from **1** + Li_2S_8 is due to partial PBI reduction by Li_2S_8 . This reduction is fully reversible upon exposure to air, which was tracked by UV-vis spectroscopy (Figure 7.9).

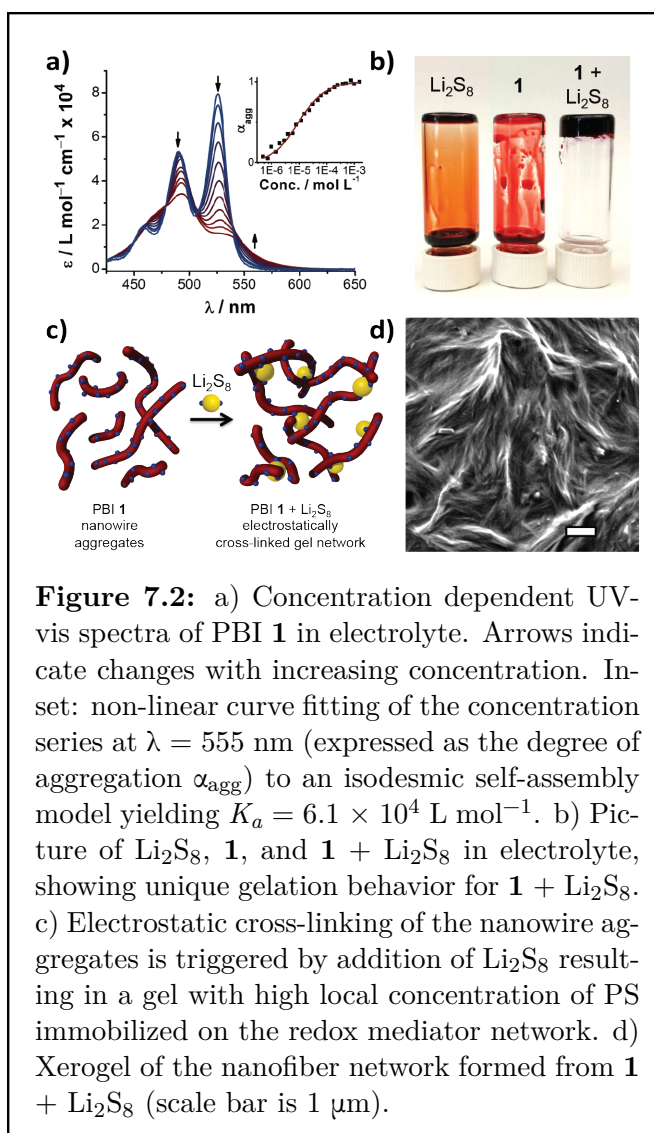


Figure 7.2: a) Concentration dependent UV-vis spectra of PBI **1** in electrolyte. Arrows indicate changes with increasing concentration. Inset: non-linear curve fitting of the concentration series at $\lambda = 555 \text{ nm}$ (expressed as the degree of aggregation α_{agg}) to an isodesmic self-assembly model yielding $K_a = 6.1 \times 10^4 \text{ L mol}^{-1}$. b) Picture of Li_2S_8 , **1**, and **1** + Li_2S_8 in electrolyte, showing unique gelation behavior for **1** + Li_2S_8 . c) Electrostatic cross-linking of the nanowire aggregates is triggered by addition of Li_2S_8 resulting in a gel with high local concentration of PS immobilized on the redox mediator network. d) Xerogel of the nanofiber network formed from **1** + Li_2S_8 (scale bar is $1 \mu\text{m}$).

Our hypothesis for the mechanism of gelation is outlined in Figure 7.2c. PBI **1** exists in electrolyte as long supramolecular nanofibers coated in a Li^+ sheath, where Li^+ interacts with the side chains of **1**. Upon introduction of S_8^{2-} , weakly associated TFSI⁻ counterions are displaced and the divalent PS act as electrostatic cross-links, weaving nanowires of **1** into a continuous fabric (Figure 7.2d). This cross-linking effectively increases the local concentration of active material in contact with the redox mediator network and may facilitate interchain electron transfer between PBI nanowires. To estimate the strength of the cross-linking reaction $2[\mathbf{1}\cdot\text{LiTFSI}] + \text{Li}_2\text{S}_8 \rightleftharpoons [\mathbf{1}\cdot\text{Li}_2\text{S}_8\cdot\mathbf{1}] + 2[\text{LiTFSI}]$ the equilibrium constant was calculated to be $K_{eq} = 64$ using a mixed density functional theory and polarizable continuum model approach (see section 7.6.2 for details). The energetically favorable cross-linking and potential density of cross-linking interactions (roughly 6:1 S_8^{2-} :PBI molar ratio) drives gelation of the PBI-PS network.

The unique nanoscale morphology of **1** + Li_2S_8 was apparent in scanning electron micrographs of dried xerogels, which showed fibrous networks spanning tens of microns (Figures 7.2d and 7.10). Although additional aggregation is expected upon evaporation of solvent, the large association constant, quantified by UV-vis spectroscopy, supports that similar networked assemblies are present prior to solvent evaporation. I anticipated that these networks of redox mediators colocalized with PS would provide new opportunities to mediate charge transfer in Li-S cells.

7.4 Supromolecular redox mediators in Li-S cells

Electrochemical testing of Li-S secondary cells (Swagelok type) was carried out using Li metal anodes, porous polymer separators, and flowable PBI-PS gel catholytes. Cells were galvanostatically cycled from 2.8 to 2.0 V in the $\text{S}_8 \rightarrow \text{S}_4^{2-}$ regime where 1C rate is defined as the reaction of 0.5 equiv of Li^+ with 1 equiv. of sulfur per hour (theoretical capacity of $418 \text{ mAh g}^{-1} \text{ S}$).^[285, 286] The catholyte composition was 2.5 mol S L^{-1} as Li_2S_8 (sulfur loading of 4 mg cm^{-2}) with 5.0% *w/w* PBI **1** when applicable. Charge/discharge curves at a C/8 rate showed a discharge plateau for the $\text{S}_8 \rightarrow \text{S}_8^{2-}$ reaction, followed by a gradual sloping regime for the $\text{S}_8^{2-} \rightarrow \text{S}_4^{2-}$ reaction (Figure 7.3a). Discharge capacities of 267 ± 6 and $193 \pm 11 \text{ mAh g}^{-1} \text{ (S)}$ for **1** + Li_2S_8 and Li_2S_8 , respectively, were measured (Tables 7.2 and 7.3). A 38% increase in sulfur utilization was observed with the nanostructured **1** + Li_2S_8 gel network compared to Li_2S_8 alone. Supramolecular catholyte **1** + Li_2S_8 exhibits a volumetric energy density of 44 Wh L^{-1} , exceeding the industry standard of $25\text{--}40 \text{ Wh L}^{-1}$ observed for advanced aqueous vanadium redox-flow technology.^[295] Although PBI is a known Li-ion storage material,^[296–298] capacities below 5 mAh g^{-1} were measured for **1** in the absence of Li_2S_8 at similar current densities, indicating that **1** does not contribute significantly to the overall capacity.

Enhanced sulfur utilization at C/8, C/4, and C/2 rates was observed for the nanostructured **1** + Li_2S_8 gel catholyte, whereas at 1C rate both catholytes showed nearly equivalent performance. Both catholytes showed rate

tolerance, recovering their initial C/8 rate capacity after cycling at higher current densities up to 1C (Figure 7.3b). Stable cycling with an average 99% capacity retention per cycle was observed for the **1** + Li₂S₈ gel catholyte and Li₂S₈ alone after 20 cycles (Figure 7.3c). Coulombic efficiencies increased with cycle number from 68–81% for **1** + Li₂S₈, and decreasing Coulombic efficiencies of 93–82% were measured for Li₂S₈ alone. Lower Coulombic efficiencies are expected due to increased PS shuttling in the absence of an ion-selective membrane or physical PS trap, especially because the 2.8–2.0 V operating voltage lies mostly in the soluble PS regime. Combining the supramolecular PBI redox mediator network with PS trapping strategies may enable extended cycling studies in the future.

Additional evidence relating these performance improvements with the **1** + Li₂S₈ catholyte gel to increased redox shuttling current was obtained from IV curves of catholyte measured with an interdigitated array electrode by sweeping a 0.5 V bias from the open circuit potential at a scan rate of 20 mV s⁻¹ (Figure 7.3d). Introduction of 10 mol % **1** relative to sulfur resulted in a 300% increase in the shuttling current at a 0.5 V bias for **1** + Li₂S₈ relative to Li₂S₈ alone. The mechanism of charge transport through self-assembled nanofibers is under further investigation; however, we hypothesize that rapid self-exchange of electrons through π -stacks of PBI nanowires, as has been previously reported,^[299] is partially responsible for the increased current. Related self-assembled nanowires of pistacked hexabenzocoronenes have also shown enhanced solution-state electron transport when chemically doped.^[300]

Having successfully demonstrated our proof of concept for a charge-transporting PBI redox mediator network, improved rate performance was further achieved by including conductive carbon cloth (C-cloth) with the dissolved PBI-PS gel catholyte. By analogy to biological vasculature, charge transport in these cells propagates through both arteries and capillaries: that is to say, current travels from the electrode surface through the 8 μ m diameter C-cloth arteries and then is locally distributed to PS by the nanoscale PBI capillary network. Galvanostatic charge/discharge curves are depicted in Figure 7.4a highlighting a clear performance improvement in both capacity and overpotential

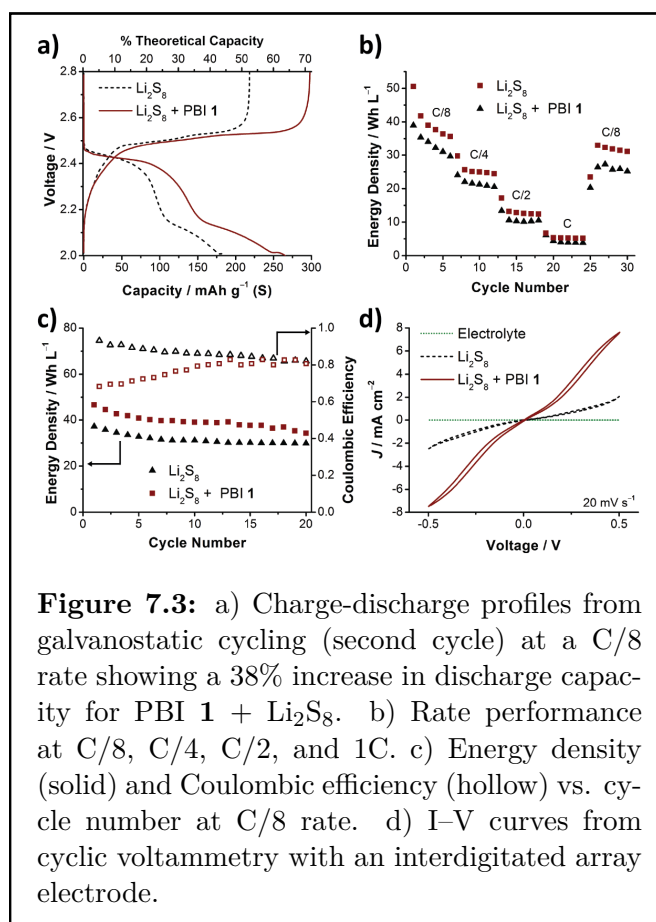


Figure 7.3: a) Charge-discharge profiles from galvanostatic cycling (second cycle) at a C/8 rate showing a 38% increase in discharge capacity for PBI **1** + Li₂S₈. b) Rate performance at C/8, C/4, C/2, and 1C. c) Energy density (solid) and Coulombic efficiency (hollow) vs. cycle number at C/8 rate. d) I-V curves from cyclic voltammetry with an interdigitated array electrode.

for C-cloth + Li_2S_8 + PBI **1** compared to the C-cloth + Li_2S_8 control without redox mediator. Discharge capacities of 328 ± 19 and 250 ± 17 mAh g^{-1} (S) were measured for C-cloth + Li_2S_8 + PBI **1** and C-cloth + Li_2S_8 alone, respectively, representing a 31% increase in sulfur utilization attributed to the redox mediator network.

Interestingly, the arteries and capillaries network exhibits a clear advantage over the control at C/8 and C/4 rates (Figure 7.4b), but at C/2 and 1C rates the trend is reversed. A caveat for this observation relates to the increased viscosity of the PBI-PS gel network impeding ion transport at higher current densities. Higher electrolyte resistance was measured for PBI-PS gel catholytes by electrochemical impedance spectroscopy (EIS) of Li-S cells at open circuit potential, and ionic conductivities of 0.007 S cm^{-1} and 0.02 S cm^{-1} were calculated for PBI-PS gel and PS alone, respectively (Figure 7.11). Because electronic conductivity was rate limiting in the absence of C-cloth, this trend was not observed in Figure 7.3b. Although high power batteries are desired for electric vehicles and frequency regulation, flow batteries are most useful for long duration grid-storage applications like load shifting and peak shaving, where a 48 h discharge time (i.e., at C/4 to C/8 rate) is ideal.

Both C-cloth + Li_2S_8 + PBI **1** and C-cloth + Li_2S_8 alone exhibit a 99% capacity retention per cycle averaged over 120 cycles at C/4 rate as depicted in Figure 7.4c. As in the case of the C-cloth free cells, lower Coulombic efficiency is measured for the catholyte containing PBI redox mediator. The fact that the lower Coulombic efficiency does not contribute to faster capacity fade suggests that the reduced efficiency results from the PBI redox mediator reversibly shuttling charge across the mesoporous separator. A microporous PS and PBI-blocking separator may be applied in the future to minimize shuttling and increase energy efficiency of supramolecular gel network catholytes.^[56]

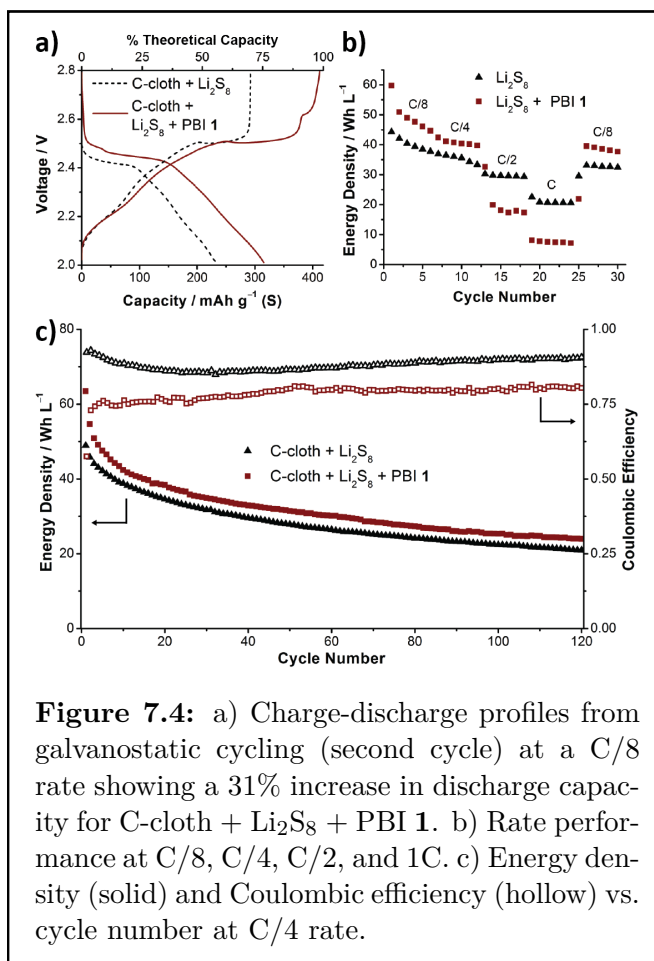


Figure 7.4: a) Charge-discharge profiles from galvanostatic cycling (second cycle) at a C/8 rate showing a 31% increase in discharge capacity for C-cloth + Li_2S_8 + PBI **1**. b) Rate performance at C/8, C/4, C/2, and 1C. c) Energy density (solid) and Coulombic efficiency (hollow) vs. cycle number at C/4 rate.

7.5 Conclusions and future work

In summary, supramolecular gel networks of π -stacked redox mediators improve sulfur utilization and rate performance of Li-S batteries, even in the absence of any conductive carbons. To my knowledge, this discovery is the first demonstration of a nanostructured yet flowable PS-organogel catholyte for electrochemical energy storage. A high-throughput computational platform was developed to rapidly screen candidate π -gelators by E_{ea} and E_i to ensure redox activity at relevant Li-S potentials. PBI was identified as a redox mediator for the soluble PS regime, and a new PBI derivative was designed that self-assembles into nanofiber networks with PS under highly reducing conditions in electrolyte. Even in this early demonstration, these supramolecular gel catholytes deliver a volumetric energy density of 44 Wh L^{-1} at sulfur loadings of 4 mg cm^{-2} . The reconfigurable nature of self-assembled nanowire gels is a promising feature for transitioning this discovery to redox flow architectures for long-duration grid-scale energy storage applications. Efforts to increase order in self-assembled nanowires for rapid charge-transport and tune the chemical potential for operation at the 2.0 V Li_2S precipitation plateau are ongoing.

7.6 Supporting information

7.6.1 Synthetic procedures and characterization

Synthesis of 1,2,3-tris(2-(2-methoxyethoxy)ethoxy)benzene (**2**)

A three-neck flask was charged with pyrogallol (12.3 g, 97.5 mmol), diethylene glycol monomethyl ether tosylate (80.0 g, 292 mmol), 18-crown-6 (7.70 g, 29.2 mmol), and acetone (350 mL). The flask was fit with a reflux condenser, and the solvent was sparged with N₂. After 30 min of sparging, pulverized and oven-dried K₂CO₃ (67.3 g, 487 mmol) was added, and the reaction was heated at 80 °C for 97 h. The beige colored suspension was cooled to room temperature, filtered, and rinsed with acetone. The filtrate was collected, concentrated under vacuum, dissolved in diethyl ether (400 mL), and washed with saturated NaHCO₃ (2 × 200 mL). The organic layer was collected, concentrated under vacuum, and dried under high vacuum to yield **2** as a pale brown oil (28.0 g, 66%). Compound **2** was used without further purification in the following reaction. Analytically pure samples were prepared by column chromatography with *n*-hexane/EtOAc as eluent (SiO₂, 20–100% EtOAc gradient).

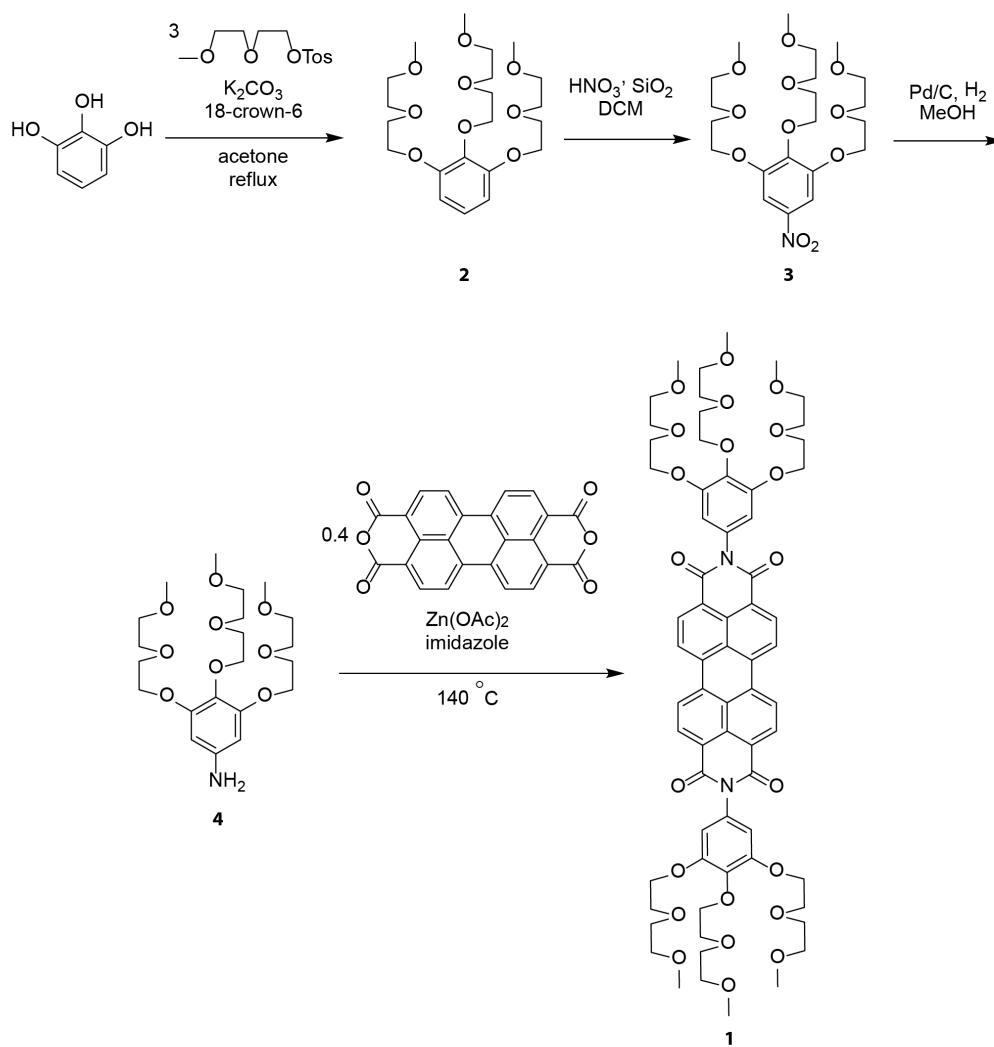
Characterization of **2**

¹H NMR (CDCl₃) δ 6.92 (t, 1H, *J*_{HH} = 7 Hz ArH), 6.58 (d, 2H, *J*_{HH} = 7 Hz, ArH), 4.16 (t, 6H, *J*_{HH} = 5 Hz, OCH₂), 3.86 (t, 4H, *J*_{HH} = 5 Hz, OCH₂), 3.81 (t, 2H, *J*_{HH} = 5 Hz, OCH₂), 3.74–3.71 (m, 6H, OCH₂), 3.57–3.55 (m, 6H, OCH₂), 3.39 (s, 9H, OCH₃); ¹³C{¹H} NMR (CDCl₃) δ 153.0, 138.6, 123.7, 107.9, 72.5, 72.22, 72.15, 70.9, 70.7, 70.6, 69.9, 68.9, 59.25, 59.22; UV/vis (CHCl₃): λ_{max}/nm (ε/L mol⁻¹ cm⁻¹): 269 (700); FT-IR (neat) $\bar{\nu}$ (cm⁻¹) 2933, 2876, 2825, 1594, 1472, 1455, 1355, 1302, 1255, 1199, 1099, 1025, 933, 849; MS (MALDI-TOF, DCTB) *m/z* = 471.17 [**2**+K]⁺, 455.20 [**2**+Na]⁺, 432.21 [**2**]⁺; Anal Calc'd for C₂₁H₃₆O₉: C, 58.32; H, 8.39; Found: C, 58.08; H, 8.49.

Synthesis of 1,2,3-tris(2-(2-methoxyethoxy)ethoxy)-5-nitrobenzene (**3**)

A round bottom flask was charged with **2** (7.86 g, 18.2 mmol) and DCM (50 mL). Upon dissolution of **2**, SiO₂ (8.0 g) was added, and the flask was fit with an addition funnel loaded with HNO₃ (10 mL, 16 mol L⁻¹). HNO₃ was added over 5 min to the stirring suspension of **3** and SiO₂. The deep red suspension was stirred for an additional 15 min then added to a separatory funnel and diluted with 50 mL of H₂O. The bottom organic fraction was collected and carefully washed with saturated NaHCO₃ (2 × 50 mL). The organic layer was then dried with MgSO₄, filtered, concentrated, and subject to column chromatography with DCM/MeOH as eluent (SiO₂, 1–8% MeOH gradient) to yield **3** as a dark yellow oil (2.83 g, 33%).

Scheme 7.1: Synthesis of PBI 1.



Characterization of **3**

^1H NMR (CDCl_3) δ 7.53 (s, 2H, ArH), 4.28 (t, 2H, $J_{\text{HH}} = 5$ Hz, OCH_2), 4.22 (t, 4H, $J_{\text{HH}} = 5$ Hz, OCH_2), 3.71–3.68 (m, 6H, OCH_2), 3.56–3.51 (m, 6H, OCH_2), 3.37 (s, 6H, OCH_3), 3.35 (s, 3H, OCH_3); $^{13}\text{C}\{^1\text{H}\}$ NMR (CDCl_3) δ 152.4, 144.3, 143.3, 103.5, 73.0, 72.21, 72.16, 71.0, 70.8, 70.7, 69.7, 69.4, 59.30, 59.24; UV/vis (CHCl_3): $\lambda_{\text{max}}/\text{nm}$ ($\epsilon/\text{L mol}^{-1} \text{cm}^{-1}$): 326 (6000); FT-IR (neat) $\bar{\nu}(\text{cm}^{-1})$ 2931, 2876, 2822, 1618, 1519, 1492, 1438, 1336, 1319, 1244, 1200, 1098, 1026, 927, 850; MS (MALDI-TOF, DCTB) $m/z = 516.15$ [**3**+K] $^+$, 500.18 [**3**+Na] $^+$; Anal Calc'd for $\text{C}_{21}\text{H}_{35}\text{NO}_{11}$: C, 52.82; H, 7.39; N, 2.93; Found: C, 52.52; H, 7.54; N, 2.92.

Synthesis of **3,4,5-tris(2-(2-methoxyethoxy)ethoxy)aniline (4)**

A round bottom flask was charged with **3** (4.65 g, 9.74 mmol), Pd/C (10% *w/w*, 450 mg), and 50 mL of MeOH. The suspension was evacuated and purged with H_2 three times then allowed to stir under an H_2 atmosphere for 18 h. Filtration of the suspension through Celite followed by concentration under reduced pressure yielded **4** as a brown oil (4.28 g, 98%). Analytically pure samples were prepared by column chromatography with EtOAc/MeOH as eluent (SiO_2 , 0–10% MeOH gradient).

Characterization of **4**

Broadening of the NH_2 protons due to H-bonding prevented their assignment; ^1H NMR (CDCl_3) δ 5.96 (s, 2H, ArH), 4.11 (t, 4H, $J_{\text{HH}} = 5$ Hz, OCH_2), 4.06 (t, 2H, $J_{\text{HH}} = 5$ Hz, OCH_2), 3.84 (t, 4H, $J_{\text{HH}} = 5$ Hz, OCH_2), 3.78 (t, 2H, $J_{\text{HH}} = 5$ Hz, OCH_2), 3.73–3.71 (m, 6H, OCH_2), 3.58–3.55 (m, 6H, OCH_2), 3.39 (s, 9H, OCH_2); $^{13}\text{C}\{^1\text{H}\}$ NMR (CDCl_3) δ 153.4, 142.8, 131.2, 95.5, 72.7, 72.3, 72.2, 70.9, 70.7, 70.6, 69.9, 68.8, 59.29, 59.25; UV/vis (CHCl_3): $\lambda_{\text{max}}/\text{nm}$ ($\epsilon/\text{L mol}^{-1} \text{cm}^{-1}$): 288 (3435), 396 (895); FT-IR (neat) $\bar{\nu}(\text{cm}^{-1})$ 3243, 2927, 2875, 2817, 1607, 1591, 1505, 1448, 1352, 1239, 1199, 1098, 1025, 934, 846; MS (MALDI-TOF, DCTB) $m/z = 486.05$ [**4**+K] $^+$, 470.08 [**4**+Na] $^+$; Anal Calc'd for $\text{C}_{21}\text{H}_{37}\text{NO}_9$: C, 56.36; H, 8.33; N, 3.13; Found: C, 55.98; H, 8.49; N, 3.35.

Synthesis of PBI **1**

A round bottom flask was charged with **4** (1.70 g, 3.84 mmol), 3,4,9,10-perylene tetracarboxylic dianhydride (685 mg, 1.75 mmol), $\text{Zn}(\text{OAc})_2$ (242 mg, 1.75 mmol), and imidazole (25 g). The flask containing the reaction mixture was evacuated and refilled with N_2 three times then heated at 140 °C. After 3 h the reaction was removed from heat, allowed to cool to ~80 °C, and 50 mL of CHCl_3 was carefully added. The deep red solution was poured into a separatory funnel, the volume of CHCl_3 increased to 150 mL, and the organic layer was washed with aqueous HCl (2.0 mol L^{-1} , 2 \times 200 mL). The organic phase was collected, concentrated under vacuum, and purified by column

chromatography with DCM/MeOH as eluent (SiO₂, 0–10% MeOH gradient). PBI **1** was isolated as a deep red solid (1.68 g, 77%).

Characterization of PBI **1**

¹H NMR (CDCl₃) δ 8.50 (br d, 4H, $J_{\text{HH}} = 7$ Hz, ArH), 8.18 (br s, 4H, ArH), 6.69 (s, 4H, ArH), 4.27 (t, 4H, $J_{\text{HH}} = 5$ Hz, OCH₂), 4.10 (bt, 8H, $J_{\text{HH}} = 5$ Hz, OCH₂), 3.90 (t, 4H, $J_{\text{HH}} = 5$ Hz, OCH₂), 3.83–3.80 (m, 12H, OCH₂), 3.72–3.70 (m, 8H, OCH₂), 3.64–3.62 (m, 4H, OCH₂), 3.57–3.55 (m, 8H, OCH₂), 3.44 (s, 6H, OCH₃), 3.38 (s, 12H, OCH₃); ¹³C{¹H} NMR (CDCl₃) δ 162.9, 153.2, 138.3, 133.8, 131.0, 130.2, 128.6, 125.5, 123.3, 123.0, 108.0, 72.8, 72.3, 72.2, 70.84, 70.79, 70.7, 69.8, 69.0, 59.28, 59.24; UV/vis (CHCl₃): λ_{max}/nm (ε/L mol⁻¹ cm⁻¹): 261 (26932), 369 (3639), 463 (16293), 493 (42001), 529 (53132); FT-IR (neat) $\bar{\nu}$ (cm⁻¹) 2959, 2924, 2870, 1698, 1661, 1576, 1463, 1441, 1402, 1350, 1318, 1247, 1220, 1181, 1103, 984, 929, 851, 809; MS (MALDI-TOF, DCTB) $m/z = 1289.16$ [1+K]⁺, 1273.20 [1+Na]⁺; Anal Calc'd for C₆₆H₇₈N₂O₂₂: C, 63.35; H, 6.28; N, 2.24; Found: C, 62.99; H, 6.49; N, 2.29.

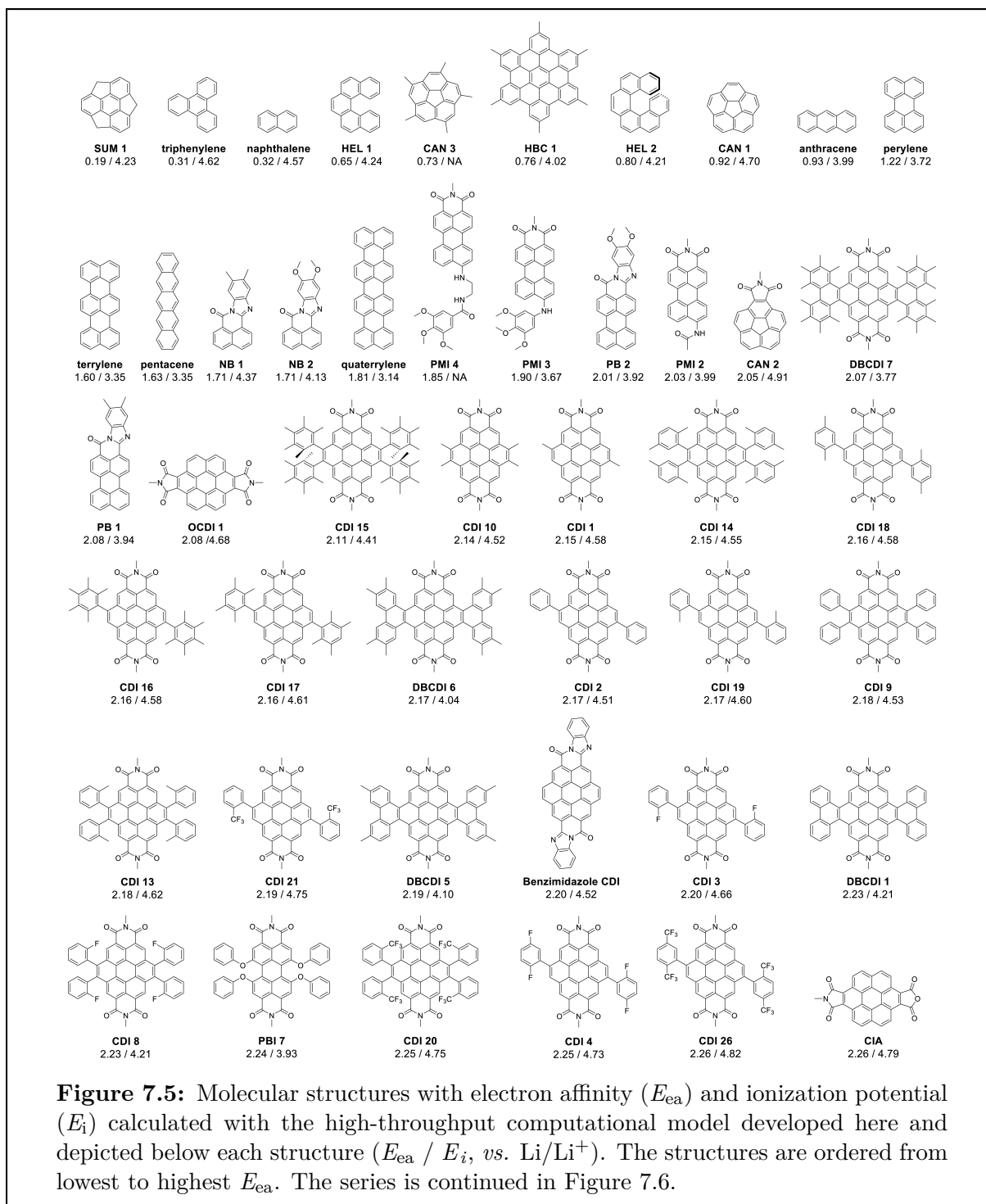
7.6.2 Computational details

Prediction of Redox Properties

The ionization energies (E_i) and electron affinities (E_{ea}) were calculated using Density Functional Theory (DFT) within a polarizable continuum medium model (with the dielectric constant set to that of water, 78.2) as implemented in the QChem software package.^[229, 301] For all molecules, the adiabatic method was employed in which the geometry was optimized separately for each charge state before performing an energy calculation. Due to the computational complexity in converging large molecules versus small ones within a high-throughput context, separate computational workflows were applied for small molecules (<50 atoms) versus larger molecules (50 atoms or higher). For small molecules, we performed geometry optimization, vibrational frequency analysis, and energy evaluation at the B3LYP/6-31+G* level of theory.^[302] For larger molecules, we performed geometry optimization at the PBE/6-31+G* level of theory^[60, 61] followed by an energy evaluation at the B3LYP/6-31+G* level. In a previous study, we have determined that both strategies produce comparable accuracy, and that using the PBE functional for the geometry optimization portion of large molecules reduces computation time and improves convergence percentage.^[60, 61]

We note that the computed E_i and E_{ea} represent the absolute oxidation and reduction potentials, respectively. To obtain the oxidation potential relative to a reference electrode, we subtract the absolute potential of the reference electrode from this value, $E_{\text{oxd}}^0 = E_i - E_{\text{ref}}^0$. Similarly, the reduction potential is calculated by $E_{\text{red}}^0 = E_{\text{ea}} - E_{\text{ref}}^0$. The reference potential for Li (E_{ref}^0) was set to 1.4 eV.

Overall, 85 structures were computed that span an E_{ea} range of 0.19 to 3.08 V *vs.* Li/Li⁺ and E_i range of 3.14 to 6.08 V *vs.* Li/Li⁺.



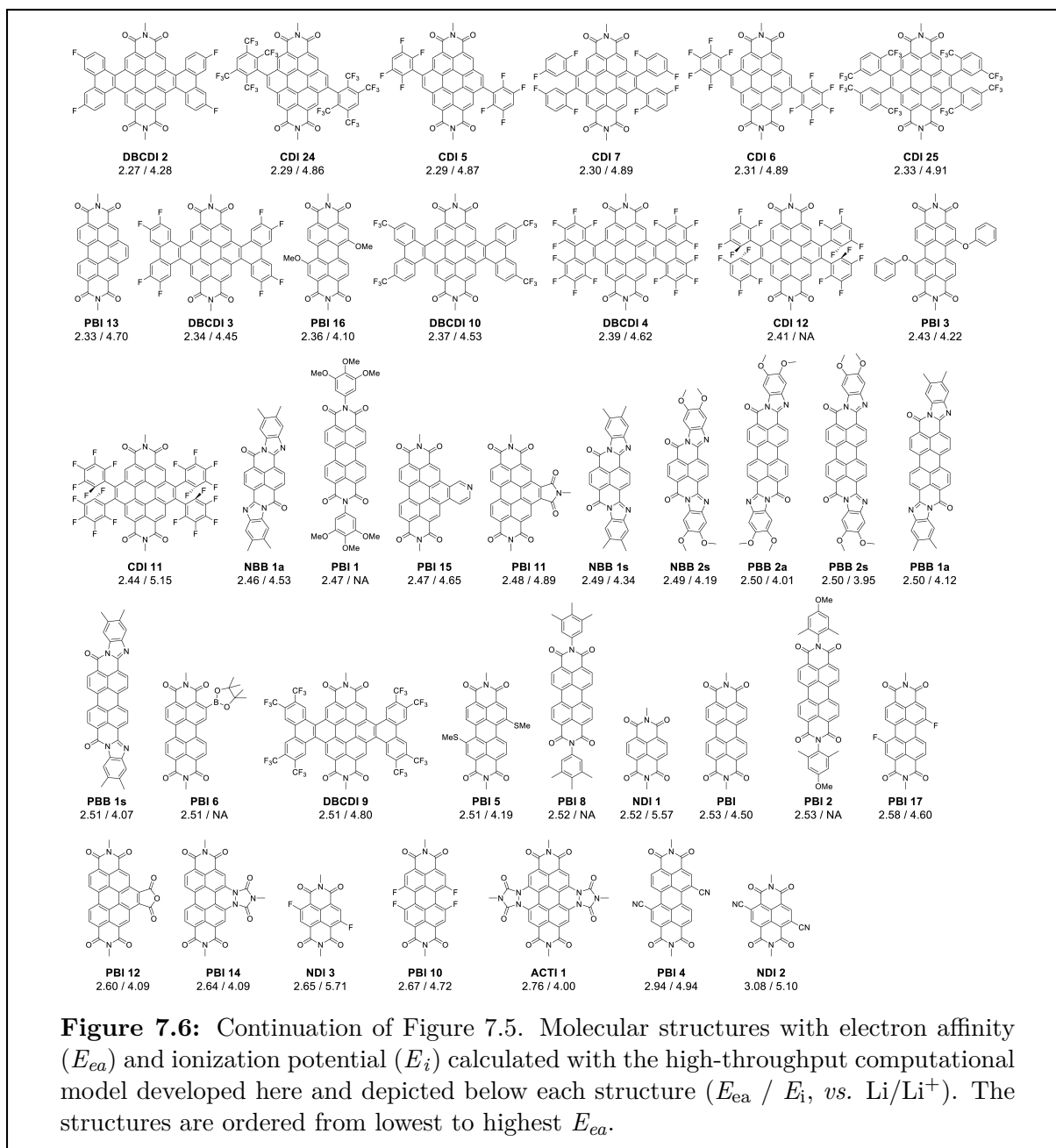
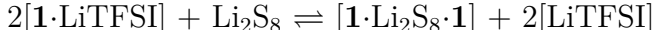


Table 7.1: List of E_{ea} and E_i values (*vs.* Li/Li⁺) computed for molecules with labels corresponding to the structures in Figures 7.5 and 7.6. The list is ordered from lowest to highest E_{ea} . The color coding is by class of molecule: polycyclic aromatic hydrocarbon (yellow), miscellaneous (green), coronene diimide (blue), and perylene bisimide (orange).

Molecule	E_{ea}	E_i	Molecule	E_{ea}	E_i	Molecule	E_{ea}	E_i
SUM 1	0.19	4.23	CDI 17	2.16	4.61	PBI 3	2.43	4.22
triphenylene	0.31	4.62	DBCDCI 6	2.17	4.04	CDI 11	2.44	5.15
naphthalene	0.32	4.57	CDI 2	2.17	4.51	NBB 1a	2.46	4.53
HEL 1	0.65	4.24	CDI 19	2.17	4.60	PBI 15	2.47	4.65
CAN 3	0.74	NA	CDI 9	2.18	4.53	PBI 1	2.47	NA
HBC 1	0.76	4.02	CDI 13	2.18	4.62	PBI 11	2.48	4.89
HEL 2	0.80	4.21	DBCDCI 5	2.19	4.10	NBB 1s	2.49	4.34
CAN 1	0.92	4.70	CDI 21	2.19	4.75	NBB 2s	2.49	4.19
anthracene	0.93	3.99	Benzimidazole	2.20	4.52	PBB 2a	2.50	4.01
perylene	1.22	3.72	CDI			PBB 1a	2.50	4.12
terrylene	1.60	3.35	CDI 3	2.20	4.66	PBB 2s	2.50	3.95
pentacene	1.63	3.35	DBCDCI 1	2.23	4.21	PBB 1s	2.51	4.07
NB 1	1.71	4.37	CDI 8	2.23	4.77	DBCDCI 9	2.51	4.80
NB 2	1.71	4.13	PBI 7	2.24	3.93	PBI 6	2.51	NA
quaterrylene	1.81	3.14	CDI 4	2.25	4.73	PBI 5	2.52	4.19
PMI 4	1.85	NA	CDI 20	2.25	4.75	NDI 1	2.52	5.57
PMI 3	1.90	3.67	CDI 26	2.26	4.82	PBI 8	2.52	NA
PB 2	2.01	3.92	CIA	2.26	4.79	PBI	2.53	4.50
PMI 2	2.03	3.99	DBCDCI 2	2.27	4.28	PBI 2	2.53	NA
CAN 2	2.05	4.91	CDI 24	2.29	4.86	PBI 17	2.58	4.60
DBCDCI 7	2.07	3.77	CDI 5	2.29	4.87	PBI 12	2.60	4.98
PB 1	2.08	3.94	CDI 7	2.30	4.89	PBI 14	2.64	4.09
OCDCI 1	2.08	4.68	CDI 6	2.31	4.89	NDI 3	2.65	5.71
CDI 15	2.11	4.41	PBI 13	2.33	4.70	PBI 10	2.67	4.72
CDI 10	2.14	4.52	CDI 25	2.33	4.91	ACTI 1	2.76	4.00
CDI 14	2.15	4.55	DBCDCI 3	2.34	4.45	PBI 4	2.94	4.94
CDI 1	2.15	4.58	PBI 16	2.36	4.10	NDI 2	3.08	6.08
CDI 18	2.16	4.58	DBCDCI 10	2.37	4.53			
CDI 16	2.16	4.58	DBCDCI 4	2.39	4.62			
			CDI 12	2.41	NA			

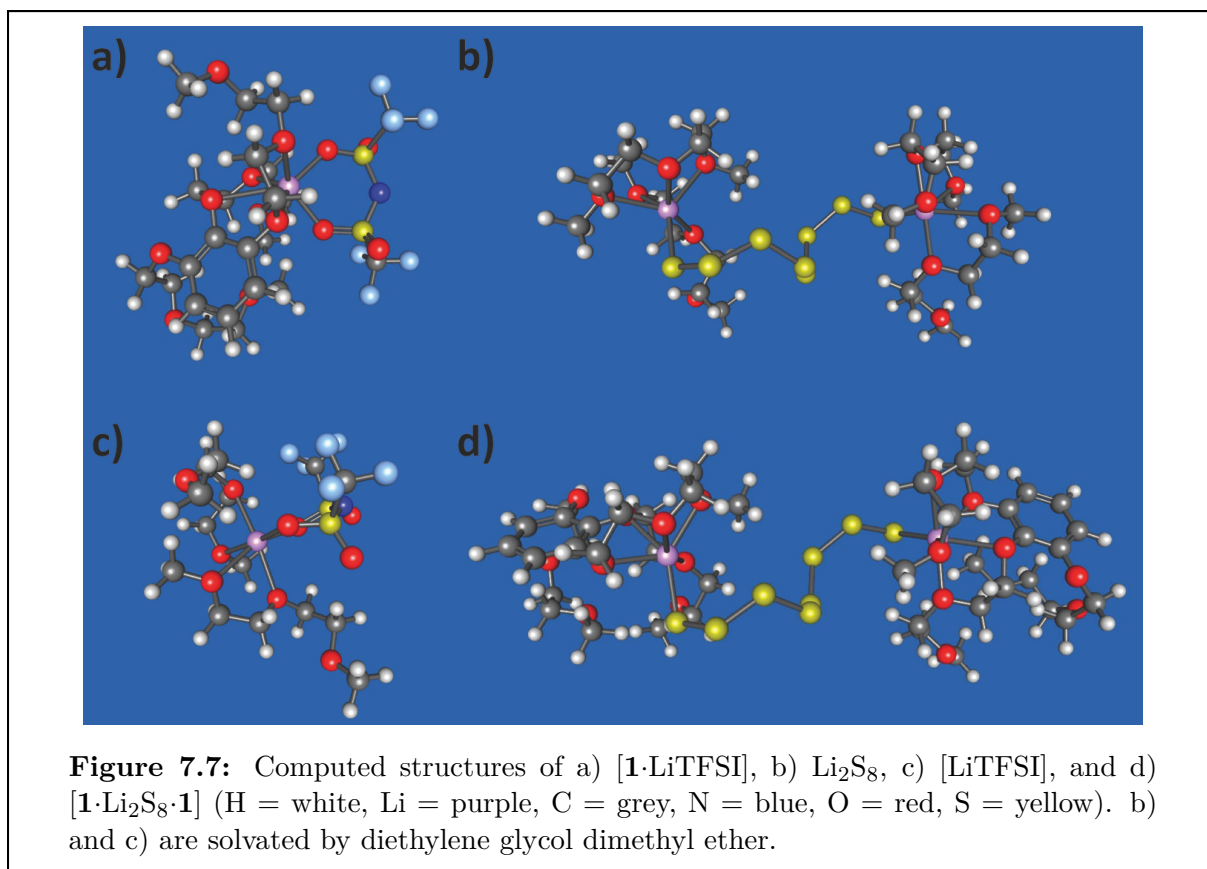
Equilibrium constant of crosslinking reaction

The equilibrium constant for the hypothesized crosslinking interaction was calculated from the following reaction:



$$-RT \ln(K_{eq}) = \Delta G_{reaction} = G_{\mathbf{1}\cdot\text{Li}_2\text{S}_8\cdot\mathbf{1}} + 2G_{\text{LiTFSI}} - G_{\text{Li}_2\text{S}_8} - 2G_{\mathbf{1}\cdot\text{LiTFSI}}$$

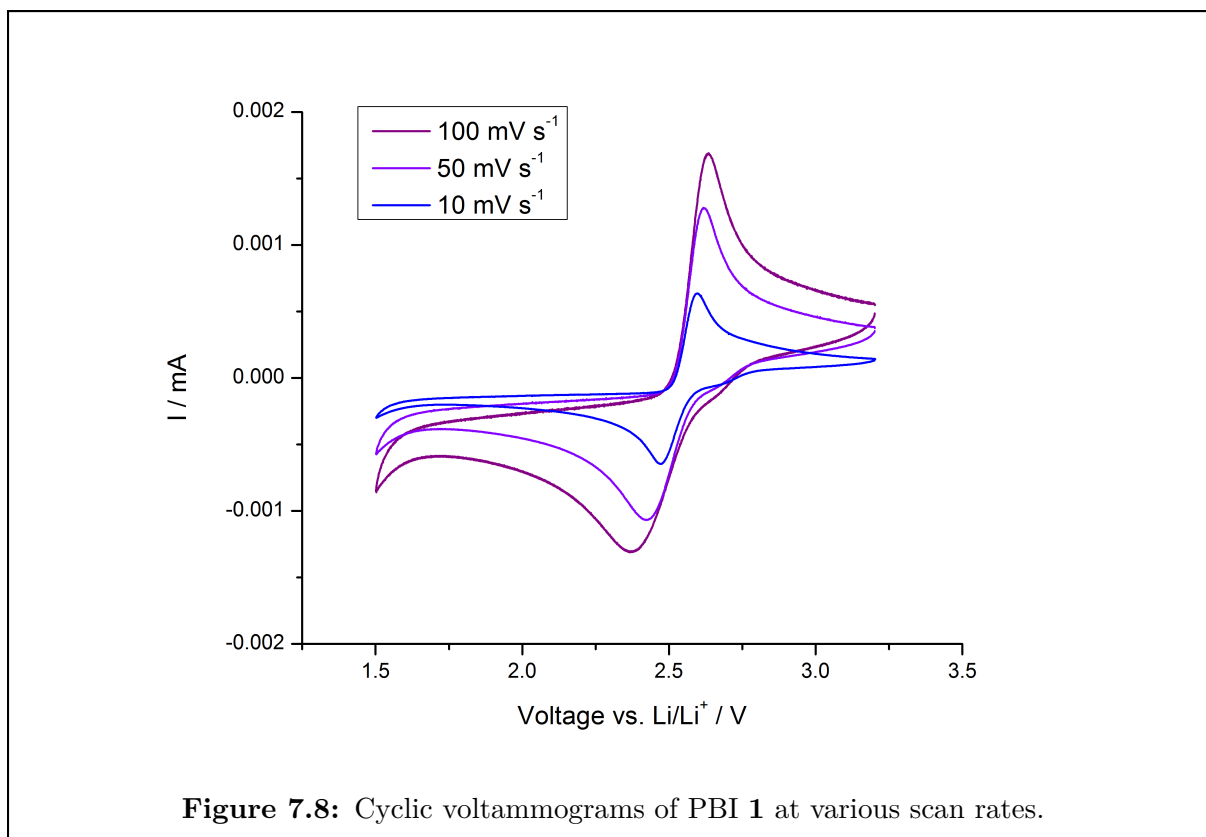
In which, Li_2S_8 and LiTFSI are the ion pairs of Li^+ cation with S_8^{2-} and TFSI^- anion, respectively. $[\mathbf{1}\cdot\text{Li}_2\text{S}_8\cdot\mathbf{1}]$ and $[\mathbf{1}\cdot\text{LiTFSI}]$ represent the crosslinking interaction with S_8^{2-} and the LiTFSI ion pair bound to the ethylene glycol solubilizing groups of PBI **1**, respectively. The individual Gibbs free energies were calculated via $G = E_{SCF} + H_{corr} - T\Delta S_{corr} + \Delta G_{solvation}$. E_{SCF} , H_{corr} , and ΔS_{corr} are electronic structure energy, enthalpic and entropic thermal corrections, respectively. $\Delta G_{solvation}$ is the solvation energy correction computed using the integral equation formalism polarizable continuum model (IEF-PCM) implicit solvent model.^[228] The geometry optimization is performed using PM7 semi-empirical quantum mechanic methods^[303] with MOPAC software package.^[304] Density functional theory is employed to calculate the single point energy at B3LYP/6-31++G** level with Q-Chem 4.3 software package.^[301, 305] To minimize the cost of the calculations PBI **1** was structurally abbreviated as the tris(oxy-diethylene glycol monomethyl ether)benzene unit found at the imide position of **1**. Diethylene glycol dimethyl ether was used as solvent for solvated Li_2S_8 and LiTFSI . Depictions of each optimized structure are found in Figure 7.7.



7.6.3 CV and Li–S cell testing

Cyclic voltammetry

Our electrochemical cell was configured with a glassy carbon working electrode and lithium metal reference and counter electrodes. Working solutions for cyclic voltammetry (CV) were separated from lithium counter and reference electrodes with a glass frit with an average pore size of ~ 7 nm and thickness of 5 mm obtained from Advanced Glass and Ceramics (St. James, NC, USA). In order to account for the potential drop across a highly resistive frit, all CV measurements were corrected for iR drop by measuring the impedance between the working and reference electrodes with an applied AC voltage with frequency of 100 kHz and correcting for 85% of the expected iR drop. CV of polysulfide alone and PBI with polysulfide were conducted in electrolyte with 0.010 mol L^{-1} **1** and $0.010 \text{ mol S L}^{-1}$ of nominal composition Li_2S_8 . CVs of PBI **1** were conducted with 0.010 mol L^{-1} PBI in electrolyte.



Interdigitated array IV measurements

A drop of catholyte (5 μL) was introduced to the IDA, covering the electrodes entirely. The concentration of Li_2S_8 was $0.50 \text{ mol S L}^{-1}$ and PBI 1 concentration was 0.050 mol L^{-1} . The concentration of polysulfide was reduced five-fold from the concentration used for cell cycling to minimize hysteresis that is likely attributed to nucleation of insulating S_8 or Li_2S on the electrode when cycling the voltage bias in the $\pm 0.5 \text{ V}$ range from the open circuit potential.

Cell preparation with PBI 1 additive

PBI 1 (15.0 mg) was heated at $120 \text{ }^\circ\text{C}$ for 30–60 min in 0.172 mL of electrolyte (TEGDME, 0.50 mol L^{-1} LiTFSI, 0.15 mol L^{-1} LiNO_3) until complete dissolution followed by cooling to room temperature. A solution of nominal composition Li_2S_8 (1.0 mol L^{-1} , or 8.0 mol S L^{-1}) was prepared in the same electrolyte and kept at $60 \text{ }^\circ\text{C}$ to prevent gradual precipitation. The Li_2S_8 solution was cooled to room temperature and then 0.078 mL was added to the solution of PBI followed by manual stirring with a spatula and brief vortexing yielding a viscous deep purple solution. Mixing was completed in less than two minutes to allow for manipulation of the catholyte as a liquid prior to gelation.

Gelation generally occurred within 5 min of mixing the polysulfide solution with the PBI 1 solution. Roughly 0.020 mL of catholyte was then pipetted into the gold-coated well (0.5 mm deep, 6.35 mm diameter) of the nickel electrode to give a final catholyte mass of 15–22 mg, whose final composition was 5.0% *w/w* PBI 1 (0.048 mol L⁻¹) and 0.313 mol L⁻¹ Li₂S₈ (i.e., 2.50 mol S L⁻¹). The catholyte was allowed to rest in the cathode well for a minimum of 30 min prior to cell assembly. Gelation results in a catholyte that is stable to inversion and has a glassy black appearance.

Lithium anodes were prepared by punching out 12.7 mm diameter circles from 1.5 mm thick lithium foil, pressing them onto nickel electrodes, and treating the exposed surface with electrolyte (TEGDME, 0.50 mol L⁻¹ LiTFSI, and 0.15 mol L⁻¹ LiNO₃) for a minimum of 30 min. A 12.7 mm diameter circle of Tonen separator was then placed on top of the lithium anode and an additional drop of electrolyte was added (~0.015 mL) before electrode assembly.

Cell preparation with no additive

All procedures were identical to PBI cell preparation with the exception that no PBI was added to the initial 0.172 mL electrolyte solution.

Cell preparation with carbon cloth and PBI 1 additive

All procedures were the same as for cells without carbon cloth with the exception that the cathode well was charged with two stacked 6.35 mm diameter disks of carbon cloth that weighed a total of 6.5–6.9 mg. Catholyte was added to the C-cloth containing well and allowed to gel for a minimum of 30 min prior to assembly. These cells were cycled from 2.8 to 2.01 V to avoid hitting the Li₂S precipitation plateau.

Cell preparation with carbon cloth and no additive

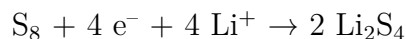
All procedures were identical to cell preparation with no additive except that the cathode well was charged with two stacked 6.35 mm diameter disks of carbon cloth that weighed a total of 6.6–6.8 mg. These cells were cycled from 2.8 to 2.01 V to avoid hitting the Li₂S precipitation plateau.

Determination of densities

The density of electrolyte with and without dissolved polysulfides was measured by weighing at least five samples each with a known volume (5.00 mL) at room temperature. The measured densities were 1.084 ± 0.003 g mL⁻¹ for electrolyte only and 1.121 ± 0.001 g mL⁻¹ for electrolyte containing 2.5 mol S L⁻¹ as Li₂S₈.

Calculation of C-rates for 2.8 to 2.0 V cycling

The 2.8 to 2.0 V window nominally covers the overall reduction process:



All C-rates are calculated for the reaction of 0.5 mol of Li^+ per 1.0 mol of S (or 0.5 mol e^-). Current for C/8 galvanostatic cycling was set with the following equations:

$$m_{\text{catholyte}} \times wt\%_{\text{Li}_2\text{S}_8 \text{ electrolyte solution}} \times (M_{\text{S}}/\rho_{\text{Li}_2\text{S}_8 \text{ electrolyte solution}}) \times 0.001 \text{ L mL}^{-1} = n_{\text{mol of S}}$$

$$n_{\text{mol of S}} \times 0.5 \text{ mol e}^{-1} \text{ per mol S} \times 96485 \text{ C per mol e}^{-1} / 28800 \text{ s} = i$$

The variables in these equations are defined as follows: $m_{\text{catholyte}}$ is the mass of the catholyte, $wt\%_{\text{Li}_2\text{S}_8 \text{ electrolyte solution}}$ is the weight percent of the catholyte that is Li_2S_8 and electrolyte (0.95 with 5% w/w PBI **1**, 1.00 for Li_2S_8 alone), and M_{S} is the molarity of S in the Li_2S_8 solution.

Calculation of energy density

The total Wh discharged on the second cycle from the representative **1** + Li_2S_8 cell depicted in Figure 7.3a was 0.829 mWh. The total catholyte mass was 20.4 mg. With a measured catholyte density of 1.12 g mL^{-1} there was 0.0182 mL of catholyte. Taking into account the total charge discharged (1.32 C measured, 2.09 C theoretical maximum) and assuming 100% excess lithium is necessary in a commercial cell, enough lithium metal must be included to provide 4.18 C of charge. From Faraday's constant, F , and the density of lithium, $\rho_{\text{Li}} = 0.534 \text{ g mL}^{-1}$, there must be $\frac{4.18 \text{ C}}{F} \times \frac{1 \text{ mol Li}}{1 \text{ mol e}^-} \times \frac{6.94 \text{ g}}{\text{mol Li}} \times \frac{\text{mL Li}}{0.534 \text{ g}} = 0.000563 \text{ mL}$ of lithium metal. The total volume of catholyte and metal anode for a theoretical cell based on these metrics is then 0.0188 mL. The volumetric energy density is $0.829 \text{ mWh} / 0.0188 \text{ mL} = 44 \text{ Wh L}^{-1}$.

Analysis of cell discharge capacities

A minimum of 21 cells were cycled for each catholyte and the second discharge capacities were recorded (Table 7.2). The collection of discharge capacities was subjected to Chauvenet's criterion to identify and reject outliers. One outlier was identified and removed from each dataset for the final statistics reported in the manuscript (Tables 7.3).

Table 7.2: Second cycle discharge capacities (mAh g^{-1} (S)) of Li-S cells cycled at C/8 rate with or without PBI 1 in the absence (cycled from 2.8 to 2.0 V) and presence (cycled from 2.80 to 2.01 V) of carbon cloth. The values highlighted in yellow were rejected from the overall data analysis using Chauvenet's criterion.

PBI 1 + Li_2S_8	Li_2S_8	C-cloth + PBI 1 + Li_2S_8	C-cloth + Li_2S_8
207	31	230	315
225	71	234	317
227	126	239	325
230	139	247	356
242	143	261	
245	148	266	
250	163	275	
251	189		
254	189		
254	192		
260	205		
265	205		
265	206		
266	211		
266	215		
267	227		
268	235		
272	240		
295	241		
295	258		
297	263		
315			
316			
322			
326			
383			
26 Cells	21 Cells	7 Cells	4 Cells

Table 7.3: Statistical analysis of second cycle discharge capacities (mAh g^{-1} (S)) of cells with PBI 1 + Li_2S_8 or Li_2S_8 alone as catholyte cycled at C/8 rate from 2.8 to 2.0 V. The average and standard error after rejection of outliers by Chauvenet's criterion are reported in the text.

Catholyte	Average (All Data)	Std. Dev. (All Data)	Std. Error of the Mean	Average (Chau- venet's)	Std. Dev. (Chau- venet's)	Std. Error of the Mean
PBI 1 + Li_2S_8	272	37.7	7.39	267	31.0	6.21
Li_2S_8	186	58.0	12.7	193	47.7	10.7

7.6.4 UV-Vis spectroscopy

Variable concentration study and determination of K_a for PBI 1

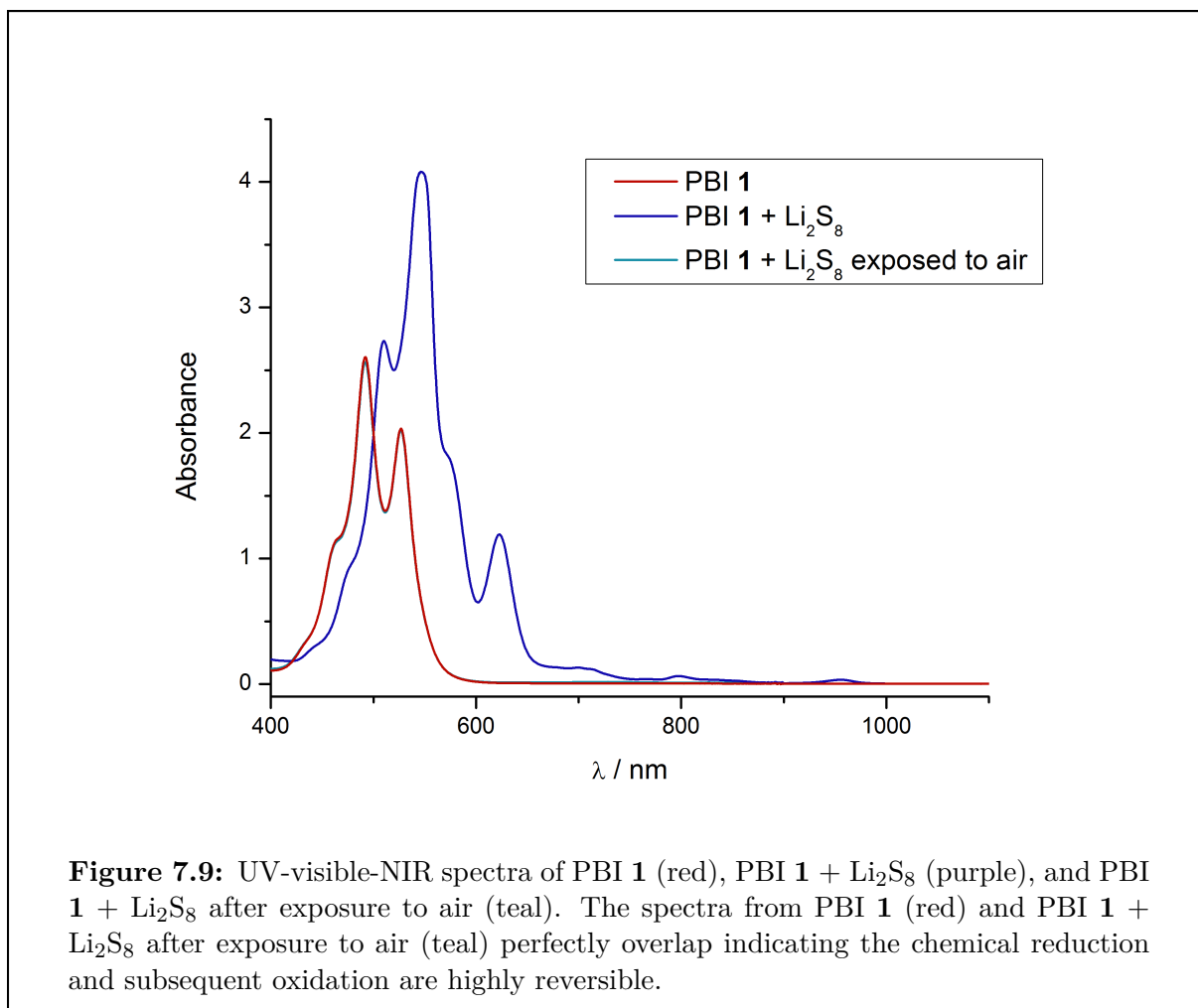
Solutions of PBI 1 in electrolyte (TEGDME, 0.5 mol L⁻¹ LiTFSI) were prepared between 1.5×10^{-3} mol L⁻¹ and 4.9×10^{-7} mol L⁻¹ and UV-visible spectra were obtained. The extinction coefficient at 555 nm was determined for each spectrum, and the data set normalized. The isodesmic model for self-assembly was then used to fit the data.^[306] Origin 8.5 (OriginLab, Northampton, MA) was used to fit the equation

$$\alpha = 1 - \frac{2K_a C + 1 - \sqrt{4K_a C + 1}}{2K_a^2 C^2}$$

where α is the mole fraction of aggregated molecules, K_a is the association constant, and C is concentration. From this procedure, an association constant of $(6.1 \pm 0.3) \times 10^4$ L mol⁻¹ was determined.

Reversible reduction of PBI 1 by Li₂S₈

In an Ar-filled glove box, a stock solution of PBI 1 (10 mL, 1.0×10^{-3} mol L⁻¹) in TEGDME containing 0.50 mol L⁻¹ LiTFSI was prepared. A portion of this stock solution (3 mL) was diluted with an additional portion of electrolyte to a final concentration of 5.4×10^{-5} mol L⁻¹. Separately, a sample of reduced PBI 1 was prepared by mixing a portion of the PBI 1 stock solution (3.0 mL) with a Li₂S₈ solution (0.60 mL, 8.0×10^{-3} mol S L⁻¹ in electrolyte) and an additional portion of electrolyte (2 mL), giving a final concentration 5.4×10^{-5} mol L⁻¹ PBI 1 and 3.2×10^{-4} mol S L⁻¹. UV-visible-NIR spectra were obtained in sealed cuvettes. The reduced PBI 1 was then exposed to air, the cuvette shaken for 2 min and another spectrum was obtained. After exposure to air, the spectrum overlays with the PBI 1 sample indicating that PBI 1 can be reversibly reduced by Li₂S₈. The results are depicted in Figure 7.9.

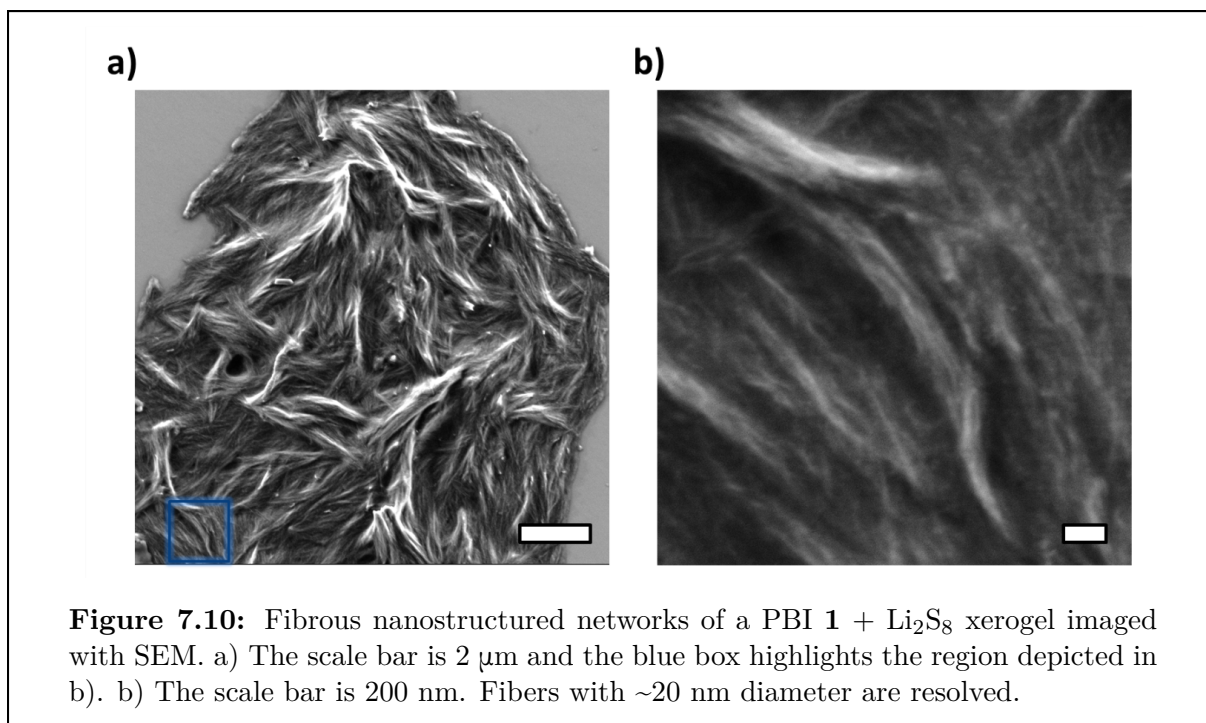


7.6.5 Scanning electron microscopy

SEM sample preparation

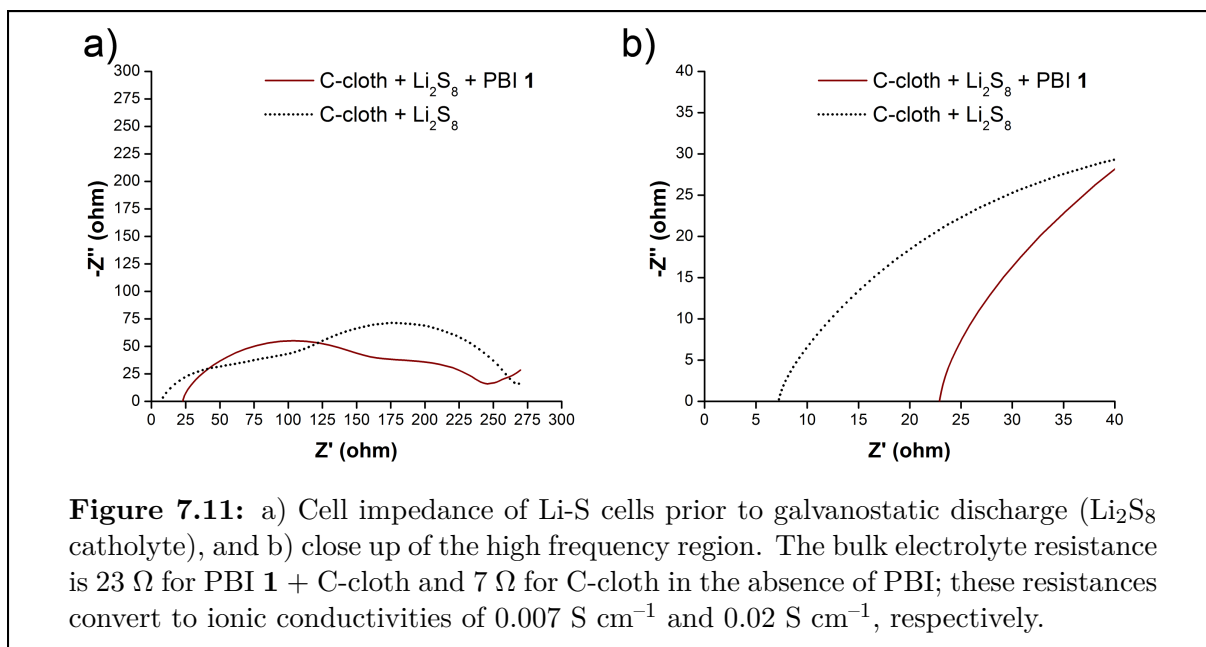
Electron microscopy of the actual catholyte gel was not feasible due to the disproportionately high concentration of salt (LiTFSI and LiNO_3) and lithium polysulfide relative to network forming PBI **1**. To prepare samples that were both representative of the supramolecular gel network catholyte and amendable to SEM imaging, samples with lower salt and lithium polysulfide concentration were prepared. A $0.25 \text{ mol S L}^{-1}$ solution (nominal Li_2S_8 composition) was prepared by diluting ten-fold a 2.5 mol S L^{-1} in TEGDME electrolyte (0.50 mol L^{-1} LiTFSI and 0.15 mol L^{-1} LiNO_3) with pure TEGDME. The $0.25 \text{ mol S L}^{-1}$ solution ($40 \mu\text{L}$) was then mixed with a 0.070 mol L^{-1} solution of PBI **1** dissolved in pure TEGDME ($43 \mu\text{L}$). The mixture was dropcast onto a polished silicon wafer and dried under reduced pressure at room temperature for 48 h prior to analysis.

Images were acquired with a secondary electron detector, a 2 keV beam energy, and a 3.7 mm working distance.

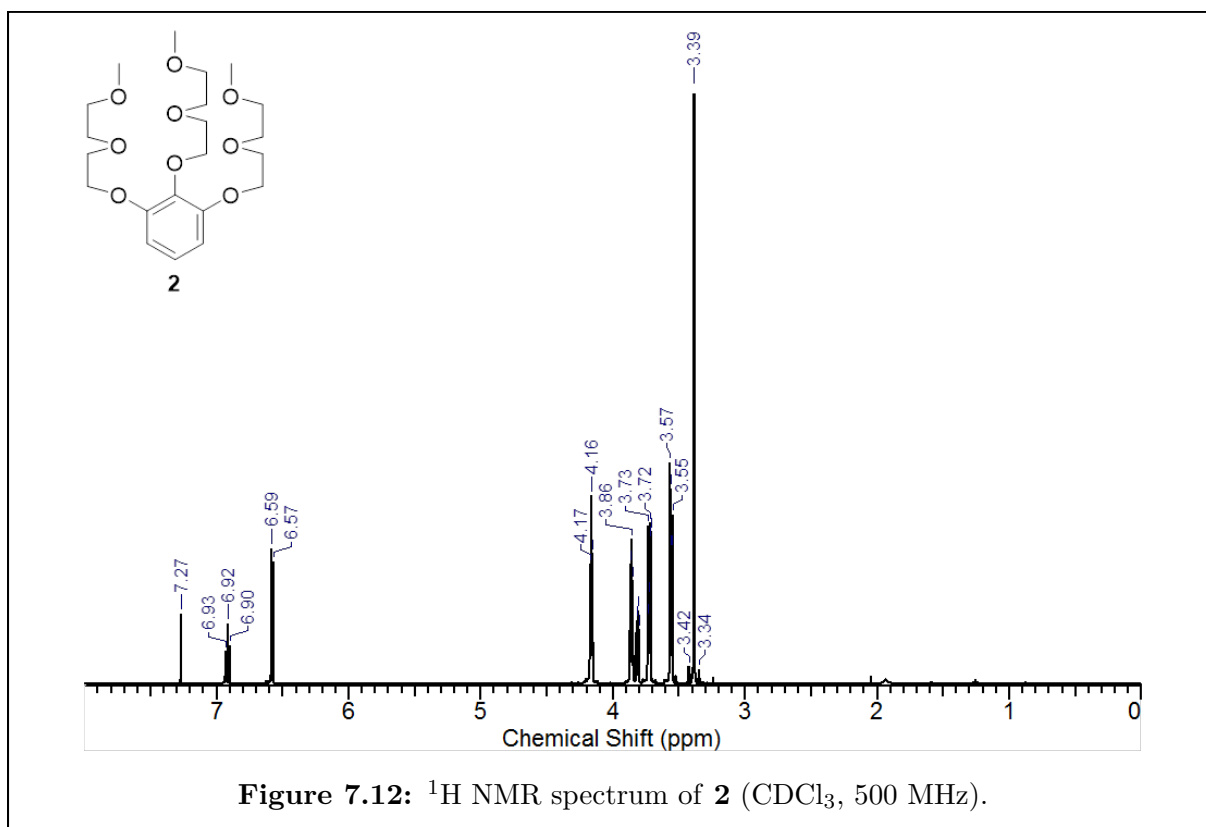


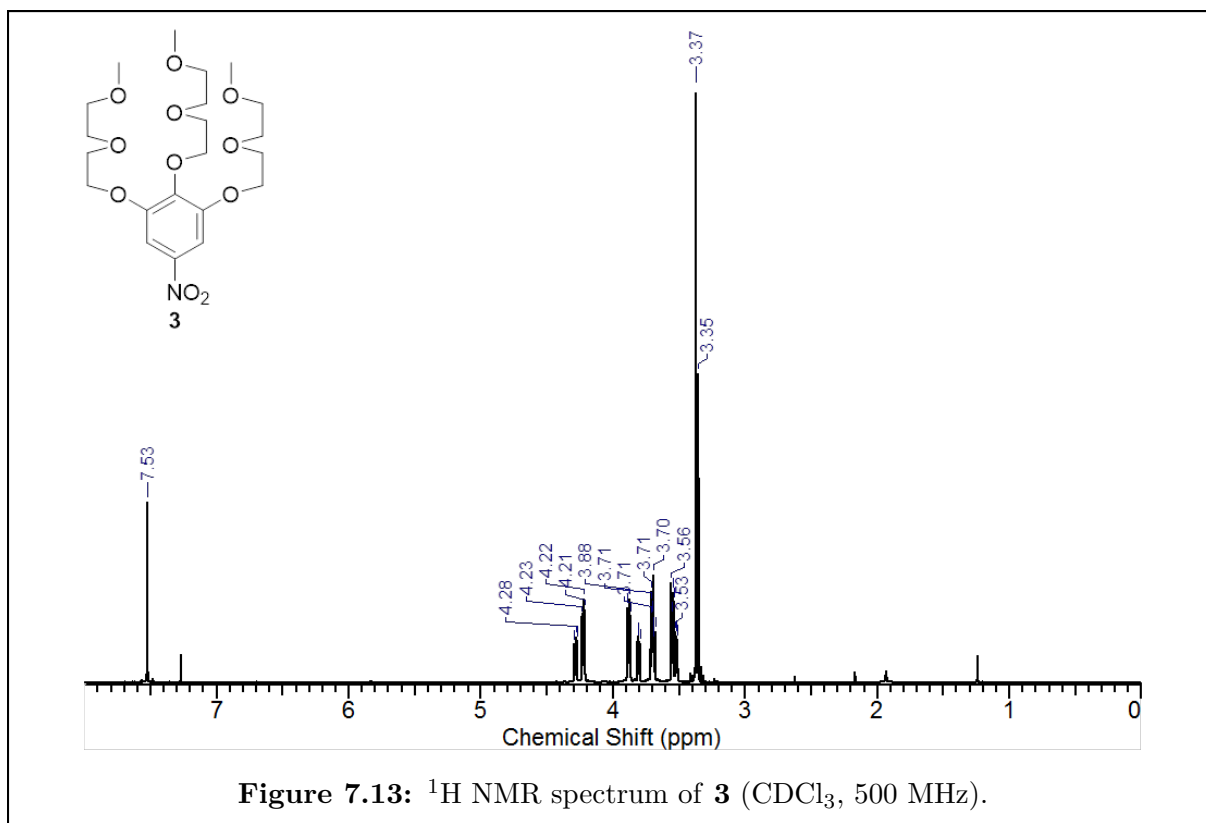
7.6.6 Electrochemical impedance spectroscopy

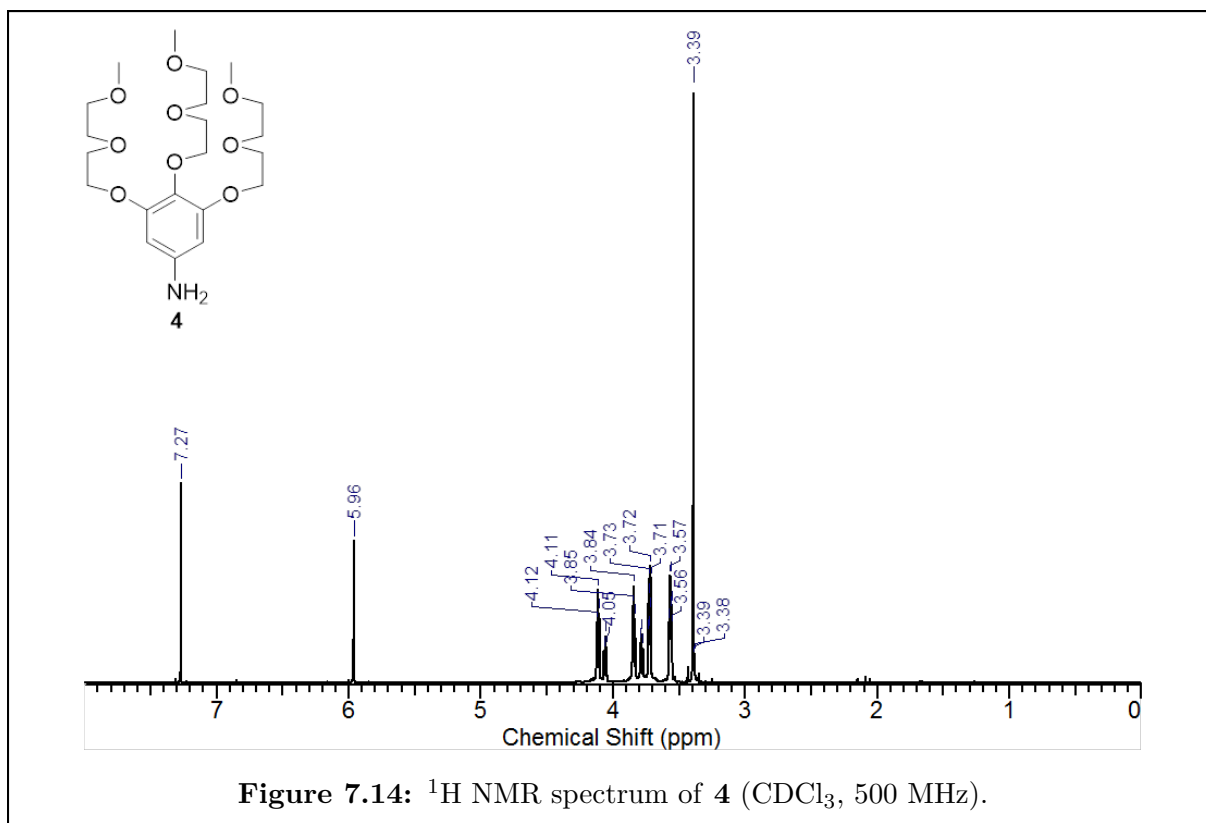
EIS was measured on Li-S cells from 1 MHz to 100 mHz with sinusoidal voltage oscillations of 50 mV amplitude applied about the cell's open circuit voltage between the two electrodes.

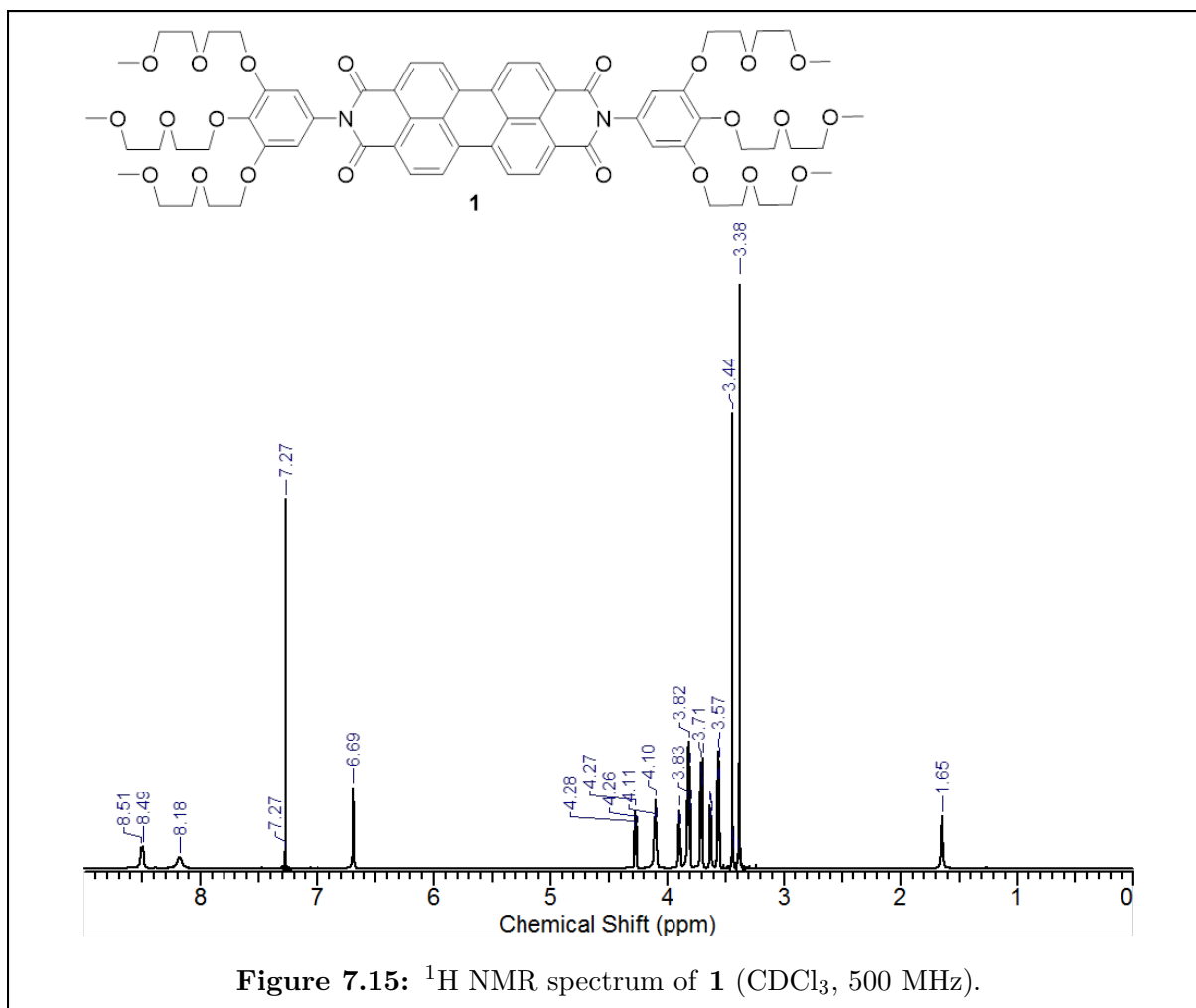


7.6.7 NMR spectra









7.6.8 Acknowledgements

This chapter is the result of a collaboration between myself, P.D. Frischmann, L.C.H. Gerber, E.Y. Tsai, F.Y. Fan, X. Qu, A. Jain, K.A. Persson, Y.-M. Chiang, and B.A. Helms, and I am thankful to all my co-authors for their help with this work. This work was supported by the Joint Center for Energy Storage Research, an Energy Innovation Hub funded by the U.S. Department of Energy, Office of Science, Office of Basic Energy Sciences. Portions of the work were carried out as a user project at the Molecular Foundry, which is supported by the Office of Science, Office of Basic Energy Sciences, of the U.S. Department of Energy under contract no. DE-AC02-05CH11231. This research used resources of the National Energy Research Scientific Computing Center, a DOE Office of Science User Facility supported by the Office of Science of the U.S. Department of Energy under Contract No. DE-AC02-05CH11231. S.E.D. was supported by the Department of Defense through the National Defense Science & Engineering Graduate Fellowship Program. E.Y.T. acknowledges support from the DOE Science Undergraduate Laboratory Internship program. We acknowledge T. E. Williams for SEM assistance.

Chapter 8

3-Dimensional Growth of Li_2S in Lithium–Sulfur Batteries Promoted by a Redox Mediator

Reproduced with permission from *Nano Lett.* **2016**, *16*(1), 549–554.
Copyright 2016 American Chemical Society.

8.1 Introduction and prior art

Promising next-generation battery chemistries, including lithium-sulfur (Li-S)^[5, 33, 34, 307] and lithium-air (Li-O₂)^[28, 29, 308, 309] rely on dissolution-precipitation as a mechanism to release and store charge in the cathode. In both cases, the discharge products are electronically insulating^[157, 310–313] (absent defects in the deposits^[314–316]). The insulating nature of these deposits can contribute to poor rate capability, low active-material utilization, and high polarization, which reduce overall energy efficiency.^[317–319] Charge-transport and charge-transfer bottlenecks in these electrochemical cells are eased through the use of electronically-conductive, high surface-area electrodes;^[171, 172, 182, 320–326] many electrode architectures have been reported yielding high-performance Li-O₂ cells,^[327–330] composite sulfur cathodes^[35, 36, 331, 332] and flowable sulfur catholytes for redox flow batteries.^[180, 182, 286] Despite these advances, challenges remain in controlling the electrodeposition of the electronically-insulating solid phase (i.e., Li₂S for Li-S cells, and Li₂O₂ for Li-O₂ cells) to maintain an accessible electrode surface, which is critical to cell performance.

Here I show that Li₂S electrodeposition on carbon current collectors can be redirected away from thin 2D layers, and instead toward micron-sized, porous 3D deposits when benzo[ghi]peryleneimide (BPI) is present as a redox mediator (Figure 8.1). Key to the design of the redox mediator is that the reduction potential of BPI is slightly less than the plateau voltage where the reduction of Li₂S₄ → Li₂S occurs. When BPI is reduced at the electrode surface and given time to diffuse away, it can reduce dissolved polysulfides to Li₂S remotely. With BPI present in the electrolyte, a 6-fold increase in Li₂S formation capacity was observed, leading to an impressive 220% increase in overall sul-

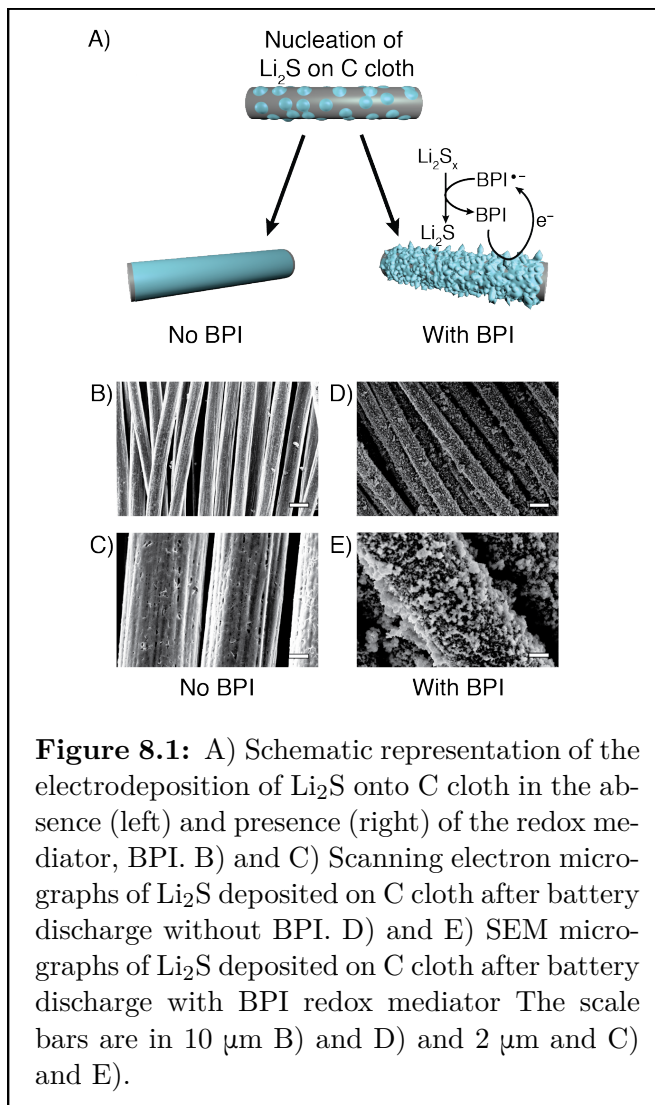


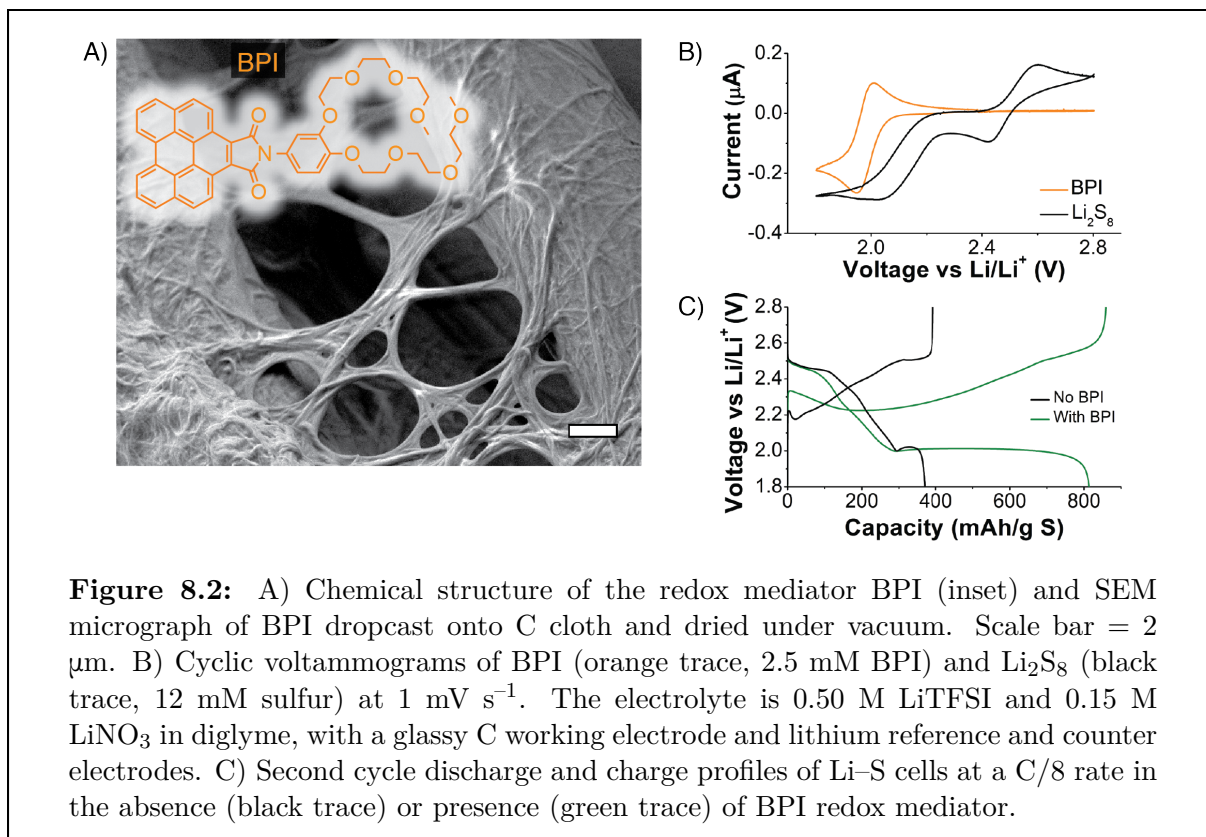
Figure 8.1: A) Schematic representation of the electrodeposition of Li₂S onto C cloth in the absence (left) and presence (right) of the redox mediator, BPI. B) and C) Scanning electron micrographs of Li₂S deposited on C cloth after battery discharge without BPI. D) and E) SEM micrographs of Li₂S deposited on C cloth after battery discharge with BPI redox mediator. The scale bars are in 10 μm (B) and D) and 2 μm (C) and E).

fur utilization. *Ex situ* analysis of Li_2S electrodeposition at different stages of discharge showed divergent trajectories for Li_2S nucleation and growth in the absence *vs.* presence of BPI. Kinetic studies linked the increased sulfur utilization to BPI’s ability to slow the impinging growth of Li_2S on the carbon electrode. By pairing conductive carbons with organic redox mediators, we gain access to hierarchical electrodes reminiscent of biological vasculature,^[219, 333–336] where conductive carbon “arteries” facilitate long-range electron transport while BPI “capillaries” mediate short-range transport and electron transfer between the storage materials and the current collector.

While soluble redox mediators have been explored widely for metal-air batteries,^[337–343] their application in Li–S batteries is still nascent. The redox chemistry of sulfur in Li–S cells is observed as two electrochemically distinct steps, a low-potential event ~ 2.1 V *vs.* Li/Li^+ attributed to the interconversion of Li_2S_4 and Li_2S and a high-potential event ~ 2.5 V *vs.* Li/Li^+ attributed to the interconversion of S_8 and Li_2S_4 .^[158, 162, 177, 199, 279] Paramount to the design of any redox mediator for Li–S cells is the careful matching of the mediator’s electrochemical potential to either of these interconversion events. With respect to the former, Aurbach *et al.* have shown that redox mediators can lower the overpotential required for the initial activation of solid-state Li_2S cathodes.^[289] With respect to the latter, we have recently reported that perylene bisimides (PBI) serve as redox mediators for the high-voltage plateau. While sulfur utilization was enhanced by 31%,^[219] this voltage window represents only 25% of the total theoretical capacity of sulfur. Therefore in this work, our focus turned to identifying a redox mediator for the 2.1 V (*vs.* Li/Li^+) reduction event, where Li_2S_4 reduction results in Li_2S precipitation onto the current collector. Although three-quarters of the theoretical capacity of sulfur is gained in this region, there are no reported redox mediators to facilitate Li_2S electrodeposition.

8.2 Computational screening of candidate molecules and synthesis of a potential-matched redox mediator

Our discovery of BPI as a redox mediator for Li_2S electrodeposition was informed by a robust computational platform known as the Electrolyte Genome that allowed us to screen the redox chemistry of polycyclic aromatic hydrocarbons (PAHs). PAHs are ideal redox mediators, owing to an exceptionally low reorganization energy required for their reduction and oxidation.^[344–346] In our previous work, we screened the electron affinities (E_{ea}) and ionization potentials (E_i) of over 80 PAHs—including acenes, phenylenes, rylenes, coronenes, and benzoperylenes.^[219] This library helped us identify PAHs with imide substituents that could be further elaborated upon to tune the E_{ea} so these molecules can serve as redox mediators for Li_2S electrodeposition. To refine the library and understand how the number and placement of imide functional groups would impact E_{ea} , a focused library of 20 additional PAH molecules was screened to hone in on a structure with a re-



duction potential (E_{ea}) of $\sim 1.8\text{--}2.0 \text{ V vs. Li/Li}^+$. This reduction potential was targeted because it would provide sufficient driving force for Li_2S formation without sacrificing cell power.

Electron affinities were obtained from the calculated energy difference between the neutral and the anion state of the molecule. All calculations were performed at the M11/6-31+G*/PBE-D3/6-31+G* level,^[186, 347] which has previously been shown to yield reliable relative trends for redox potentials across thousands of molecules (for more details, see section 8.6.1).^[60, 61] Trends from the computational results show that increasing the size of the aromatic core from perylene to benzoperylene to coronene lowers the reduction potential from 1.07 to 0.78 to 0.50 V vs. Li/Li^+ . On the other hand, increasing the number of electron-withdrawing groups raises the reduction potential; the addition of one imide substituent raises the reduction potential $>0.9 \text{ V}$, and additional imide substituents beyond that increase E_{ea} by an additional 0.5 V at most. In general, the placement of the electron-withdrawing imide substituents around the PAH core results in only small differences in E_{ea} . By balancing the effects of the size of aromatic core and number of electron-withdrawing groups, several candidates were found with calculated E_{ea} values between 1.8 and 2.0 V vs. Li/Li^+ (Figure 8.5). Due to its synthetic accessibility, the BPI structure was chosen for further study (Figure 8.2A).

Guided by these predictions from the Electrolyte Genome, we designed and synthesized gram-scale quantities of a new *N*-aryl-substituted benzo[ghi]peryleneimide (BPI, Scheme

8.1) bearing two tri(ethylene oxide) substituents. These substituents provided for BPI solubility in ether-based electrolytes commonly used in Li-S cells. Owing to the single imide substituent, BPI undergoes a single electron reduction in the operating window of the Li-S battery (1.8–2.8 V *vs.* Li/Li⁺), leading to an open-shell radical anion (BPI^{•-}). Using cyclic voltammetry in diglyme-based electrolyte, we determined the reduction potential ($E_{1/2}$) of BPI to be 1.980 V *vs.* Li/Li⁺ (Figure 8.2B, orange trace), which agreed well with the calculated value of 1.99 V *vs.* Li/Li⁺ when a Li⁺ counter-ion was included in the calculation (Figure 8.5). Thus, BPI provides ~100 mV driving force for the reduction of sulfur species. This small overpotential ensures that BPI should be able to reduce all sulfur species to Li₂S, but is not expected to significantly lower the operating voltage of the Li-S cell.

8.3 Performance of Li-S batteries with the addition of a redox mediator matched to the Li₂S deposition potential

BPI can be introduced to Li-S cells by dissolution in the electrolyte or by dropcasting onto C cloths (3% *w/w* BPI with respect to the sulfur catholyte), with similar results. Our implementation of C cloth electrodes, which feature 8 micron-thick carbon fibers, were chosen because they allow for careful visualization of Li₂S electrodeposition throughout the battery's operation. A hierarchical morphology of the BPI-C cloth hybrid in the dry state was apparent in the scanning electron micrograph (Figure 8.2A) where BPI assemblies, microns in length and formed through π -stacking of the aromatics, both covered and traversed the larger-diameter carbon fibers. Once polysulfide-containing electrolyte is added, these nanowire assemblies are expected to dissolve and circulate into the electrolyte volume, with the persistence length of the assemblies considerably shortened.^[306, 348]

To ascertain whether BPI has an affect on Li₂S electrodeposition, galvanostatic cycling was carried out on Li-S cells (Swagelok type) prepared with dissolved polysulfide cathodes alongside C cloth electrodes either with or without BPI. In the absence of BPI, the first complete discharge capacity was 316 ± 18 mAh g⁻¹ S ($N=16$). On the other hand, with BPI present (3% *w/w* with respect to catholyte), the capacity increased to 691 ± 18 mAh g⁻¹ S ($N=16$). This corresponds to an impressive 2.2-fold increase in discharge capacity (Figure 8.2C). Notably, this increase in capacity was due to a greatly extended 2.0 V-plateau, indicative of increased Li₂S formation as would be predicted for BPI were it serving as a redox mediator. No difference in cell performance was observed when BPI was introduced to the system by dissolution in the electrolyte as opposed to dropcasting on C cloth. Cells with dissolved BPI show a discharge capacity of 696 ± 41 mAh g⁻¹ S ($N=7$), indicating that BPI on the C surface is not simply serving as a nucleation point for Li₂S. Further experiments were conducted with the BPI dropcast onto C cloth for ease of cell assembly.

To quantify the respective gains in capacity between the high- and low-voltage regimes, I divided the discharge curve between the soluble regime ($\text{S}_8 + 4 \text{Li}^+ + 4 \text{e}^- \rightarrow 2 \text{Li}_2\text{S}_4$) and the Li_2S precipitation plateau ($\text{Li}_2\text{S}_4 + 6 \text{Li}^+ + 6 \text{e}^- \rightarrow 4 \text{Li}_2\text{S}$) at the position of the dip in the discharge curves at $\sim 2.0 \text{ V}$ in Figure 8.2C, which is attributed to the overpotential required for nucleation of Li_2S .^[220] The average capacities for the soluble regime are essentially identical (within error): $242 \pm 18 \text{ mAh g}^{-1} \text{ S}$ without BPI and $250 \pm 18 \text{ mAh g}^{-1} \text{ S}$ with BPI. However, the average capacity for Li_2S electrodeposition was $446 \pm 12 \text{ mAh g}^{-1} \text{ S}$ with BPI present, whereas it was only $74 \pm 2 \text{ mAh g}^{-1} \text{ S}$ for cells lacking BPI. Thus, the presence of BPI redox mediator resulted in a 6-fold increase in Li_2S electrodeposition. Additional control experiments confirmed that both redox mediator and C cloth are essential for the observed enhancement in sulfur utilization (Figure 8.8). Battery rate tolerance (Figure 8.9) and cycling data (Figures 8.10 and 8.11) are shown in section 8.6.

8.4 Electron microscopy and electrochemical experiments to understand the effect of the redox mediator on Li_2S morphology

In order to better understand nucleation and growth of Li_2S on C cloth with BPI present, I carried out *ex situ* analysis of Li–S cells at different states-of-charge (SOC). At specified points along the discharge and recharge (Figure 8.3A), I disassembled the cells, retrieved the C cloth from those cells, washed away the electrolyte containing salts, polysulfides and BPI, and then imaged the Li_2S discharge products using scanning electron microscopy (SEM); I also collected energy-dispersive x-ray (EDX) spectra of those samples to verify the chemical identity of the discharge products. Upon nucleation (Figure 8.3A, Point 1), small islands of Li_2S were distributed over the C microfibers both when BPI was present (Figure 8.3F) and absent (Figure 8.3B) from the cell. The presence of a soluble redox mediator is not expected to change Li_2S nucleation, and does not appear to do so here. With BPI present, a globular Li_2S morphology started to form (Figure 8.3G) mid-way through the 2.0 V plateau (Point 2), yet the underlying C cloth remained visible. On the other hand, without BPI present, islands of Li_2S began to impinge (Figure 8.3C), leaving little of the C surface available for further redox chemistry with dissolved polysulfides. By the end of discharge (Point 3), the carbon cloth from the cells with BPI showed even larger, porous Li_2S deposits, up to $3.8 \mu\text{m}$, growing outward until the underlying carbon cloth current collector was no longer visible (Figure 8.3H). EDX spectra were consistent with the assignment as Li_2S or insoluble polysulfide species (Table 8.1). These porous 3D growths of Li_2S at the end of the discharge were substantively different from the thin, conformal coatings observed when BPI was absent (Figure 8.3C)—such conformal coatings are consistent with previous studies.^[220] A similar change in morphology of Li_2O_2 has been observed when a soluble redox mediator is used in Li-air cells.^[342] Upon

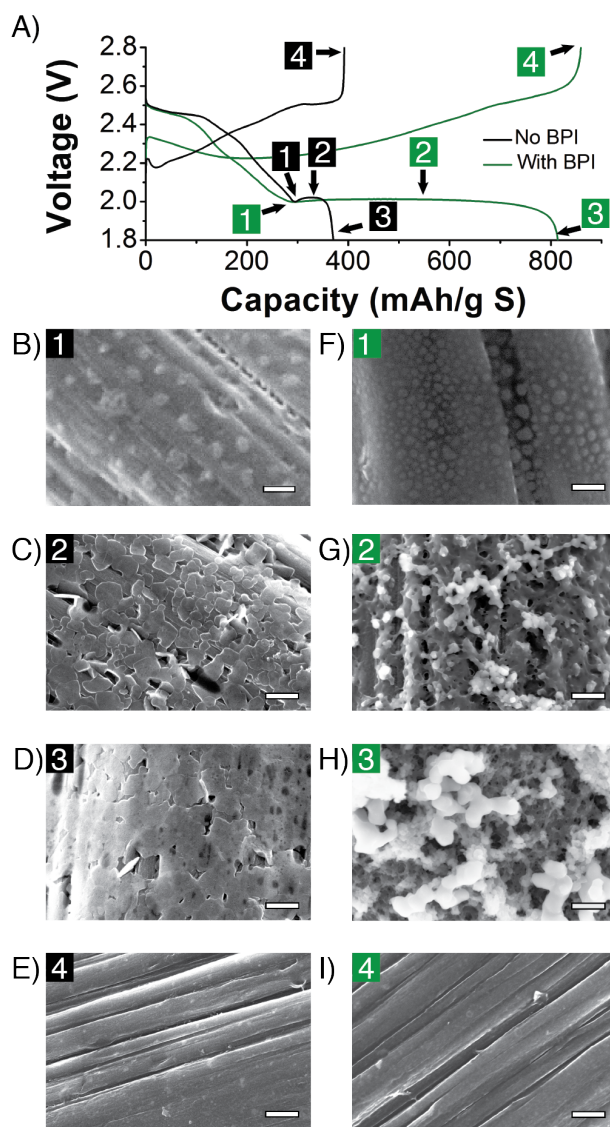


Figure 8.3: Progressive electrodeposition of Li_2S on C cloth, imaged at different states-of-charge in Li-S cells with BPI absent (left) and BPI present (right) A) The first discharge/charge cycle at C/8 rate. States-of-charge are indicated as Points 1–4 where separate cells were stopped to image the Li_2S deposits on the C cloth. SEM images of Li_2S electrodeposition on C cloth from a cell without BPI are shown: B) at nucleation (Point 1); C) during the Li_2S voltage plateau (Point 2); D) at the end of discharge (Point 3); and E) after recharge (Point 4). SEM images of Li_2S electrodeposition on C cloth from a cell with BPI: F) at nucleation (Point 1); G) during the Li_2S voltage plateau (Point 2); H) at the end of discharge (Point 3); and I) after recharge (Point 4). Scale bars = 500 nm.

charging to 100% SOC (Point 4), scant Li_2S remains on either carbon surface, without or with BPI added, as expected after complete oxidation of Li_2S (Figure 8.3E and 8.3I, respectively).

The growth trajectory of these 3D deposits involves reduction of BPI at the C cloth surface, followed by diffusion and circulation of $\text{BPI}^{\bullet-}$ into the catholyte solution where it reduces polysulfides to Li_2S which can deposit onto either Li_2S or C surfaces resulting in the observed 3D morphologies. This process is competitive with the direct reduction of polysulfides at the electrode surface, which instead coats the C surface in thin conformal layers. To understand the relative rates of these competitive processes, we further studied these Li-S cells under potentiostatic discharge. To do so, the cells were initially discharged potentiostatically to 2.09 V to reduce all S_8 and higher order polysulfides to Li_2S_4 (nominally), in order to study only the electrodeposition of Li_2S . The current was then monitored over time upon lowering the potential to either 2.00 or 1.95 V to provide a driving force for Li_2S nucleation and growth (Figure 8.4). In both cases, the current trended towards 0 whether or not BPI was present, which indicated that sulfur utilization is ultimately limited by

impingement of insulating Li_2S blocking the carbon surface. If Li_2S were to continue to be reduced after the electronically conductive C cloth surface were covered, a horizontal asymptote would instead be expected at a current density $> 0 \text{ mA cm}^{-2}$. At 1.95 V, the current density peaks at a higher value and at a later time when BPI is included, leading to a 3.1-fold increase in capacity due to Li_2S deposition (Figure 8.4A). At 2.00 V, while the cell with BPI does not obtain a higher current density than without BPI, this current density is maintained for much longer when BPI is present, leading to a 5.5-fold increase in capacity due to Li_2S deposition (Figure 8.4B).

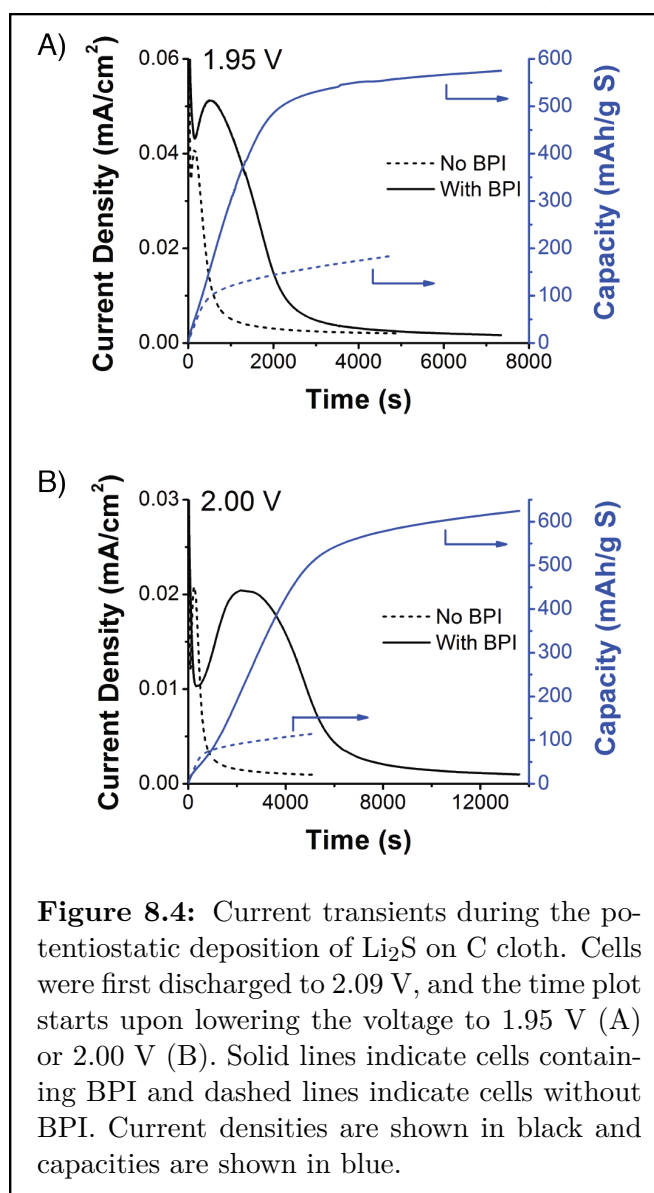


Figure 8.4: Current transients during the potentiostatic deposition of Li_2S on C cloth. Cells were first discharged to 2.09 V, and the time plot starts upon lowering the voltage to 1.95 V (A) or 2.00 V (B). Solid lines indicate cells containing BPI and dashed lines indicate cells without BPI. Current densities are shown in black and capacities are shown in blue.

The potentiostatic electrodeposition of Li_2S was fit by a current density (J) vs. time (t) relation of the form:

$$\frac{J}{J_m} = \left(\frac{t}{t_m} + c\right) \exp\left[-\frac{1}{2}\left(\frac{t^2}{t_m^2} - 1\right)\right]$$

where J_m and t_m are the maximum current density and the time at which the maximum current density occurs, respectively.^[349, 350] This equation is a modified form of the Avrami equation that models instantaneous nucleation of Li_2S and growth of islands to impingement. The exponential term represents the probability that a given area of the electrode remains uncovered by Li_2S and is therefore available for reaction. The term c accounts for additional current due to the redox mediator; when no redox mediator is present $c = 0$, but this term is required when BPI is present ($c = 1.24$ at 1.95 V and $c = 0.14$ at 2.00 V). This model fits the data both with and without redox mediator, indicating that in both cases the current is proportional to the remaining free surface of carbon. This implies that both with and without redox mediator, impingement of insulating Li_2S deposits covering the carbon surface ended discharge prior to reaching the theoretical limit; however, the addition of BPI redox mediator dramatically enhanced sulfur utilization prior to impingement.

The width of the peak fit by the modified Avrami equation can be used to determine the rate constant of lateral growth of Li_2S , k (where lateral growth is the disappearance of C surface available for reaction) from the relation: $t_m = (2\pi N_0 k^2)^{(-1/2)}$ where N_0 is the areal density of nuclei. The term $N_0 k^2$ can be compared as an effective rate constant for coverage of the C cloth surface by Li_2S . Without redox mediator, $N_0 k^2 = 4.21 \times 10^{-6} \text{ s}^{-2}$ and $2.52 \times 10^{-6} \text{ s}^{-2}$, at 1.95 and 2.00 V, respectively, and with redox mediator, $N_0 k^2 = 1.51 \times 10^{-7} \text{ s}^{-2}$ and $2.35 \times 10^{-8} \text{ s}^{-2}$, at 1.95 and 2.00 V, respectively. Addition of BPI results in a 28-fold reduction in the coverage rate at 1.95 V and a 107-fold reduction at 2.00 V. In both cases, having the soluble redox mediator slows the coverage of C cloth surface by allowing deposition of Li_2S onto previously formed Li_2S and not just at the carbon surface. The coverage of the C surface is likely slowed by (1) direct competition between BPI and polysulfides for reduction at the carbon surface, and (2) $\text{BPI}^{\bullet-}$ intercepting incoming soluble polysulfides and reducing them to Li_2S away from the C cloth surface, effectively lowering the local concentration of polysulfide at the carbon surface.

8.5 Conclusions and future work

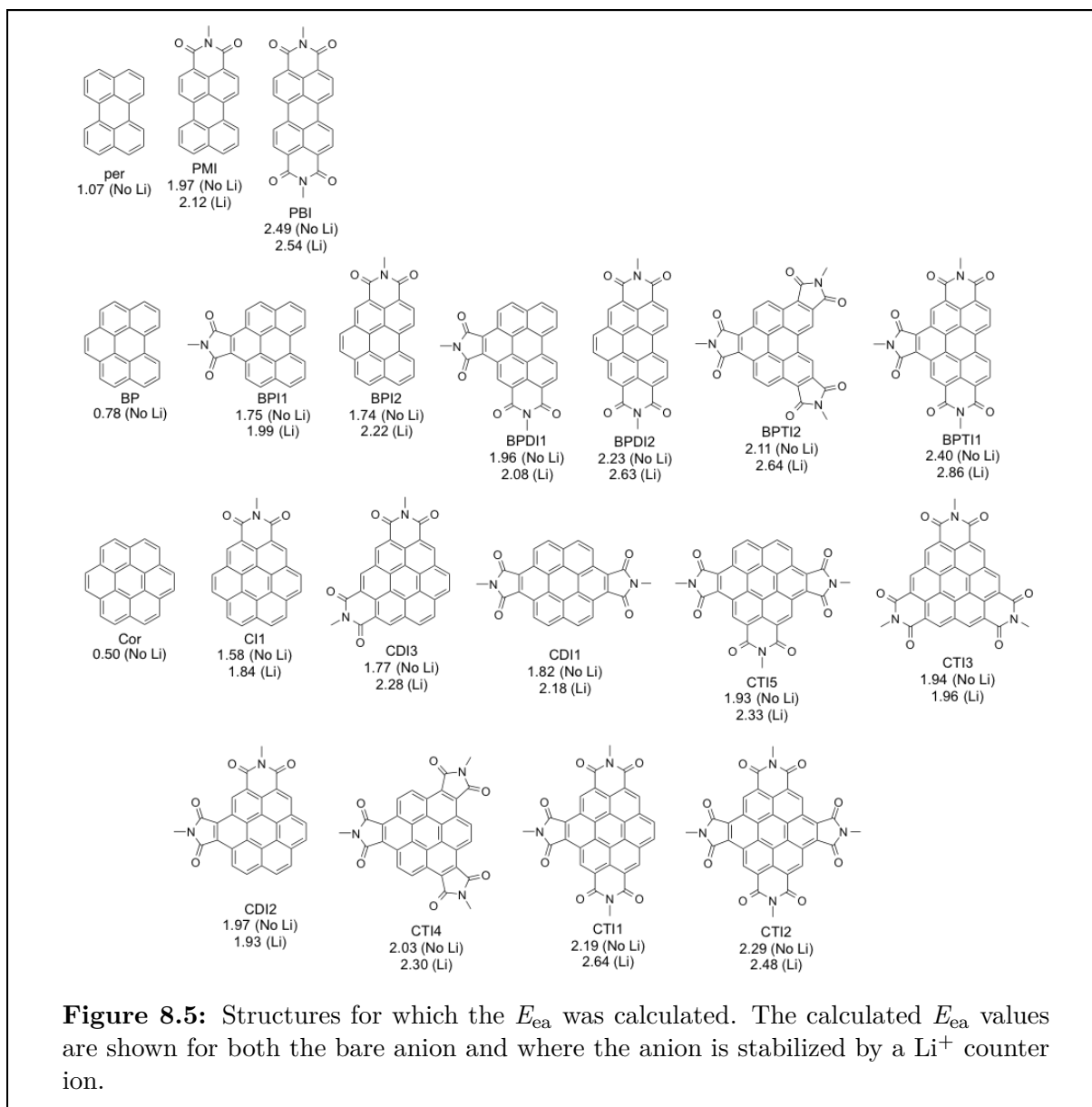
In conclusion, with a redox mediator that is tuned to the potential of Li_2S electrodeposition, I am able to mitigate the limitations imposed by the surface area required for nucleation and growth of Li_2S by providing a new mechanism for Li_2S deposition. Both the potentiostatic and galvanostatic discharge experiments confirm that the addition of 3% (w/w) BPI redox mediator increases the amount of Li_2S produced 6-fold. By adding an equivalent mass of C cloth, only an additional 24 mAh g^{-1} S could be added to the

capacity, based on the additional surface area available for 2D deposition of Li_2S . Without BPI, polysulfides are reduced at the C cloth surface to form an insulating, conformal coating of Li_2S , but with redox mediator, BPI reduces polysulfides to Li_2S away from the surface, allowing deposition of Li_2S not only on the C cloth surface, but on previously deposited Li_2S . This forms porous, 3-dimensional structures of Li_2S and delays coverage of the electroactive C cloth with an insulating Li_2S layer that ends discharge. This implies that for a given amount of Li_2S formed during cycling, less conductive carbon additive should be required, allowing for a greater percentage of the battery to be dedicated to active material. With an understanding of the mechanism by which BPI redox mediator extends sulfur utilization, rapid development of Li-S cells with an increased energy density is underway though the integration of BPI with high surface area current collectors at high sulfur loadings.

8.6 Supporting information

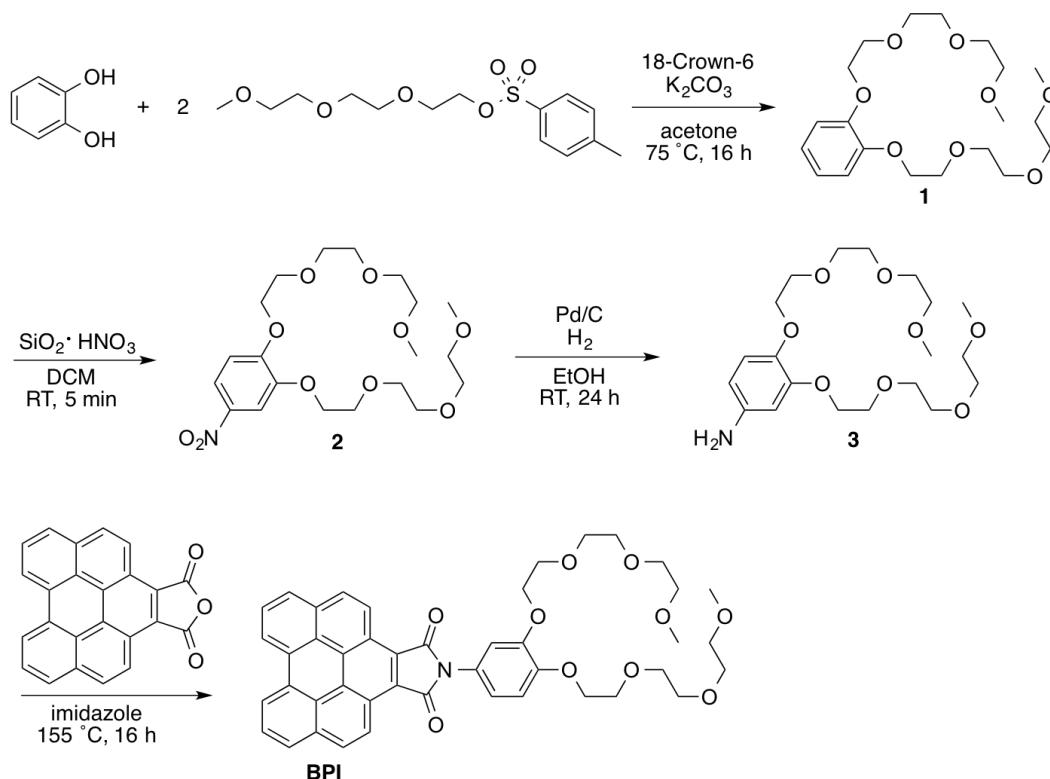
8.6.1 Computational details

Density Functional Theory (DFT) calculations were employed to predict the electron affinities (E_{ea}) to screen candidates for experimental validation. E_{ea} is correlated to reduction limit of the electrochemical stability window. E_{ea} was calculated by the energy difference between the neutral and anion state of the molecule. The choice of computational method is a balance between accuracy and computational cost. The relatively low cost PBE functional^[186] is used to optimize the structure, while the more accurate M11 hybrid functional^[347] is used for accurate energy calculations. Grimme’s dispersion correction is included for PBE to capture the missing dispersion interaction, which can be partially accounted for by the HF exchange in M11. All the structures at different charge states are fully relaxed at the PBE/6-31+G* level, while all the single point energies are evaluated at the M11/6-31+G* level. The IEF-PCM dielectric continuum model is employed to capture the solvent effect in a qualitative way, and a dielectric constant of 9 was applied. All the DFT calculations have been carried out using quantum chemistry package QChem 4.^[229] The job monitoring, error fixing and data parsing are automated by a workflow infrastructure developed by the Electrolyte Genome project.^[60, 61]



8.6.2 Synthetic procedures and characterization

Scheme 8.1: Chemical synthesis of BPI



Synthesis of 1

Catechol (7.96 g, 72 mmol), tri(ethylene glycol) monomethyl ether tosylate (46 g, 144 mmol), K_2CO_3 (33 g, 239 mmol), 18-Crown-6 (3.75 g, 14 mmol), and acetone (200 mL) were added to an oven-dried 500 mL 3-necked flask. The reaction mixture was sparged with N_2 for 30 min, fitted with a reflux condenser, and refluxed ($75\text{ }^\circ\text{C}$) for 16 h. The solvent was removed under reduced pressure. Dichloromethane was added, and the solution was washed with 50 mL saturated $NaHCO_3$, $2 \times 50\text{ mL H}_2O$, dried over $MgSO_4$, and filtered. The volatiles were removed *in vacuo* to isolate **1** as a colorless oil (26.71 g, 92%). Spectra were consistent with those previously published.^[351]

Synthesis of 2

Compound **1** (8.4 g, 20.87 mmol) and dichloromethane (50 mL) were added to a 150 mL round bottom flask. After **1** dissolved, 20% $HNO_3 \cdot SiO_2$ (16.95 g of $HNO_3 \cdot SiO_2$, 53.8 mmol HNO_3) was added, and the suspension was stirred for 5 min. The suspension was filtered through a pad of Celite on a fritted filter, and solvent was then removed from

the filtrate under reduced pressure. The mixture was purified by column chromatography with DCM/MeOH as the eluent (SiO₂, 0–8% MeOH). Column fractions containing pure and impure product were combined and solvent was removed under reduced pressure. The resulting mixture was purified again by column chromatography with 50:50 DCM:EtOAc as eluent to yield **2** as a dark orange oil (5.06 g, 54%).

Characterization of **2**

¹H NMR (CDCl₃) δ 7.84 (dd, 1H, $J_{HH} = 9, 3$ Hz, ArH), 7.76 (d, 1H, $J_{HH} = 3$ Hz, ArH), 6.92 (d, 1H, $J_{HH} = 9$ Hz, ArH), 4.22 (m, 4 H, OCH₂), 3.87 (m, 4H, OCH₂), 3.71 (m, 4H, OCH₂), 3.65 – 3.61 (overlapping m, 8H, OCH₂), 3.51 (m, 4H, OCH₂), 3.34 (s, 6H, OCH₃); ¹³C{¹H} δ 154.5, 148.6, 141.5, 118.1, 112.0, 109.1, 71.99 (2C), 71.02 (2C), 70.76, 70.75, 70.64, 70.62, 69.6, 69.5, 69.2, 69.1, 59.1 (2C); FT-IR (neat) ν (cm⁻¹) 2926, 2875, 1586, 1515, 1455, 1336, 1273, 1233, 1200, 1094, 1047, 1031, 970, 948, 864, 806, 745, 723; UV/vis (CHCl₃): λ_{max}/nm (ε/M⁻¹ cm⁻¹): 305 (5954), 338 (7291); Anal Calc'd for C₂₀H₃₃NO₁₀: C, 53.68; H, 7.43; N, 3.13; Found: C, 53.46, H, 7.30; N, 3.19; ESI-MS (MeOH) $m/z = 470.20$ [M + Na]⁺

Synthesis of **3**

Compound **2** (2.67 g, 5.97 mmol) and ethanol (120 mL) were added to a 250 mL flask. The flask was evacuated and refilled with N₂ three times before adding 10% *w/w* Pd/C (313 mg, 0.294 mmol Pd) as a dispersion in EtOH. The flask was fitted with a 3-way valve connected to a H₂-filled balloon. The suspension was evacuated and refilled with H₂ three times and then allowed to stir under an H₂ atmosphere for 24 h. The reaction mixture was filtered through a glass frit containing a pad of Celite and the filtrate was concentrated under reduced pressure to yield **3** as a brown oil (1.98 g, 80%).

Characterization of **3**

¹H NMR (CDCl₃) δ 6.77 (d, 1H, $J_{HH} = 9$ Hz, ArH), 6.33 (d, 1H, $J_{HH} = 3$ Hz, ArH), 6.22 (dd, 1H, $J_{HH} = 9$ Hz, 3 Hz, ArH), 4.12 (t, 2H, $J_{HH} = 5$ Hz, OCH₂), 4.08 (t, 2H, $J_{HH} = 5$ Hz, OCH₂), 3.84 (t, 2H, $J_{HH} = 5$ Hz, OCH₂), 3.79 (t, 2H, $J_{HH} = 5$ Hz, OCH₂), 3.74 – 3.71 (overlapping m, 4H, OCH₂), 3.68 – 3.64 (overlapping m, 8 H, OCH₂), 3.56 – 3.54 (overlapping m, 4 H, OCH₂), 3.38 (s, 6H, OCH₃), 2.00 (br s, NH₂); ¹³C{¹H} δ 150.4, 142.0, 141.6, 118.4, 107.6, 103.4, 72.0 (2C), 70.9, 70.78 (2C), 70.77, 70.6 (2C), 70.4, 70.1, 69.8, 68.7, 59.14, 59.12; FT-IR (neat) ν (cm⁻¹) 2981, 2923, 2914, 2886, 2871, 2825, 1634, 1614, 1594, 1512, 1470, 1463, 1456, 1447, 1351, 1327, 1295, 1224, 1199, 1185, 1090, 1060, 1052, 1043, 1027, 986, 940, 890, 848, 844, 800, 759, 751, 710; UV/vis (CHCl₃): λ_{max}/nm (ε/L mol⁻¹ cm⁻¹): 298 (7704); Anal Calc'd for C₂₀H₃₅NO₈: C, 57.54; H, 8.45, N, 3.35; Found: C, 57.03; H, 8.36; N, 3.33; ESI-MS (MeOH) $m/z = 440.20$ [M + Na]⁺

Synthesis of BPI

Compound **3** (0.993 g 2.379 mmol), benzoperylene anhydride (0.641 g, 1.840 mmol), imidazole (6.3 g, 92.1 mmol), and a stir bar were added to a 40 mL septum-capped vial. The vial was evacuated and refilled with N₂ three times, and stirred at 155 °C for 16 h over which time the orange suspension becomes a brown solution. The vial was removed from heat and 30 mL CHCl₃ was added before the imidazole solidified. The solution was washed with 1.0 M HCl (3 × 30 mL), dried over MgSO₄, filtered, and concentrated under reduced pressure. The crude product was purified with a SiO₂ plug. Perylene (yellow with blue fluorescence) was eluted first with DCM. The orange product, BPI, was eluted with 5% MeOH in DCM. The solvent was removed under reduced pressure to isolate BPI as a dark orange solid (1.159 g, 84%).

Characterization of BPI

¹H NMR (CDCl₃) δ 8.12 (d, 2H, *J*_{HH} = 8 Hz, Ar*H*), 7.99 (d, 2H, *J*_{HH} = 8 Hz, Ar*H*), 7.57 (t, 2H, *J*_{HH} = 8 Hz, Ar*H*), 7.52 (d, 2H, *J*_{HH} = 8 Hz, Ar*H*), 7.22 – 7.17 (overlapping m, 5H, Ar*H*), 4.35 (t, 4H, *J*_{HH} = 5 Hz, OCH₂), 3.99 (q, 4H, *J*_{HH} = 5 Hz, OCH₂), 3.86 (m, 4H, OCH₂), 3.79 (m, 4H, OCH₂), 3.74 (m, 4H, OCH₂), 3.70 (m, 4H, OCH₂), 3.64 (m, 4H, OCH₂), 3.58 (m, 4H, OCH₂), 3.45 (s, 3H, OCH₃), 3.38 (s, 3H, OCH₃); ¹³C{¹H} NMR (CDCl₃) δ 186.1, 149.4, 148.5, 131.0, 129.2, 128.7, 127.0, 126.9, 125.7, 125.1, 122.7, 122.7, 121.6, 121.5, 121.0, 119.7, 114.9, 113.4, 72.21, 72.16, 71.15, 71.11, 70.98, 70.96, 70.84, 70.78, 70.01, 69.95, 69.4, 69.3, 59.3, 59.2; FT-IR (neat) ν (cm⁻¹) 2980, 2923, 2876, 2866, 2833, 2821, 2811, 1760, 1597, 1516, 1485, 1456, 1436, 1403, 1394, 1348, 1326, 1290, 1256, 1227, 1208, 1198, 1143, 1116, 1105, 1099, 1091, 1051, 1040, 1026, 963, 950, 943, 932, 927, 901, 892, 865, 854, 837, 795, 785, 771, 752, 725; UV/vis (CHCl₃): λ_{max}/nm (ε/L mol⁻¹ cm⁻¹): 330 (32257), 342 (56880), 368 (18725), 391 (17815), 459 (4881), 485 (6760); Anal Calc'd for C₄₄H₄₃NO₁₀: C, 70.86; H, 5.81, N, 1.88; Found: C, 70.62; H, 6.09; N, 2.09; MS (MALDI-TOF, DCTB) *m/z* = 784.0837 [M+K]⁺, 768.1177 [M+Na]⁺

8.6.3 Electrochemistry

The electrochemical cell was configured with a glassy carbon working electrode and lithium metal reference and counter electrodes. Working solutions for cyclic voltammetry (CV) were separated from lithium counter and reference electrodes with a glass frit with an average pore size of ~7 nm and thickness of 5 mm obtained from Advanced Glass and Ceramics (St. James, NC, USA). In order to account for the potential drop across a highly resistive frit, all CV measurements were corrected for iR drop by measuring the impedance between the working and reference electrodes with an applied AC voltage with frequency of 100 kHz and correcting for 85% of the expected iR drop. CVs of polysulfide alone, BPI alone, and BPI with polysulfide were conducted in electrolyte with 2.5 mM BPI and 12 mM sulfur of nominal composition Li₂S₈ at 1 mV s⁻¹.

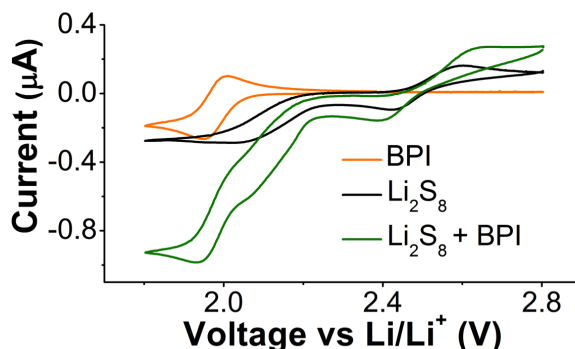


Figure 8.6: Cyclic voltammograms of BPI (orange trace, 2.5 mM BPI), Li₂S₈ (black trace, 12 mM sulfur), and BPI and Li₂S₈ (green trace, 12 mM sulfur, 2.5 mM BPI) at 1 mV s⁻¹. The electrolyte is 0.50 M LiTFSI and 0.15 M LiNO₃ in diglyme, with a glassy C working electrode and lithium reference and counter electrodes.

8.6.4 Li–S cell testing

Dropcast BPI on C cloth

0.600 mL tetraglyme was added to BPI (19 mg) and the mixture was heated at 80 °C until the BPI dissolved. A circular piece of C cloth (5 cm diameter) was heated to 80 °C in a Petri dish. The BPI solution was dropcast evenly across the C cloth. The C cloth was then cooled to ambient temperature and dried under reduced pressure for 3 days.

Li–S cell assembly with BPI dropcast on C cloth

Lithium disks (3/8 inch diameter) were punched from 1.5 mm thick Li foil and soaked in electrolyte for > 1 h. One side of the Li disk was scraped with a spatula to expose a shiny Li surface. The scraped side was pressed onto a nickel or stainless steel electrode, 6 µL electrolyte and a piece of Celgard (1/2 inch diameter) were placed on top. Two pieces of C cloth (with or without BPI) were placed in the well (0.5 mm deep, 1/4 inch diameter) of a gold-coated nickel electrode. About 18 µL catholyte (1.0 M sulfur as Li₂S₈ in electrolyte, $\rho = 1.05 \text{ g mL}^{-1}$) was added to the well with the C cloth (16–22 mg weight of catholyte), the weight was recorded, and the cell assembled.

Solubility of BPI

Solutions of BPI in electrolyte were prepared with 1, 2, 3, 4, and 5 wt% BPI by heating the mixture at 80 °C and allowing the solutions to cool to ambient temperature. The samples containing 1 and 2 wt% BPI remained free-flowing liquids, while samples with 3–5% BPI became gels (as indicated when the electrolyte no longer flows on short time-scales and is stable to inversion), see Figure 8.7. When catholyte solutions of 3 wt% BPI

with 1.0 M Sulfur (as Li_2S_8 in electrolyte) are prepared as specified below, the mixture becomes more viscous, but is not a gel as indicated by being stable to inversion.

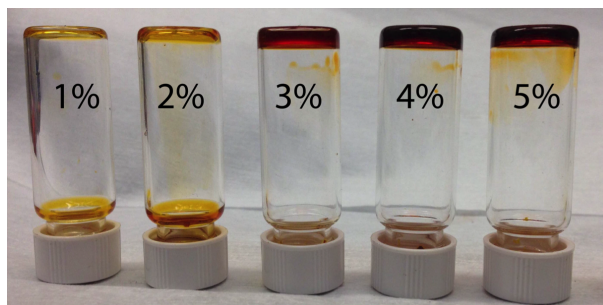


Figure 8.7: BPI at 1–5 *wt%* in electrolyte. At 1 and 2 *wt%* BPI, the mixtures remain free-flowing liquids, while at 3 *wt%* and above gels form, as shown by being stable to inversion.

Li–S cell assembly with BPI in solution

8.1 mg BPI and 219 μL electrolyte were added to a vial and heated to 120 $^{\circ}\text{C}$ until dissolved. The vial was moved to a 60 $^{\circ}\text{C}$ stir plate for 30 m. 31.2 μL of a solution of Li_2S_8 (8.0 M sulfur in electrolyte) was added to the vial, the mixture was vortexed to mix, and the mixture kept at 60 $^{\circ}\text{C}$ until it was added to the cell. Lithium disks (3/8 inch diameter) were punched from 1.5 mm thick Li foil and soaked in electrolyte for > 1 h. One side of the Li disk was scraped with a spatula to expose a shiny Li surface. The scraped side was pressed onto a nickel or stainless steel electrode, 6 μL electrolyte and a piece of Celgard (1/2 inch diameter) were placed on top. Two pieces of C cloth were placed in the well (0.5 mm deep, 1/4 inch diameter) of a gold-coated nickel electrode. About 18 μL catholyte was added to the well with the C cloth (16–22 mg weight of catholyte), the weight was recorded, and the cell assembled.

Control Li–S cells without carbon cloth

Electrochemical cells were assembled as above, but without C cloth.

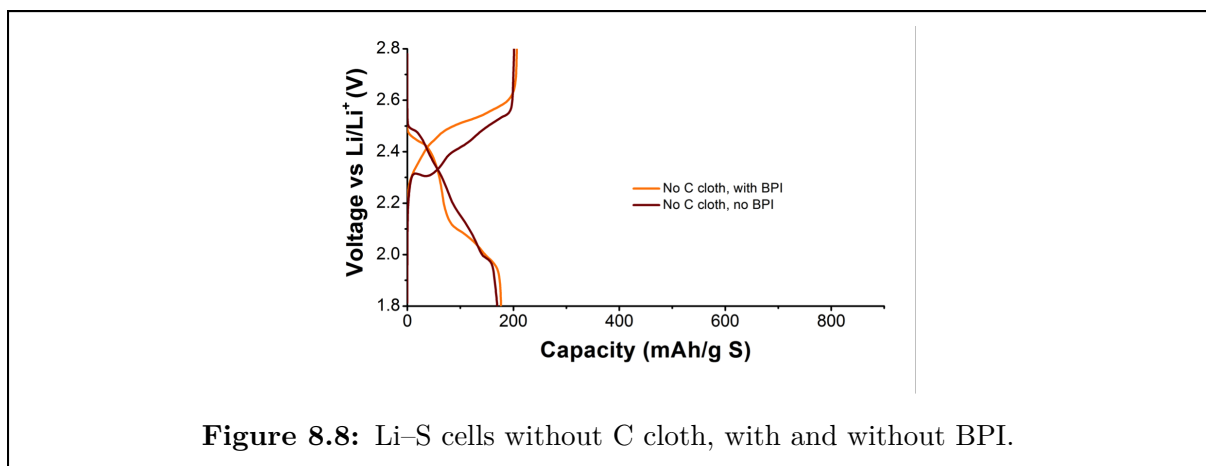
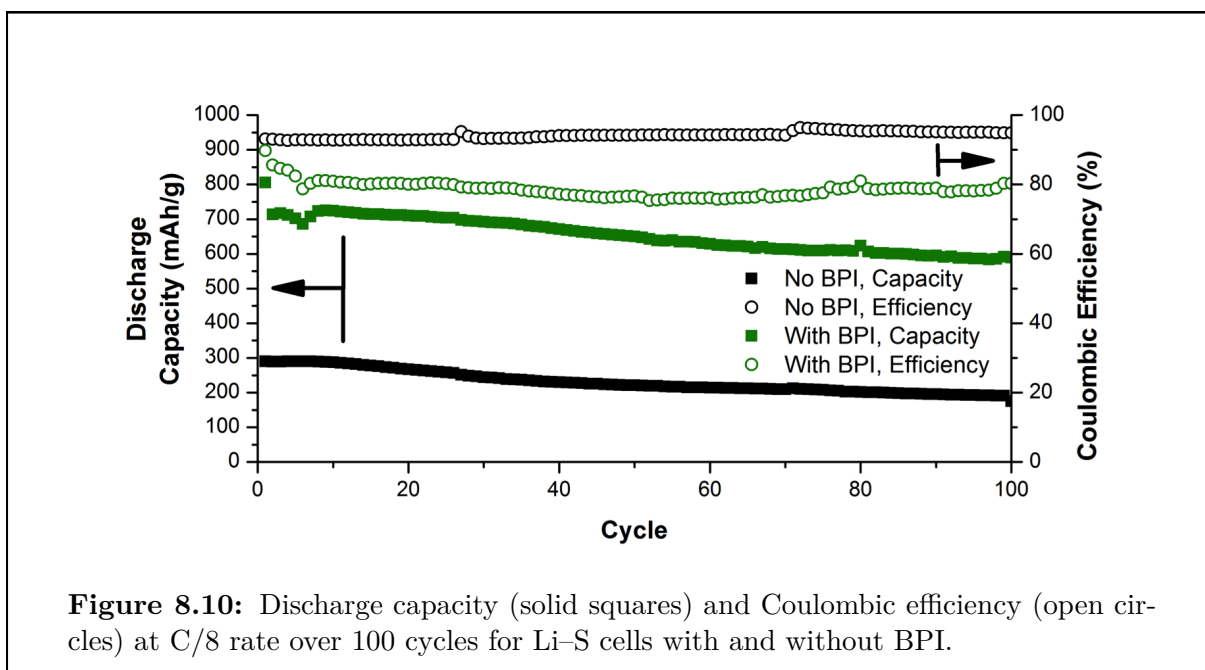
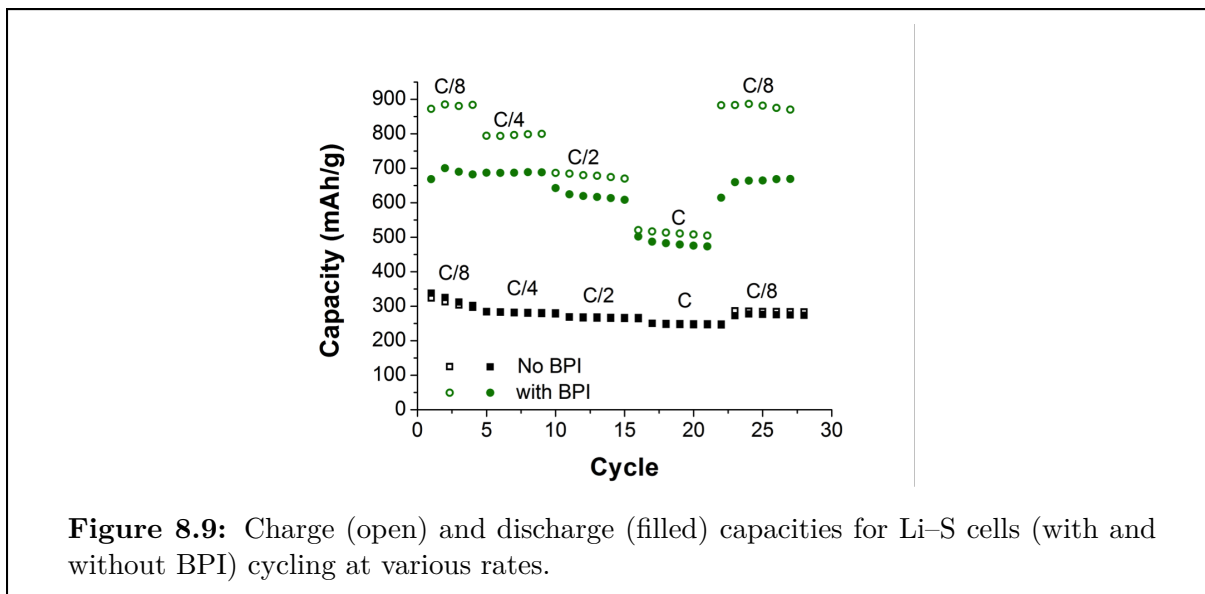
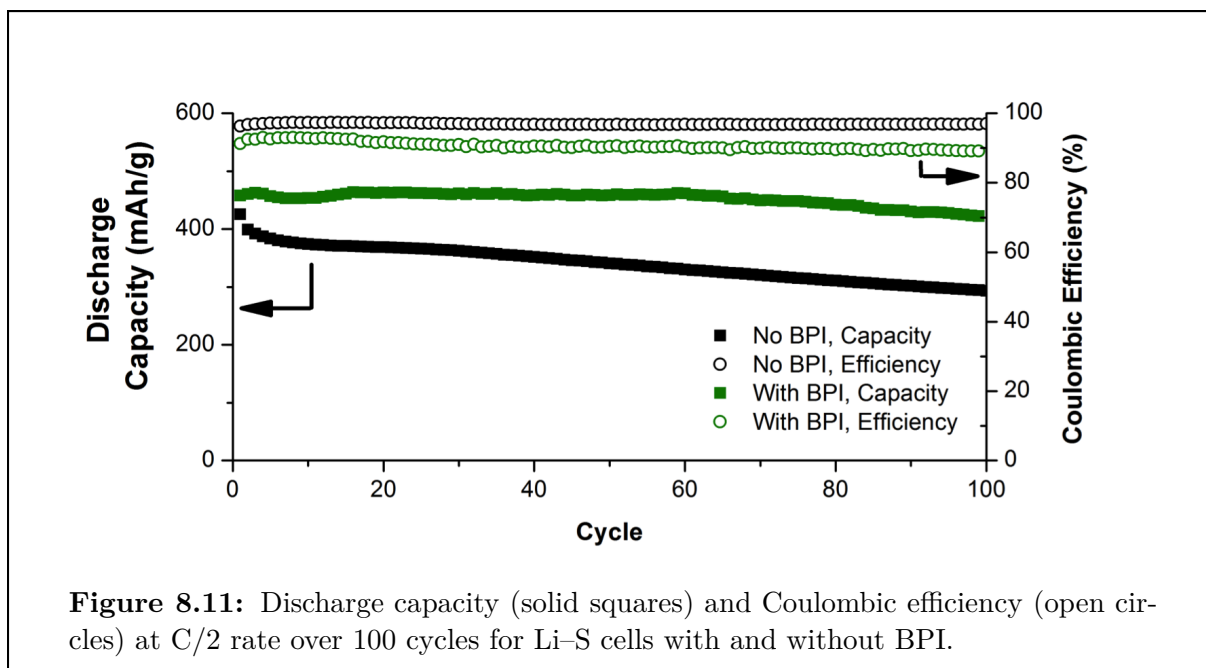


Figure 8.8: Li-S cells without C cloth, with and without BPI.

Control Li-S cells without sulfur

In order to test if BPI is contributing to the observed capacities, Li-S cells were prepared with BPI, but no sulfur species. Cells were assembled as above, using C cloth containing BPI, but rather than polysulfide solution, 18 μL of electrolyte was used to fill the well in the electrode. The cells were cycled at similar current densities to cells with polysulfide (the electrolyte was weighed, and a C/8 current density was calculated as if 1.0 M sulfur as Li_2S_8 in electrolyte had been added). Of three Li-S cells run, the greatest charge observed due to BPI was 3.72×10^{-3} mAh. The electrochemical cells with BPI and 1.0 M sulfur average 0.42 mAh. The charging of BPI contributes at maximum 0.9% of the total capacity of the cell.





8.6.5 Scanning electron microscopy at various states of charge

Sample preparation

Li-S cells were assembled as described above, both with and without BPI. They were cycled at C/8. The cells were stopped at different states of discharge: (1) nucleation of Li_2S , (2) during the plateau, (3) discharged, and (4) recharged, as indicated in Figures 8.13 and 8.14. After the cells were stopped, they were immediately disassembled inside the glove box. The top piece of the two carbon cloth pieces was removed and washed with CHCl_3 (5 x 0.5 mL), and dried under vacuum for 5 min. The samples were affixed to the stage for the SEM inside the glove box, brought to the SEM in a sealed jar, and transferred to the microscope sample chamber with < 5 s exposure to air.

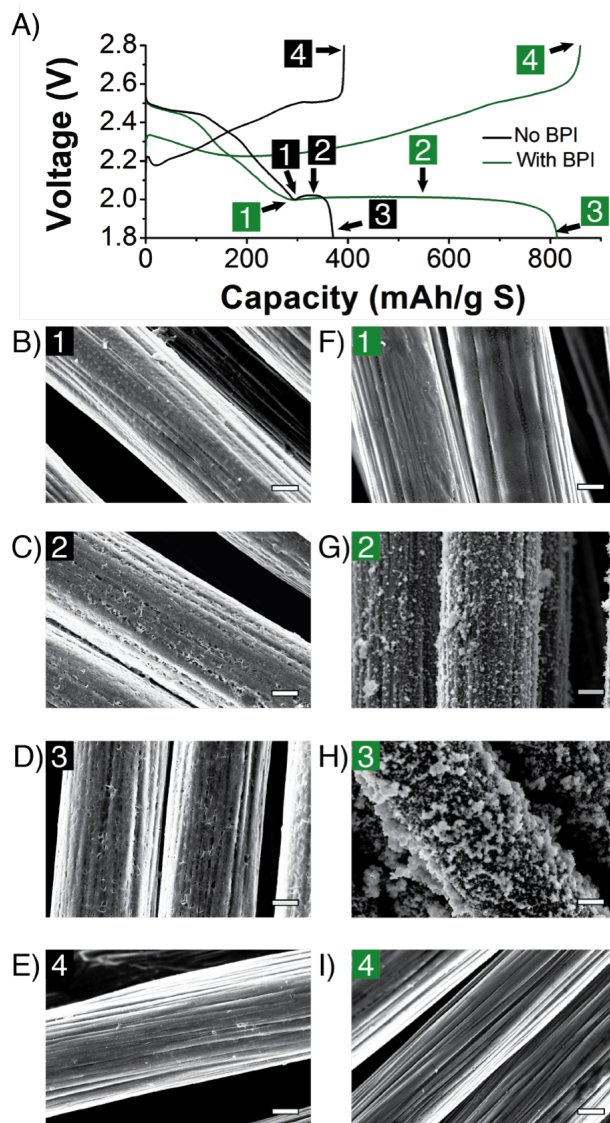
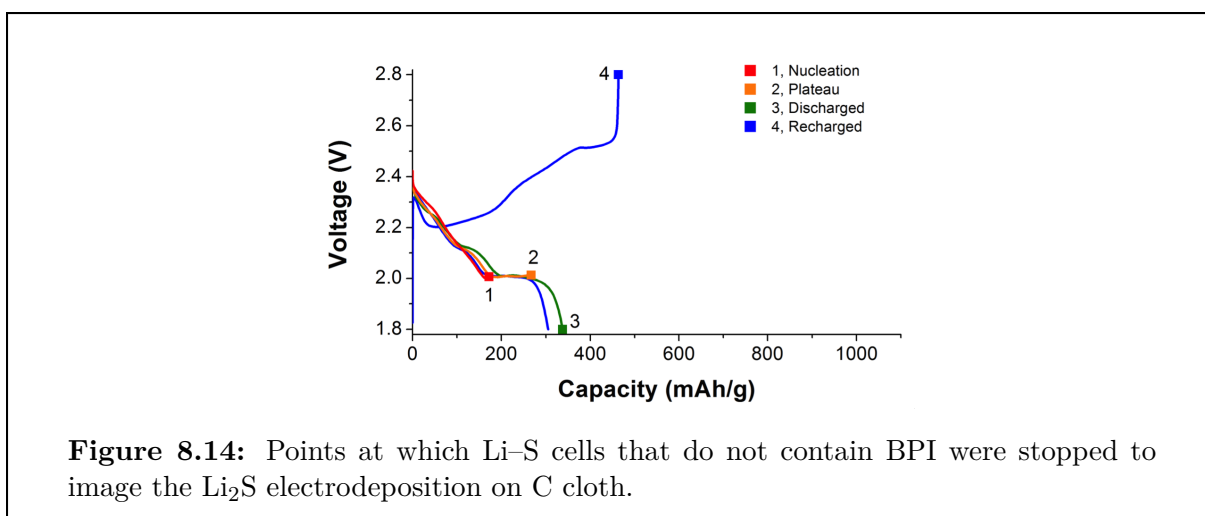
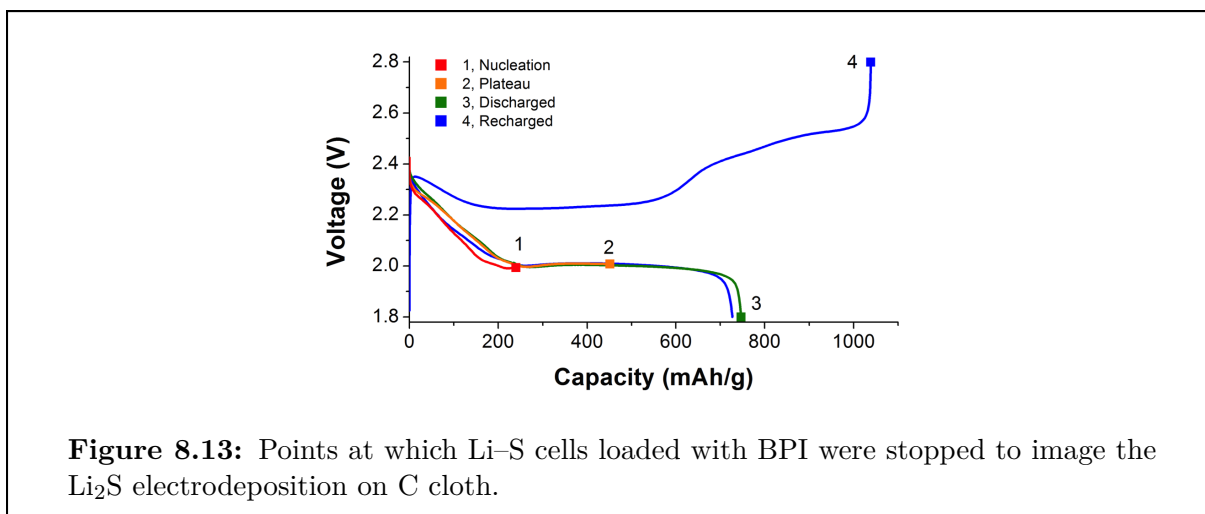


Figure 8.12: Progressive electrodeposition of Li_2S on C cloth, imaged at different states-of-charge in Li-S cells with BPI absent (left) and BPI present (right) and presented here at lower magnification than in Figure 8.3. A) The first discharge/charge cycle at $C/8$ rate. States-of-charge are indicated as Points 1–4 where separate cells were stopped to image the Li_2S deposits on the C cloth. SEM images of Li_2S electrodeposition on C cloth from a cell without BPI are shown: B) at nucleation (Point 1); C) during the Li_2S voltage plateau (Point 2); D) at the end of discharge (Point 3); and E) after recharge (Point 4). SEM images of Li_2S electrodeposition on C cloth from a cell with BPI: F) at nucleation (Point 1); G) during the Li_2S voltage plateau (Point 2); H) at the end of discharge (Point 3); and I) after recharge (Point 4). Scale bars = 2 μm .



Morphology of Li_2S from dissolved BPI cell

Similar porous, 3D morphologies of Li_2S are observed on C cloth after discharge when BPI is introduced as dissolved in electrolyte rather than dropcast on C cloth.

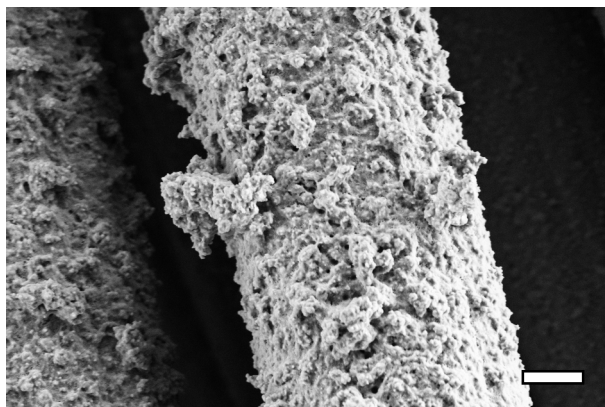
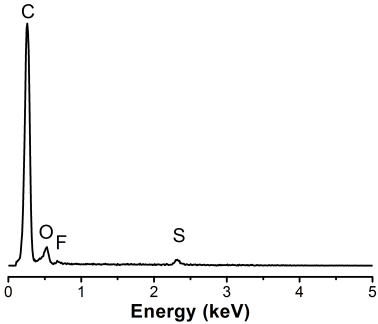
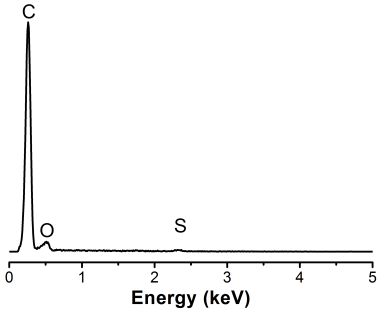
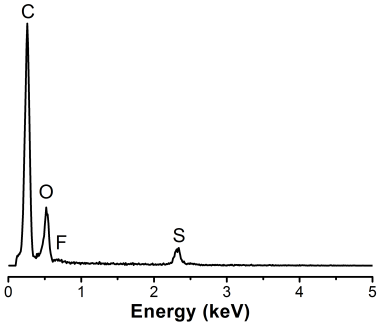
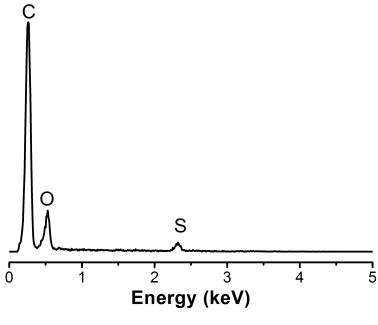
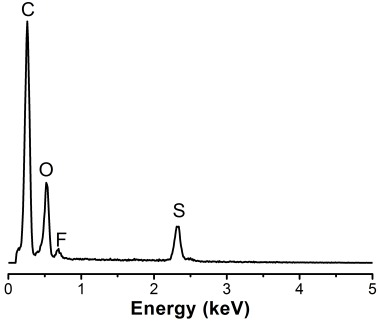
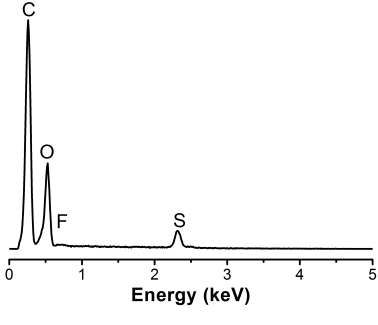


Figure 8.15: Li_2S on C cloth after discharge of a cell containing BPI, but introduced as part of the electrolyte. C cloth was removed and washed by the standard procedure. Scale bar = 2 μm .

Table 8.1: EDX spectra Li_2S deposited on C cloth at various states of charge. Oxygen is present due to the formation of LiOH upon brief (< 5 s) exposure of the samples to ambient moisture when transferring the samples to the instrument. The number corresponds to the points labeled in Figure 8.3 and 8.12.

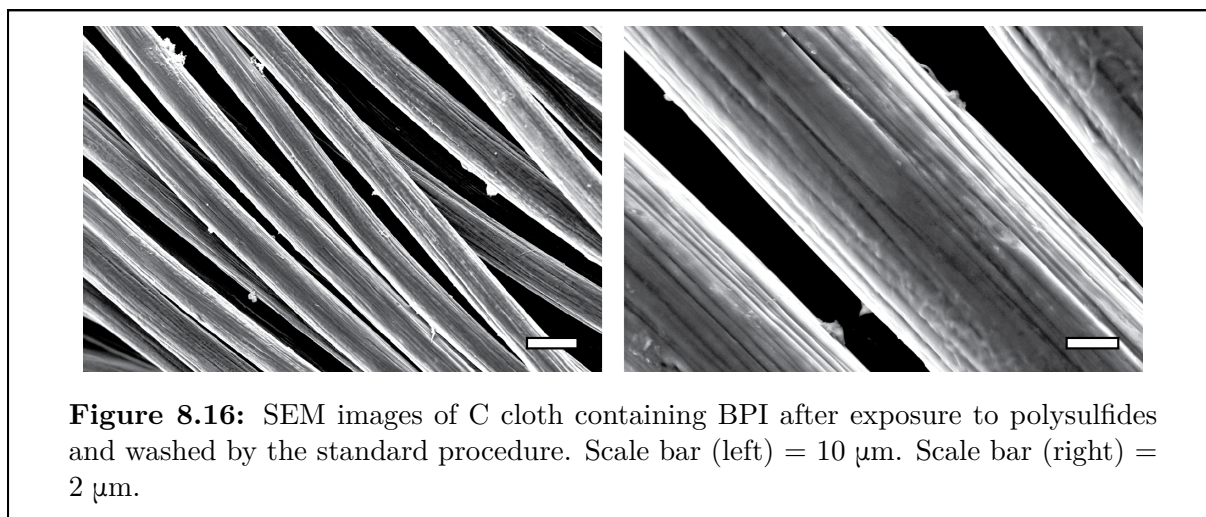
State of Charge	With BPI	No BPI
Li-S Cell with No Polysulfide – Discharged		
Before Cycling		

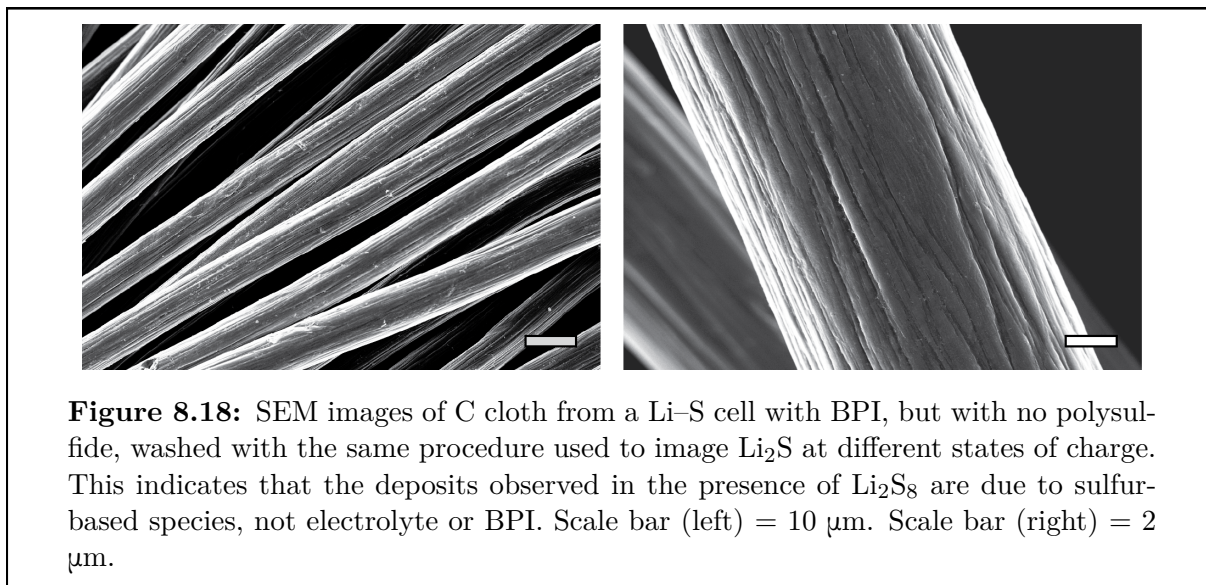
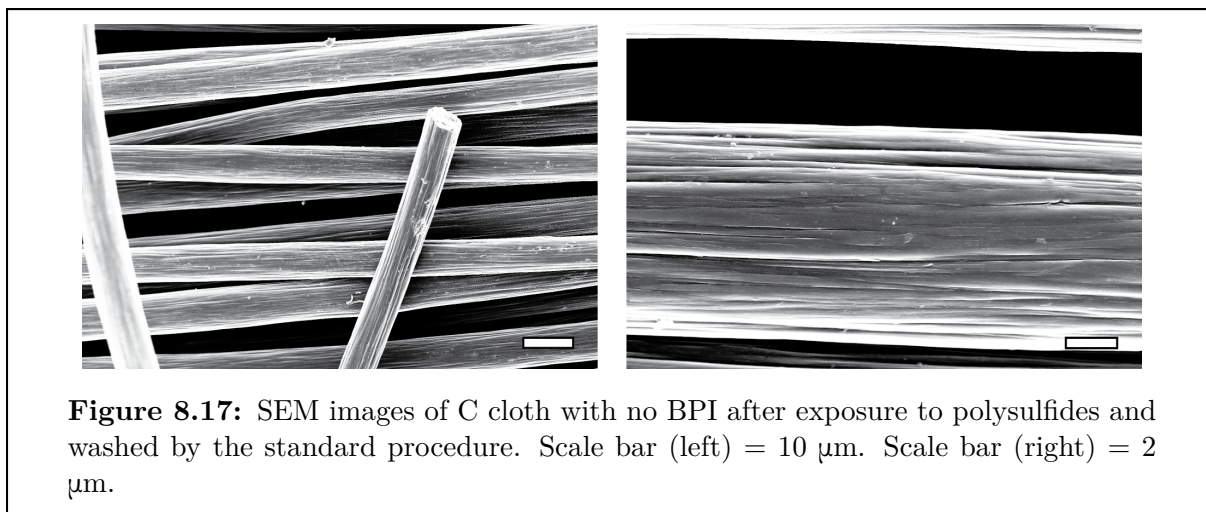
State of Charge	With BPI	No BPI
Nucleation (1)		
Plateau (2)		
Discharged (3)		

State of Charge	With BPI	No BPI
Charged (4)		

Images of C Cloth before Li–S cell cycling

Two C cloth disks (with or without BPI) were placed in an electrode well. The sulfur catholyte (18 μL , 1.0 M sulfur as Li_2S_8 in electrolyte) was added and the mixture was allowed to sit for 10 min. The C cloth disks were then removed and washed with the same procedure as described above. Figures 8.16–8.18 indicate that the washing procedure removes polysulfides, electrolyte, and BPI.





8.6.6 Potentiostatic electrodeposition experiments

Procedure

Cells were initially held at 2.09 V for up to 9 h, or until current fell below 6 μA , to minimize the amount of higher-order polysulfides in the solution. The cells were then held at 1.95 V or 2.00 V to initiate nucleation and growth of Li_2S .

Model of electrodeposition

In this work, electrodeposition is modeled as being on a planar surface, which we believe is a reasonable assumption considering that deposited layers are thin compared to the diameter of the carbon fibers. Furthermore, in a previous work we have shown that electrodeposition kinetics are limited by surface reaction rate rather than diffusion, and that the deposited insulating sulfide forms a passivating film that progressively reduces the carbon surface area available for deposition, resulting in two-dimensional growth and a thin film-like morphology.^[220]

For potentiostatic electrodeposition under these conditions, the current density *vs.* time relation is of the form:

$$\frac{J}{J_m} = \left(\frac{t}{t_m}\right) \exp\left[-\frac{1}{2}\left(\frac{t^2}{t_m^2} - 1\right)\right]$$

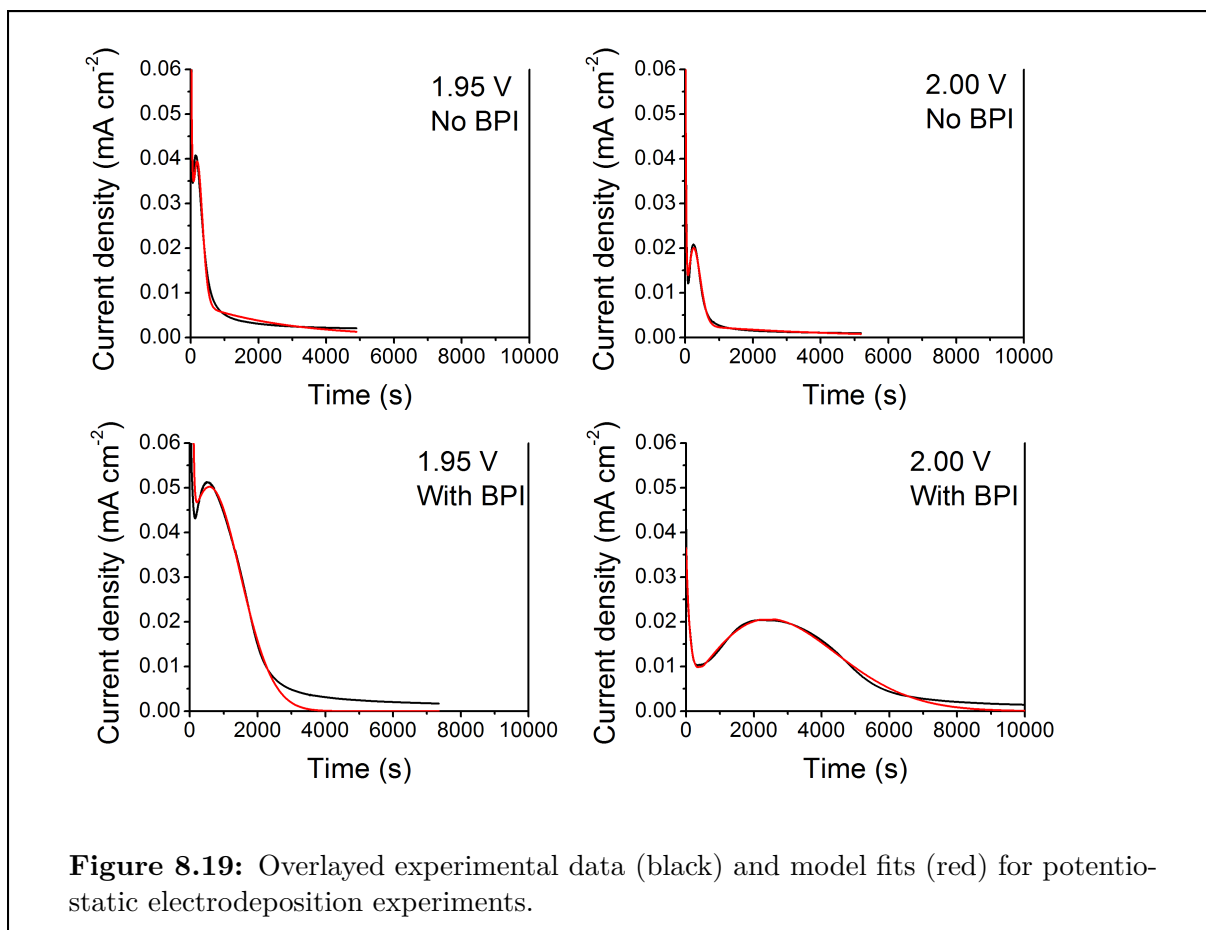
where J_m and t_m are the maximum current and the time at which the maximum current occurs, respectively.^[349, 350] This equation follows from the Avrami equation, which accounts for the impingement of islands after growth. In particular, the exponential factor represents the probability (from the Poisson distribution) that a given area element of the electrode is un-transformed and therefore available for further reaction. The width of the peak can be used to determine the growth rate constant k :

$$t_m = \left(2\pi N_0 k^2\right)^{-1/2}$$

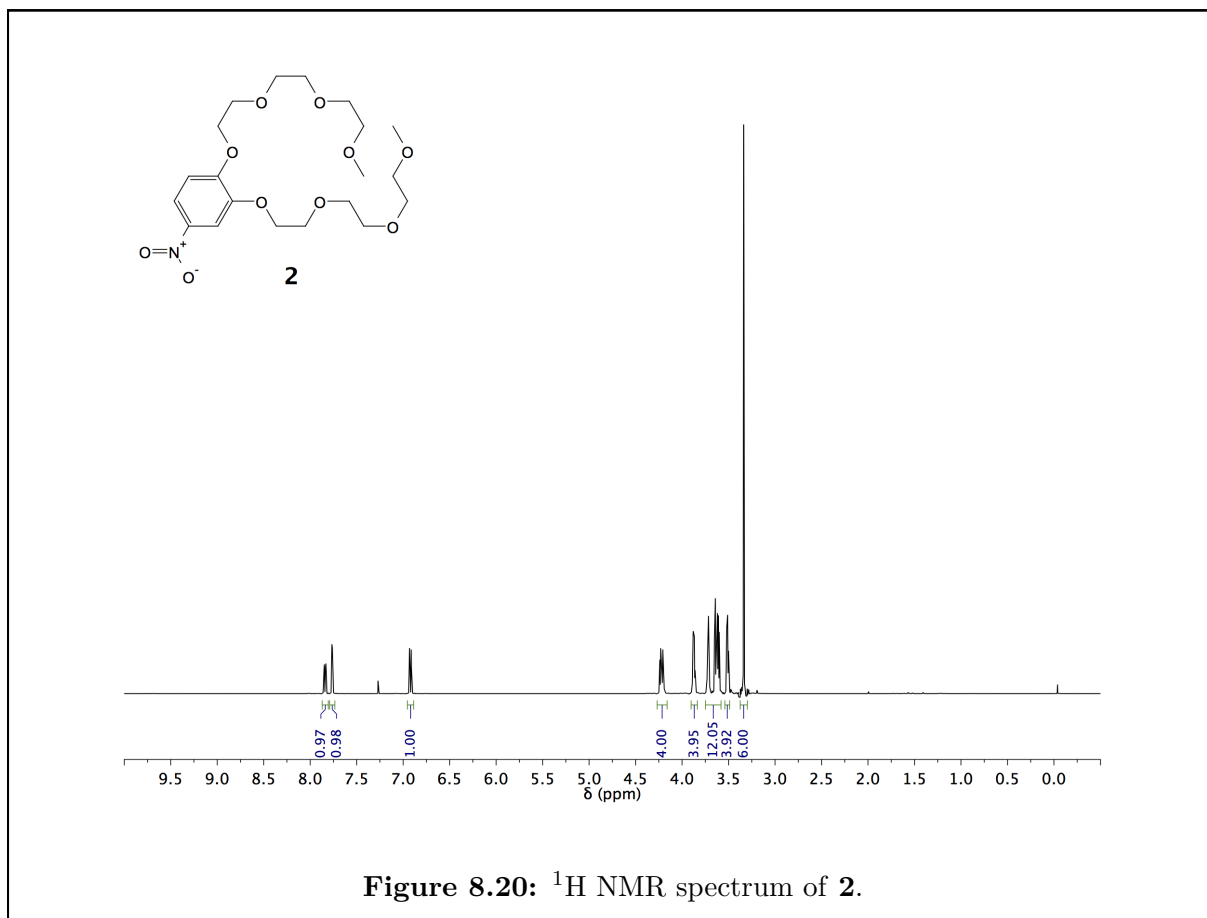
where N_0 is the number density of nuclei.

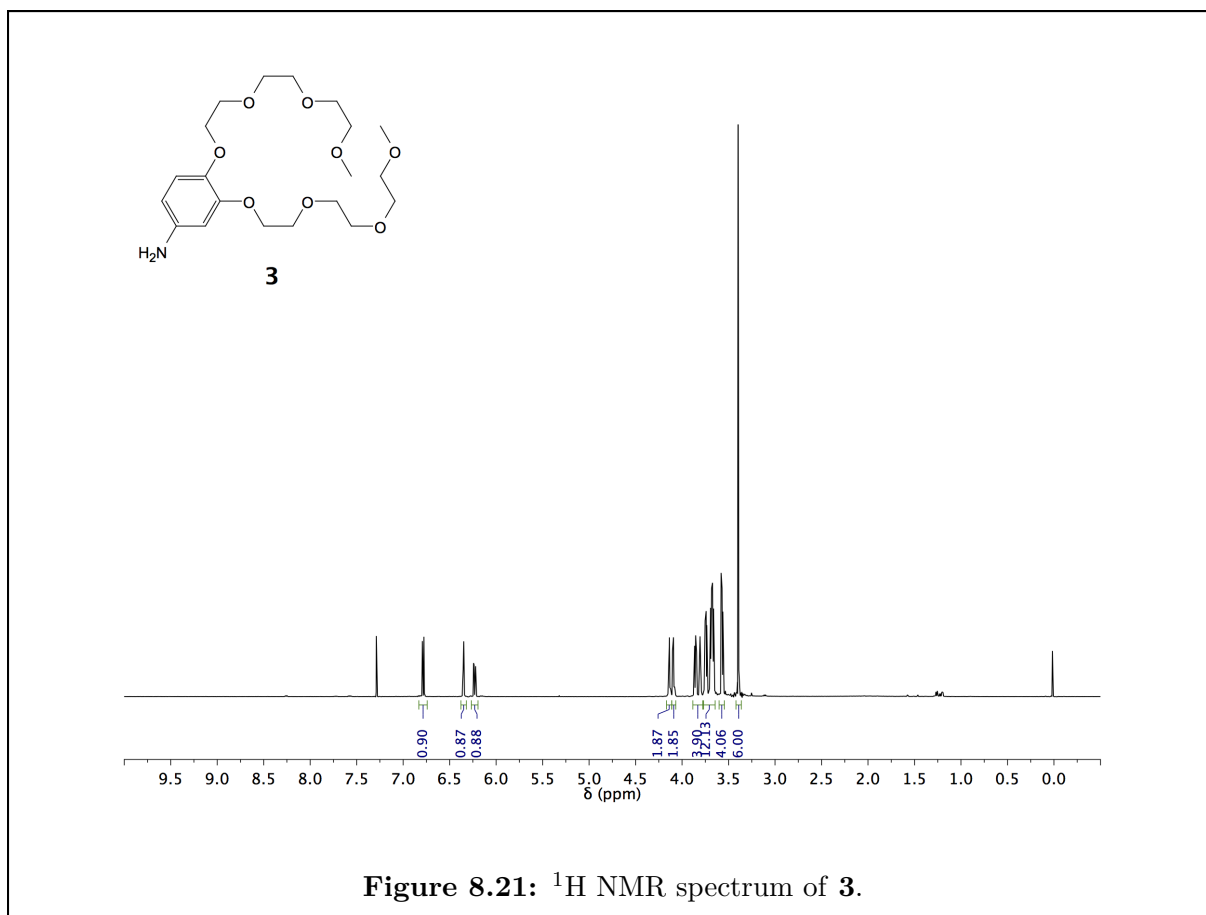
In the case of electrodeposition of Li_2S involving the redox mediator BPI, we model the additional current due to the mediator (which was assumed to be limited by the available surface area of the C cloth) with the term c . We assume that the rate-limiting step is due to BPI. If this were not the case, a horizontal asymptote would be present in the current-time plot. The resulting current due to BPI is c times the available surface area of the electrode. Our modified current-time relation is:

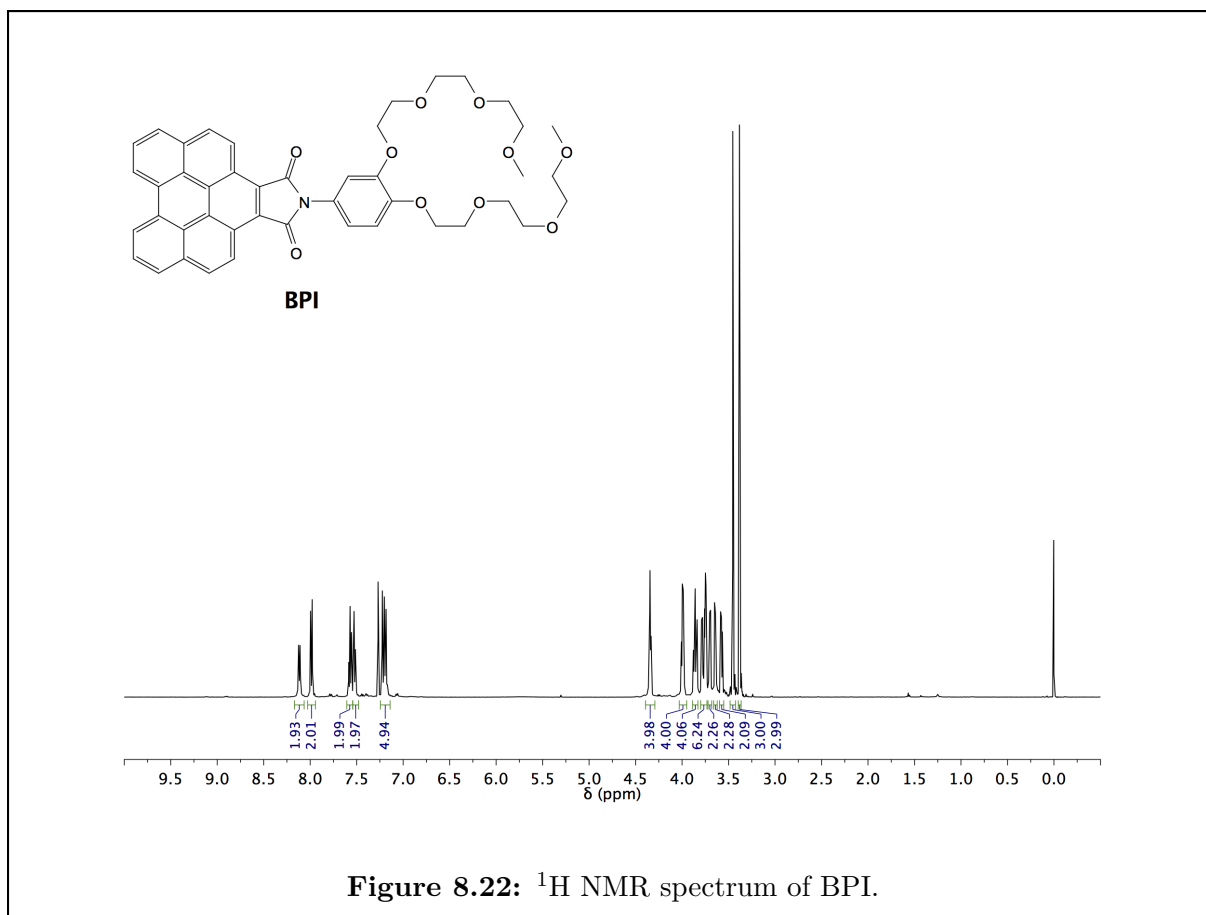
$$\frac{J}{J_m} = \left(\frac{t}{t_m} + c\right) \exp\left[-\frac{1}{2}\left(\frac{t^2}{t_m^2} - 1\right)\right]$$



8.6.7 NMR spectra







8.6.8 Acknowledgements

This chapter is the result of a collaboration between myself, L.C.H. Gerber, P.D. Frischmann, F.Y. Fan, X. Qu, A.M. Scheuermann, K. Persson, Y.-M. Chiang, and B.A. Helms, and I am thankful to all my co-authors for their help with this work. This work was supported by the Joint Center for Energy Storage Research, an Energy Innovation Hub funded by the U.S. Department of Energy, Office of Science, Office of Basic Energy Sciences. Portions of the work—including BPI synthesis, characterization, and experimental validation as a redox mediator in Li-S cells—were carried out as a user project at the Molecular Foundry, which is supported by the Office of Science, Office of Basic Energy Sciences, of the U.S. Department of Energy under contract no. DE-AC02-05CH11231. This research used resources of the National Energy Research Scientific Computing Center, a DOE Office of Science User Facility supported by the Office of Science of the U.S. Department of Energy under Contract No. DE-AC02-05CH11231. S.E.D. was supported by the Department of Defense through the National Defense Science & Engineering Graduate Fellowship Program.

Chapter 9

Conclusion and Outlook

Improving our molecular-level understanding of electrochemical materials is critical if society is to convert, use, and store energy efficiently. In this dissertation, I outlined my work with three different classes of electrochemical materials: nanocrystals, membranes, and redox mediators. In each case, my work opens up a number of exciting future research directions, which I have outlined below.

9.1 Controlling nanocrystal surface chemistry

In chapter 2, I described my work in developing a new approach for removing surface-bound ligands from colloidal nanocrystals (NCs). By stabilizing the NC surface during ligand-stripping, I was able to prepare inks of “naked” NCs for a wider variety of compositions than was previously possible. This work opens up a number of interesting future directions for studying NC surface chemistry and its effect on their electrochemical properties. The colloidal stability of naked NC inks is promising for their use as dispersed electrocatalysts and flowable energy storage materials. Of particular interest is understanding the role of electrochemical reactions on the NCs colloidal dispersability. In addition to applications that use naked NC inks directly as functional materials, these inks will also enable scientists to prepare highly ordered ligand-free films of NCs and NC/polymer composites. These materials have been difficult to prepare in the past, particularly for technologically relevant materials like the lead chalcogenides. Now that these materials are accessible, it should be possible to study the role of NC ordering on thermal and electronic transport in a more systematic way. Finally, naked NC inks are expected to be useful in the preparation of energy storage and conversion devices, including batteries, capacitors, and thermoelectrics. They will be particularly useful in the case of printed devices, where the colloidal stability of naked NC inks is critical.

9.2 Size-selective membranes for energy storage applications

In chapters 3–6, I described my work with size-sieving membranes based on polymers of intrinsic microporosity (PIMs). My results show that this class of membrane materials is promising for next-generation energy storage devices. However, further improvements can be made with continued study of these materials. In particular, there is a pressing need for understanding the effect of electrolyte infiltration on the pore structure of PIM membranes, the role of cross-linking in controlling membrane swelling, and the mechanism of ion conduction through PIM membranes.

9.2.1 The effect of electrolyte on PIM pore structure

PIMs were originally designed for gas separation, and most of the characterization of their pore structure was in the dry state.^[59] Upon infiltrating the pores of PIM membranes with electrolyte, it is likely that the pore structure changes. However, little is known about the pore structure of electrolyte-filled PIM membranes. There are several approaches to understanding the pore structure of electrolyte-filled PIM membranes, including computational chemistry,^[146] scattering experiments,^[215, 352] and NMR relaxation experiments.^[353] By understanding the effects of electrolyte-infiltration on the pore structure of PIM membranes, we can choose electrolytes and PIM chemistries that lead to desirable pore-size distributions and structures.

9.2.2 The role of cross-linking in controlling membrane swelling

In addition to understanding the effect of electrolyte infiltration on pore structure, it is also important to have a means of controlling the change in pore structure that occurs upon electrolyte infiltration. In chapter 4, I showed that reactivity of PIM membranes with lithium polysulfides led to a change in their degree of swelling, which changed their blocking properties. I was able to prevent this undesirable change in membrane swelling by cross-linking the membrane. This shows that cross-linking is a viable strategy for controlling the pore structure of electrolyte-filled PIM membranes. However, relatively little is known about the effect of cross-linking on the porosity and tortuosity of PIM membranes. To address this knowledge gap, it is critical that we develop new cross-linking chemistries and study their effect on the polymer structure with the same techniques described in section 9.2.1.

9.2.3 The mechanism for ion conduction in PIM membranes

Relatively little work has been done in understanding the mechanism of ion conduction in electrolyte-filled membranes, although this is clearly an important research direction. In chapter 3, I showed that the ionic conductivity of electrolyte-filled PIMs generally scaled with the electrolyte conductivity, which suggests that ionic current is carried by electrolyte that fills the pore voids. However, it is not known if this is general to all electrolytes or what, if any, role the membrane's polymer chain mobility plays in ion conduction. This can be addressed by studying the ionic conductivity of PIM membranes as a function of temperature for different electrolytes. By monitoring the temperature-dependence of ionic conductivity, the role of polymer chain mobility should become more clear. It will also be important to systematically study the effect of ion and solvent size on ionic conductivity and transference number, as these properties are critical to the PIM membrane's role in a battery.

9.3 Controlling the electrodeposition of insulating active-species in batteries

In chapters 7–8, I described my work with redox-mediators that aid in the electrodeposition of insulating active-species in Li–S batteries. While the performance gains upon incorporating redox mediators were impressive, we know relatively little about the effects of redox-mediator self-assembly, electron transfer kinetics, and electrode surface chemistry on the electrodeposition process. By advancing our knowledge in these areas, new redox-mediators and electrodes can be designed that will move Li–S battery chemistry closer to implementation.

As described in section 1.4.1, the redox-mediator’s redox potential controls both the thermodynamics of the reaction between the redox-mediator and active-species and the kinetics of electron transfer to and from the redox-mediator. In my discussion, I arbitrarily picked values for the equilibrium and rate constants that would allow for remote electrodeposition of insulating active-species. However, it is not clear what redox-mediator potential will give the most sustained electrodeposition of active material. For example, consider two redox-mediators intended to aid in cathodic electrodeposition of an insulating active-species, where one redox-mediator’s formal potential is 40 mV negative of the active-species, and the other redox-mediator’s formal potential is 80 mV negative of the active-species. Clearly, the first redox-mediator will have faster reduction kinetics at a given potential than the redox-mediator with the more negative reduction potential. However, the first redox-mediator will also have less driving force to react with the active-species, which will allow more active-species to reach the electrode surface, which will in turn speed up the active-species reduction kinetics. Thus, there is a non-obvious tradeoff between thermodynamics and kinetics that must be balanced to maximize the electrodeposition of an insulating active-species. This can be addressed by simulating, for different battery discharge conditions, the mass transport and kinetics of both the redox-mediator and active-species. Another area of interest is the role of redox-mediator self-assembly on the electrodeposition of insulating active-species. For redox-mediators that can self-assemble, charge transport can happen either through diffusion of the redox-mediator or charge-hopping along a network of redox-mediators. This alternate pathway may allow for electrodeposition farther from the electrode surface, but has not been systematically studied. Once each of these knowledge gaps are addressed, redox mediators will be invaluable for next-generation energy storage technologies.

Bibliography

- [1] Nakicenovic, N., Swart, R., Eds. *Special Report on Emissions Scenarios*; 2000.
- [2] Grätzel, M. *J. Photochem. Photobiol., A* **2004**, *164*, 3.
- [3] Kamat, P. V. *J. Phys. Chem. C* **2008**, *112*, 18737.
- [4] Lewis, N. S. *Science* **2016**, *351*, aad1920.
- [5] Dunn, B.; Kamath, H.; Tarascon, J.-M. *Science* **2011**, *334*, 928.
- [6] Thackeray, M. M.; Wolverton, C.; Isaacs, E. D. *Energy Environ. Sci.* **2012**, *5*, 7854.
- [7] Bell, L. E. *Science* **2008**, *321*, 1457.
- [8] Haase, M.; Schäfer, H. *Angew. Chem., Int. Ed.* **2011**, *50*, 5808.
- [9] Rogach, A. L.; Gaponik, N.; Lupton, J. M.; Bertoni, C.; Gallardo, D. E.; Dunn, S.; Pira, N. L.; Paderi, M.; Repetto, P.; Romanov, S. G.; O'Dwyer, C.; Torres, C. M. S.; Eychmüller, A. *Angew. Chem., Int. Ed.* **2008**, *47*, 6538.
- [10] Wang, C.; Shim, M.; Guyot-Sionnest, P. *Science* **2001**, *291*, 2390.
- [11] Goriparti, S.; Miele, E.; De Angelis, F.; Di Fabrizio, E.; Zaccaria, R. P.; Capiglia, C. *J. Power Sources* **2014**, *257*, 421.
- [12] Wang, R. Y.; Feser, J. P.; Lee, J.-S.; Talapin, D. V.; Segalman, R. A.; Majumdar, A. *Nano Lett.* **2008**, *8*, 2283.
- [13] Talapin, D. V.; Murray, C. B. *Science* **2005**, *310*, 86.
- [14] Law, M.; Luther, J. M.; Song, Q.; Hughes, B. K.; Perkins, C. L.; Nozik, A. J. *J. Am. Chem. Soc.* **2008**, *130*, 5974.
- [15] Zarghami, M. H.; Liu, Y.; Gibbs, M.; Gebremichael, E.; Webster, C.; Law, M. *ACS Nano* **2010**, *4*, 2475.
- [16] Anderson, N. C.; Hendricks, M. P.; Choi, J. J.; Owen, J. S. *J. Am. Chem. Soc.* **2013**, *135*, 18536.

- [17] Moreels, I.; Fritzinger, B.; Martins, J. C.; Hens, Z. *J. Am. Chem. Soc.* **2008**, *130*, 15081.
- [18] De Roo, J.; Van den Broeck, F.; De Keukeleere, K.; Martins, J. C.; Van Driessche, I.; Hens, Z. *J. Am. Chem. Soc.* **2014**, *136*, 9650.
- [19] Owen, J. S.; Park, J.; Trudeau, P.-E.; Alivisatos, A. P. *J. Am. Chem. Soc.* **2008**, *130*, 12279.
- [20] Ji, X.; Copenhaver, D.; Sichmeller, C.; Peng, X. *J. Am. Chem. Soc.* **2008**, *130*, 5726.
- [21] Fritzinger, B.; Capek, R. K.; Lambert, K.; Martins, J. C.; Hens, Z. *J. Am. Chem. Soc.* **2010**, *132*, 10195.
- [22] Morris-Cohen, A. J.; Vasilenko, V.; Amin, V. A.; Reuter, M. G.; Weiss, E. A. *ACS Nano* **2012**, *6*, 557.
- [23] Peterson, M. D.; Jensen, S. C.; Weinberg, D. J.; Weiss, E. A. *ACS Nano* **2014**, *8*, 2826.
- [24] Rosen, E. L.; Buonsanti, R.; Llordes, A.; Sawvel, A. M.; Milliron, D. J.; Helms, B. A. *Angew. Chem., Int. Ed.* **2012**, *51*, 684.
- [25] Rosen, E. L.; Sawvel, A. M.; Milliron, D. J.; Helms, B. A. *Chem. Mater.* **2014**, *26*, 2214.
- [26] Doris, S. E.; J., L. J.; Li, C.; Wills, A. W.; Urban, J. J.; Helms, B. A. *J. Am. Chem. Soc.* **2014**, *136*, 15702.
- [27] Ondry, J. C.; Robbennolt, S.; Kang, H.; Yan, Y.; Tolbert, S. H. *Chem. Mater.* **2016**, *28*, 6105.
- [28] Girishkumar, G.; McCloskey, B.; Luntz, A. C.; Swanson, S.; Wilcke, W. *J. Phys. Chem. Lett.* **2010**, *1*, 2193.
- [29] Christensen, J.; Albertus, P.; Sanchez-Carrera, R. S.; Lohmann, T.; Kozinsky, B.; Liedtke, R.; Ahmed, J.; Kojic, A. *J. Electrochem. Soc.* **2012**, *159*, R1.
- [30] Bruce, P. G.; Freunberger, S. A.; Hardwick, L. J.; Tarascon, J.-M. *Nat. Mater.* **2012**, *11*, 19.
- [31] Manthiram, A.; Chung, S.-H.; Zu, C. *Adv. Mater.* **2015**, *27*, 1980.
- [32] Ji, X.; Nazar, L. F. *J. Mater. Chem.* **2010**, *20*, 9821.

- [33] Manthiram, A.; Fu, Y.; Chung, S.-H.; Zu, C.; Su, Y.-S. *Chem. Rev.* **2014**, *114*, 11751.
- [34] Yin, Y.-X.; Xin, S.; Guo, Y.-G.; Wan, L.-J. *Angew. Chem., Int. Ed.* **2013**, *52*, 13186.
- [35] Ji, X.; Lee, K. T.; Nazar, L. F. *Nat. Mater.* **2009**, *8*, 500.
- [36] Yang, Y.; Zheng, G.; Cui, Y. *Chem. Soc. Rev.* **2013**, *42*, 3018.
- [37] Darling, R.; Gallagher, K. G.; Kowalski, J. A.; Ha, S.; Brushett, F. R. *Energy Environ. Sci.* **2014**, *7*, 3459.
- [38] Brushett, F. R.; Vaughey, J. T.; Jansen, A. N. *Adv. Energy Mater.* **2012**, *2*, 1390.
- [39] Sevov, C. S.; Brooner, R. E. M.; Chénard, E.; Assary, R. S.; Moore, J. S.; Rodríguez-López, J.; Sanford, M. S. *J. Am. Chem. Soc.* **2015**, *137*, 14465.
- [40] Wang, W.; Luo, Q.; Li, B.; Wei, X.; Li, L.; Yang, Z. *Adv. Funct. Mater.* **2013**, *23*, 970.
- [41] Knauth, P. *Solid State Ionics* **2009**, *180*, 911.
- [42] Wang, M.; Zhao, F.; Dong, S. *J. Phys. Chem. B* **2004**, *108*, 1365.
- [43] Jin, Z.; Xie, K.; Hong, X.; Hu, Z.; Liu, X. *J. Power Sources* **2012**, *218*, 163.
- [44] Hallinan, D., Jr.; Balsara, N. P. *Annu. Rev. Mater. Res.* **2013**, *43*, 503.
- [45] Giddings, J. C.; Kucera, E.; P., R. C.; Myers, M. N. *J. Phys. Chem.* **1968**, *72*, 4397.
- [46] Mason, E. A.; Lonsdale, H. K. *J. Membr. Sci.* **1990**, *51*, 1.
- [47] Caro, J.; Noack, M. *Microporous Mesoporous Mater.* **2008**, *115*, 215.
- [48] Yaghi, O. M.; O’Keeffe, M.; Ockwig, N. W.; Chae, H. K.; Eddaoudi, M.; Kim, J. *Nature* **1999**, *402*, 276.
- [49] Kitagawa, S.; Kitaura, R.; Noro, S. *Angew. Chem., Int. Ed.* **2004**, *43*, 2334.
- [50] Chung, T.-S.; Jiang, L. Y.; Li, Y.; Kulprathipanja, S. *Prog. Polym. Sci.* **2007**, *32*, 483.
- [51] Martin, C. R.; Lakshmi, B. B.; Fisher, E. R.; Che, G. *Nature* **1998**, *393*, 346.
- [52] Hinds, B. J.; Chopra, N.; Rantell, T.; Andrews, R.; Gavalas, V.; Bachas, L. G. *Science* **2004**, *303*, 62.

- [53] Geng, J.; Kim, K.; Zhang, J.; Escalada, A.; Tunuguntla, R.; Comolli, L. R.; Allen, F. I.; Shnyrova, A. V.; Cho, K. R.; Munoz, D.; Wang, Y. M.; Grigoropoulos, C. P.; Ajo-Franklin, C. M.; Frolov, V. A.; Noy, A. *Nature* **2014**, *514*, 612.
- [54] McKeown, N. B.; Budd, P. M. *Chem. Soc. Rev.* **2006**, *35*, 675.
- [55] Budd, P. M.; McKeown, N. B. *Polym. Chem.* **2010**, *1*, 63.
- [56] Li, C.; Ward, A. L.; Doris, S. E.; Pascal, T. A.; Prendergast, D.; Helms, B. A. *Nano Lett.* **2015**, *15*, 5724.
- [57] Doris, S. E.; Ward, A. L.; Frischmann, P. D.; Li, L.; Helms, B. A. *J. Mater. Chem. A* **2016**, *In press*, DOI: 10.1039/c6ta06401a.
- [58] Budd, P. M.; Ghanem, B. S.; Makhseed, S.; McKeown, N. B.; Msayib, K. J.; Tattershall, C. E. *Chem. Commun.* **2004**, 230.
- [59] McKeown, N. B.; Budd, P. M. *Macromolecules* **2010**, *43*, 5163.
- [60] Qu, X.; Jain, A.; Rajput, N. N.; Cheng, L.; Zhang, Y.; Ong, S. P.; Brafman, M.; Maginn, E.; Curtiss, L. A.; Persson, K. A. *Comput. Mater. Sci.* **2015**, *103*, 56.
- [61] Cheng, L.; Assary, R. S.; Qu, X.; Jain, A.; Ong, S. P.; Rajput, N. N.; Persson, K.; Curtiss, L. A. *J. Phys. Chem. Lett.* **2015**, *6*, 283.
- [62] Thompson, R. B.; Ginzburg, V. V.; Matsen, M. W.; Balazs, A. C. *Macromolecules* **2002**, *35*, 1060.
- [63] Min, Y.; Akbulut, M.; Kristiansen, K.; Golan, Y.; Israelachvili, J. *Nat. Mater.* **2008**, *7*, 527.
- [64] Orilall, M. C.; Wiesner, U. *Chem. Soc. Rev.* **2011**, *40*, 520.
- [65] Kao, J.; Thorkelsson, K.; Bai, P.; Rancatore, B. J.; Xu, T. *Chem. Soc. Rev.* **2013**, *42*, 2654.
- [66] Milliron, D. J.; Buonsanti, R.; Llordes, A.; Helms, B. A. *Acc. Chem. Res.* **2014**, *47*, 236.
- [67] Maier, J. *Nat. Mater.* **2005**, *4*, 805.
- [68] Aricó, A. S.; Bruce, P.; Scrosati, B.; Tarascon, J.-M.; van Schalkwijk, W. *Nat. Mater.* **2005**, *4*, 366.
- [69] Snyder, G. J.; Toberer, E. S. *Nat. Mater.* **2008**, *7*, 105.
- [70] Zabet-Khosousi, A.; Dhirani, A.-A. *Chem. Rev.* **2008**, *108*, 4072.

- [71] See, K. C.; Feser, J. P.; Chen, C. E.; Majumdar, A.; Urban, J. J.; Segalman, R. A. *Nano Lett.* **2010**, *10*, 4664.
- [72] Wang, R. Y.; Tangirala, R.; Raoux, S.; Jordan-Sweet, J. L.; Milliron, D. J. *Adv. Mater.* **2012**, *24*, 99.
- [73] Ong, W.-L.; Rupich, S. M.; Talapin, D. V.; McGaughey, A. J. H.; Malen, J. A. *Nat. Mater.* **2013**, *12*, 410.
- [74] Dong, A.; Jiao, Y.; Milliron, D. J. *ACS Nano* **2013**, *7*, 10978.
- [75] Kaushik, A. P.; Lukose, B.; Clancy, P. *ACS Nano* **2014**, *8*, 2302.
- [76] Akselrod, G. M.; Prins, F.; Poulidakos, L. V.; Lee, E. M. Y.; Weidman, M. C.; Mork, A. J.; Willard, A. P.; Bulović, V.; Tisdale, W. A. *Nano Lett.* **2014**, *14*, 3556.
- [77] Warren, S. C.; Messina, L. C.; Slaughter, L. S.; Kamperman, M.; Zhou, Q.; Gruner, S. M.; DiSalvo, F. J.; Wiesner, U. *Science* **2008**, *320*, 1748.
- [78] Brezesinski, T.; Wang, J.; Polleux, J.; Dunn, B.; Tolbert, S. H. *J. Am. Chem. Soc.* **2009**, *131*, 1802.
- [79] Kim, J.; Green, P. F. *Macromolecules* **2010**, *43*, 10452.
- [80] Hur, K.; Hennig, R. G.; Escobedo, F. A.; Wiesner, U. *Nano Lett.* **2012**, *12*, 3218.
- [81] Buonsanti, R.; Pick, T. E.; Krins, N.; Richardson, T. J.; Helms, B. A.; Milliron, D. J. *Nano Lett.* **2012**, *12*, 3872.
- [82] Rauda, I. E.; Buonsanti, R.; Saldarriaga-Lopez, L. C.; Benjauthrit, K.; Schelhas, L. T.; Stefik, M.; Augustyn, V.; Ko, J.; Dunn, B.; Wiesner, U.; Milliron, D. J.; Tolbert, S. H. *ACS Nano* **2012**, *6*, 6386.
- [83] Rauda, I. E.; Saldarriaga-Lopez, L. C.; Helms, B. A.; Schelhas, L. T.; Membreno, D.; Milliron, D. J.; Tolbert, S. H. *Adv. Mater.* **2013**, *25*, 1315.
- [84] Kao, J.; Bai, P.; Lucas, J. M.; Alivisatos, A. P.; Xu, T. *J. Am. Chem. Soc.* **2013**, *135*, 1680.
- [85] Rivest, J. B.; Buonsanti, R.; Pick, T. E.; Zhu, L.; Lim, E.; Clavero, C.; Schaible, E.; Helms, B. A.; Milliron, D. J. *J. Am. Chem. Soc.* **2013**, *135*, 7446.
- [86] Kovalenko, M. V.; Scheele, M.; Talapin, D. V. *Science* **2009**, *324*, 1417.
- [87] Tangirala, R.; Baker, J. L.; Alivisatos, A. P.; Milliron, D. J. *Angew. Chem., Int. Ed.* **2010**, *49*, 2878.

- [88] Caldwell, M. A.; Albers, A. E.; Levy, S. C.; Pick, T. E.; Cohen, B. E.; Helms, B. A.; Milliron, D. J. *Chem. Commun.* **2011**, *47*, 556.
- [89] Llordes, A.; Hammack, A. T.; Buonsanti, R.; Tangirala, R.; Aloni, S.; Helms, B. A.; Milliron, D. J. *J. Mater. Chem.* **2011**, *21*, 11631.
- [90] Dong, A.; Ye, X.; Chen, J.; Kang, Y.; Gordon, T.; Kikkawa, J. M.; Murray, C. B. *J. Am. Chem. Soc.* **2011**, *133*, 998.
- [91] Nag, A.; Kovalenko, M. V.; Lee, J.-S.; Liu, W.; Spokoyny, B.; Talapin, D. V. *J. Am. Chem. Soc.* **2011**, *133*, 10612.
- [92] Fafarman, A. T.; Koh, W.-K.; Diroll, B. T.; Kim, D. K.; Ko, D.-K.; Oh, S. J.; Ye, X.; Doan-Nguyen, V.; Crump, M. R.; Reifsnnyder, D. C.; Murray, C. B.; Kagan, C. R. *J. Am. Chem. Soc.* **2011**, *133*, 15753.
- [93] Tang, J.; Kemp, K. W.; Hoogland, S.; Jeong, K. S.; Liu, H.; Levina, L.; Furukawa, M.; Wang, X.; Debnath, R.; Cha, D.; Chou, K. W.; Fischer, A.; Amassian, A.; Asbury, J. B.; Sargent, E. H. *Nat. Mater.* **2011**, *10*, 765.
- [94] Zhang, H.; Hu, B.; Sun, L.; Hovden, R.; Wise, F. W.; Muller, D. A.; Robinson, R. D. *Nano Lett.* **2011**, *11*, 5356.
- [95] Anderson, N. C.; Owen, J. S. *Chem. Mater.* **2013**, *25*, 69.
- [96] Zanella, M.; Maserati, L.; Leal, M. P.; Prato, M.; Lavieville, R.; Povia, M.; Krahne, R.; Manna, L. *Chem. Mater.* **2013**, *25*, 1423.
- [97] Dirin, D. N.; Dreyfuss, S.; Bodnarchuk, M. I.; Nedelcu, G.; Papagiorgis, P.; Itskos, G.; Kovalenko, M. V. *J. Am. Chem. Soc.* **2014**, *136*, 6550.
- [98] Norman, Z. M.; Anderson, N. C.; Owen, J. S. *ACS Nano* **2014**, *8*, 7513.
- [99] Zhang, H.; Jang, J.; Liu, W.; Talapin, D. V. *ACS Nano* **2014**, *8*, 7359.
- [100] Kohlmann, O.; Steinmetz, W. E.; Mao, X.-A.; Wuelfing, W. P.; Templeton, A. C.; Murray, R. W.; Johnson, C. S. *J. Phys. Chem. B* **2001**, *105*, 8801.
- [101] Hens, Z.; Moreels, I.; Martins, J. C. *ChemPhysChem* **2005**, *6*, 2578.
- [102] Hens, Z.; Martins, J. C. *Chem. Mater.* **2013**, *25*, 1211.
- [103] Moreels, I.; Lambert, K.; De Muynck, D.; Vanhaecke, F.; Poelman, D.; Martins, J. C.; Allan, G.; Hens, Z. *Chem. Mater.* **2007**, *19*, 6101.
- [104] Hartman, J. S.; Ilnicki, E. I.; Shoemaker, J. A. W.; Szerminski, W. R.; Yuan, Z. *Can. J. Chem.* **1998**, *76*, 1317.

- [105] Brownstein, S.; Latremouille, G. *Can. J. Chem.* **1978**, *56*, 2764.
- [106] Konstantatos, G.; Howard, I.; Fischer, A.; Hoogland, S.; Clifford, J.; Klem, E.; Levina, L.; Sargent, E. H. *Nature* **2006**, *442*, 180.
- [107] Luther, J. M.; Law, M.; Beard, M. C.; Song, Q.; Reese, M. O.; Ellingson, R. J.; Nozik, A. J. *Nano Lett.* **2008**, *8*, 3488.
- [108] Hillhouse, H. W.; Beard, M. C. *Curr. Opin. Colloid Interface Sci.* **2009**, *14*, 245.
- [109] Choi, J. J.; Lim, Y.-F.; Santiago-Berrios, M. B.; Oh, M.; Hyun, B.-R.; Sun, L.; Bartnik, A. C.; Goedhart, A.; Malliaras, G. G.; Abruña, H. D.; Wise, F. W.; Hanrath, T. *Nano Lett.* **2009**, *9*, 3749.
- [110] Semonin, O. E.; Luther, J. M.; Choi, S.; Chen, H.-Y.; Gao, J.; Nozik, A. J.; Beard, M. C. *Science* **2011**, *334*, 1530.
- [111] Liu, Y.; Tolentino, J.; Gibbs, M.; Ihly, R.; Perkins, C. L.; Liu, Y.; Crawford, N.; Hemminger, J. C.; Law, M. *Nano Lett.* **2013**, *13*, 1578.
- [112] Sandeep, C. S. S.; ten Cate, S.; Schins, J. M.; Savenije, T. J.; Liu, Y.; Law, M.; Kinge, S.; Houtepen, A. J.; Siebbeles, L. D. A. *Nat. Commun.* **2013**, *4*, 2360.
- [113] Ocier, C. R.; Whitham, K.; Hanrath, T.; Robinson, R. D. *J. Phys. Chem. C* **2014**, *118*, 3377.
- [114] Chuang, C. H. M.; Brown, P. R.; Bulović, V.; Bawendi, M. G. *Nat. Mater.* **2014**, *13*, 796.
- [115] Baumgardner, W. J.; Whitham, K.; Hanrath, T. *Nano Lett.* **2013**, *13*, 3225.
- [116] Fang, C.; van Huis, M. A.; Vanmaekelbergh, D.; Zandbergen, H. W. *ACS Nano* **2010**, *4*, 211.
- [117] Thomas, E. L.; Kinning, D. J.; Alward, D. B.; Henkee, C. S. *Macromolecules* **1987**, *20*, 2934.
- [118] Bishop, K. J. M.; Wilmer, C. E.; Soh, S.; Grzybowski, B. A. *Small* **2009**, *5*, 1600.
- [119] Yu, W. W.; Falkner, J. C.; Shih, B. S.; Colvin, V. L. *Chem. Mater.* **2004**, *16*, 3318.
- [120] Kriegel, I.; Jiang, C.; Rodríguez-Fernández, J.; Schaller, R. D.; Talapin, D. V.; da Como, E.; Feldmann, J. *J. Am. Chem. Soc.* **2012**, *134*, 1583.
- [121] Carenco, S.; Boissière, C.; Nicole, L.; Sanchez, C.; Le Floch, P.; Mézailles, N. *Chem. Mater.* **2010**, *22*, 1340.

- [122] Yu, T.; Moon, J.; Park, J.; Park, Y.; Na, H.; Kim, B.; Song, I.; Moon, W.; Hyeon, T. *Chem. Mater.* **2009**, *21*, 2272.
- [123] Koch, U.; Fojtik, A.; Weller, H.; Henglein, A. *Chem. Phys. Lett.* **1985**, *122*, 507.
- [124] Sun, D.; Wong, M.; Sun, L.; Li, Y.; Miyatake, N.; Sue, H.-J. *J. Sol-Gel Sci. Technol.* **2007**, *43*, 237.
- [125] Cozzoli, P.; Kornowski, A.; Weller, H. *J. Am. Chem. Soc.* **2003**, *125*, 14539.
- [126] Steele, B. C. H.; Heinzl, A. *Nature* **2001**, *414*, 345.
- [127] Kerres, J. A. *J. Membr. Sci.* **2001**, *185*, 3.
- [128] Borup, R. et al. *Chem. Rev.* **2007**, *107*, 3904.
- [129] Skyllas-Kazacos, M.; Rychcik, M.; Robins, R. G.; Fane, A. G.; Green, M. A. *J. Electrochem. Soc.* **1986**, *133*, 1057.
- [130] Lopez-Atalaya, M.; Codina, G.; Perez, J. R.; Vazquez, J. L.; Aldaz, A. *J. Power Sources* **1992**, *39*, 147.
- [131] Fabjan, C.; Garche, J.; Harrer, B.; Jörissen, L.; Kolbeck, C.; Philippi, F.; Tomazic, G.; Wagner, F. *Electrochim. Acta* **2001**, *47*, 825.
- [132] Joerissen, L.; Garche, J.; Fabjan, C.; Tomazic, G. *J. Power Sources* **2004**, *127*, 98.
- [133] Weber, A. Z.; Mench, M. M.; Meyers, J. P.; Ross, P. N.; Gostick, J. T.; Liu, Q. *J. Appl. Electrochem.* **2011**, *41*, 1137.
- [134] Huang, Q.; Wang, Q. *ChemPlusChem* **2015**, *80*, 312.
- [135] Arora, P.; Zhang, Z. *Chem. Rev.* **2004**, *104*, 4419.
- [136] Huang, J.-Q.; Zhang, Q.; Peng, H.; Chen, C.; Wei, F. *Energy Environ. Sci.* **2014**, *7*, 347.
- [137] Bauer, I.; Thieme, S.; Bruckner, J.; Althues, H.; Kaskel, S. *J. Power Sources* **2014**, *251*, 417.
- [138] Thomas, A. *Angew. Chem., Int. Ed.* **2010**, *49*, 8328.
- [139] Colson, J. W.; Dichtel, W. R. *Nat. Chem.* **2013**, *5*, 453.
- [140] Ghadiri, M. R.; Granja, J. R.; Buehler, L. K. *Nature* **1994**, *369*, 301.
- [141] Xu, T.; Zhao, N.; Ren, F.; Hourani, R.; Lee, M. T.; Shu, J. Y.; Mao, S.; Helms, B. A. *ACS Nano* **2011**, *5*, 1376.

- [142] Hourani, R.; Zhang, C.; van der Weegen, R.; Ruiz, L.; Li, C.; Ketten, S.; Helms, B. A.; Xu, T. *J. Am. Chem. Soc.* **2011**, *133*, 15296.
- [143] Budd, P. M.; Msayib, K. J.; Tattershall, C. E.; Ghanem, B. S.; Reynolds, K. J.; McKeown, N. B.; Fritsch, D. *J. Membr. Sci.* **2005**, *251*, 263.
- [144] Staiger, C. L.; Pas, S. J.; Hill, A. J.; Cornelius, C. J. *Chem. Mater.* **2008**, *20*, 2606.
- [145] Du, N.; Dal-Cin, M. M.; Pinnau, I.; Nicalek, A.; Robertson, G. P.; Guiver, M. D. *Macromol. Rapid Commun.* **2011**, *32*, 631.
- [146] Heuchel, M.; Fritsch, D.; Budd, P. M.; McKeown, N. B.; Hofmann, D. *J. Membr. Sci.* **2008**, *318*, 84.
- [147] Du, N.; Park, H. B.; Robertson, G. P.; Dal-Cin, M. M.; Visser, T.; Scoles, L.; Guiver, M. D. *Nat. Mater.* **2011**, *10*, 372.
- [148] Carta, M.; Malpass-Evans, R.; Croad, M.; Rogan, Y.; Jansen, J. C.; Bernardo, P.; Bazzarelli, F.; McKeown, N. B. *Science* **2013**, *339*, 303.
- [149] Shamsipur, H.; Dawood, B. A.; Budd, P. M.; Bernardo, P.; Clarizia, G.; Jansen, J. C. *Macromolecules* **2014**, *47*, 5595.
- [150] Li, X.; Zhang, H.; Mai, Z.; Zhang, H.; Vankelecom, I. *Energy Environ. Sci.* **2011**, *4*, 1147.
- [151] Gu, M.; Lee, J.; Kim, Y.; Kim, J. S.; Jang, B. Y.; Lee, K. T.; Kim, B.-S. *RSC Adv.* **2014**, *4*, 46940.
- [152] Liu, Q.; Sleightholme, A. E. S.; Shinkle, A. A.; Li, Y.; Thompson, L. T. *Electrochem. Commun.* **2009**, *11*, 2312.
- [153] Duduta, M.; Ho, B.; Wood, V. C.; Limthongkul, P.; Brunini, V. E.; Carter, W. C.; Chiang, Y.-M. *Adv. Energy Mater.* **2011**, *1*, 511.
- [154] Leung, P.; Li, X.; Ponce, d. L. C.; Berlouis, L.; Low, C. T. J.; Walsh, F. C. *RSC Adv.* **2012**, *2*, 10125.
- [155] Shin, S.-H.; Yun, S.-H.; Moon, S.-H. *RSC Adv.* **2013**, *3*, 9095.
- [156] Huang, Q.; Li, H.; Grätzel, M.; Wang, Q. *Phys. Chem. Chem. Phys.* **2013**, *15*, 1793.
- [157] Rauh, R. D.; Abraham, K. M.; Pearson, G. F.; Surprenant, J. K.; Brummer, S. B. *J. Electrochem. Soc.* **1979**, *126*, 523.
- [158] Cuisinier, M.; Cabelguen, P.-E.; Evers, S.; He, G.; Kolbeck, M.; Garsuch, A.; Bolin, T.; Balasubramanian, M.; Nazar, L. F. *J. Phys. Chem. Lett.* **2013**, *4*, 3227.

- [159] Barghamadi, M.; Kapoor, A.; Wen, C. *J. Electrochem. Soc.* **2013**, *160*, A1256.
- [160] Assary, R. S.; Curtiss, L. A.; Moore, J. S. *J. Phys. Chem. C* **2014**, *118*, 11545.
- [161] Vijayakumar, M.; Govind, N.; Walter, E.; Burton, S. D.; Shukla, A.; Devaraj, A.; Xiao, J.; Liu, J.; Wang, C.; Karima, A.; Thevuthasana, S. *Phys. Chem. Chem. Phys.* **2014**, *16*, 10923.
- [162] Wu, H.-L.; Huff, L. A.; Gewirth, A. A. *ACS Appl. Mater. Interfaces* **2015**, *7*, 1709.
- [163] Aurbach, D.; Pollak, E.; Elazari, R.; Salitra, G.; Kelley, C. S.; Affinito, J. *J. Electrochem. Soc.* **2009**, *156*, A694.
- [164] Zhang, S. S. *Electrochim. Acta* **2012**, *70*, 344.
- [165] Rosenman, A.; Elazari, R.; Salitra, G.; Markevich, E.; Aurbach, D.; Garsuch, A. *J. Electrochem. Soc.* **2015**, *162*, A470.
- [166] Su, Y. S.; Manthiram, A. *Nat. Commun.* **2012**, *3*, 1166.
- [167] Zhou, G.; Pei, S.; Li, L.; Wang, D.-W.; Wang, S.; Huang, K.; Yin, L.; Li, F.; Cheng, H.-M. *Adv. Mater.* **2014**, *26*, 625.
- [168] Yao, H.; Yan, K.; Li, W.; Zheng, G.; Kong, D.; Seh, Z. W.; Narasimhan, V. K.; Liang, Z.; Cui, Y. *Energy Environ. Sci.* **2014**, *7*, 3381.
- [169] Huang, J.-Q.; Zhuang, T.; Zhang, Q.; Peng, H.; Chen, C.; Wei, F. *ACS Nano* **2015**, *9*, 3002.
- [170] Hart, C. J.; Cuisinier, M.; Liang, X.; Kundu, D.; Garsuch, A.; Nazar, L. F. *Chem. Commun.* **2015**, *51*, 2308.
- [171] Pang, Q.; Kundu, D.; Cuisinier, M.; Nazar, L. F. *Nat. Commun.* **2014**, *5*, 4759.
- [172] Tao, X.; Wang, J.; Ying, Z.; Cai, Q.; Zheng, G.; Gan, Y.; Huang, H.; Xia, Y.; Liang, C.; Zhang, W.; Cui, Y. *Nano Lett.* **2014**, *14*, 5288.
- [173] Wang, Z.; Dong, Y.; Li, H.; Zhao, Z.; Bin, W. H.; Hao, C.; Liu, S.; Qiu, J.; Lou, X. W. *Nat. Commun.* **2014**, *5*, 5002.
- [174] Zhang, Q.; Wang, Y.; Seh, Z. W.; Fu, Z.; Zhang, R.; Cui, Y. *Nano Lett.* **2015**, *15*, 3780.
- [175] Henderson, W. A.; Brooks, N. R.; Young, V. G. *Chem. Mater.* **2003**, *15*, 4685.
- [176] Henderson, W. A.; McKenna, F.; Khan, M. A.; Brooks, N. R.; Young, V. G.; Frech, R. *Chem. Mater.* **2005**, *17*, 2284.

- [177] Pascal, T. A.; Wujcik, K. H.; Velasco-Velez, J.; Wu, C.; Teran, A. A.; Kapi-lashrami, M.; Cabana, J.; Guo, J.; Salmeron, M.; Balsara, N.; Prendergast, D. *J. Phys. Chem. Lett.* **2014**, *5*, 1547.
- [178] Song, J.; Du, N.; Dai, Y.; Robertson, G. P.; Guiver, M. D.; Thomas, S.; Pinnau, I. *Macromolecules* **2008**, *41*, 7411.
- [179] Budd, P. M.; Elabas, E. S.; Ghanem, B. S.; Makhseed, S.; McKeown, N. B.; Msayib, K. J.; Tattershall, C. E.; Wang, D. *Adv. Mater.* **2004**, *16*, 456.
- [180] Fan, F. Y.; Woodford, W. H.; Li, Z.; Baram, N.; Smith, K. C.; Helal, A.; McKin-ley, G. H.; Carter, W. C.; Chiang, Y.-M. *Nano Lett.* **2014**, *14*, 2210.
- [181] Choquette, Y.; Brisard, G.; Parent, M.; Brouillette, D.; Perron, G.; Desnoyers, J. E.; Armand, M.; Gravel, D.; Slougui, N. *J. Electrochem. Soc.* **1998**, *145*, 3500.
- [182] Chen, H.; Zou, Q.; Liang, Z.; Liu, H.; Li, Q.; Lu, Y. *Nat. Commun.* **2015**, *6*, 5877.
- [183] Lippert, G.; Hutter, J.; Parrinello, M. *Mol. Phys.* **1997**, *92*, 477.
- [184] van de Vondele, J.; Krack, M.; Mohamed, F.; Parrinello, M.; Chassaing, T.; Hut-ter, J. *Comput. Phys. Commun.* **2005**, *167*, 103.
- [185] van de Vondele, J.; Hutter, J. *J. Chem. Phys.* **2007**, *127*, 114105.
- [186] Perdew, J. P.; Burke, K.; Ernzerhof, M. *Phys. Rev. Lett.* **1996**, *77*, 3865.
- [187] Zhang, Y.; Yang, W. *Phys. Rev. Lett.* **1998**, *80*, 890.
- [188] Goedecker, S.; Teter, M.; Hutter, J. *Phys. Rev. B* **1996**, *54*, 1703.
- [189] Krack, M. *Theor. Chem. Acc.* **2005**, *114*, 145.
- [190] Genovese, L.; Deutsch, T.; Goedecker, S. *J. Chem. Phys.* **2007**, *127*, 054704.
- [191] Grimme, S.; Antony, J.; Ehrlich, S.; Krieg, H. *J. Chem. Phys.* **2010**, *132*, 154104.
- [192] Darling, R. M.; Gallagher, K. G.; Xie, W.; Su, L.; Brushett, F. R. *J. Electrochem. Soc.* **2016**, *163*, A5029.
- [193] Mikhaylik, Y. V.; Akridge, J. R. *J. Electrochem. Soc.* **2004**, *151*, A1969.
- [194] Busche, M. R.; Adelhelm, P.; Sommer, H.; Schneider, H.; Leitner, K.; Janek, J. *J. Power Sources* **2014**, *259*, 289.
- [195] Pang, Q.; Liang, X.; Kwok, C. Y.; Nazar, L. F. *J. Electrochem. Soc.* **2015**, *162*, A2567.

- [196] Yim, T.; Park, M.-S.; Yu, J.-S.; Kim, K.; Im, K.; Kim, J.-H.; Jeong, G.; Jo, Y.; Woo, S.-G.; Kang, K.; Lee, I.; Kim, Y.-J. *Electrochim. Acta* **2013**, *107*, 454.
- [197] Aurbach, D.; Granot, E. *Electrochim. Acta* **1997**, *42*, 697.
- [198] Zhang, S.; Ueno, K.; Dokko, K.; Watanabe, M. *Adv. Energy Mater.* **2015**, *5*, 1500117.
- [199] Wujcik, K. H.; Velasco-Velez, J.; Wu, C. H.; Pascal, T. A.; Teran, A. A.; Marcus, M. A.; Cabana, J.; Guo, J.; Prendergast, D.; Salmeron, M.; Balsara, N. P. *J. Electrochem. Soc.* **2014**, *161*, A1100.
- [200] Lin-Vien, D.; Colthup, N. B.; Fateley, W. G.; Grasselli, J. G. *The Handbook of Infrared and Raman Characteristic Frequencies of Organic Molecules*; Academic Press, San Diego, 1991; pp 236–238.
- [201] Hua, G.; Li, Y.; Slawin, A. M. Z.; Woollins, J. D. *Org. Lett.* **2006**, *8*, 5251.
- [202] Moss, R. A.; Tian, J. *Org Lett.* **2006**, *8*, 1245.
- [203] Verma, P.; Kumar, N.; Sharma, U.; Bala, M.; Kumar, V.; Singh, B. *Synth. Commun.* **2013**, *43*, 2867.
- [204] Daw, P.; Sinha, A.; Rahaman, S.; Dinda, S.; Bera, J. *Organometallics* **2012**, *31*, 3790.
- [205] Veisi, H.; Maleki, B.; Hamelian, M.; Ashrafi, S. *RSC Adv.* **2015**, *5*, 6365.
- [206] Jeromenok, J.; Weber, J. *Langmuir* **2013**, *29*, 12982.
- [207] Chen, S.; Yi, W.; Duhamel, J.; Heinrich, K.; Bengtson, G.; Fritsch, D. *J. Phys. Chem. B* **2013**, *117*, 5249.
- [208] Jagiello, J. *Langmuir* **1994**, *10*, 2778.
- [209] Jagiello, J.; Olivier, J. P. *Carbon* **2013**, *55*, 70.
- [210] Zu, C.; Fu, Y.; Manthiram, A. *J. Mater. Chem. A* **2013**, *1*, 10362.
- [211] Zhang, S. S. *J. Power Sources* **2007**, *164*, 351.
- [212] Jain, A.; Shin, Y.; Persson, K. A. *Nat. Rev. Mater.* **2016**, *1*, 15004.
- [213] Li, W.; Yao, H.; Yan, K.; Zheng, G.; Liang, Z.; Chiang, Y. M.; Cui, Y. *Nature Commun.* **2015**, *6*, 7436.
- [214] Fang, W.; Zhang, L.; Jiang, J. *Mol. Sim.* **2010**, *36*, 992.

- [215] McDermott, A. G.; Budd, P. M.; McKeown, N. B.; Colina, C. M.; Runt, J. *J. Mater. Chem. A* **2014**, *2*, 11742.
- [216] Konnertz, N.; Ding, Y.; Harrison, W. J.; Budd, P. M.; Schönhals, A.; Böhning, M. *ACS Macro Lett.* **2016**, *5*, 528.
- [217] Jue, M. L.; McKay, C. S.; McCool, B. A.; Finn, M. G.; Lively, R. P. *Macromolecules* **2015**, *48*, 5780.
- [218] Gorgojo, P.; Karan, S.; Wong, H.; Jimenez-Solomon, M.; Cabral, J.; Livingston, A. *Adv. Funct. Mater.* **2014**, *24*, 4729.
- [219] Frischmann, P. D.; Gerber, L. C. H.; Doris, S. E.; Tsai, E. Y.; Fan, F. Y.; Qu, X.; Jain, A.; Persson, K. A.; Chiang, Y.-M.; Helms, B. A. *Chem. Mater.* **2015**, *27*, 6765.
- [220] Fan, F. Y.; Carter, W. C.; Chiang, Y.-M. *Adv. Mater.* **2015**, *27*, 5203.
- [221] Gerber, L.; Frischmann, P. D.; Fan, F. Y.; Doris, S. E.; Qu, X.; Scheuermann, A.; Persson, K.; Chiang, Y.-M.; Helms, B. A. *Nano Lett.* **2016**, *16*, 549.
- [222] Zhang, Z.; Lai, Y.; Zhang, Z.; Zhang, K.; Li, J. *Electrochim. Acta* **2014**, *129*, 55.
- [223] Li, W.; Hicks-Garner, J.; Wang, J.; Liu, J.; Gross, A. F.; Sherman, E.; Graetz, J.; Vajo, J. J.; Liu, P. *Chem. Mater.* **2014**, *26*, 3403.
- [224] Bai, S.; Liu, X.; Zhu, K.; Wu, S.; Zhou, H. *Nat. Energy* **2016**, *1*, 16094.
- [225] Hohenberg, P.; Kohn, W. *Phys. Rev.* **1964**, *136*, B864.
- [226] Kohn, W.; Sham, L. J. *Phys. Rev* **1965**, *140*, A1133.
- [227] Zhao, Y.; Truhlar, D. G. *J. Chem. Theory Comput.* **2008**, *4*, 1849.
- [228] Tomasi, J.; Mennucci, B.; Cancés, E. *J. Mol. Struct. THEOCHEM* **1999**, *464*, 211.
- [229] Shao, Y.; Gan, Z.; Epifanovsky, E.; Gilbert, A. T. B.; Wormit, M.; Kussmann, J.; Lange, A.; Behn, A.; Deng, J. *Mol. Phys.* **2015**, *113*, 184.
- [230] Ghanem, B. S.; McKeown, N. B.; Budd, P. M.; Fritsch, D. *Macromolecules* **2008**, *41*, 1640.
- [231] Marenich, A. V.; Cramer, C. J.; Truhlar, D. G. *J. Phys. Chem. B* **2009**, *113*, 6378.
- [232] Jeong, S.; Hu, L.; Lee, H. R.; Garnett, E.; Choi, J. W.; Cui, Y. *Nano Lett.* **2010**, *10*, 2989.
- [233] Duan, W. et al. *J. Mater. Chem. A* **2016**, *4*, 5448.

- [234] Wei, X.; Xu, W.; Huang, J.; Zhang, L.; Walter, E.; Lawrence, C.; Vijayakumar, M.; Henderson, W. A.; Liu, T.; Cosimbescu, L.; Li, B.; Sprenkle, V.; Wang, W. *Angew. Chem., Int. Ed.* **2015**, *54*, 8684.
- [235] Nagarjuna, G.; Hui, J.; Cheng, K. J.; Lichtenstein, T.; Shen, M.; Moore, J. S.; Rodríguez-López, J. *J. Am. Chem. Soc.* **2014**, *136*, 16309.
- [236] Burgess, M.; Moore, J. S.; Rodríguez-López, J. *Acc. Chem. Res.* **2016**, *Article ASAP*, DOI: 10.1021/acs.accounts.6b00341.
- [237] Montoto, E. C.; Nagarjuna, G.; Hui, J.; Burgess, M.; Sekerak, N. M.; Hernández-Burgos, K.; Wei, T.-S.; Kneer, M.; Grolman, J.; Cheng, K. J.; Lewis, J. A.; Moore, J. S.; Rodríguez-López, J. *J. Am. Chem. Soc.* **2016**, *138*, 13230.
- [238] Janoschka, T.; Martin, N.; Martin, U.; Friebe, C.; Morgenstern, S.; Hiller, H.; Hager, M. D.; Schubert, U. S. *Nature* **2015**, *527*, 78.
- [239] Winsberg, J.; Hagemann, T.; Muench, S.; Friebe, C.; Häupler, B.; Janoschka, T.; Morgenstern, S.; Hager, M. D.; Schubert, U. S. *Chem. Mater.* **2016**, *28*, 3401.
- [240] Burgess, M.; Chénard, E.; Hernandez-Burgos, K.; Nagarjuna, G.; Assary, R. S.; Hui, J.; Moore, J. S.; Rodríguez-López, J. *Chem. Mater.* **2016**, *Article ASAP*, DOI: 10.1021/acs.chemmater.6b02825.
- [241] Wang, J.; Wolf, R. M.; Caldwell, J. W.; Kollman, P. A.; Case, D. A. *J. Comput. Chem.* **2004**, *25*, 1157.
- [242] Laio, A.; Parinello, M. *Proc. Natl. Acad. Sci.* **2002**, *99*, 12562.
- [243] Bussi, G.; Laio, A.; Parinello, M. *Phys. Rev. Lett.* **2006**, *96*, 090601.
- [244] Ufimtsev, I. S.; Martinez, T. J. *J. Chem. Theory Comput.* **2009**, *5*, 2619.
- [245] Zahn, S.; MacFarlane, D. R.; Izgorodina, E. I. *Phys. Chem. Chem. Phys.* **2013**, *15*, 13664.
- [246] Kästner, J.; Carr, J. M.; Keal, T. W.; Thiel, W.; Wander, A.; Sherwood, P. *J. Phys. Chem. A* **2009**, *113*, 11856.
- [247] Plimpton, S. *J. Comp. Phys.* **1995**, *117*, 1.
- [248] Nosé, S. A. *J. Chem. Phys.* **1984**, *81*, 511.
- [249] Hoover, W. G. *Phys. Rev. A: At. Mol. Opt. Phys.* **1985**, *31*, 1965.
- [250] Macchioni, A.; Ciancaleoni, G.; Zuccaccia, C.; Zuccaccia, D. *Chem. Soc. Rev.* **2008**, *37*, 479.

- [251] Chen, H. C.; Chen, S. H. *J. Phys. Chem.* **1984**, *88*, 5118.
- [252] Perrin, F. *J. Phys. Radium* **1936**, *7*, 1.
- [253] Goodenough, J. B. *Energy Environ. Sci.* **2014**, *7*, 14.
- [254] Wang, C.; Wu, H.; Chen, Z.; McDowell, M. T.; Cui, Y.; Bao, Z. *Nat. Chem.* **2013**, *5*, 1042.
- [255] Wang, B.; Richardson, T. J.; Chen, G. *J. Electrochem. Soc.* **2014**, *161*, A1039.
- [256] Wu, M.; Xiao, X.; Vukmirovic, N.; Xun, S.; Das, P. K.; Song, X.; Olalde-Velasco, P.; Wang, D.; Weber, A. Z.; Wang, L.-W.; Battaglia, V. S.; Yang, W.; Liu, G. *J. Am. Chem. Soc.* **2013**, *135*, 12048.
- [257] Bouchet, R.; Maria, S.; Meziane, R.; Aboulaich, A.; Lienafa, L.; Bonnet, J.-P.; Phan, T. N. T.; Bertin, D.; Gignes, D.; Devaux, D.; Denoyel, R.; Armand, M. *Nat. Mater.* **2013**, *12*, 452.
- [258] Javier, A. E.; Patel, S. N.; Hallinan, D. T., Jr.; Srinivasan, V.; Balsara, N. P. *Angew. Chem., Int. Ed.* **2011**, *50*, 9848.
- [259] Kumar, B. V. V. S. P.; Rao, K. V.; Sampath, S.; George, S. J.; Eswaramoorthy, M. *Angew. Chem., Int. Ed.* **2014**, *53*, 13073.
- [260] Liang, Y.; Tao, Z.; Chen, J. *Adv. Energy Mater.* **2012**, *2*, 742.
- [261] Huskinson, B.; Marshak, M. P.; Suh, C.; Er, S.; Gerhardt, M. R.; Galvin, C. J.; Chen, X.; Aspuru-Guzik, A.; Gordon, R. G.; Aziz, M. J. *Nature* **2014**, *505*, 195.
- [262] Simmonds, A. G.; Griebel, J. J.; Park, J.; Kim, K. R.; Chung, W. J.; Oleshko, V. P.; Kim, J.; Kim, E. T.; Glass, R. S.; Soles, C. L.; Sung, Y.-E.; Char, K.; Pyun, J. *ACS Macro Lett.* **2014**, *3*, 229.
- [263] Huang, J.; Cheng, L.; Assary, R. S.; Wang, P.; Xue, Z.; Burrell, A. K.; Curtiss, L. A.; Zhang, L. *Adv. Energy Mater.* **2015**, *5*, 1401782.
- [264] Wei, X.; Xu, W.; Vijayakumar, M.; Cosimbescu, L.; Liu, T.; Sprenkle, V.; Wang, W. *Adv. Mater.* **2014**, *26*, 7649.
- [265] Aida, T.; Meijer, E. W.; Stupp, S. I. *Science* **2012**, *335*, 813.
- [266] Pisula, W.; Feng, X.; Müllen, K. *Adv. Mater.* **2010**, *22*, 3634.
- [267] Lehn, J.-M. *Chem. Soc. Rev.* **2007**, *36*, 151.
- [268] Babu, S. S.; Praveen, V. K.; Ajayaghosh, A. *Chem. Rev.* **2014**, *114*, 1973.

- [269] Weiss, R. G. *J. Am. Chem. Soc.* **2014**, *136*, 7519.
- [270] Amabilino, D. B.; Puigmartí-Luis, J. *Soft Matter* **2010**, *6*, 1605.
- [271] Chen, L.; Mali, K. S.; Puniredd, S. R.; Baumgarten, M.; Parvez, K.; Pisula, W.; De, F. S.; Müllen, K. *J. Am. Chem. Soc.* **2013**, *135*, 13531.
- [272] Kumar, R. J.; MacDonald, J. M.; Singh, T. B.; Waddington, L. J.; Holmes, A. B. *J. Am. Chem. Soc.* **2011**, *133*, 8564.
- [273] Stone, D. A.; Tayi, A. S.; Goldberger, J. E.; Palmer, L. C.; Stupp, S. I. *Chem. Commun.* **2011**, *47*, 5702.
- [274] Diring, S.; Camerel, F.; Donnio, B.; Dintzer, T.; Toffanin, S.; Capelli, R.; Muccini, M.; Ziessel, R. *J. Am. Chem. Soc.* **2009**, *131*, 18177.
- [275] Mukhopadhyay, P.; Iwashita, Y.; Shirakawa, M.; Kawano, S.; Fujita, N.; Shinkai, S. *Angew. Chem., Int. Ed.* **2006**, *45*, 1592.
- [276] Sugiyasu, K.; Kawano, S.; Fujita, N.; Shinkai, S. *Chem. Mater.* **2008**, *20*, 2863.
- [277] Würthner, F.; Bauer, C.; Stepanenko, V.; Yagai, S. *Adv. Mater.* **2008**, *20*, 1695.
- [278] Weingarten, A. S.; Kazantsev, R. V.; Palmer, L. C.; McClendon, M.; Koltonow, A. R.; Samuel, A. P. S.; Kiebal, D. J.; Wasielewski, M. R.; Stupp, S. I. *Nat. Chem.* **2014**, *6*, 964.
- [279] Zhang, S. S. *J. Power Sources* **2013**, *231*, 153.
- [280] Choi, N.-S.; Chen, Z.; Freunberger, S. A.; Ji, X.; Sun, Y.-K.; Amine, K.; Yushin, G.; Nazar, L. F.; Cho, J.; Bruce, P. G. *Angew. Chem., Int. Ed.* **2012**, *51*, 9994.
- [281] Kim, J.; Lee, D.-J.; Jung, H.-G.; Sun, Y.-K.; Hassoun, J.; Scrosati, B. *Adv. Funct. Mater.* **2013**, *23*, 1076.
- [282] Guo, J.; Yang, Z.; Yu, Y.; Abruña, H. D.; Archer, L. A. *J. Am. Chem. Soc.* **2013**, *135*, 763.
- [283] Song, M.-K.; Zhang, Y.; Cairns, E. J. *Nano Lett.* **2013**, *13*, 5891.
- [284] Pu, X.; Yang, G.; Yu, C. *Adv. Mater.* **2014**, *26*, 7456.
- [285] Su, Y.-S.; Fu, Y.; Guo, B.; Dai, S.; Manthiram, A. *Chem. - Eur. J.* **2013**, *19*, 8621.
- [286] Yang, Y.; Zheng, G.; Cui, Y. *Energy Environ. Sci.* **2013**, *6*, 1552.
- [287] Demir-Cakan, R.; Morcrette, M.; Gangulibabu, A., G.; Dedryvère, R.; Tarascon, J.-M. *Energy Environ. Sci.* **2013**, *6*, 176.

- [288] Mikhaylik, Y. V. Electrolytes for Lithium Sulfur Cells. US Patent 7,354,680, 2008.
- [289] Meini, S.; Elazari, R.; Rosenman, A.; Garsuch, A.; Aurbach, D. *J. Phys. Chem. Lett.* **2014**, *5*, 915.
- [290] Smith, K. C.; Chiang, Y.-M.; Carter, W. C. *J. Electrochem. Soc.* **2014**, *161*, A486.
- [291] Zhan, X.; Facchetti, A.; Barlow, S.; Marks, T. J.; Ratner, M. A.; Wasielewski, M. R.; Marder, S. R. *Adv. Mater.* **2011**, *23*, 268.
- [292] Würthner, F. *Chem. Commun.* **2004**, 1564.
- [293] Barchasz, C.; Molton, F.; Duboc, C.; Leprêtre, J.-C.; Patoux, S.; Alloin, F. *Anal. Chem.* **2012**, *84*, 3973.
- [294] Gao, J.; Lowe, M. A.; Kiya, Y.; Abruña, H. D. *J. Phys. Chem. C* **2011**, *115*, 25132.
- [295] Larcher, D.; Tarascon, J.-M. *Nat. Chem.* **2015**, *7*, 19.
- [296] Tian, D.; Zhang, H.-Z.; Zhang, D.-S.; Chang, Z.; Han, J.; Gao, X.-P.; Bu, X.-H. *RSC Adv.* **2014**, *4*, 7506.
- [297] Sharma, P.; Damien, D.; Nagarajan, K.; Shaijumon, M. M.; Hariharan, M. *J. Phys. Chem. Lett.* **2013**, *4*, 3192.
- [298] Han, X.; Chang, C.; Yuan, L.; Sun, T.; Sun, J. *Adv. Mater.* **2007**, *19*, 1616.
- [299] Williams, M. E.; Murray, R. W. *Chem. Mater.* **1998**, *10*, 3603.
- [300] Gerber, L. C. H.; Frischmann, P. D.; Williams, T. E.; Tichelaar, M.; Tsai, E. Y.; Liu, Y.-S.; Guo, J.; Pemmaraju, C. D.; Prendergast, D.; Helms, B. A. *Polym. Chem.* **2015**, *6*, 5560.
- [301] Krylov, A. I.; Gill, P. M. W. *WIREs Comput. Mol. Sci.* **2013**, *3*, 317.
- [302] Becke, A. D. *J. Chem. Phys.* **1993**, *98*.
- [303] Stewart, J. J. P. *J. Mol. Model* **2013**, *19*, 1.
- [304] Stewart, J. J. P. MOPAC2012.
- [305] Cohen, A. J.; Mori-Sánchez, P.; Yang, W. *Chem. Rev.* **2012**, *112*, 289.
- [306] Chen, Z.; Lohr, A.; Saha-Möller, C. R.; Würthner, F. *Chem. Soc. Rev.* **2009**, *38*, 564.
- [307] Evers, S.; Nazar, L. F. *Acc. Chem. Res.* **2013**, *46*, 1135.

- [308] Black, R.; Adams, B.; Nazar, L. F. *Adv. Energy Mater.* **2012**, *2*, 801.
- [309] Gallagher, K. G.; Goebel, S.; Greszler, T.; Mathias, M.; Oelerich, W.; Eroglu, D.; Srinivasan, V. *Energy Environ. Sci.* **2014**, *7*, 1555.
- [310] Radin, M. D.; Siegel, D. J. *Energy Environ. Sci.* **2013**, *6*, 2370.
- [311] Viswanathan, V.; Thygesen, K. S.; Hummelshøj, J. S.; Nørskov, J. K.; Girishkumar, G.; McCloskey, B. D.; Luntz, A. C. *J. Chem. Phys.* **2011**, *135*, 214704.
- [312] Albertus, P.; Girishkumar, G.; McCloskey, B.; Sánchez-Carrera, R. S.; Kozinsky, B.; Christensen, J.; Luntz, A. C. *J. Electrochem. Soc.* **2011**, *158*, A343.
- [313] Yang, Y.; Zheng, G.; Misra, S.; Nelson, J.; Toney, M. F.; Cui, Y. *J. Am. Chem. Soc.* **2012**, *134*, 15387.
- [314] Lu, Y.-C.; Gallant, B. M.; Kwabi, D. G.; Harding, J. R.; Mitchell, R. R.; Whittingham, M. S.; Shao-Horn, Y. *Energy Environ. Sci.* **2013**, *6*, 750.
- [315] Hummelshøj, J. S.; Blomqvist, J.; Datta, S.; Vegge, T.; Rossmeisl, J.; Thygesen, K. S.; Luntz, A. C.; Jacobsen, K. W.; Nørskov, J. K. *J. Chem. Phys.* **2010**, *132*, 071101.
- [316] Radin, M. D.; Monroe, C. W.; Siegel, D. J. *Chem. Mater.* **2015**, *27*, 839.
- [317] Cheon, S.-E.; Ko, K.-S.; Cho, J.-H.; Kim, S.-W.; Chin, E.-Y.; Kim, H.-T. *J. Electrochem. Soc.* **2003**, *150*, A796.
- [318] Barchasz, C.; Leprêtre, J.-C.; Alloin, F.; Patoux, S. *J. Power Sources* **2012**, *199*, 322.
- [319] Read, J. *J. Electrochem. Soc.* **2002**, *149*, A1190.
- [320] Zhang, K.; Hu, Z.; Chen, J. *J. Energy Chem.* **2013**, *22*, 214.
- [321] Liang, X.; Garsuch, A.; Nazar, L. F. *Angew. Chem., Int. Ed.* **2015**, *54*, 3907.
- [322] Wang, J.; Yang, J.; Wan, C.; Du, K.; Xie, J.; Xu, N. *Adv. Funct. Mater.* **2003**, *13*, 487.
- [323] Yang, X.-H.; He, P.; Xia, Y.-Y. *Electrochem. Commun.* **2009**, *11*, 1127.
- [324] Kuboki, T.; Okuyama, T.; Ohsaki, T.; Takami, N. *J. Power Sources* **2005**, *146*, 766.
- [325] Tran, C.; Yang, X.-Q.; Qu, D. *J. Power Sources* **2010**, *195*, 2057.

- [326] Xiao, J.; Wang, D.; Xu, W.; Wang, D.; Williford, R. E.; Liu, J.; Zhang, J.-G. *J. Electrochem. Soc.* **2010**, *157*, A487.
- [327] Abraham, K. M.; Jiang, Z. *J. Electrochem. Soc.* **1996**, *143*, 1.
- [328] Mitchell, R. R.; Gallant, B. M.; Thompson, C. V.; Shao-Horn, Y. *Energy Environ. Sci.* **2011**, *4*, 2952.
- [329] Xiao, J.; Mei, D.; Li, X.; Xu, W.; Wang, D.; Graff, G. L.; Bennett, W. D.; Nie, Z.; Saraf, L. V.; Aksay, I. A.; Liu, J.; Zhang, J.-G. *Nano Lett.* **2011**, *11*, 5071.
- [330] Wang, Y.; Zhou, H. *J. Power Sources* **2010**, *195*, 358.
- [331] Wang, J. L.; Yang, J.; Xie, J. Y.; Xu, N. X.; Li, Y. *Electrochem. Commun.* **2002**, *4*, 499.
- [332] Manthiram, A.; Fu, Y.; Su, Y.-S. *Acc. Chem. Res.* **2013**, *46*, 1125.
- [333] Toohey, K. S.; Sottos, N. R.; Lewis, J. A.; Moore, J. S.; White, S. R. *Nat. Mater.* **2007**, *6*, 581.
- [334] Nguyen, D. T.; Leho, Y. T.; Esser-Kahn, A. P. *Lab Chip* **2012**, *12*, 1246.
- [335] Esser-Kahn, A. P.; Thakre, P. R.; Dong, H.; Patrick, J. F.; Vlasko-Vlasov, V. K.; Sottos, N. R.; Moore, J. S.; White, S. R. *Adv. Mater.* **2011**, *23*, 3654.
- [336] Patrick, J. F.; Hart, K. R.; Krull, B. P.; Diesendruck, C. E.; Moore, J. S.; White, S. R.; Sottos, N. R. *Adv. Mater.* **2014**, *26*, 4302.
- [337] Chen, Y.; Freunberger, S. A.; Peng, Z.; Fontaine, O.; Bruce, P. G. *Nat. Chem.* **2013**, *5*, 489.
- [338] Lim, H.-D.; Song, H.; Kim, J.; Gwon, H.; Bae, Y.; Park, K.-Y.; Hong, J.; Kim, H.; Kim, T.; Kim, Y. H.; Lepró, X.; Ovalle-Robles, R.; Baughman, R. H.; Kang, K. *Angew. Chem., Int. Ed.* **2014**, *53*, 3926.
- [339] Bergner, B. J.; Schürmann, A.; Peppler, K.; Garsuch, A.; Janek, J. *J. Am. Chem. Soc.* **2014**, *136*, 15054.
- [340] Feng, N.; He, P.; Zhou, H. *ChemSusChem* **2015**, *8*, 600.
- [341] Lacey, M. J.; Frith, J. T.; Owen, J. R. *Electrochem. Commun.* **2013**, *26*, 74.
- [342] Sun, D.; Shen, Y.; Zhang, W.; Yu, L.; Yi, Z.; Yin, W.; Wang, D.; Huang, Y.; Wang, J.; Wang, D.; Goodenough, J. B. *J. Am. Chem. Soc.* **2014**, *136*, 8941.
- [343] Xia, C.; Black, R.; Fernandes, R.; Adams, B.; Nazar, L. F. *Nat. Chem.* **2015**, *7*, 496.

- [344] Kojima, H.; Bard, A. J. *J. Am. Chem. Soc.* **1975**, *97*, 6317.
- [345] Ruoff, R. S.; Kadish, K. M.; Boulas, P.; Chen, E. C. M. *J. Phys. Chem.* **1995**, *99*, 8843.
- [346] Bard, A. J.; Faulkner, L. R. *Electrochemical Methods: Fundamentals and Applications*, 2nd ed.; John Wiley and Sons, Inc., 2001; p 96.
- [347] Peverati, R.; Truhlar, D. G. *J. Phys. Chem. Lett.* **2011**, *2*, 2810.
- [348] De Greef, T. F. A.; Smulders, M. M. J.; Wolffs, M.; Schenning, A. P. H. J.; Sijbesma, R. P.; Meijer, E. W. *Chem. Rev.* **2009**, *109*, 5687.
- [349] Jafarian, M.; Mahjani, M. G.; Gobal, F.; Danaee, I. *J. Electroanal. Chem.* **2006**, *588*, 190.
- [350] Fleischmann, M.; Thirsk, H. R. In *Advances in Electrochemistry and Electrochemical Engineering, Vol. 3*; Delahey, P., Ed.; John Wiley & Sons, 1963; pp 123–210.
- [351] Bhosale, S. V.; Jani, C. H.; Lalander, C. H.; Langford, S. J.; Nerush, I.; Shapter, J. J.; Villamaina, D.; Vauthey, E. *Chem. Commun.* **2011**, *47*, 8226.
- [352] McDermott, A. G.; Larsen, G. S.; Budd, P. M.; Colina, C. M.; Runt, J. *Macromolecules* **2011**, *44*, 14.
- [353] Petrov, O. V.; Furó, I. *Prog. Nucl. Magn. Reson. Spectrosc.* **2009**, *54*, 97.
- [354] Tanaka, M.; Yoshioka, K.; Hirata, Y.; Fujumaki, M.; Kuwahara, M.; Niwa, O. *Langmuir* **2013**, *29*, 13111.
- [355] Chen, H.; Yang, Y.; Wang, Y.; Wu, L. *Chem. Eur. J.* **2013**, *19*, 11051.
- [356] Clar, E.; Zander, M. *J. Chem. Soc.* **1957**, 4616.
- [357] Tapia, R.; Torres, G.; Valderrama, J. A. *Synth. Commun.* **1986**, *16*, 681.
- [358] Hexemer, A.; Bras, W.; Glossinger, J.; Schaible, E.; Gann, E.; Kirian, R.; MacDowell, A.; Church, M.; Rude, B.; Padmore, H. *J. Phys.: Conf. Ser.* **2010**, *247*, 012007.
- [359] Ilavsky, J. *J. Appl. Crystallogr.* **2012**, *45*, 324.

Appendix A

Materials and Methods

A.1 Materials

A.1.1 Reagents and chemicals

Acetone (anhydrous, 99.9%), ammonium hexafluorophosphate, benzene- d_6 (99.6% atom D), 4,4-bipyridine, bromomethylbenzene, 1,3-bis(bromomethyl)benzene, 1,3,5-tris(bromomethyl)benzene, 4-*tert*-butylcatechol (98%), copper (I) chloride (99%), chloroform (anhydrous, 99%), chloroform- d_3 (99.5% atom D), 18-crown-6, diethylene glycol dimethyl ether (diglyme/G2, anhydrous, 99.5%), 1,2-dimethoxyethane (glyme/DME, anhydrous, 99.5%) 1,4-dioxane (anhydrous, 99.8%), diphenylphosphine (98%), ethanol (anhydrous, 99.5%), ethyl iodide, hexamethylphosphoramide (HMPA, 99%), hexanes (anhydrous, 99%), imidazole, lead(II) nitrate (99.99%), lead (II) oxide (99.999% trace metals grade), manganese (II) acetate (98%), *N,N*-dimethylformamide (DMF, anhydrous, 99.8%), *N,N*-dimethylformamide- d_7 (99.5% atom D), nitric acid (70%, 99.999% trace metals grade), 1-octadecene (90% tech. grade), octane (anhydrous, 99%), oleic acid (OA, 90% tech. grade), Pd/C, 3,4,9,10-perylene tetracarboxylic dianhydride, pyrogallol, potassium carbonate, propylene carbonate (PC, 99.7%, anhydrous), selenium (shot 99.999% trace metals grade and powder 99.99%), silver (I) hexafluorophosphate (99.99% trace metals grade), tetrabutylammonium hexafluorophosphate (TBAPF₆, 99.0%) tetraethylene glycol dimethyl ether (tetraglyme/G4, anhydrous), tetrafluoroterephthalonitrile (99%), tetrahydrofuran- d_8 (99.5% atom D), 3,3,3',3'-tetramethyl-1,1'-spirobisindane-5,5',6,6'-tetraol (96%), toluene (anhydrous, 99.8%), toluene- d_8 (99.6% atom D), *p*-toluenesulfonyl chloride, triethylene glycol dimethyl ether (triglyme/G3, anhydrous), α,α,α -trifluorotoluene (anhydrous, 99%), trimethylamine-*N*-oxide (98%), and zinc acetate dihydrate (99%) were obtained from Sigma-Aldrich. Boron trifluoride etherate (BF₃:Et₂O, 48% BF₃ basis) and oleylamine (OAm, 80-90%) were obtained from Acros Organics. Diethylene glycol monomethyl ether, lithium foil (99.9%, 1.5 and 0.75 mm thick), lithium nitrate, lithium sulfide (99.9% metals basis), nickel (II) 2,4-pentanedionate hydrate (95%), sulfur (Puratronic, 99.9995 % metals basis), and tri-*n*-octylphosphine (TOP, 90% tech. grade) were obtained from Alfa Aesar. Lithium bis(trifluoromethane)sulfonimide (LiTFSI) was purchased from 3M. Battery grade lithium hexafluorophosphate (LiPF₆) (99.9+%) was obtained from STREM Chemicals, Inc. Pb and Se standards for ICP-AES were obtained from Fluka. 2,6-Bis(4-azidobenzylidene)cyclohexanone (wetted with ca. 30% water, >90% purity) was obtained from TCI. Sodium oleate (97%) was obtained from Pfaltz & Bauer. Potassium hydroxide (ACS grade) and xylene (98.5%) were obtained from BDH chemicals. Chloroform (HPLC grade), isopropanol (99.9%) and methanol (99.8%) were obtained from EMD Millipore. Acetonitrile, *N,N*-dimethylformamide (DMF) and tetrahydrofuran (THF) were taken from a JC Meyer solvent system. Nanopure water with a minimum resistivity of 18 M Ω cm⁻¹ was used. Lead oleate was prepared by metathesis of lead(II) nitrate and sodium oleate. Di(ethylene glycol) monomethyl ether tosylate,^[354] tri(ethylene glycol) monomethyl ether tosylate,^[355] benzoperylene anhydride,^[356] and 20% HNO₃·SiO₂^[357] were synthesized according to literature procedures. All chemicals were

used as received unless otherwise noted.

A.1.2 Electrodes for Swagelok cells

Swagelok batteries were constructed using Swagelok unions purchased from Swagelok Northern California. Associated electrodes were made in-house from nickel 200 rods with outer diameters of 1.27 cm. Wells, which were 0.635 cm in diameter and 0.508 mm deep, were machined into the cathode current collectors. Gold was sputtered onto the cathode current collector surface. Anode current collectors were flat, bare nickel 200 surfaces.

A.1.3 Other materials

Carbon cloth was purchased from Fuel Cell Store, AvCarb1071HBC. Celgard[®] 2325 was purchased from MTI Corporation. Celgard[®] 2400 was obtained from Celgard (Charlotte, NC). Tonen separator was purchased from Tonen Chemical Corporation. Daramic[®] 175 was received as a free sample from Daramic (Charlotte, NC). Ketjen-black EC-600JD was purchased from AkzoNobel. Glassy carbon electrodes with 1 mm diameter were purchased from BAS Inc. (West Lafayette, IN) and polished before each experiment with 3- μm diamond paste. A custom-purposed glass H-cell with an aperture diameter of 1.6 cm for crossover measurements was obtained from Adams & Chittenden Scientific Glass (Berkeley, CA). Ag/Ag⁺ reference electrodes were purchased from CH instruments (Austin, TX) and filled with 10 mM silver (I) hexafluorophosphate in 0.5 M LiPF₆ in ACN (for experiments in ACN) or 0.1 M TBAPF₆ in PC or DME (for experiments in PC or DME, respectively). Gold interdigitated array (IDA) electrodes with 65 pairs of electrodes with width, length, and spacing of 10 μm , 2 mm, and 5 μm , respectively, were purchased from CH Instruments (Austin, TX, USA).

A.1.4 Preparation of electrolytes and polysulfides

All electrolytes used in this work consisted of LiTFSI, LiNO₃, LiPF₆, and/or TBAPF₆ in either diglyme, triglyme, tetraglyme, acetonitrile, propylene carbonate, or 1,2-dimethoxyethane. For all electrolytes, the solvents were dried over 3 Å molecular sieves until the water content was < 20 ppm H₂O. Furthermore, diglyme was tested for peroxides prior to use; if any were measured, it was stirred with alumina, filtered, and sparged with argon. The salts were all dried at elevated temperature under vacuum for 16 h at 150 °C, 110 °C, 100 °C, and 90 °C for LiTFSI, LiNO₃, LiPF₆, and TBAPF₆, respectively. This procedure resulted in electrolytes that were all < 30 ppm H₂O. Solutions of Li₂S₈ (2.50 mol S L⁻¹ in electrolyte) in the ethereal electrolytes were prepared by mixing Li₂S (0.287 g, 6.25 mmol), sulfur (1.40 g, 5.47 mmol), and 20 mL of electrolyte and heating at 60 °C until all solids were dissolved. Li₂S₈ solutions were kept at 60 °C in order to prevent precipitation of insoluble species and cooled to room temperature prior

to use. Cathode slurries with 5% *w/w* conductive additive were made by adding 30.8 mg of Ketjen-black to 500 μ L of Li_2S_8 solution and sonicating for 15 min.

A.2 Instrumentation

A.2.1 Spectroscopy

^1H , ^{13}C , and ^{19}F NMR spectra were recorded on Bruker Avance II 500 MHz, Varian Unity 500, and VXR 500 NMR spectrometers at 500 MHz for ^1H , 125 MHz for ^{13}C , and 470 MHz for ^{19}F . ^1H and ^{13}C chemical shifts were referenced with respect to residual solvent peaks (CD_3CN : 1.94 for ^1H , 1.32 for ^{13}C ; CDCl_3 : 7.26 for ^1H , 77.23 for ^{13}C ; $\text{DMSO-}d_6$: 2.50 for ^1H , 39.51 for ^{13}C ; $\text{THF-}d_8$: 1.72 for ^1H). ^{19}F shifts were internally referenced to α,α,α -trifluorotoluene (-63.72 ppm from CFCl_3) as a secondary standard. Coupling constants (J) are expressed in Hertz (Hz). Splitting patterns are designated as s(singlet), d(doublet), t(triplet), q(quartet), dd(doublet of doublets), and m(multiplet). Pb and Se content of NC samples were measured by ICP-AES on a Varian 720-ES spectrometer using an argon plasma. Prior to analysis, dried NC samples were digested in 70% nitric acid in a closed Teflon container for several days. UV-visible-NIR spectra were measured with a Cary 5000 UV-Vis-NIR spectrophotometer. FT-IR spectra were measured with a Perkin Elmer Spectrum One or Varian 3100 FT-IR spectrometer. *In situ* FT-IR spectroscopy of PIM-1 in the presence of lithium polysulfides was performed with a Mettler Toledo ReactIR 15 spectrometer.

A.2.2 Imaging

SEM images were obtained with a Zeiss Gemini Ultra-55 analytical scanning electron microscope equipped with in-lens and secondary electron detectors at a beam energy of 2–5 keV. EDX measurements were obtained on the same microscope using the equipped EDAX detector. TEM images were recorded on an Analytical JEOL-2100F FETEM equipped with a Gatan camera and using beam energy of 200 kV.

A.2.3 Electrochemistry

Electrochemical experiments and battery testing were conducted with a BioLogic VMP3 potentiostat and Arbin 2043 battery cycler. Cyclic voltammograms were acquired with iR drop compensation by measuring the uncompensated resistance with a 100 kHz impedance measurement and correcting for 85% of the expected drop.

A.2.4 Mass spectrometry

High-resolution ESI-MS spectra were obtained on Bruker microTOF Q and Synapt G2 Q-ToF high-resolution mass spectrometers. High-resolution ESI-MS was also performed

by the University of California, Berkeley QB3/Chemistry Mass Spectrometry Facility. MALDI-TOF mass spectrometry was obtained with an AB SCIEX TF4800 MALDI TOF-TOF Mass Spectrometer. Low- and high-resolution EI mass spectra were recorded on a Micromass 70-VSE spectrometer.

A.2.5 Other instrumentation and general details

Unless otherwise mentioned, all manipulations were performed in an argon or nitrogen glovebox with oxygen and water levels below 5 and 1 ppm, respectively. Zeta potentials were measured in DMF on a Malvern Zetasizer Nano ZS. XRD patterns were recorded on a Bruker Gadds-8 diffractometer with Cu-K α source operating at 40 kV and 20 mA. Grazing incidence small angle X-ray scattering measurements were made at beamline 7.3.3 of the Advanced Light Source, Lawrence Berkeley National Laboratory, using an incident angle of 0.16°, a wavelength of 0.124 nm (10 keV), a detector distance of 3.9 m, and recorded on a Pilatus 1M flat detector.^[358] The resulting data were processed with the Nika 2D SAS software package in Igor Pro.^[359] Water content was tested with a Mettler Toledo C20 Coulometric KF Titrator Karl-Fischer apparatus. Elemental analyses were performed by the University of California, Berkeley College of Chemistry Microanalytical Facility. Column chromatography was performed using Biotage HPFC SP4 Flash Purification System with Biotage SNAP cartridges containing KP-Sil. Ellipsometric porosimetry (EP) was performed on a Semilab PS-1100 instrument with toluene or isopropanol. Weight average (M_w) and number average (M_n) polymer molecular weight were measured using size-exclusion chromatography using a Malvern Viscotek TDA 302 system operating with either a THF or a CHCl₃ mobile phase and calibrated with a 99 kDa monodisperse polystyrene standard. Nitrogen adsorption measurements were performed at liquid nitrogen temperature (~77 K) with a Micromeritics Tristar II 3020 adsorption system.

Appendix B

Theory

B.1 Crossover analysis

B.1.1 Calculation of D_{eff} from measured $C(t)$

At any moment, the flux of active-species across the membrane (J , mmol cm⁻² s⁻¹) can be described with Fick's first law:

$$J = D_{eff} \frac{\partial C}{\partial x} = D_{eff} \frac{C_{retentate}(t) - C_{permeate}(t)}{l}$$

Where D_{eff} is the effective diffusion coefficient in cm² s⁻¹, C is the concentration in mmol cm⁻³ and l is the membrane thickness in cm. For short times, the difference $C_{retentate}(t) - C_{permeate}(t)$ does not change significantly from its initial value of $C_{retentate}(t_0) - C_{permeate}(t_0) = C_0$, and the flux is constant with time:

$$J(t \approx 0) = D_{eff} \frac{C_0}{l}$$

The concentration of active species in the permeate compartment can be calculated by integrating the flux of active species over time from 0 to t , multiplying by the membrane area, A , and dividing by the volume of solution in the permeate compartment, $V_{permeate}$:

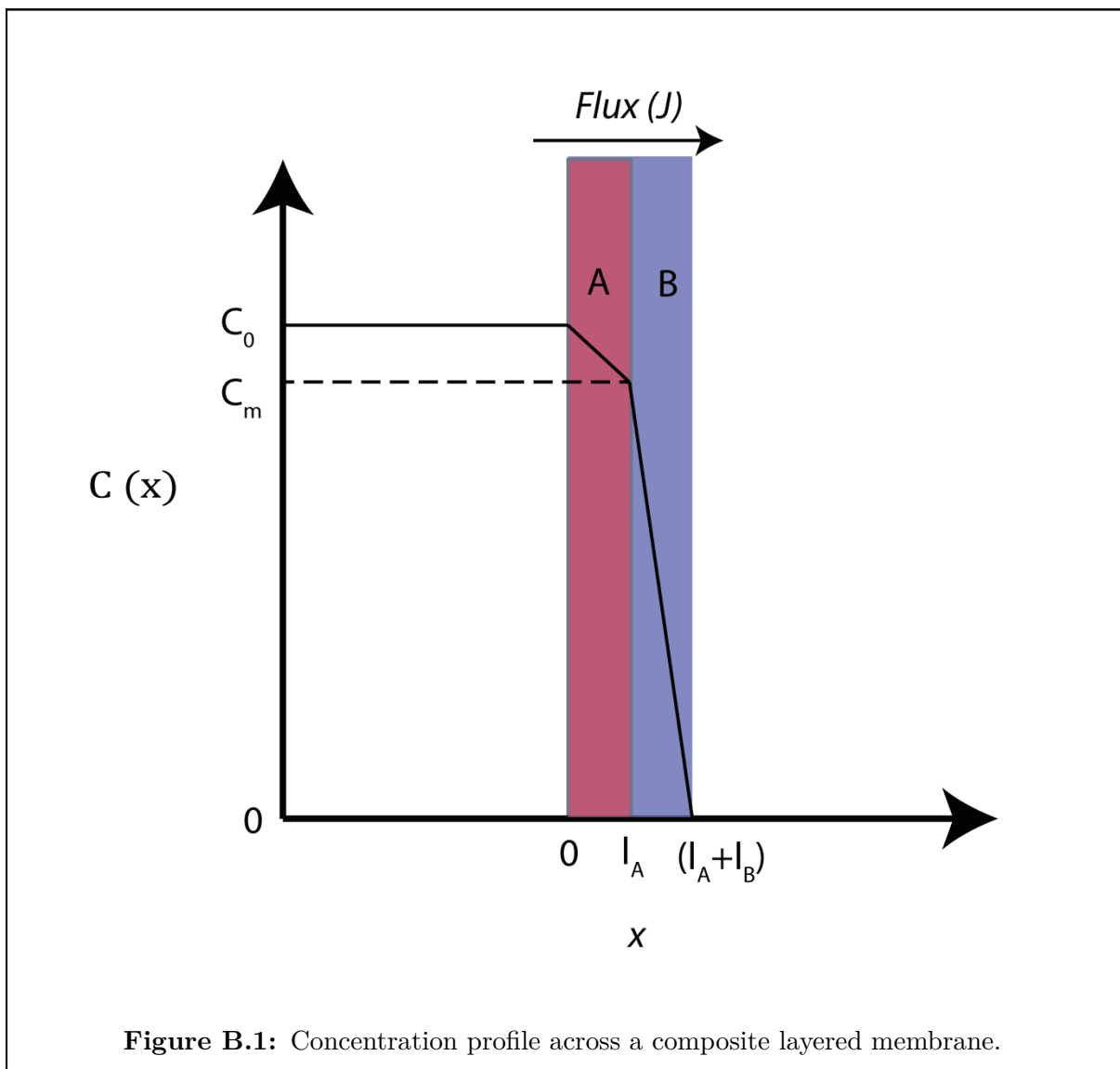
$$C_{permeate}(t) = \frac{A \int_0^t J(t) dt}{V_{permeate}} = \frac{D_{eff} C_0 A}{l V_{permeate}} t$$

By measuring active-species concentration in the permeate compartment and plotting these values as a function of time, the effective diffusion coefficient of the active-species through the membrane can be quantified.

B.1.2 Calculation of D_{eff} for multi-layer membranes

It is occasionally useful to prepare composite membranes with a layered structure for improved mechanical properties or selectivity. For these materials, the above derivation can be modified to account for the layered structure as follows:

Consider the layered structure depicted in Figure B.1. The structure consists of two materials, labelled A and B, which have different transport properties. Each layer has its own thickness and effective diffusion coefficient of active material, denoted as $l_{A/B}$ and $D_{eff,A/B}$, respectively. The retentate solution is shown to the left of the layered structure, and the permeate solution is on the right. The concentration as a function of location (for $t \sim 0$) is superimposed on the structure. As above, the initial concentration of active species in the retentate is C_0 , and the concentration of active species at the interface between A and B is termed C_m . At any moment in time, there is a flux of active material through A and B (termed J_A and J_B) that is proportional to the effective diffusion coefficient through A or B and the concentration gradient across A or B. By introducing a steady-state approximation, we can set $J_A = J_B = J_{Total}$, where:



$$J_A = D_{eff,A} \frac{C_0 - C_m}{l_A}$$

$$J_B = D_{eff,B} \frac{C_m}{l_B}$$

$$J_{Total} = D_{eff,Total} \frac{C_0}{l_{Total}}$$

This set of equations allows us to solve for the transport properties of one of the layers A or B, provided that the properties of the other layer are already known. This is the case for supported membranes on inert porous supports, where the transport properties of the porous support are readily measured. First, C_m can be solved for from the equality $J_{Total} = J_B$ to give:

$$C_m = \left(\frac{D_{eff,Total}}{D_{eff,B}} \right) \left(\frac{C_0 l_B}{l_{Total}} \right)$$

Next, substitution of this quantity for C_m in the equality $J_{Total} = J_A$ and solving for $D_{eff,A}$ yields:

$$D_{eff,A} = \frac{D_{eff,Total} C_0 l_A}{l_{Total} \left(C_0 - \left(\frac{D_{eff,Total}}{D_{eff,B}} \right) \left(\frac{C_0 l_B}{l_{Total}} \right) \right)}$$

B.2 Membrane ionic conductivity

Membranes with a diameter of 14 mm were soaked in electrolyte and sandwiched between two 12 mm diameter stainless steel electrodes in a Swagelok cell, with the excess membrane folded around one of the electrodes. Electrochemical impedance spectra were acquired at a 0 V DC bias and 10 mV AC bias from 200 kHz to 1 kHz. The data were fitted to an equivalent circuit (Fig. B.2) with the EC-Lab software by minimizing the fitting error, χ^2 given by $\chi^2 = \sum_i \frac{(Z_{meas}(f_i) - Z_{fit}(f_i))^2}{|Z_{meas}(f_i)|}$. The equivalent circuit accounts for the resistance and inductance of the wiring connecting the potentiostat and the conductivity cell, which were measured to be 0.34 Ω and 2.7×10^{-6} H, respectively. All capacitors were modeled as constant phase elements, which have an impedance given by $Z(f) = [Q(j2\pi f)^\alpha]^{-1}$. When α is 0, the CPE acts as a perfect resistor, and when α is 1, it acts as a perfect capacitor. For intermediate values of α , the CPE acts as a “leaky capacitor.” The membrane conductivity was calculated from the membrane resistance using the relation $\sigma = l(A R_M)^{-1}$, where σ is the membrane conductivity in S cm^{-1} , l is the membrane thickness in cm, A is the electrode area in cm^2 , and R_M is the membrane resistance in Ω .

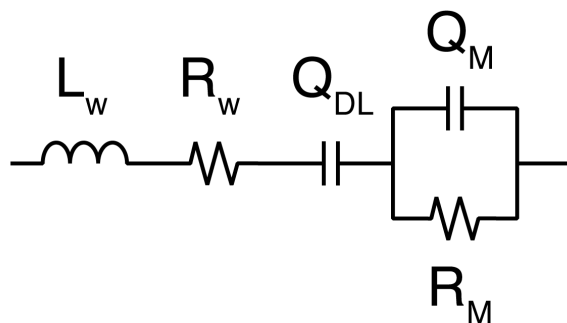


Figure B.2: Equivalent circuit used to model electrochemical impedance spectra of membranes soaked in electrolyte. R_w and L_w correspond to the resistance and inductance of the wiring leading from the potentiostat to the conductivity cell, respectively. Q_{DL} and Q_M correspond to the double layer and membrane capacitances, respectively, and R_M corresponds to the ionic resistance of the membrane.